University of Cambridge

Materials, photophysics and device designs for high efficiency photovoltaics

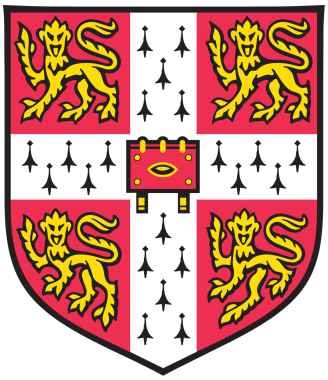

Arfa Husainali Karani
Department of Physics: Cavendish Laboratory

A thesis submitted for the degree of
Doctor of Philosophy

Homerton College May 2019

Declaration

I hereby declare that except where specific reference is made to the work of others, the contents of this dissertation are original and have not been submitted in whole or in part for consideration for any other degree or qualification in this, or any other University. This dissertation is the result of my own work and includes nothing which is the outcome of work done in collaboration, except where specifically indicated in the text or Acknowledgements. I further state that no substantial part of my dissertation has already been submitted, or, is being concurrently submitted for any such degree, diploma or other qualification at the University of Cambridge or any other University or similar institution except as specified in the text. This dissertation contains fewer than 60,000 words including appendices, bibliography, footnotes, tables and equations and has less than 150 figures.

Abstract

Author: Arfa Husainali Karani

Title: Materials, photophysics and device designs for high efficiency photovoltaics.

The development of inexpensive and sustainable renewable energy technologies is of critical importance in fulfilling rapidly growing global energy demand. The seriousness of this endeavour is also amplified by the urgent need to eliminate the usage of fossil-fuels. In the recent past, the cost of power generated using solar photovoltaics (PVs) has dropped below that of power generated by oil and gas, making them an attractive candidate in the renewable energy market.

The Shockley-Queisser limit (S-Q limit), also known as the detailed balance limit, refers to the maximum theoretical efficiency that can be achieved using a single p-n junction solar cell. Silicon PVs, which account for about 90 % of the solar-PVs market share, have achieved an overall power conversion efficiency of $\sim 27\,\%$ which is very close to its threshold S-Q limit of $\sim 30\,\%$. Therefore, in order to further reduce the cost of solar power, it is essential to find technologies capable of surpassing the S-Q limit. In this thesis we discuss three main strategies for surpassing the S-Q limit: (i) tandem solar cells, (ii) singlet fission sensitized solar cells and (iii) triplet-triplet annihilation assisted upconversion.

Following a review of the relevant background theory for organic semiconductors, colloidal quantum dot (CQD) semiconductors and perovskite semiconductors, we discuss their applications in inexpensive, solution-processed, optoelectronic devices. We commence by demonstrating the first prototype of a solution-processed, monolithic tandem solar cell with perovskite and CQDs as the top-cell and bottom-cell active materials respectively. Using a detailed balance model we show that the radiative coupling between the two sub-cells can result in an absolute gain of $\sim 11\,\%$ in the tandem cells efficiency. Next, we study a novel solution-processed pentacene precursor for applications in singlet fission sensitized photovoltaics and photon downconversion systems. We observe significant contribution from singlet fission to the photocurrent generated in these devices. Finally, we study organic light-emitting diodes (OLEDs) that are prepared using an efficient singlet fission (SF) molecule to investigate the physics of triplet-triplet annihilation (TTA) in such molecules. We develop a kinetic model based on the Merrifield theory to explain the magnetic-field effect on SF and TTA in these OLEDs.

To my parents...

Acknowledgements

I would like to first express immense gratitude for having had the opportunity to experience the intellectually stimulating environment at the University of Cambridge. I would like to thank Professor Neil Greenham, my supervisor, for providing me with the opportunity to pursue a PhD under his guidance and supervision - thank you for all the stimulating scientific discussions and guidance throughout my PhD. I'm also very grateful for the generous financial support from the Nehru Trust, the Trinity Henry-Barlow scholarship, the Haidar Scholarship and the sponsorship from Rana Denim Pvt. Ltd.

I extend my deep gratitude to Dr. Le Yang and Dr. Dawei Di for constantly guiding me and working by my side to realise an almost impossible project- thank you for teaching me the art of science! I would also like to thank Dr. Maxim Tabachnyk, Dr. Marcus Boehm, Dr. Tom Jellico, Dr. Zhilong Zhang, Dr. Renren Deng and James Xiao for collaborations on various projects and for helping me learn the intricacies of quantum dot chemistry and providing materials for research presented in this thesis. I would like to thank Dr. Andrew Pearson for encouraging me and helping me learn techniques for analysing film morphologies in my first year. To Emrys Evans and Stuart Macpherson - thanks for helping me build the magneto-EL setup which has resulted in some novel insights into singlet fission LEDs presented in this thesis.

Working to reinstate the SPIE student chapter and then leading it with Jiangbin Zhang, Haralds Abolins, Sascha Feldmann, Dale Waterhouse and Qifei Gu has been a great experience and it has helped me develop many interpersonal skills for which I'm very grateful. I would also like to thank the Energy@Cambridge strategic group, Isaac Newton Trust and the Energy Policy Research Group for allowing me the opportunity to carry out a one-off research project in Tanzania to study the off-grid solar market and gain inspiration for my PhD research. These activities including working with Innovation Forum to bridge the gap between academia and industry with Dr. Mareky Tyl, Dr. Yi Lei Tan, Yiyun Zhang and Benjamin Droguet have helped me understand my responsibility as a scientist. I would like to thank all these people for being wonderful colleagues and friends throughout my PhD and the time here in Cambridge.

I would like to specially thank my dear friend Dr. Le Yang for teaching me many of the experimental techniques I know today, including logging my work regularly and organizing it to make the PhD an enjoyable rather than a stressful experience. Her support and

motivation through the toughest times have truly kept me going! I would like to extend immense gratitude to Alexandre Daoud for being a true friend, an inspiration, my LaTeX teacher and an invincible pillar of support through all the ups and downs during my journey.

I would also like to mention and thank the important role-models from OE: Dr. Hannah Stern, Dr. Leah Weiss, Dr. Baodan Zhao, Heather Goodwin and Dr. Le Yang who have been a constant source of inspiration and have lead the way for female scientists with utmost elegance. I'm grateful for having had the chance to work with an incredible pool of driven scientists at OE and would like to thank them for making my experience in this lab a memorable one.

Finally, I would like to thank my family and all my close friends without whom I wouldn't have been able to overcome the toughest of days during the course of my PhD. My father for constantly supporting me and my mother for having this vision for me and my sister- thank you! Also, a big thank you to my little sister for being a true inspiration and a source of joy through the past few years!

Contents

List of Figures

Chapter 1

Introduction

Considering the urgency of swiftly commercialising photovoltaics (PVs) in the context of climate change [1], it is of significant importance to develop sustainable and efficient photovoltaics at low cost. In 2017, energy generated by solar photovoltaics reached 460 TWh which is about 2 % of the global energy output (IEA, 2019). In order to further increase the adaptation of solar photovoltaics in the energy industry it is essential to develop affordable, efficient and easily scalable technologies. The majority of the costs of solar PVs come from the additional hardware required along with the PV module (including cables/wiring, insulation materials, etc) and installation costs (electrical, mechanical) which all scale with the area of the PV module. Furthermore, the cost of the semiconductor active layer used in a solar cell can change with different semiconductors but the overall module cost are still dominated by the other layers. Thus improving the power conversion efficiency of the PV module itself can significantly reduce the solar electricity costs. The Shockley-Queisser limit (S-Q limit) also known as the detailed balance limit refers to the maximum theoretical efficiency that can be achieved using a single p-n junction solar cell [2]. For silicon solar cells, which account for about 95 % of the total global production (Fraunhofer ISE, 2019) of PV technologies, this S-Q limit is calculated to be $\approx$ 30 %. In this work, we investigate different materials, mechanisms and devices and study the underlying photophysical processes to provide pathways for surpassing the S-Q limit.

Multijunction tandem solar cells have successfully achieved efficiencies as high as 38.8 % using III-V semiconductors [3]. However, complex fabrication processes make large-scale production of such photovoltaics uneconomical. Solar PVs based on solution processable materials including lead chalcogenide CQDs, perovskites and organic materials provide promising alternatives to the traditional inorganic PVs. Low-temperature and high-throughput processing of these materials along with abundance of availability promise great potential for such technologies although it is also important to carefully consider the limitations of these materials. Presently the cost of chemical synthesis of these materials (CQDs and organic compounds for transport layers in perovskite devices)

is relatively high. However, some strategies to make these solution processed technologies commercially viable are discussed in detail references [4, 5]. In Chapter 4 we demonstrate the first prototype of a monolithic, solution processable tandem solar cell using perovskite and colloidal quantum dots (CQDs) as an affordable alternative. Using methylammonimum lead iodide ($MAPbI_3$, 1.55 eV bandgap) and lead sulphide (PbS) CQDs (1.0 eV bandgap) as the active materials, we calculate theoretical efficiency of 43 % under 1-sun illumination. Interestingly, we find that radiative coupling between these two luminescent active materials contributes substantially (> 11 % absolute gain) to the total efficiency, via photon recycling [6]. Using the insights from this model we design a monolithic tandem solar cell employing luminescent materials. We describe the device fabrication process and performance in detail and discuss the challenges of realising a monolithic tandem solar cell with multiple solution-processed layers. Although our monolithic tandem solar cells were limited at 1 % PCE, combining the theoretical model with the state-of-art data from literature in Section 4.4, we project that a power conversion efficiency of 29 % can be achieved using $MAPbI_3$ as the top-cell semiconductor and PbS CQDs as the bottom-cell semiconductor in a two-terminal tandem architecture, proposed by our work.

While tandem solar cells address the concept of harvesting photons from all regions of the solar spectrum, singlet fission (SF) is a mechanism that ensures efficient utilisation of every harvested high-energy photon [7]. Known to occur in organic semiconductors, singlet fission is a process whereby a singlet exciton (generated by absorption of high-energy photon) splits into two low-energy triplet excitons. SF is shown to be up to 200 % efficient in some acenes [8–10].

Pentacene is one of the most commonly used singlet fission sensitizer for solar cells [11–13]. Triplet diffusion is limited to ≈ 40 nm [14] in the singlet-fission domains of SF sensitized solar cells made using pentacene. Thus, SF-generated triplet excitons need to be separated into individual charges within this distance in order to employ pentacene in solar cells. However, poor solubility of these molecules in organic solvents means that they cannot be deposited via solution processing and hence have to deposited via vacuum deposition. This restricts the active layer design to a layered structure as opposed to bulk heterojunction. This further limits the overall performance of pentacene solar cells as the SF layer thicknesses cannot exceed the triplet diffusion length scales of ~ 40 nm thus limiting the amount of light that can be absorbed in such devices.

Although various substituted pentacene molecules like triisopropylsilyethynyl-pentacene

(TIPS-pc) are used to enhance the solubility of the core pentacene molecule, the bulky side groups provide steric hindrance affecting the carrier mobilities in thin films [15]. In Chapter 5, we propose a novel solution-processed precursor (p-Pc) that fully converts to pentacene on annealing at temperatures $> 150\,^{\circ}\mathrm{C}$ in solid state, to develop bulk heterojunction solar cells with pentacene. We demonstrate that SF is still found to be 200 % efficient in thin-films prepared from p-Pc and the triplet lifetimes are calculated to be $\approx 4\,\mathrm{ns}$ in our published work [8]. We report on incorporating p-Pc into bilayer, bulk heterojunction and hybrid solar cells using C_{60}, phenyl-C_{61}-butyric acid methyl ester (PCBM), lead-sulfide (PbS) and lead-selenide (PbSe) CQDs as electron acceptors respectively. We find that defect states in p-Pc films prevent efficient extraction of triplets in our devices. We also explore the prospects of incorporating p-Pc in a downconversion system using CQDs sensitized p-Pc films as a photon multiplier and learn that the annealing step of pentacene precursor conversion results in CQD aggregation. We thus propose using novel organogel matrices as an innovative nanostructure to suspend CQDs without aggregation.

Triplet-triplet annihilation (TTA) or triplet-fusion is the reverse process of singlet fission whereby two low-energy triplet excitons annihilate to form a singlet exciton [16]. TTA is investigated as an important strategy to enhance solar cell performances by capturing photons with energies lower than the active-semiconductor bandgap [17, 18]. In organic light-emitting diodes (OLEDs), presence of TTA in the active layer is known to enhance their external quantum efficiencies [19, 20]. An OLED can thus be thought of as an electrical upconversion system where both singlets and triplets can be generated via electrical excitation and TTA can occur if the energetics are favourable. Di et al. recently observed significant contribution from TTA to electroluminescence (EL) of TIPS-pc doped organic light-emitting diodes (OLEDs) [21]. In order to investigate this capability of an efficient SF molecule to undergo TTA and understand the underlying spin-dependent photophysics we study the magnetic-field effects on the electroluminescence from these OLEDs in Chapter 6.

Bibliography

1. Allen, M., Antwi-Agyei, P., Aragon-Durand, F., Babiker, M., Bertoldi, P., Bind, M., Brown, S., Buckeridge, M., Camilloni, I., Cartwright, A. *et al. Technical Summary: Global warming of* 1.5 °*C.* (Intergovernmental Panel on Climate Change, 2019).

2. Shockley, W. & Queisser, H. J. Detailed balance limit of efficiency of p-n junction solar cells. *Journal of Applied Physics* **32,** 510–519 (1961).

3. Chiu, P., Law, D., Woo, R., Singer, S., Bhusari, D., Hong, W., Zakaria, A., Boisvert, J., Mesropian, S., King, R. *et al.* 35.8 % *space and* 38.8 % *terrestrial 5J direct bonded cells* in *2014 IEEE 40th Photovoltaic Specialist Conference (PVSC)* (2014), 0011–0013.

4. Jean, J., Xiao, J., Nick, R., Moody, N., Nasilowski, M., Bawendi, M. & Bulović, V. Synthesis cost dictates the commercial viability of lead sulfide and perovskite quantum dot photovoltaics. *Energy & Environmental Science* **11,** 2295–2305 (2018).

5. Huang, F., Li, M., Siffalovic, P., Cao, G. & Tian, J. From scalable solution fabrication of perovskite films towards commercialization of solar cells. *Energy & Environmental Science* **12,** 518–549 (2019).

6. Karani, A., Yang, L., Bai, S., Futscher, M. H., Snaith, H. J., Ehrler, B., Greenham, N. C. & Di, D. Perovskite/colloidal quantum dot tandem solar cells: theoretical modeling and monolithic structure. *ACS Energy Letters* **3,** 869–874 (2018).

7. Smith, M. B. & Michl, J. Singlet fission. *Chemical Reviews* **110,** 6891–6936 (2010).

8. Tabachnyk, M., Karani, A. H., Broch, K., Pazos-Outón, L. M., Xiao, J., Jellicoe, T. C., Novák, J., Harkin, D., Pearson, A. J., Rao, A. *et al.* Efficient singlet exciton fission in pentacene prepared from a soluble precursor. *APL Materials* **4,** 116112 (2016).

9. Zimmerman, P. M., Zhang, Z. & Musgrave, C. B. Singlet fission in pentacene through multi-exciton quantum states. *Nature Chemistry* **2,** 648 (2010).

10. Walker, B. J., Musser, A. J., Beljonne, D. & Friend, R. H. Singlet exciton fission in solution. *Nature Chemistry* **5,** 1019 (2013).

11. Ehrler, B., Walker, B. J., Böhm, M. L., Wilson, M. W., Vaynzof, Y., Friend, R. H. & Greenham, N. C. In situ measurement of exciton energy in hybrid singlet-fission solar cells. *Nature Communications* **3,** 1019 (2012).

12. Congreve, D. N., Lee, J., Thompson, N. J., Hontz, E., Yost, S. R., Reusswig, P. D., Bahlke, M. E., Reineke, S., Van Voorhis, T. & Baldo, M. A. External quantum efficiency above 100% in a singlet-exciton-fission–based organic photovoltaic cell. *Science* **340,** 334–337 (2013).

13. Yang, L., Tabachnyk, M., Bayliss, S. L., Böhm, M. L., Broch, K., Greenham, N. C., Friend, R. H. & Ehrler, B. Solution-processable singlet fission photovoltaic devices. *Nano Letters* **15,** 354–358 (2014).

14. Tabachnyk, M., Ehrler, B., Bayliss, S., Friend, R. H. & Greenham, N. C. Triplet diffusion in singlet exciton fission sensitized pentacene solar cells. *Applied Physics Letters* **103,** 190_1 (2013).

15. Giri, G., Verploegen, E., Mannsfeld, S. C., Atahan-Evrenk, S., Kim, D. H., Lee, S. Y., Becerril, H. A., Aspuru-Guzik, A., Toney, M. F. & Bao, Z. Tuning charge transport in solution-sheared organic semiconductors using lattice strain. *Nature* **480,** 504 (2011).

16. Merrifield, R. Diffusion and mutual annihilation of triplet excitons in organic crystals. *Accounts of Chemical Research* **1,** 129–135 (1968).

17. Singh-Rachford, T. N. & Castellano, F. N. Photon upconversion based on sensitized triplet–triplet annihilation. *Coordination Chemistry Reviews* **254,** 2560–2573 (2010).

18. Wu, M., Congreve, D. N., Wilson, M. W., Jean, J., Geva, N., Welborn, M., Van Voorhis, T., Bulović, V., Bawendi, M. G. & Baldo, M. A. Solid-state infrared-to-visible upconversion sensitized by colloidal nanocrystals. *Nature Photonics* **10,** 31 (2016).

19. Kondakov, D. Characterization of triplet-triplet annihilation in organic light-emitting diodes based on anthracene derivatives. *Journal of Applied Physics* **102,** 114504 (2007).

20. Wallikewitz, B. H., Kabra, D., Gélinas, S. & Friend, R. H. Triplet dynamics in fluorescent polymer light-emitting diodes. *Physical Review B* **85,** 045209 (2012).

21. Di, D., Yang, L., Richter, J. M., Meraldi, L., Altamimi, R. M., Alyamani, A. Y., Credgington, D., Musselman, K. P., MacManus-Driscoll, J. L. & Friend, R. H. Efficient Triplet Exciton Fusion in Molecularly Doped Polymer Light-Emitting Diodes. *Advanced Materials* **29,** 1605987 (2017).

Chapter 2

Background

In this chapter, we review the three types of semiconductor materials studied in this thesis and provide the theoretical tools to understand their optoelectronic properties. We mainly focus on the theory required to explain the excitons formed in organic semiconductors as a lot of the work in this thesis focuses on harvesting the triplets formed via singlet fission and also on the reverse process of triplet fusion forming singlets. We begin by looking at the organic semiconductors and discuss their electronic structure, types of prevalent electronic transitions and excitation transport in solid films used for applications in optoelectronic devices. Next, we review the quantum confinement properties of colloidal quantum dots and discuss the type of excitations and transport properties of this material class. Finally we discuss the advantages and disadvantages of perovskite crystal structures and review the properties which make perovskites an attractive candidate for application in highly efficient solar cells.

2.1 Organic Semiconductors

Organic semiconductors are mainly composed of hydrogen and carbon atoms. Each carbon in the molecule has six electrons and each hydrogen atom adds an additional electron. In this section we will describe the theoretical tools required to explain the interaction of light with such many-body systems.

2.1.1 Electronic Structure

2.1.1.1 Many-body system

Using quantum mechanics, we can define the total energy of many-body systems using a Hamiltonian. For systems containing multiple nuclei (n) and electrons (e) for example, a molecule, we define this Hamiltonian as

$$\hat{H} = \hat{H}_{n-n} + \hat{H}_{n-e} + \hat{H}_{e-e}\,, \tag{2.1}$$

where $\hat{H}_{n-n}$ defines the inter-nuclear, $\hat{H}_{n-e}$ the nuclear-electron and $\hat{H}_{e-e}$ the electron-electron interaction respectively. Each of these terms can be defined by considering the kinetic energy of each particle involved and the coulomb interaction between each pair as follows

$$\hat{H}_{n-n} = \sum_{\alpha} \frac{P_{\alpha}^2}{2M_{\alpha}} + \frac{1}{8\pi\varepsilon_0} \sum_{\alpha \neq \beta} \frac{Z_{\alpha} Z_{\beta} q^2}{|R_{\alpha} - R_{\beta}|} \,, \tag{2.2}$$

$$\hat{H}_{n-e} = -\frac{1}{8\pi\varepsilon_0} \sum_{\alpha,i} \frac{Z_{\alpha} q^2}{|R_{\alpha} - r_i|} \,, \tag{2.3}$$

$$\hat{H}_{e-e} = \sum_{i} \frac{p_i^2}{2m_i} + \frac{1}{8\pi\varepsilon_0} \sum_{i \neq j} \frac{q^2}{|r_i - r_j|} \,, \tag{2.4}$$

where ε_0 is the vacuum permittivity, $\{R_{\alpha}, M_{\alpha}, P_{\alpha}, Z_{\alpha} q\}$ and $\{r_i, m_e, p_i, q\}$ represent the position, mass, momentum and charge of the nuclei and electrons respectively [1].

Solving the time-independent Shrödinger equation for a molecular state wavefunction $\Psi(r, R)$ given by

$$\hat{H}\Psi(r, R) = E\Psi(R, r) \,, \tag{2.5}$$

where E is the energy of the molecular state $\Psi(r, R)$, we can get information about the energetic structure of the molecule. However considering the complexity of the Hamiltonian, we will now discuss the necessary approximations that allow us to treat the weaker interactions perturbatively.

We begin with the *Born-Oppenheimer (BO) approximation* [2] which allows us to decouple the motion of the nucleus and the electrons. Considering that the mass of an electron is much smaller (approximately 10^3 times) than that of the nuclei, the motion of the two is well-separated in time. Therefore the electrons experience a static nuclear potential whereas the nuclei experience an effective Coulomb screening due to the average configuration of the surrounding electrons. Thus, considering a static nuclear position R and separating the molecular state wavefunction into nuclear and electronic wavefunctions as $\Psi_{n,e} = |\phi_n(R)\rangle \, |\phi_e(r, R)\rangle$ we can write for the electronic wavefunction

$$\hat{H}_{BO} \, |\phi_e\rangle = E \, |\phi_e\rangle \ , \tag{2.6}$$

where $\hat{H}_{BO}$ is the Born-Oppenheimer Hamiltonian given by

$$[V_{\text{eff}}(r, R) + \hat{H}_{n-e}(r, R) + \hat{H}_{e-e}(r, R)] \, |\phi_e(r, R)\rangle = E \, |\phi_e(r, R)\rangle \ ; \tag{2.7}$$

V_{eff} is the effective nuclear potential for a given electron and nuclear positions r and R respectively; and $|\phi_e(r, R)\rangle$ is the electronic wavefunction which depends parametrically on

the nuclear configuration. This approach allows us to begin by solving for single-electron wavefunction using

$$\hat{H}_{BO} = \frac{p_e^2}{2m_e} + V_{\text{eff}}(r, R)\,, \tag{2.8}$$

where V_{eff} is the effective static nuclear potential for a position R and the first term is the kinetic energy of an electron. The other electrons can then be added by modifying the dielectric screening of the nuclear potential. The BO approximation provides a tractable starting point for understanding the electronic states in molecules. However, this approximation breaks down when the electronic energy splitting approaches nuclear vibration frequencies and as the electronic manifolds approach degeneracy.

2.1.1.2 Atomic and molecular orbitals

The notation $n(\alpha_l)^m$ is used to denote the electronic configuration in any atom where n is the principal quantum number (or the electronic shell number), $l = 0, 1, 2, ...$ is the orbital angular momentum quantum number and m is the number of electrons occupying the electronic state. α_l ={s,p,d,f,...} is the spectroscopic notation which denotes distinct spatial electron probability distributions. Hydrogen and carbon atoms form the backbone of organic molecules and we can write the electronic configuration in these atoms as 1s for hydrogen and $1s^2 2s^2 2p^2$ for carbon. The only electron in hydrogen occupies the first s-orbital and in carbon the first two electrons occupy the 1s orbital, the next two occupy the 2s orbital and the final two electrons occupy the 2p orbital. While the s-orbitals are spherically symmetric, the p-orbitals are dumbbell shaped with lobes aligned in a particular (x, y or z) direction as shown in Figure 2.1.

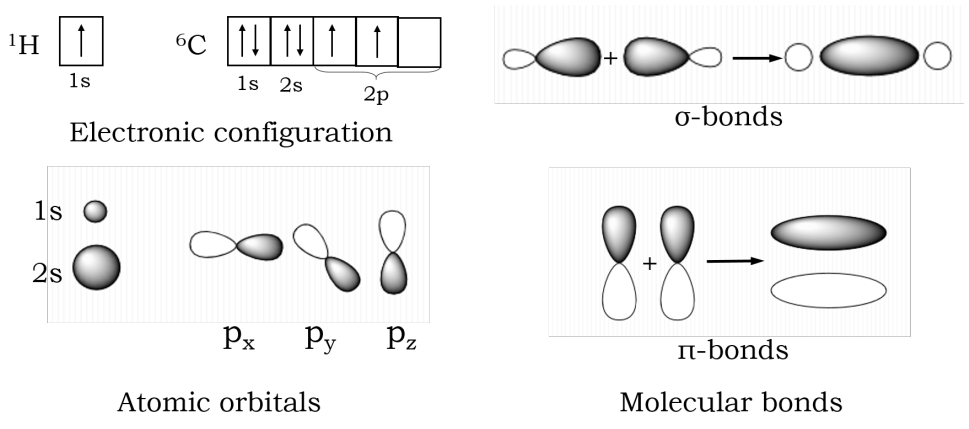

Figure 2.1: Illustration of atomic orbitals and molecular bonds.

In molecules, the individual atomic orbitals are altered in the presence of other atoms.

Thus molecular orbitals can be formed by using the LCOA (linear combination of atomic orbitals) approximation whereby depending on the energy gain from bond formation with surrounding atoms, new orbitals can be formed. Atomic orbital hybridization specifically for the s- and p-orbitals in carbon-based molecules are of three types: sp, sp^2 and sp^3 where the superscript describes the number of p-orbitals participating in the hybridization. sp hybridization is found in acetylene (H−C≡C−H), a linear molecule, sp^2 in ethylene ($H_2C{=}CH_2$), a planar molecule and sp^3 in methane (CH_4), a tetrahedral molecule. The hybridized orbitals are called $\sigma-$orbitals and the unhybridized p-orbitals are called $\pi-$orbitals. The $\sigma-$orbitals have cylindrical symmetry along the bonding axis and thus are highly directional and form strong covalent bonds. The $\pi-$orbitals are orthogonal to the $\sigma-$orbitals thus obstructing the molecular rotation around the bond axis. Thus atomic orbital hybridization allows directional optimization and energy gain for molecular bonds (see Figure 2.1).

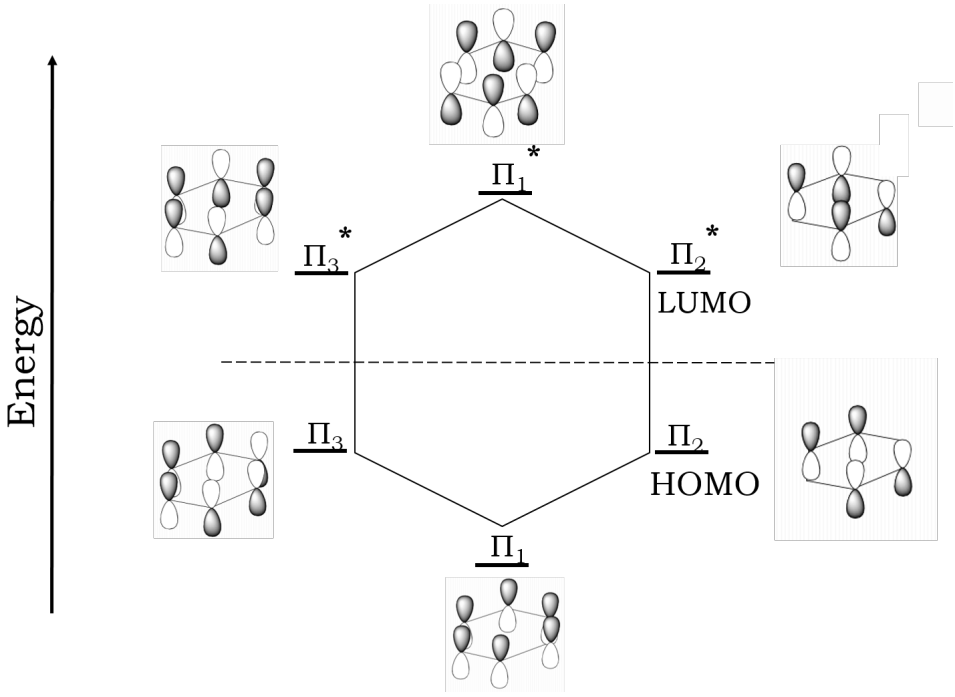

Figure 2.2: Illustration of σ and π bonds formation in Benzene molecule. The blue shaded lobes indicate filled π-orbitals.

The strength of the carbon-based molecules is around 10 eV, and these bonds define the molecular structure. The electrons in σ bonds however, do not participate in optical processes on interaction with sunlight as photons from the solar irradiation have energies between 1 eV to 3 eV. It is the electrons in the unhybridized π orbitals, which can overlap and delocalize over multiple carbon atoms thus resulting in *conjugation*, that provide organic semiconductors their optoelectronic properties. Electronic conjugation between

multiple atoms results in formation of bonding (π) states where the $\pi-$orbitals are in phase with each other and anti-bonding (π^*) states when they are not in phase. Figure 2.2 demonstrates the highest occupied molecular orbital (HOMO) and the lowest unoccupied molecular orbital (LUMO) in a benzene ring based on these bonding and anti-bonding states. Extended regions of bonding and anti-bonding states cause broadening of state energies thus providing an analogue to a 'bandgap' in conventional semiconductors based on the energy difference between the HOMO and the LUMO [3].

The single-electron Hamiltonian described earlier in equation 2.8 can be rewritten in terms of a suitable basis $\{\Psi_i\}$ as

$$\hat{H}_{BO} = \sum_{i,j} \tilde{t}_{i,j} \left|\Psi_i\right\rangle \left\langle\Psi_j\right| , \tag{2.9}$$

where $\tilde{t}_{i,j}$ is given by

$$\tilde{t}_{i,j} = \int \Psi_j^*(r) \left[\frac{p_e^2}{2m_e} + V_p(r,R)\right] \Psi_i(r) d^3r , \tag{2.10}$$

such that when $i = j$, $\tilde{t}_{ii}$ describes the energy of an electron in state i and when $i = j$, $\tilde{t}_{ij}$ describes the mixing between the two wavefunctions $|\Psi_i\rangle$ and $|\Psi_j\rangle$ in a molecule.

2.1.2 Energy level splitting

Multi-particle wavefunctions can be built based on the single-particle wavefunctions described above. The first constraint imposed while doing so is having multiple particles (electrons) in one given state [4, 5]. The ground state, for instance, is occupied by two electrons of opposite spin (according to the Pauli exclusion principle). Considering the unpaired π-electrons in the highest occupied molecular orbital (HOMO, ϕ_h) in the ground state (ϕ_{GS}), we can write its spatial wavefunction as

$$\phi_{GS}(r_1, r_2) \propto \phi_h(r_1)\phi_h(r_2) , \tag{2.11}$$

where r_1 and r_2 are the positions of the two electrons occupying this state. This spatial part of the wavefunction is symmetric with respect to exchange of two electrons, therefore the spin part of the full wavefunction must be antisymmetric as we know from experiments that the total wavefunction for two indistinguishable fermions changes sign upon exchanging the coordinates of any two particles. This antisymmetric spin wavefunction is given by

$$|S = 0, m_S = 0\rangle = \sqrt{\frac{1}{2}}(|\uparrow,\downarrow\rangle - |\downarrow,\uparrow\rangle) , \tag{2.12}$$

where S is the total spin of the system with two electrons (each with spin quantum number $s = \frac{1}{2}$ and $m_s = +\frac{1}{2}$, $|\uparrow\rangle$ or $m_s = -\frac{1}{2}$, $|\downarrow\rangle$) and m_S is the total spin projection quantum number.

Having looked at the ground state wavefunctions we can now discuss the excited state wavefunction by exciting one electron from the HOMO to the LUMO to give

$$\phi^{\pm}_{ES}(r_1, r_2) = \phi_h(r_1)\phi_l(r_2) \pm \phi_l(r_1)\phi_h(r_2)\,, \tag{2.13}$$

where $\phi^{\pm}_{ES}$ define the symmetry of the wavefunction with respect to exchange of the two electrons. The corresponding spin wavefunctions can again be antisymmetric (as given by eq. (2.12)) or symmetric for the total wavefunction to be antisymmetric. The symmetric wavefunctions, for total spin $S = 1$ and $m_S = \{-1, 0, +1\}$ can be given by

$$|1, -1\rangle = |\downarrow, \downarrow\rangle\ , \tag{2.14}$$

$$|1, 0\rangle = \sqrt{\frac{1}{2}}(|\uparrow, \downarrow\rangle - |\downarrow, \uparrow\rangle)\,, \tag{2.15}$$

$$|1, +1\rangle = |\uparrow, \uparrow\rangle\ . \tag{2.16}$$

These four excited states including one with symmetric spatial wavefunction $\phi^{+}_{ES}\,|0, 0\rangle$ (singlet state) and three with antisymmetric spatial wavefunction $\phi^{-}_{ES}\,|1, -1\rangle$, $\phi^{-}_{ES}\,|1, 0\rangle$ and $\phi^{-}_{ES}\,|1, +1\rangle$ (triplet states) are all degenerate in absence of interactions between the involved particles. However, in presence of interactions between the two electrons these states all acquire different energies. We can model their energies by altering eq. (2.9) above for the one-electron Hamiltonian. While still working in the basis of products of one-electron states we include the electron-electron interactions as follows

$$\hat{H}_{BO} = \sum_{i,j} \tilde{t}_{i,j}\,|\Psi_i\rangle\,\langle\Psi_j| + \underbrace{\sum_{ijkl} |\phi_i\phi_j\rangle\,\langle\phi_k\phi_l|}_{\tilde{V}_{ijkl}}\,, \tag{2.17}$$

where we have included a perturbative potential to represent the interaction of the form

$$\tilde{V}_{ijkl} = \iint \phi^*_k(r_1)\phi^*_l(r_2)\left[\frac{p_e^2}{2m_e} + V_{\text{eff}}(r_1 - r_2)\right]\phi_i(r_1)\phi_j(r_2)d^3r_1 d^3r_2 \tag{2.18}$$

where $\phi_n(r)$ is the spatial wavefunction of an electron in the n^{th} state.

In organic semiconductors, the Coulomb interaction (responsible for electron-hole binding) and the exchange interaction (responsible for singlet-triplet energy splitting) can be used to explain the energy splitting of electronic states. Building upon the above two-electron Hamiltonian we can write the integral for Coulomb interaction for two elec-

trons in the HOMO and LUMO as

$$C = \tilde{V}_{hlhl} = \iint \phi_h^*(r_1)\phi_l^*(r_2)\left[\frac{p_e^2}{2m_e} + V_{\text{eff}}(r_1 - r_2)\right]\phi_h(r_1)\phi_l(r_2)d^3r_1 d^3r_2\,, \tag{2.19}$$

and one for the exchange interaction as

$$K = \tilde{V}_{hllh} = \iint \phi_h^*(r_1)\phi_l^*(r_2)\left[\frac{p_e^2}{2m_e} + V_{\text{eff}}(r_1 - r_2)\right]\phi_l(r_1)\phi_h(r_2)d^3r_1 d^3r_2\,, \tag{2.20}$$

where the static potential $V_{\text{eff}}(r_1 - r_2)$ is now the effective shielding potential from all the bound electrons in filled states defining the effective dielectric constant (~ 3 in organic semiconductors [6]).

By including the spin wavefunctions and taking both the C and K integrals into consideration we find the energy difference between a singlet state (S_1) and a triplet state (T_1) relative to the ground state (S_0) to be

$$E_S = E(S_1) - E(S_0) = E_g - C + K\,, \tag{2.21}$$

$$E_T = E(T_1) - E(S_0) = E_g - C - K\,, \tag{2.22}$$

$$\Delta E_{ST} = E_S - E_T = 2K\,, \tag{2.23}$$

where E_g is the energy gap between the HOMO and LUMO levels. This relatively simple model tells us that the triplet state(s) is lower in energy as compared to the singlet state by $2K$. The exchange and Coulomb interaction energies in organic semiconductors are on the scale of $\sim 1\,\text{eV}$ [6] thus causing the excitons to be 'bound' strongly (Frenkel excitons) as compared to loosely bound excitons in inorganic semiconductors (binding energy $\lesssim 100\,\text{meV}$, Wannier-Mott excitons). These bound and highly localized electron-hole pairs diffuse as quasi-particles in organic semiconductors defining their electronic properties. One of the efficiency determining step in photovoltaics is the charge separation (or electron-hole separation). In inorganic semiconductors like silicon for instance, the thermal fluctuations at room temperature are enough to separate the loosely bound excitons whereas in organic semiconductors this is not true. Thus one of the main challenges of organic photovoltaics is to be able to efficiently separate the charges as will be discussed later in this work.

The polyacenes (used as model singlet fission system in this thesis) with general formula $C_{4n+2}H_{2n+4}$ (with $n = 2, 3, 4$) are aromatic compounds of the catacondensed family. This means that each carbon atom in a polyacene molecule is shared by no more than two rings and all carbon atoms are in the periphery of the conjugated π-system. Polyacenes satisfy Huckel's rule of aromacity as each molecule has $4n + 2$ π-electrons. For a general

N-ring acene molecule, the energy levels can be given by

$$E_i = \alpha + \beta\lambda_i^{(s,a)}\,, \tag{2.24}$$

where $\lambda_i^{(s,a)}$ can be given explicitly by

$$\lambda_0^s = 1, \lambda_{k\pm}^s = +\frac{1}{2}\left\{1 \pm \sqrt{9 + 8\cos\left(\frac{k\pi}{N+1}\right)}\right\}\, k \in [1, N] \tag{2.25}$$

$$\lambda_0^a = -1, \lambda_{k\pm}^a = -\frac{1}{2}\left\{1 \pm \sqrt{9 + 8\cos\left(\frac{k\pi}{N+1}\right)}\right\}\, k \in [1, N] \tag{2.26}$$

where

$$\hat{H}_{BO}^{ij} = \begin{cases} \alpha & \text{for } i = j \\ \beta & \text{for adjacent sites} \\ 0 & \text{for non-adjacent sites} \end{cases} \tag{2.27}$$

where i, j correspond to nuclear coordinate indices in a basis of atomic orbitals centered on each nucleus [7]. This shows that as the number of rings (N) in a polyacene molecule increases the gap diminishes. In order to obtain efficient singlet fission, we require the system to satisfy $E_S \geq 2E_T$ and polyacenes have been known to satisfy this requirement for singlet energies (E_S) in the visible region. The synthetic tunability of acene molecules also means that all trends in changing of absorption and fluorescence properties of these polyacenes can be attributed to the increase in number of rings in these polyacene molecules.

2.1.3 Electronic transitions

Having established the energy level splitting in the previous section we now describe the possible transitions in between these energy levels and discuss the interaction of such electronic systems with photons. A summary of these transitions is illustrated using the Jablonski diagram [8] in Figure 2.3.

2.1.3.1 Absorption and emission

Electronic transitions between an initial ground state $|i\rangle$ and a final excited state $|f\rangle$ can be induced by interaction with light. The rate of these transitions depend upon the overlap of the energy level difference (Δ) with the energy of the photon. This transition rate is given by *Fermi's Golden Rule* in the absence of nuclear degrees of freedom and

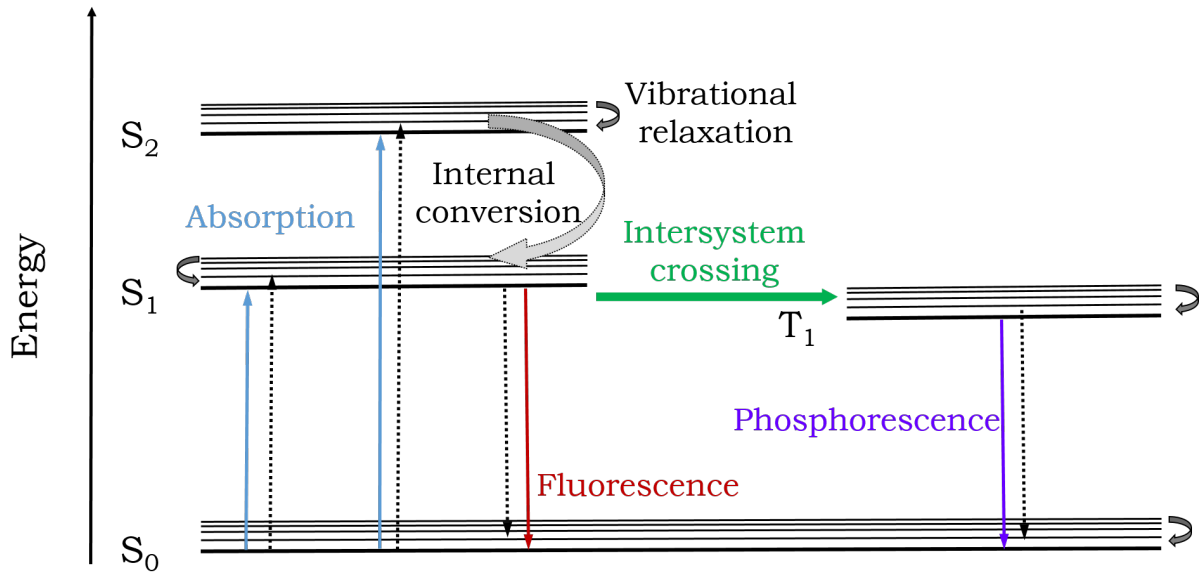

Figure 2.3: Jablonski diagram describing the different types of intramolecular electronic transitions. Different states in each spin manifold represent different molecular vibrational modes.

interactions between the electrons as

$$K_{i\to f} \propto |M_{i\to f}|^2 \rho_f(E)\,, \tag{2.28}$$

where $\rho_f(E)$ is the density of final states at energy E. $|M_{i\to f}|^2$ is the transition dipole matrix element given by

$$|M_{i\to f}|^2 \propto \langle f|\hat{\mu}\cdot\hat{\epsilon}|i\rangle\ , \tag{2.29}$$

where $\hat{\mu}$ is the electric dipole operator $\hat{\mu} = -q\hat{r}$ and $\hat{\epsilon}$ is the electromagnetic field operator. Electrons thus excited decay back to the ground state and release a photon of energy Δ on interaction with the quantized electromagnetic field. Since the transition dipole depends only on the spatial wavefunctions, the rate of absorption of a photon or its emission depend on the overlap of the spin states of $|i\rangle$ and $|f\rangle$ as follows

$$K_{i\to f} \propto |M_{i\to f}|^2 \rho_f(E)\cdot|\langle f_S, f_{m_S}|0,0\rangle|^2\,, \tag{2.30}$$

where $|f_S, f_{m_S}\rangle$ is the spin wavefunction of the final state with total spin f_S and the corresponding spin projection quantum number f_{m_S}. Thus it can be seen that for a transition to occur between the intial and final state, f_S must be 0 as $K_{i\to f} = 0$ if $f_S = 1$. This implies that as the ground state is a spin-singlet state (*i.e.* total spin $S = 0$) the allowed optical transitions from the ground state can only occur from and to other states with $S = 0$. As a consequence of spin-orbit coupling in organic semiconductors, radiative

transitions from spin-triplet states $S = 1$ are only weakly allowed. Such transitions are called phosphorescence and have transition rates at least $10 - 10^3$ times slower than direct emission from the singlet state [8].

The nuclear motion of a molecule also affects the energy-level splitting thus affecting the transitions in the molecule. However, as mentioned earlier, the optical transition frequencies are much higher than the vibrational frequencies of the molecule. Nuclear vibration and rotation about its centre of mass, resulting from bond-stretching and bond-bending for instance, can be described using the molecular normal modes. Approximating small displacements about an equilibrium nuclear position as a harmonic oscillator, its energy eigenstates E_n are given by

$$E_n = (\frac{1}{2} + n)\hbar\omega \,, \tag{2.31}$$

where we can interpret n as the occupied molecular normal mode number and ω as the angular frequency of a given vibrational mode. We can refine our transition rates using the Franck-Condon model which applies Born-Oppenheimer approximation to electronic transitions by assuming that the nuclear position remains static during an electronic transition. According to this model the rate of transition in terms of the initial nuclear vibrational state $|\chi_i\rangle$ and final nuclear vibrational state $|\chi_f\rangle$ is given by

$$K_{i\to f} \propto |M_{i\to f}|^2 \rho_f(E) \cdot |\langle f_S, f_{m_S}|0,0\rangle|^2 \cdot |\langle \chi_f|\chi_i\rangle|^2 \,. \tag{2.32}$$

This implies that the rate of transition depends upon the overlap of the initial and final nuclear vibrational states including any changes in the nuclear geometry caused by the electronic transition. The relative shift in the final nuclear geometry relative to the initial state determines which two vibrational states will efficiently couple to allow a transition between them, thus defining the features of an absorption and emission spectrum as shown in Figure 2.4. Such a transition is termed a 'vertical transition' as the nuclear coordinates are static through the transition, but just in a different vibrational mode (labelled ν_i for i different vibrational modes in Figure 2.4). As the timescale for vibrational relaxation is typically sub-picoseconds, the absorption and emission transitions usually happen from the lowest energy vibrational states as illustrated in Figure 2.4 resulting in mirrored features of the absorption and emission spectra. Detailed description of the effect of this approximation on the absorption and emission spectra of organics can be found in reference [9].

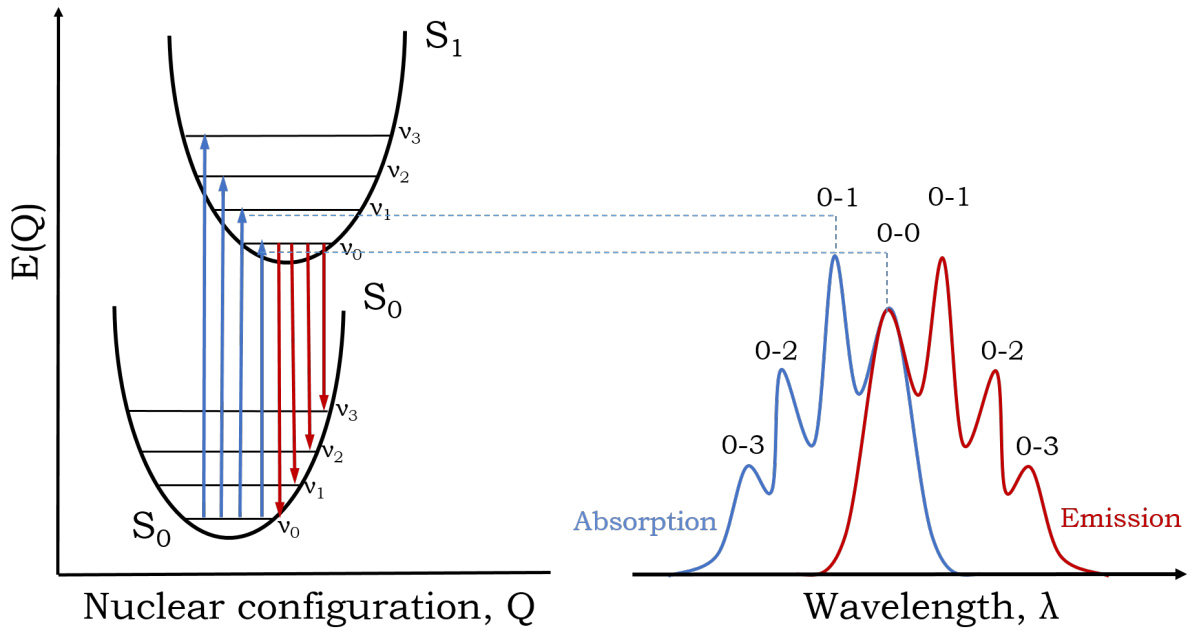

Figure 2.4: Electronic transitions modelled with respect to nuclear motion using the Franck-Condon approximation, giving rise to features in absorption and emission spectra.

2.1.3.2 Non-radiative transitions

So far we have discussed electronic transitions that proceed with either absorption or emission of a photon. These transitions between electronic states can also proceed non-radiatively. The two main types of such transitions are *internal conversion* and *intersystem crossing* where the former refers to transition between electronic states within the same spin manifold and the latter refers to transitions across different spin manifolds.

Using Fermi's golden rule the rate for internal conversion can be given by

$$K_{IC} \propto \exp(-\gamma \Delta E)\,, \tag{2.33}$$

where γ is a molecular parameter which includes the highest-energy vibrational mode involved in the transition and ΔE is the energy difference between the initial and final electronic states (both in their lowest vibrational state ν_0) [10]. This indicates that the rate of internal conversion decreases exponentially with increasing energy gap between the initial and final states also known as the *energy gap law* [11, 12]. As the higher energy singlet-states have much lower energy gap between them when compared to the energy gap between S_0 and S_1 state, the relaxation from those S_n states with $n > 1$ to S_1 is relatively fast ($< 100\,\text{fs}$). The longer lifetime of the S_1 state thus allows for photoluminescence (radiative transition) to occur selectively from this state.

Transitions between states with different spin cannot proceed due to the spin conservation within the Franck-Condon approximation. Such transitions can only be allowed when spin-orbit coupling leads to mixing of the spin and orbital degrees of freedom. Using Fermi's golden rule the rate of intersystem crossing between the singlet and triplet manifold can be given by

$$K_{ISC} = \frac{2\pi}{\hbar}|\langle S_1|\hat{H}_{SO}|T_1\rangle|^2 F_{0\to f}\rho_f(E)\,, \tag{2.34}$$

where $F_{0\to f}$ is the Franck-Condon factor associated with the ν_0^{th} vibrational level of the S_1 state and ν_f^{th} vibrational level of the T_1 state; and $\rho_f(E)$ is the density of vibrational levels in the triplet state [3]. The spin-orbit Hamiltonian $\hat{H}_{SO}$ is given by

$$\hat{H}_{SO}^{(i)} = \alpha^2 \sum_n^N \frac{Z_n}{R_{ni}^3} \hat{L}_i^{(n)} \cdot \hat{S}_i\,, \tag{2.35}$$

where $\hat{H}_{SO}^{(i)}$ is summed over N_e electrons as $\hat{H}_{SO} = \sum_i^{N_e} \hat{H}_{SO}^{(i)}$, the sum n is over N nuclei and R_{ni} is the distance between the n^{th} nucleus and the i^{th} electron, Z_n is the effective charge of the n^{th} nucleus, $\hat{S}_i$ is the spin operator for the i^{th} electron, $\hat{L}_i^{(n)}$ is the angular momentum operator for the i^{th} electron associated with the n^{th} nucleus and finally, α is the fine structure constant $\sim 7.3 \times 10^{-3}$ [3].

In organic semiconductors the exchange interaction is on the order of 1 eV whereas the spin-orbit matrix elements are on the order of $10^{-3} - 10^{-4}$ eV which limits the timescales for intersystem crossing to the order of milliseconds. Even in a transition assisted by vibrational coupling (for instance from S_1 to T_2), the large energy gap means the transition rates K_{ISC} are limited to $\sim 10^7\,\mathrm{s}^{-1}$. The typical rate of radiative decay of a singlet is $\sim 10^9\,\mathrm{s}^{-1}$ therefore it is evident that the yield of triplets via intersystem crossing from the S_1 state are on the order of 1 % [3].

2.1.4 Excitation transport

Excitations transport is governed by the overlap and coupling of initial and final states as discussed earlier. In this section we discuss the specific types of excitation transport applicable to organic and inorganic semiconductors.

2.1.4.1 Exciton diffusion

As discussed earlier, once an electron is excited from the ground state to an excited state, it remains strongly bound to a hole in the ground state forming an exciton. Once

generated these excitons can diffuse in the material depending on their spin-states and the local molecular environment which impact their lifetime and decay pathways. It is the exchange and Coulomb interactions between the ground state excitons and the excited state excitons on neighbouring molecules that cause the exciton to diffuse.

Spin-singlet excitations diffuse predominantly via a process called *Förster resonant energy transfer* (FRET, see Figure 2.5). This is a dipole-dipole interaction whose rate is determined by the equation

$$K_{FRET} \propto \frac{n^4 \kappa^2 \mu_D^2 \mu_A^2}{\hbar^2 R_{DA}^6} \int \sigma_A^{abs}(\omega) \sigma_D^{em}(\omega) d\omega \,, \tag{2.36}$$

where μ_D is the dipole transition moment of the donor molecule from the excited state to the ground state, μ_A is the dipole transition moment of the acceptor molecule from the ground state to the excited state, n is the refractive index of the medium,κ is the dipole orientation factor, R_{DA} is the distance between the donor-acceptor sites and finally σ_A^{abs} and σ_D^{em} are the expressions for the acceptor absorption and the donor emission spectra respectively [3]. Thus, the rate K_{FRET} depends on the spectral overlap between the donor emission and the acceptor absorption spectra. FRET is a resonant energy transfer process describing the simultaneous emission from the donor and absorption of the energy by the acceptor in an energy conserving process. Using the point-dipole approximation a Förster radius (R_F) can be defined such that for molecules separated by distance smaller than R_F, exciton transfer via FRET is more likely than radiative emission. The above rate of exciton transfer can then be written as

$$K_{FRET} = k_r \left(\frac{R_F}{R_{DA}} \right)^6 , \tag{2.37}$$

where k_r is the rate of radiative emission. Typically singlet diffusion lengths are on the order of $\sim 10 - 100\,\text{nm}$ [13, 14] allowing for long-range transport.

Spin-triplet excitaions on the other hand have no transition dipole to the ground state. Thus, triplet excitons transfer through exchange interactions between neighbouring sites in a process called *Dexter transfer* (see Figure 2.5) [15]. The rate of Dexter transfer is given by

$$K_D \propto J \exp(-2R_{DA}/L) \tag{2.38}$$

where J is the same acceptor absorption and donor emission spectral overlap integral as defined in eq. (2.36), normalized such that integrating over the full spectrum results in $J = 1$ and L the sum of the Van der Waals radii of the donor and acceptor. Note

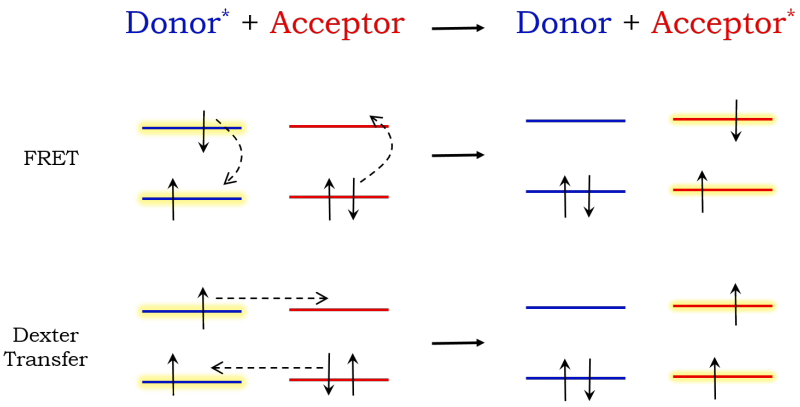

Figure 2.5: Schematic diagram illustrating Förster resonant energy transfer and Dexter transfer with up and down arrow representing spin-up and spin-down electrons respectively.

that, unlike K_{FRET}, K_D is independent of the transition dipole moments involved. As a consequence of $K_D \propto \frac{1}{R_{DA}}$, the Dexter transfer can only occur over very short distances, on the order of $\sim 1\,\text{nm}$ [15, 16]. Thus FRET for singlet excitons in efficient organic semiconductors is typically fast (on the order of $\ll ps$), the triplet hopping times are much slower. However due to the long triplet lifetimes, triplet excitons can have long diffusion lengths of up to several μm [17].

2.1.4.2 Singlet fission

Intermolecular interactions between excitons on neighbouring molecules are responsible for a range of phenomena used for optoelectronic applications. Singlet fission is one such phenomenon whereby a singlet exciton converts to two triplet excitons. Conversion from one singlet exciton to one triplet exciton is spin-forbidden as explained earlier. However, in a four-particle or two-exciton system, there can be two states (coupled together) with a total spin zero. Considering two molecules A and B, the singlet state can be denoted in the direct-product basis as

$$|S\rangle = \frac{1}{2}[|\uparrow\downarrow\rangle_A - |\downarrow\uparrow\rangle_A][|\uparrow\downarrow\rangle_B - |\downarrow\uparrow\rangle_B]\,, \tag{2.39}$$

and the triplet state as

$$|TT\rangle = \sqrt{\frac{1}{3}}[|\uparrow\uparrow\rangle_A|\downarrow\downarrow\rangle_B + |\downarrow\downarrow\rangle_A|\uparrow\uparrow\rangle_B] - \frac{1}{2}\sqrt{\frac{1}{3}}[(|\uparrow\downarrow\rangle_A + |\downarrow\uparrow\rangle_A)(|\uparrow\downarrow\rangle_B + |\downarrow\uparrow\rangle_B)]\,, \tag{2.40}$$

where the $|S\rangle$ state is separable into individual states of molecules A and B, but the $|TT\rangle$ state is not. The $|TT\rangle$ state describes a superposition of two triplet states on neighbouring molecules coupled together and is referred to as the triplet pair spin state.

The full wavefunctions of the singlet state and the triplet pair state are given by

$$|\Phi_S\rangle = |S_1\rangle_A |S_0\rangle_B |S\rangle \ , \tag{2.41}$$

$$|\Phi_{TT}\rangle = |T_1\rangle_A |T_1\rangle_B |TT\rangle \ . \tag{2.42}$$

The rate of singlet fission can be qualitatively predicted by modelling the electronic overlap of the two states as $E_{SF} = \langle S|\hat{H}|TT\rangle$. In the regime where the energy difference between the two states (ΔE) is similar to the electronic overlap (given by the transfer integral identical to C in eq. (2.19)) between the two states, the singlet and triplet-pair manifolds mix as a function of the nuclear coordinates and the rate of singlet fission is controlled by the speed of nuclear rearrangement [18]. The reaction proceeds in the adiabatic regime when $E_{SF} \sim \Delta E$ and in the non-adiabatic regime otherwise. In both the regimes, singlet fission occurs on ultrafast (1 fs to 100 ps) timescales outcompeting singlet decay via other pathways in most cases [19–22]. The exact mechanism of conversion of a singlet state into two free triplets via the intermediate state is a topic of active debate in the field [23, 24]. In this thesis, we look at the application of molecules capable of singlet fission, in optoelectronic devices in Chapter 5 and in Chapter 6 we study the simultaneous presence of SF and TTA in pentacene OLEDs.

2.1.4.3 Triplet triplet annihilation

Excitons diffusing through materials often interact and depending on their energetics and spin can annihilate providing additional non-radiative loss pathways. In some cases however, two annihilating triplets can form a singlet exciton which can then be harnessed for luminescence [25, 26] thus converting the dark triplets into bright singlets. Triplet-triplet annihilation (TTA) can form the following states

$$|T_1\rangle + |T_1\rangle = \begin{cases} |S_0\rangle + |S_n\rangle & \text{for } E_{total} \geq E_{S_n} \\ |S_0\rangle + |T_n\rangle & \text{for } E_{total} \geq E_{T_n} \\ |S_0\rangle + |Q_n\rangle & \text{for } E_{total} \geq E_{Q_n} \end{cases} \tag{2.43}$$

where E_{total} is the total energy of the two annihilating triplet excitons, E_{X_n} is the energy of the newly formed singlet, triplet or quintet exciton $\{X = S, T, Q\}$ in the n^{th} vibrational level. The quintet levels are energetically inaccessible in most molecules and thus the singlet and triplet decay channels are the most prominent decay pathways [27] when two triplets annihilate.

Singlet excitons formed from TTA can be utilized in light emitting diodes to enhance

the quantum yield by converting the dark triplet excitons (formed 75 % of the time on charge recombination) into emissive singlet excitons. Also, TTA is a promising strategy to convert low-energy (sub-bandgap) photons into high-energy (above bandgap) photons in order to harvest the otherwise lost photons for power conversion in solar cells. Generally known as the TTA-upconversion (TTA-UC) process, photon upconversion proceeds as follows: (i) the triplet donor, also known as the triplet sensitizer, accepts a low-energy photon to generate a singlet exciton; (ii) this singlet exciton rapidly and efficiently converts to a triplet exciton via inter-system crossing; (iii) the triplet exciton is transferred to the triplet manifold of the acceptor molecule via triplet-triplet energy transfer (TTET); (iv) bimolecular TTA occurs on the acceptor molecules, forming singlets; (v) finally, the acceptor emits photons with energy greater than that of the absorbed photon (see figure 2.6). In this way, sub-bandgap photons which would not be absorbed by a semiconductor with a bandgap greater than the energy of these photons can be absorbed by employing a TTA-UC unit behind a photovoltaic.

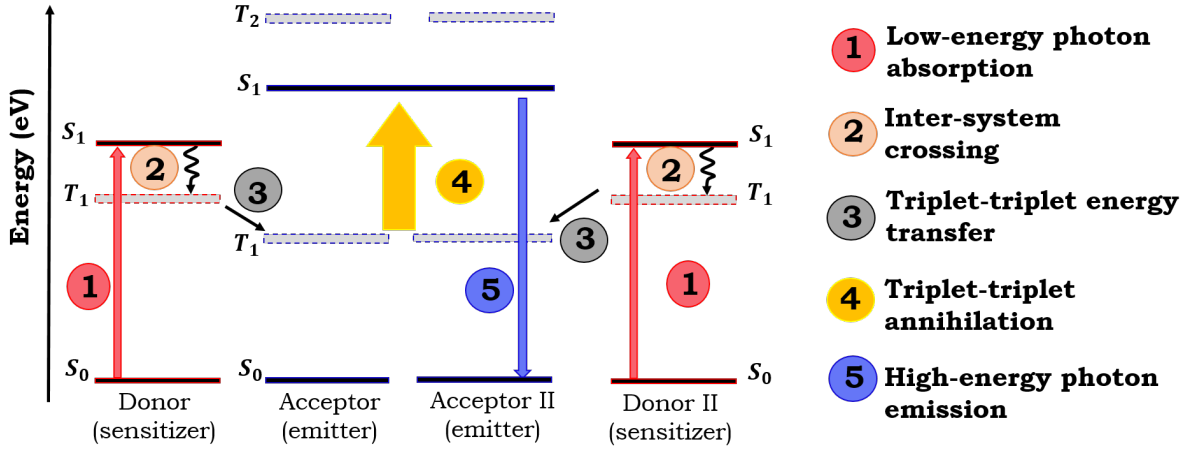

Figure 2.6: Schematic diagram illustrating the triplet-triplet annihilation-upconversion (TTA-UC) process. In step 4, the two triplet excitons generated on two different acceptor molecules combine together and emit from the singlet manifold of one of the two molecules.

Another system performing efficient TTA is an organic light-emitting diode (OLED) [26]. OLEDs provide a way to generate singlet and triplet excitons simultaneously by electrical excitation. The recombining electrons and holes occupy the singlet and triplet states with 25 % and 75 % probabilities respectively. In this thesis we study TTA in an extremely efficient singlet fission molecule, pentacene, by incorporating it in a host-guest OLED. As TTA is the reverse process of singlet fission, gaining insight into the formation of singlets from two annihilating triplets can provide useful information about possible

pathways available for singlet fission. In Chapter 6 we study the competition between singlet fission and TTA in pentacene and discuss the role of triplet-pair intermediate state in the two processes.

2.1.4.4 Charge transfer

For photovoltaic applications, excitons generated in semiconductors need to be separated to form free charges. The separated electrons need to be transferred from the donor molecule to the acceptor molecule at the heterojunction. This charge transfer process can be described by considering the transfer of an excited electron from the donor molecule to the acceptor molecule using Marcus theory [28]. According to the Marcus theory the rate of charge transfer (K_{CT}) is described by

$$K_{CT} \propto |M_{|i\rangle \to |f\rangle}|^2 exp(-\frac{(\lambda + \Delta G)^2}{4\lambda k_B T}) \,, \tag{2.44}$$

where k_B is the Boltzmann-constant, T is the temperature, λ is the reorganization energy, $|M_{|i\rangle \to |f\rangle}|$ is the electronic transition matrix element describing the overlap between the $|S_1\rangle$ state of the reactant and the final charge-transfer state $|CT\rangle$. ΔG is the change in the Gibbs free energy going from the initial excited state to the final charge-transfer state. Marcus theory has been used successfully to explain charge transfer in various solid state systems [29, 30]. Recently however, various other theories including coherent transfer to delocalized states are being adapted to explain charge transfer in organic photovoltaics. A summary of these theories can be found in reference [31].

2.1.5 Organic Solar Cells

In this section we discuss the basic principles of solar cell operation and list the possible loss mechanisms using organic solar cells as an example.

2.1.5.1 Basic principles

An organic photovoltaic (OPV) operation involves four steps: (i) Photon absorption, (ii) excitation transport, (iii) exciton separation, (iv) charge transport and (v) charge extraction. The product of efficiency of all of these steps ultimately determines the efficiency of power conversion in a photovoltaic device. The main component of an OPV is the active layer which consists of an electron-donor molecule and an electron-acceptor molecule. Light absorption in the active layer leads to formation of excitons which need to diffuse

to the donor-acceptor interface to find favourable energetics for separation into individual electrons and holes. Finally, the separated charges are extracted by respective electrodes to generate current.

The main characteristic of a photovoltaic is its power conversion efficiency (PCE) defined as a ratio of the power extracted from a photovoltaic to the power incident on it. The power extracted from a photovoltaic is calculated from its current density and voltage (J-V) characteristics shown in Figure 2.7. The short-circuit current density (J_{SC}) is the current generated when no voltage bias is applied and the open-circuit voltage (V_{OC}) is the voltage difference between the two electrodes of the photovoltaic under illumination at zero current density. The maximum power point (P_{max}) is the point on the J-V curve where the photovoltaic produces maximum power, *i.e.* where the product $J \cdot V$ is maximised. The ratio of P_{max} to the product of J_{SC} and V_{OC} is called the fill-factor (FF). The PCE can then be expressed in terms of these parameters as

$$PCE = \frac{J_{SC} \cdot V_{OC} \cdot FF}{\text{Incident light intensity}} \tag{2.45}$$

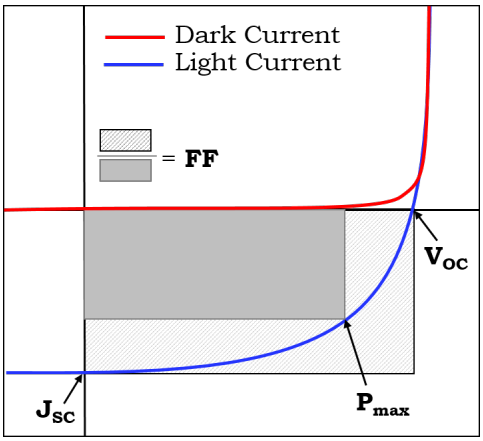

Figure 2.7: Characteristic J-V curve for a photovoltaic (dark) under no illumination and (light) 1-sun illumination showing: the short-circuit current J_{SC}, the open-circuit voltage V_{OC} and the fill factor as the ratio of P_{max} to product $J_{SC} \cdot V_{OC}$.

Another useful and informative way of assessing photovoltaic performance is by measuring its external quantum efficiency (EQE). The EQE of a solar cell is calculated as the ratio of current extracted per photon that is incident on the solar cell. This measurements provides useful information about which photons contribute towards photocurrent generation. For singlet-fission sensitized solar cells in Chapter 5 we show the contribution from singlet fission to the device photocurrent using EQE. The EQE spectrum shows the current generated at every wavelength which provides an important evidence of the presence of the SF mechanism [21, 32].

2.1.5.2 Loss mechanisms

Using the characteristics described above we can assign a quantum efficiency parameter to each operational step of photocurrent generation in an OPV as follows

1. Photon absorption: $\eta_A = \frac{\text{No. of excitons generated}}{\text{No. of photons incident}}$;
2. Excitation transport: $\eta_T = \frac{\text{No. of excitons reaching the donor-acceptor heterojunction}}{\text{No. of photogenerated excitons}}$;
3. Exciton separation: $\eta_S = \frac{\text{No. of free electrons generated}}{\text{No. of excitons reaching the donor-acceptor heterojunction}}$;
4. Charge extraction: $\eta_E = \frac{\text{No. of extracted electrons}}{\text{No. of free electrons generated}}$.

The total quantum efficiency of conversion of a photon into free charges by the OPV can be given as a product of all these parameters by

$$\eta_{total} = \eta_A \cdot \eta_T \cdot \eta_S \cdot \eta_E = \frac{\text{No. of extracted charges}}{\text{No. of photons incident}}\,, \tag{2.46}$$

which also corresponds to the EQE at a given wavenlength. Thus in order to optimise the device efficiency, each of the above mentioned steps for current generation and extraction needs to be optimised.

The overall efficiency of OPVs is mainly known to be limited by the voltage loss as compared to the bandgap of the active semiconductors which is as high as $\sim 0.5\,\text{V}$ to $1\,\text{V}$ in OPVs as compared to only $0.3\,\text{V}$ loss in silicon or $0.4\,\text{V}$ in gallium arsenide PVs [33, 34]. The donor-acceptor energy offset at the interface and the non-radiative recombination pathways in OPVs are being studied actively in the field to reduce the voltage losses while maintaining high PCEs. Non-fullerene acceptors have been shown to reduce these losses further and are currently leading the OPV efficiency chart [35].

Another important reason limiting solar cell efficiencies is the spectral loss. Electrons excited by absorption of photons with energies above the active semiconductor bandgap usually relax to the lowest vibrational levels at the band edge before they can be extracted to generate photocurrent. This relaxation process is referred to as *cooling*. Due to this charge cooling, significant energy from the absorbed photon is lost as heat and this process is known as *thermalisation loss*. About $\sim 30\,\%$ of the incident light is lost due to thermalisation [36, 37]. Photons with energies less than the semiconductor bandgap are not absorbed in the solar cell and also contribute towards the spectral loss. These fundamental thermodynamic losses result in the Shockley-Queisser limit [38] on the maximum

achievable power conversion efficiency of a single-junction photovoltaic which will be discussed detail in Chapter 4. Tandem solar cells provide a way to reduce this thermalisation loss by stacking multiple semiconductors with different bandgaps to harvest different parts of the spectrum as discussed in Chapter 4. Photon up and down conversion using singlet fission and triplet fusion provide ways of further reducing the spectral loss as will be discussed in Chapters 5 and 6.

2.1.6 Organic Light Emitting Diodes (OLEDs)

In a light emitting diode electrons and holes are injected from the two electrodes into the active layer where they form an exciton and recombine to emit a photon. The performance of an OLED can be assessed by measuring it's external quantum efficiency given by

$$EQE = \frac{\text{No. of photons emitted}}{\text{No. of charge pairs injected}} = \eta_{balance} \times \eta_{exciton} \times \eta_{radiative} \times \eta_{outcoupling}\,, \tag{2.47}$$

where $\eta_{balance}$ is the probability of balanced charge injection ($\eta_{balance} = 1$, when the number of holes and electrons injected into the LED are equal), $\eta_{exciton}$ is the probability of forming an exciton from the injected charge pairs, $\eta_{radiative}$ is the probability that the excitons recombine radiatively and $\eta_{outcoupling}$ is the optical outcoupling co-efficient [39, 40]. The LED's power efficiency can then be determined using the EQE as

$$\text{Power efficiency} = \frac{\text{Optical power extracted}}{\text{Input electrical power}} = EQE \times \frac{h\nu}{qV}\,, \tag{2.48}$$

where $h\nu$ is the photon energy, q the electron charge and V the applied voltage. Luminous efficacy determined as the power efficiency of the device (lumen per watt) quantifies the performance of the LED in relation to how well the device emits visible light per unit input power. In chapter 6 we use LEDs as devices used to study the triplet-triplet annihilation process.

2.2 Quantum Dots

In Chapter 4 we discuss the concept of using multiple semiconductors in tandem configuration to reduce spectral losses by absorbing the low-energy photons using colloidal quantum dots (CQDs). Furthermore, in Chapter 5 we discuss the application of singlet fission materials in a photon multiplication system to generate multiple low-energy photons from a single high-energy photon. For both of these projects, we work with lead sulphide

(PbS) and lead selenide (PbSe) quantum dots. Semiconductor CQDs are nanocrystals that offer a range of unique properties including easily tunable optoelectronic properties and solution processibility for light harvesting and emitting applications [21, 41–44]. In this section we discuss the properties of CQDs and review the relevant theory. *Note: We use the two terms CQDs and nanocrystals interchangeably throughout this section.*

2.2.1 Quantum Confinement

For certain semiconductors like the lead-chalcogenides (sulfide and selenide) used in this work, the Bohr radius of an exciton (defined as the average distance between electron and hole in the bulk material) is larger than the size of the nanocrystal. This causes spatial restriction on the exciton and results in the continuous energy bands of the bulk semiconductor splitting into discrete energy levels. This effect is called *quantum confinement*. The discrete energy levels are analogous to those of individual atoms thus allowing the nanocrystals to behave as artificial atoms whose properties can be tuned by tuning the energy level splitting. We can describe the size dependent properties of nanocrystrals using a particle-in-a-sphere model. This model considers a particle inside a spherical potential such that

$$V(r) = \begin{cases} 0 & \text{if } r < a \\ \infty & \text{if } r > a \end{cases} , \tag{2.49}$$

where r is the distance of the electron from the centre of the nanocrystal and a is the radius of the nanocrystal. Solving the one-particle Schrödinger equation of the form

$$\left[-\frac{\hbar^2}{2m_e}\nabla^2 + V(r) \right] \Psi(r) = E\Psi(r) \,, \tag{2.50}$$

we arrive at the wavefunction

$$\Psi_{n,l,m}(r,\theta,\phi) = C \cdot \frac{j_l(k_{n,l}, r) Y_{l,m}(\theta,\phi)}{r} \,, \tag{2.51}$$

where C is the normalisation constant, $Y_{l,m}(\theta,\phi)$ is a spherical harmonic and $j_l(k_{n,l}, r)$ is the l^{th} order spherical Bessel function [45]. The energy of the particle is given by

$$E_{n,l} = \frac{\hbar^2 k_{n,l}^2}{2m} = \frac{\hbar^2 \alpha_{n,l}^2}{2ma^2} \,, \tag{2.52}$$

where $\alpha_{n,l}$ is the n^{th} zero of j_l. The energy levels are labelled analogous to those of individual atoms with principal quantum number n and orbital quantum numbers l which are labelled with $\{S, P, D, F, ...\}$ [45]. As evident from eq. (2.52) the energy increases with decreasing nanocrystal radius a explaining the size dependence of CQDs bandgap.

Although the above model helps us understand the energy-size relationship of the nanocrystals, it has several weaknesses. Firstly, it is important to note that the electronic wavefunctions generally leak out of the nanocrystal as the potential barriers at the edges are not infinite. Secondly, this model neglects that the growth rate of different nanocrystal facets are different when the nanocrystals are growing during synthesis. Thus the crystal symmetry is usually not exactly spherical. Also, considering the large surface to volume ratio of nanocrystals, a lot of the nanocrystal atoms are at its surface and consequently are prone to defects. The nanocrystal surface is generally covered with ligands to passivate the dangling bonds but this passivation is not perfect and leads to trap states at the surface, affecting the electronic and optical properties of the nanocrystals [46].

2.2.2 Excitations in CQDs

In a similar fashion to excitation decay in molecules, the excitation formed in CQDs also decay via three main pathways: radiative decay, non-radiative decay and energy transfer. Radiative decay, also known as spontaneous emission, occurs when an excited electron decays back to the ground state emitting a photon whose energy is the same as the energy difference between the excited state and the ground state. Photogenerated excitons can also decay via non-radiative energy transfer processes in CQDs just as in molecular films. As a consequence of strong spatial confinement of the electronic wavefunctions in CQDs, Auger recombination is highly prevalent. Auger recombination is a two-particle process whereby an exciton decays to the ground state by transferring its energy to a nearby excited state which then forms a hot exciton (electron excited to a higher energy state, away from the band edge). The hot exciton then rapidly relaxes to the lowest energy vibrational state. As Auger recombination requires two excited states to interact, it is only a concern when the charge-carrier densities are relatively high. Along with the non-radiative decay pathway, excitons in CQDs are also transported via radiative transfer processes such as FRET and Dexter energy transfer processes explained earlier in Section 2.1.4.

2.2.3 Charge transport and extraction

To efficiently convert light into electricity using photovoltaics, it is essential to separate the excitons into individual charges as discussed earlier. The energy driving this charge

separation needs to be greater than the binding energy of the exciton. For organics, this binding energy can be as high as 0.5 eV whereas for CQDs it is in the order of $10 - 100$ meV [45]. The separated charges then need to be efficiently transported to the respective electrodes for extraction.

As discussed earlier, nanocrystals are capped with ligands to passivate the dangling bonds on the surface. These ligands electronically separate the CQDs from one another and the charge transport is limited by interparticle tunneling. The tunneling probabilities decrease as the width of the barrier increases and hence it is extremely important to have closely packed arrays of nanocrystals for charge transport in CQD thin films. Significant research efforts have been made to replace the long oleic acid ligands (generally used to cap the PbS and PbSe CQDs) with shorter ligands for application in CQD solar cells [47–50]. In order to harvest significant amount of the incident light, thick layers of CQDs need to be deposited where the CQDs have short ligands attached. While layer-by-layer solid-state ligand exchange is a proven method to do so, it is also very time consuming [43, 47]. Alternative methods are being investigated to perform the ligand exchange in solution phase prior to thin-film deposition [51]. However, CQDs aggregation and surface passivation of the dots still remains a significant challenge [52].

As synthesized, CQDs usually have a distribution of sizes and thus bandgap energy as a result of difference in confinement strengths [53, 54]. This results in excitons and charges hopping to the lowest energy dots and limits the amount of energy that can be extracted from them [44]. Additionally presence of trap states on the surface atoms further reduce the exciton energies and dominate the charge transport [55]. These trap states significantly affect the charge transport in thin films confining electrons in low energy regions. Hence, although semiconductor CQDs provide interesting optoelectronic properties, their application in devices is limited by the challenges of efficiently extracting charges from CQD thin films.

2.3 Perovskites

Perovskite solar cells have achieved remarkable power conversion efficiencies since the first efficeint device reported in mid-2012 [56] and are presently being developed for commercialisation with perovskite-silicon tandem solar cells [57]. In this section we discuss the properties of perovskites that make them promising materials for optoelectronic applica-

tions and in Chapter 4 we employ perovskite solar cells as the top cell in a perovskite-CQD monolithic tandem solar cell.

2.3.1 ABX_3 crystal structure

Perovskites are crystal structures found in compounds with formula ABX_3 where A and B are cations with A being larger than B, and X is an anion. One of the most studied cubic perovskite crystals MAPI (methylammonium lead iodide), consists of an organic anion methylammonium $CH_3NH_3^+$ as cation A, lead (Pb^{2+}) as cation B and a halogen atom iodine (I^-) as the anion. The radii of these elements can be used to calculate a tolerance factor t given by

$$t = \frac{r_A + r_X}{\sqrt{2}(r_B + r_X)}, \tag{2.53}$$

where r is the radius of the respective element. The hybrid organic-inorganic halide perovskite materials attain the ideal cubic structure when the tolerance factor is in the range $0.8 < t < 1$. The perovskite forms an orthorombic structure when $t < 0.8$ and hexagonal structure when $t > 1$ [58]. However in methylammonium lead halide perovskites for instance, both iodide and bromide are stable at room temperature and so are the mixtures of the two. Perovskite structures are capable of incorporating various elemental variations and dopants which can improve the device stability, charge mobility and change the bandgaps [59, 60]. Not only does the crystalline structure yield useful electronic properties but it also makes perovskites solution processable which is another major advantage of this class of semiconductors. Low temperature solution processing makes perovskite deposition easily scalable and inexpensive for applications in optoelectronic devices.

2.3.2 Electronic properties

In 2012 Miller et al. popularized the idea that a good solar cell must also be a good light emitting diode [61]. Considering that when all the non-radiative decay pathways are eliminated, charges in a solar cell will combine radiatively and emit a photon on recombination. Measuring the external radiative efficiency of a solar cell (fraction of dark current that results in light emission) is a good indication of how well the non-radiative decay channels have been curbed in the device. While the indirect bandgap of Si limits silicon PV ERE to $\sim 2\,\%$, photon recycling in GaAs PV allows its ERE to reach $\sim 22\,\%$ [62]. Perovskites have been reported to demonstrate exception light emission properties

[60] and are also shown to demonstrate photon recycling [63] thus highlighting low non-radiative recombination present in these materials.

Along with the radiative recombination and Auger recombination mentioned earlier another prominent recombination pathway in semiconductors is known as the Shockley-Read-Hall (SRH) recombinations. SRH recombination occurs due to the presence of defects (or traps) in the semiconductors. These trap states introduce electronic states within the semiconductor bandgap that have energies either very close to the conduction or valence band or in the middle of the bandgap. Recombination occurs when an electron falls into such a defect state and a hole also moves into this defect state before the electron is excited back to the conduction band. Thus, the closer the defect state is to the edge of the bandgap the lower is the rate of these defect mediated recombinations. Defect states can be introduced intentionally or unintentionally in a material for instance by doping or in case of perovskites, by altering the perovskite composition.

Perovskite compounds are largely held together by ionic bonding. This makes them highly tolerant to crystalline defects and also facilitates deposition of highly crystalline films via solution processing [64]. Defect-tolerant semiconductors tend to have long charge carrier lifetimes regardless of presence of defects in the material. These defects can either be intrinsically present point defects or they can be introduced extrinsically (via doping or structural deformation of the lattice for instance). Lead-halide perovskites in particular are known to have long carrier lifetimes as a result of slow electron-hole recombination kinetics at the defect sites and the reasons for such a behaviour are discussed in detail in reference [65].Another advantage of perovskites is the high electron and hole mobilities observed in these materials, reaching $\sim 100\,\mathrm{cm}^2/\mathrm{Vs}$ for single crystals [66, 67]. MAPI perovskites demonstrate low degrees of recombination from defects which only account for shallow trap states if any [64, 68]. The defect physics is still not well understood for perovskites, however the defect sites are shown to have energies close to the band edge and/or outside the bandgaps [64, 69]. This subdued non-radiative decay due to defect states in perovskites has helped devices reach high efficiencies.

The current-voltage (J-V) characteristics of perovskite solar cells exhibit hysteresis. The J-V characteristics are shown to vary with numerous parameters including the direction of the voltage scan (forward or reverse biased), scan rate and light intensities under which the devices were measured. Various explanations for the observed hysteresis have been reported including unfilled surface and grain-boundary trap states [70, 71] and ion

migration [72] in perovskites. Better understanding of the causes of hysteresis followed by its elimination using improved device architectures has led to significant enhancement device performances.

2.3.3 Applications in solar cells

High absorption with bandgaps close to those required for maximum theoretical efficiency of 33 % [38] and the unique crystalline structure with high carrier mobilities make metal-halide perovskites a great candidate for applications in solar cells. Metal-halide perovskite crystals are solution processable making them desirable for large-scale commercialization. However, solution processibility of lead-containing perovskites is also a danger when it comes to large scale deployment of perovskite solar cells. Although there has been some success in replacing the lead with tin, breakdown products such as SnI_2 can be formed which have similar toxic effects [73]. 'Double perovskites' with formula $A_3B_2X_9$ containing two metal ions such as $Cs_3Sb_2I_9$ (caesium-antimony iodide) are being investigated to eliminate both lead and tin and to develop all inorganic perovskites [74]. In order to improve the stability and durability of the perovskites for device applications, a range of solutions are being investigated. These include better encapsulation to prevent active layer interaction with moisture or air, optimising the metal electrodes to prevent active layer reactions with the electrode and varying the perovskite composition by adding materials such as caesium and formamidinium to maintain the optical properties while improving the perovskite stability [75, 76].

Lead-iodide perovskites are ideal when it comes to application in solar cells. With methylammonium as the cation A, MAPI perovskites have a bandgap of 1.55 eV whereas formamidinium lead iodide (FAPI) yields a bandgap of 1.45 eV which is closer to the maximum efficiency bandgap defined by the Shockley-Queisser limit. However, FAPI is less stable thermodynamically as it can rapidly change its crystal structure to a hexagonal crystal structure known as the yellow δ-phase [77]. Considering the solution processibility, ease of bandgap tunability along with remarkable efficiencies achieved by single-junction devices [59, 78], perovskites provide a great promise for applications in tandem solar cells.

Bibliography

1. Atkins, P. W. & Friedman, R. S. *Molecular quantum mechanics* (Oxford University Press, 2011).
2. Born, M. & Oppenheimer, R. Zur quantentheorie der molekeln. *Annalen der Physik* **389,** 457–484 (1927).
3. Barford, W. *Electronic and optical properties of conjugated polymers* (Oxford University Press, 2013).
4. Tang, C. L. *Fundamentals of quantum mechanics: for solid state electronics and optics* (Cambridge University Press, 2005).
5. Kittel, C. *et al. Introduction to solid state physics* (Wiley New York, 1976).
6. Pope, M. & Swenberg, C. E. Electronic processes in organic solids. *Annual Review of Physical Chemistry* **35,** 613–655 (1984).
7. Coulson, C. A. & Streitwieser, A. *Dictionary of pi-electron calculations* (Freeman, 1965).
8. Turro, N. J., Ramamurthy, V., Scaiano, J. C. *et al. Modern molecular photochemistry of organic molecules* (University Science Books, 2010).
9. Hestand, N. J. & Spano, F. C. Expanded theory of h-and j-molecular aggregates: The effects of vibronic coupling and intermolecular charge transfer. *Chemical Reviews* **118,** 7069–7163 (2018).
10. Dimitrov, S., Schroeder, B., Nielsen, C., Bronstein, H., Fei, Z., McCulloch, I., Heeney, M. & Durrant, J. Singlet exciton lifetimes in conjugated polymer films for organic solar cells. *Polymers* **8,** 14 (2016).
11. Siebrand, W. Radiationless transitions in polyatomic molecules. I. Calculation of Franck—Condon factors. *The Journal of Chemical Physics* **46,** 440–447 (1967).
12. Manneback, C. Computation of the intensities of vibrational spectra of electronic bands in diatomic molecules. *Physica* **17,** 1001–1010 (1951).

13. Markov, D. E., Amsterdam, E., Blom, P. W., Sieval, A. B. & Hummelen, J. C. Accurate measurement of the exciton diffusion length in a conjugated polymer using a heterostructure with a side-chain cross-linked fullerene layer. *The Journal of Physical Chemistry A* **109,** 5266–5274 (2005).

14. Lunt, R. R., Giebink, N. C., Belak, A. A., Benziger, J. B. & Forrest, S. R. Exciton diffusion lengths of organic semiconductor thin films measured by spectrally resolved photoluminescence quenching. *Journal of Applied Physics* **105,** 053711 (2009).

15. Dexter, D. L. A theory of sensitized luminescence in solids. *The Journal of Chemical Physics* **21,** 836–850 (1953).

16. Olaya-Castro, A. & Scholes, G. D. Energy transfer from Förster–Dexter theory to quantum coherent light-harvesting. *International Reviews in Physical Chemistry* **30,** 49–77 (2011).

17. Köhler, A. & Bässler, H. Triplet states in organic semiconductors. *Materials Science and Engineering R: Reports* **66,** 71–109 (2009).

18. Yost, S. R., Lee, J., Wilson, M. W., Wu, T., McMahon, D. P., Parkhurst, R. R., Thompson, N. J., Congreve, D. N., Rao, A., Johnson, K. *et al.* A transferable model for singlet-fission kinetics. *Nature Chemistry* **6,** 492 (2014).

19. Tabachnyk, M., Karani, A. H., Broch, K., Pazos-Outón, L. M., Xiao, J., Jellicoe, T. C., Novák, J., Harkin, D., Pearson, A. J., Rao, A. *et al.* Efficient singlet exciton fission in pentacene prepared from a soluble precursor. *APL Materials* **4,** 116112 (2016).

20. Zimmerman, P. M., Zhang, Z. & Musgrave, C. B. Singlet fission in pentacene through multi-exciton quantum states. *Nature Chemistry* **2,** 648 (2010).

21. Ehrler, B., Walker, B. J., Böhm, M. L., Wilson, M. W., Vaynzof, Y., Friend, R. H. & Greenham, N. C. In situ measurement of exciton energy in hybrid singlet-fission solar cells. *Nature Communications* **3,** 1019 (2012).

22. Walker, B. J., Musser, A. J., Beljonne, D. & Friend, R. H. Singlet exciton fission in solution. *Nature Chemistry* **5,** 1019 (2013).

23. Stern, H. L., Musser, A. J., Gelinas, S., Parkinson, P., Herz, L. M., Bruzek, M. J., Anthony, J., Friend, R. H. & Walker, B. J. Identification of a triplet pair intermediate in singlet exciton fission in solution. *Proceedings of the National Academy of Sciences* **112,** 7656–7661 (2015).

24. Dover, C. B., Gallaher, J. K., Frazer, L., Tapping, P. C., Petty II, A. J., Crossley, M. J., Anthony, J. E., Kee, T. W. & Schmidt, T. W. Endothermic singlet fission is hindered by excimer formation. *Nature Chemistry* **10,** 305 (2018).

25. Singh-Rachford, T. N. & Castellano, F. N. Photon upconversion based on sensitized triplet–triplet annihilation. *Coordination Chemistry Reviews* **254,** 2560–2573 (2010).

26. Di, D., Yang, L., Richter, J. M., Meraldi, L., Altamimi, R. M., Alyamani, A. Y., Credgington, D., Musselman, K. P., MacManus-Driscoll, J. L. & Friend, R. H. Efficient Triplet Exciton Fusion in Molecularly Doped Polymer Light-Emitting Diodes. *Advanced Materials* **29,** 1605987 (2017).

27. Dick, B. & Nickel, B. Accessibility of the lowest quintet state of organic molecules through triplet-triplet annihilation; an INDO CI study. *Chemical Physics* **78,** 1–16 (1983).

28. Marcus, R. A. & Sutin, N. Electron transfers in chemistry and biology. *Biochimica et Biophysica Acta (BBA)-Reviews on Bioenergetics* **811,** 265–322 (1985).

29. Coffey, D. C., Larson, B. W., Hains, A. W., Whitaker, J. B., Kopidakis, N., Boltalina, O. V., Strauss, S. H. & Rumbles, G. An optimal driving force for converting excitons into free carriers in excitonic solar cells. *The Journal of Physical Chemistry C* **116,** 8916–8923 (2012).

30. Ward, A. J., Ruseckas, A., Kareem, M. M., Ebenhoch, B., Serrano, L. A., Al-Eid, M., Fitzpatrick, B., Rotello, V. M., Cooke, G. & Samuel, I. D. The impact of driving force on electron transfer rates in photovoltaic donor–acceptor blends. *Advanced Materials* **27,** 2496–2500 (2015).

31. Bässler, H. & Köhler, A. "Hot or cold": how do charge transfer states at the donor–acceptor interface of an organic solar cell dissociate? *Physical Chemistry Chemical Physics* **17,** 28451–28462 (2015).

32. Congreve, D. N., Lee, J., Thompson, N. J., Hontz, E., Yost, S. R., Reusswig, P. D., Bahlke, M. E., Reineke, S., Van Voorhis, T. & Baldo, M. A. External quantum efficiency above 100% in a singlet-exciton-fission–based organic photovoltaic cell. *Science* **340,** 334–337 (2013).

33. Menke, S. M., Ran, N. A., Bazan, G. C. & Friend, R. H. Understanding energy loss in organic solar cells: toward a new efficiency regime. *Joule* **2,** 25–35 (2018).

34. Burke, T. M., Sweetnam, S., Vandewal, K. & McGehee, M. D. Beyond Langevin recombination: How equilibrium between free carriers and charge transfer states determines the open-circuit voltage of organic solar cells. *Advanced Energy Materials* **5,** 1500123 (2015).

35. Hou, J., Inganäs, O., Friend, R. H. & Gao, F. Organic solar cells based on non-fullerene acceptors. *Nature Materials* **17,** 119 (2018).

36. Semonin, O. E. Multiple Exciton Generation in Quantum Dot Solar Cells. *SPIE Newsroom* (2012).

37. Rao, A. & Friend, R. H. Harnessing singlet exciton fission to break the Shockley–Queisser limit. *Nature Reviews Materials* **2,** 17063 (2017).

38. Shockley, W. & Queisser, H. J. Detailed balance limit of efficiency of p-n junction solar cells. *Journal of Applied Physics* **32,** 510–519 (1961).

39. Stranks, S. D., Hoye, R. L., Di, D., Friend, R. H. & Deschler, F. The Physics of Light Emission in Halide Perovskite Devices. *Advanced Materials,* 1803336 (2018).

40. Hoye, R. L., Lai, M.-L., Anaya, M., Tong, Y., Galkowski, K., Doherty, T., Li, W., Huq, T. N., Mackowski, S., Polavarapu, L. *et al.* Identifying and Reducing Interfacial Losses to Enhance Color-pure Electroluminescence in Blue-emitting Perovskite Nanoplatelet Light-emitting Diodes. *ACS Energy Letters* (2019).

41. Bohm, M. L., Jellicoe, T. C., Rivett, J. P., Sadhanala, A., Davis, N. J., Morgenstern, F. S., Godell, K. C., Govindasamy, J., Benson, C. G., Greenham, N. C. *et al.* Size and energy level tuning of quantum dot solids via a hybrid ligand complex. *The Journal of Physical Chemistry Letters* **6,** 3510–3514 (2015).

42. Tabachnyk, M., Ehrler, B., Gélinas, S., Böhm, M. L., Walker, B. J., Musselman, K. P., Greenham, N. C., Friend, R. H. & Rao, A. Resonant energy transfer of triplet excitons from pentacene to PbSe nanocrystals. *Nature Materials* **13,** 1033–1038 (2014).

43. Yang, L., Tabachnyk, M., Bayliss, S. L., Böhm, M. L., Broch, K., Greenham, N. C., Friend, R. H. & Ehrler, B. Solution-processable singlet fission photovoltaic devices. *Nano Letters* **15,** 354–358 (2014).

44. Davis, N. J., Allardice, J. R., Xiao, J., Karani, A., Jellicoe, T. C., Rao, A. & Greenham, N. C. Improving the photoluminescence quantum yields of quantum dot films through a donor/acceptor system for near-IR LEDs. *Materials Horizons* **6,** 137–143 (2019).

45. Klimov, V. I. *Nanocrystal Quantum Dots* (CRC Press, 2010).

46. Alivisatos, A. P. Semiconductor clusters, nanocrystals, and quantum dots. *Science* **271,** 933–937 (1996).

47. Chuang, C.-H. M., Brown, P. R., Bulović, V. & Bawendi, M. G. Improved performance and stability in quantum dot solar cells through band alignment engineering. *Nature Materials* **13,** 796 (2014).

48. Zhang, Z., Chen, Z., Yuan, L., Chen, W., Yang, J., Wang, B., Wen, X., Zhang, J., Hu, L., Stride, J. A. *et al.* A New Passivation Route Leading to Over 8% Efficient PbSe Quantum-Dot Solar Cells via Direct Ion Exchange with Perovskite Nanocrystals. *Advanced Materials* **29,** 1703214 (2017).

49. Carey, G. H., Abdelhady, A. L., Ning, Z., Thon, S. M., Bakr, O. M. & Sargent, E. H. Colloidal quantum dot solar cells. *Chemical Reviews* **115,** 12732–12763 (2015).

50. Sargent, E. H. Colloidal quantum dot solar cells. *Nature Photonics* **6,** 133 (2012).

51. Liu, M., Voznyy, O., Sabatini, R., de Arquer, F. P. G., Munir, R., Balawi, A. H., Lan, X., Fan, F., Walters, G., Kirmani, A. R. *et al.* Hybrid organic–inorganic inks flatten the energy landscape in colloidal quantum dot solids. *Nature Materials* **16,** 258 (2017).

52. Ahmad, Z., Najeeb, M. A., Shakoor, R., Al-Muhtaseb, S. A. & Touati, F. Limits and possible solutions in quantum dot organic solar cells. *Renewable and Sustainable Energy Reviews* **82,** 1551–1564 (2018).

53. Liu, Y., Gibbs, M., Puthussery, J., Gaik, S., Ihly, R., Hillhouse, H. W. & Law, M. Dependence of carrier mobility on nanocrystal size and ligand length in PbSe nanocrystal solids. *Nano Letters* **10,** 1960–1969 (2010).

54. Zhitomirsky, D., Kramer, I. J., Labelle, A. J., Fischer, A., Debnath, R., Pan, J., Bakr, O. M. & Sargent, E. H. Colloidal quantum dot photovoltaics: the effect of polydispersity. *Nano Letters* **12,** 1007–1012 (2012).

55. Mentzel, T., Porter, V., Geyer, S., MacLean, K., Bawendi, M. G. & Kastner, M. Charge transport in PbSe nanocrystal arrays. *Physical Review B* **77,** 075316 (2008).

56. Snaith, H. J. Present status and future prospects of perovskite photovoltaics. *Nature Materials* **17,** 372 (2018).

57. Snaith, H. J. & Lilliu, S. The Path to Perovskite on Silicon PV. *Scientific Video Protocols* **1,** 1 (2018).

58. Li, Z., Yang, M., Park, J.-S., Wei, S.-H., Berry, J. J. & Zhu, K. Stabilizing perovskite structures by tuning tolerance factor: formation of formamidinium and cesium lead iodide solid-state alloys. *Chemistry of Materials* **28,** 284–292 (2015).

59. Abdi-Jalebi, M., Andaji-Garmaroudi, Z., Cacovich, S., Stavrakas, C., Philippe, B., Richter, J. M., Alsari, M., Booker, E. P., Hutter, E. M., Pearson, A. J. *et al.* Maximizing and stabilizing luminescence from halide perovskites with potassium passivation. *Nature* **555,** 497 (2018).

60. Zhao, B., Bai, S., Kim, V., Lamboll, R., Shivanna, R., Auras, F., Richter, J. M., Yang, L., Dai, L., Alsari, M. *et al.* High-efficiency perovskite–polymer bulk heterostructure light-emitting diodes. *Nature Photonics* **12,** 783 (2018).

61. Miller, O. D., Yablonovitch, E. & Kurtz, S. R. Strong internal and external luminescence as solar cells approach the Shockley–Queisser limit. *IEEE Journal of Photovoltaics* **2,** 303–311 (2012).

62. Green, M. A. Radiative efficiency of state-of-the-art photovoltaic cells. *Progress in Photovoltaics: Research and Applications* **20,** 472–476 (2012).

63. Richter, J. M., Abdi-Jalebi, M., Sadhanala, A., Tabachnyk, M., Rivett, J. P., Pazos-Outón, L. M., Gödel, K. C., Price, M., Deschler, F. & Friend, R. H. Enhancing photoluminescence yields in lead halide perovskites by photon recycling and light out-coupling. *Nature Communications* **7,** 13941 (2016).

64. Kim, J., Lee, S.-H., Lee, J. H. & Hong, K.-H. The role of intrinsic defects in methylammonium lead iodide perovskite. *The Journal of Physical Chemistry Letters* **5,** 1312–1317 (2014).

65. Brandt, R. E., Poindexter, J. R., Gorai, P., Kurchin, R. C., Hoye, R. L., Nienhaus, L., Wilson, M. W., Polizzotti, J. A., Sereika, R., Žaltauskas, R. *et al.* Searching for "defect-tolerant" photovoltaic materials: combined theoretical and experimental screening. *Chemistry of Materials* **29,** 4667–4674 (2017).

66. Stranks, S. D., Eperon, G. E., Grancini, G., Menelaou, C., Alcocer, M. J., Leijtens, T., Herz, L. M., Petrozza, A. & Snaith, H. J. Electron-hole diffusion lengths exceeding 1 micrometer in an organometal trihalide perovskite absorber. *Science* **342,** 341–344 (2013).

67. Xing, G., Mathews, N., Sun, S., Lim, S. S., Lam, Y. M., Grätzel, M., Mhaisalkar, S. & Sum, T. C. Long-range balanced electron-and hole-transport lengths in organic-inorganic $CH_3NH_3PbI_3$. *Science* **342,** 344–347 (2013).

68. Yin, W.-J., Shi, T. & Yan, Y. Unusual defect physics in $CH_3NH_3PbI_3$ perovskite solar cell absorber. *Applied Physics Letters* **104,** 063903 (2014).

69. Steirer, K. X., Schulz, P., Teeter, G., Stevanovic, V., Yang, M., Zhu, K. & Berry, J. J. Defect tolerance in methylammonium lead triiodide perovskite. *ACS Energy Letters* **1,** 360–366 (2016).

70. Shao, Y., Xiao, Z., Bi, C., Yuan, Y. & Huang, J. Origin and elimination of photocurrent hysteresis by fullerene passivation in $CH_3NH_3PbI_3$ planar heterojunction solar cells. *Nature Communications* **5,** 5784 (2014).

71. Van Reenen, S., Kemerink, M. & Snaith, H. J. Modeling anomalous hysteresis in perovskite solar cells. *The Journal of Physical Chemistry Letters* **6,** 3808–3814 (2015).

72. Courtier, N. E., Cave, J. M., Foster, J. M., Walker, A. B. & Richardson, G. How transport layer properties affect perovskite solar cell performance: insights from a coupled charge transport/ion migration model. *Energy & Environmental Science* **12,** 396–409 (2019).

73. Babayigit, A., Ethirajan, A., Muller, M. & Conings, B. Toxicity of organometal halide perovskite solar cells. *Nature Materials* **15,** 247 (2016).

74. Kamat, P. V., Bisquert, J. & Buriak, J. Lead-free perovskite solar cells. *ACS Energy Letters* **2,** 904–905 (2017).

75. Asghar, M., Zhang, J., Wang, H. & Lund, P. Device stability of perovskite solar cells–A review. *Renewable and Sustainable Energy Reviews* **77,** 131–146 (2017).

76. Yang, Y. & You, J. Make perovskite solar cells stable. *Nature News* **544,** 155 (2017).

77. Charles, B., Dillon, J., Weber, O. J., Islam, M. S. & Weller, M. T. Understanding the stability of mixed A-cation lead iodide perovskites. *Journal of Materials Chemistry A* **5,** 22495–22499 (2017).

78. Yang, W. S., Park, B.-W., Jung, E. H., Jeon, N. J., Kim, Y. C., Lee, D. U., Shin, S. S., Seo, J., Kim, E. K., Noh, J. H. *et al.* Iodide management in formamidinium-lead-halide–based perovskite layers for efficient solar cells. *Science* **356,** 1376–1379 (2017).

Chapter 3

Experimental methods

3.1 Introduction

In this chapter we describe the detailed experimental methods used for device fabrication and measurements. We also describe the steady-state and time-resolved spectroscopy set-ups used. Various microscopy techniques that have been used to understand the thin-film morphologies in this work have also been covered in this chapter.

3.2 Colloidal Quantum Dot (CQD) synthesis

Lead-sulfide and lead-selenide are the two types of colloidal quantum dots (CQDs) used in this study. The CQDs, kindly synthesized by Le Yang, Tom Jellico, Marcus Boehm, James Xiao and Zhilong Zhang, were used for parts of this project. For CQD solar cells optimization and incorporation in working tandem solar cells, PbS CQDs were synthesized by the current author and prepared using the hot injection method described below.

3.2.1 The hot-injection synthesis method

In a typical batch of PbS CQDs synthesized using a Schlenk line, 0.625 g (2.8 mmol) of lead (II) oxide (PbO, 99.999% purchased from sigma aldrich) was added along with 2.1 mL (6.6 mmol) of oleic acid (OA,90% technical grade) and 25 mL 1-octadecene (ODE, 90% technical grade) to a three-neck flask and stirred under vacuum ($\leq$ 0.01 mbar) to degas for two hours. The temperature of the flask was gradually increased from room temperature to 95 °C. In a separate three-neck flask, 25 mL of ODE was degassed separately at 90 °C for two-hours. Once the mixture with PbO turned clear after 2h, it was put under nitrogen and temperature was set to 115 °C. 20 mL of degassed ODE was mixed with 296 µL (1.39 mmol) of bis(trimethylsilyl)sulfide $(TMS)_2S$ and 144 µL (0.83 mmol) of diphenhylphosphine (DPP) in a nitrogen glove box. The temperature of the PbO mixture three-neck flask was briefly increased to 120 °C and was allowed to drop back to 115 °C.

At 115 °C, the sulphur precursor mixture was swiftly injected into the PbO flask. After injection, the mixture was allowed to cool to 36 °C and the reaction was halted at this point by stopping the stirring. The mixture was then transferred to another degassed Schlenk flask in order to transfer it to an argon glovebox for purification.

In the glovebox, the CQDs were extracted by adding a mixture of butanol and ethanol (99.8%, anhydrous) followed by centrifugation at 5000 rpm for 5 minutes. The transparent supernatant was disposed of inside the glovebox and a mixture of hexane (99.8%, anhydrous) and ethanol (1:3 ratio by volume) was added and the solutions were centrifuged as before. The final step was repeated and the purified CQDs were dried under nitrogen. Finally, the dried CQDs were subsequently suspended in anhydrous octane (95%) and stored inside the glovebox.

3.3 Device fabrication

Indium tin oxide (ITO, $\approx 100\,\text{nm}$) coated glass substrates, 1.2 cm x 1.2 cm were used for fabricating all devices in this study. The substrates were cleaned by submerging the substrate holder into an acetone containing beaker and sonicating the beaker in an ultrasonic cleaner for 15 minutes followed by repeating the process with isopropanol. Subsequently, the substrates were dried using a nitrogen gun. Poly(3,4-ethylenedioxythiophene) polystyrene sulfonate (PEDOT:PSS) (Clevios PV P AI4083) was spun coated at 4000-5000 rpm from an aqueous solution onto the substrates (for organic devices). Finally, the substrates were annealed at 200 °C for 20 minutes under flowing nitrogen to ensure complete evaporation of any remaining water before depositing the next layers. The substrates were slowly cooled to below 50 °C on the hot plate after switching it off and before moving it to deposit the following layers. These substrates will be referred to as *PEDOT-substrates* from here onwards.

3.3.1 Bilayer p-Pc/C_{60} solar cells

As shown in Figure 3.1 13,6-N-sulfinylacetamido pentacene (p-Pc) and C_{60} were deposited on PEDOT-substrates followed by the final aluminium electrode. p-Pc was dissolved in chloroform, in various concentrations ranging from $2\,\text{mg}\,\text{mL}^{-1}$ to $7\,\text{mg}\,\text{mL}^{-1}$ and spun-cast (1500 rpm for 60 s) on PEDOT substrates. These films were then annealed at a range of temperatures from 150 °C to 300 °C and allowed to cool on a metal block post

annealing. The precursor needs to be annealed for at least 10 minutes at 150 °C to obtain a complete conversion to core pentacene. The annealing time was further optimized for devices, as will be discussed in Chapter 5. For comparison, evaporated pristine pentacene (e-Pc) devices identical to these bilayer devices were prepared and e-Pc was deposited via thermal annealing to obtain 40 nm thick films. The C_{60} layer was deposited via thermal evaporation under vacuum with pressures below 10^{-6} mbar. The deposition rate was maintained to in the range of 0.1 $Å s^{-1}$ to 0.2 $Å s^{-1}$ to obtain a 40 nm thick film. Finally, 100 nm of aluminium (Al) was thermally evaporated with a deposition rate of 0.1 $Å s^{-1}$ to 0.2 $Å s^{-1}$ for the first 20 nm and of 0.2 $Å s^{-1}$ to 0.4 $Å s^{-1}$ for the rest. The devices were encapsulated using slow drying epoxy resin and hardener.

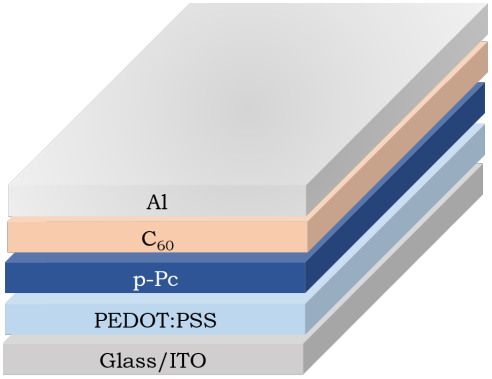

Figure 3.1: Device structure showing each layer deposited for a bilayer p-Pc/C_{60} solar cell.

3.3.2 Bulkheterojunction p-Pc/$PC_{61}BM$ solar cells

The active layer for bulk-heterojunction devices were prepared by dissolving p-Pc and Phenyl-C61-butyric acid methyl ester (PCBM) in 10:1 molar ratio in chloroform. Two concentrations of combined-solute were used in our study: 40 mg mL^{-1} (thin) and 70 mg mL^{-1} (thick). The blend film was spin coated to form a thin-film for AFM charcterization.

The p-Pc/PCBM bulk-heterojunction devices were fabricated and characterised by Dr. Marcus Boehm and the fabrication process is explained here for completion.

For device fabrication, the thin and thick blends were deposited via spin coating on PEDOT-substrates followed by annealing at various temperatures in the range of 150 °C to 300 °C. We also deposited (via spin-coating) an additional PCBM (20 mg mL^{-1}) layer to ensure that the p-Pc crystals do not come in contact with the top electrode. Finally, 100 nm of aluminium (Al) was thermally evaporated with a deposition rate in the range

of 0.1 Ås^{-1} to 0.2 Ås^{-1} for the first 20 nm and in the range 0.2 Ås^{-1} to 0.4 Ås^{-1} for the rest.

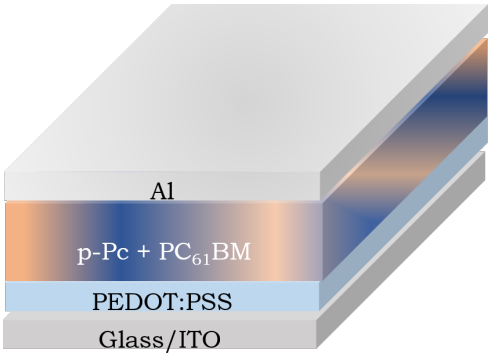

Figure 3.2: Device structure showing each layer deposited for the bulkheterojunction p-Pc/$PC_{61}BM$ solar cell.

3.3.3 Hybrid p-Pc/CQD devices

Pentacene precursor was employed in various device architectures to harvest triplets generated via singlet fission using CQDs as electron acceptors. Figure 3.3 shows four different architectures with different electron and hole-transport layers employed in each. The detailed deposition method for titanium dioxide (TiO_2) and zinc-oxide(ZnO) layers is described in the following Section 3.3.4.1. Layer-by-layer CQD deposition is also described in detail in Section 3.3.4. p-Pc layer for these devices (Figures 3.3a-c)) is deposited in an identical fashion to the one described previously in Section 3.3.1.

The active layer for device shown in Figure 3.3d is prepared by combining p-Pc (7 mg mL^{-1}) and CQDs (25 mg mL^{-1}) in a chloroform solution and depositing it via spin-coating on TiO_2 coated ITO-substrates. Spin speeds of 1500-2500 rpm for 45 s to 60 s are used for this deposition. Molybdenum trioxide (MoOx, 10 nm) and gold (Au, 80 nm) are thermally evaporated under vacuum with pressures below 10^{-6} mbar. The deposition rate is maintained in the range of 0.1 Ås^{-1} to 0.2 Ås^{-1} for MoOx and the first 20 nm of Au, and is increased to 0.2 Ås^{-1} to 0.4 Ås^{-1} for the final 60 nm of Au.

3.3.4 CQD solar cells

CQD device fabrication and optimization has been a crucial part of this work. In this section we will describe all different methods used to fabricate CQD devices including the various materials and deposition methods used.

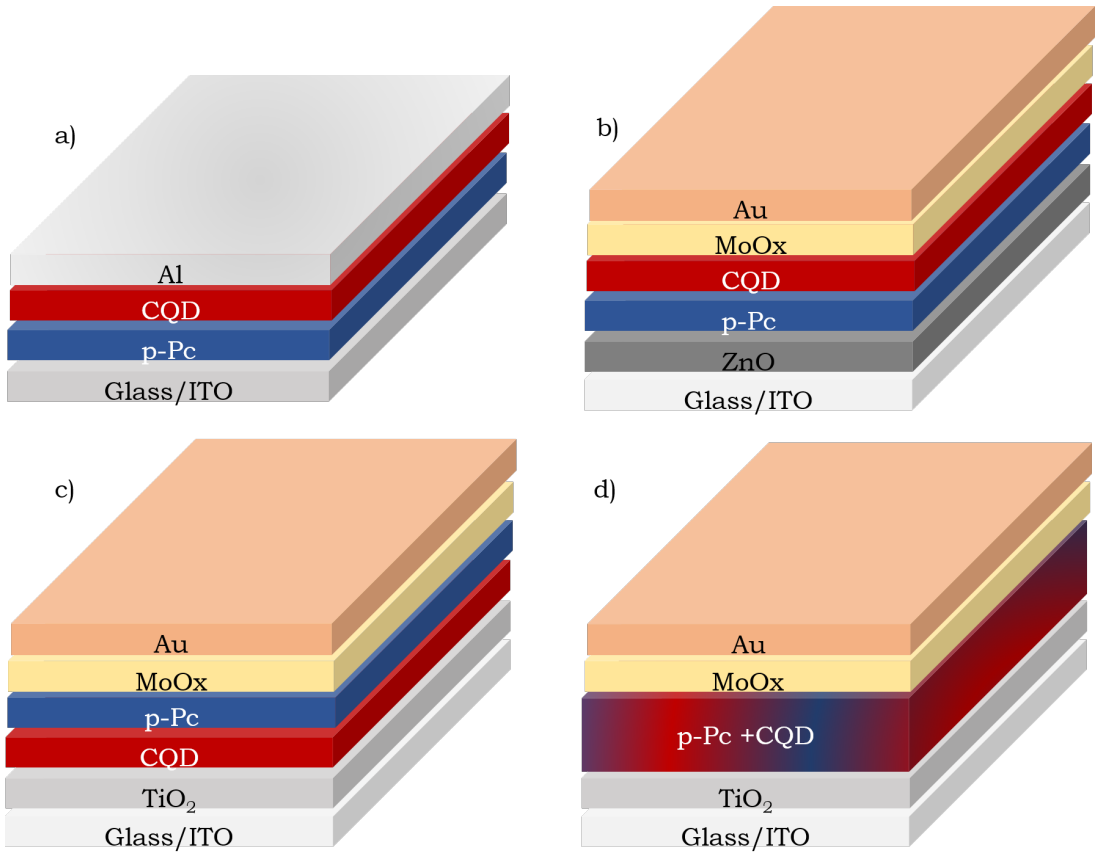

Figure 3.3: Device structure showing each layer deposited for three different architectures of p-Pc/CQD bilayer devices (a-c) and a p-Pc/CQD blend device (d).

3.3.4.1 Metal-oxide charge-transport layers

Various different types of zinc-oxide (ZnO) nanoparticles were used in this study as they play an important role in charge extraction from the CQD devices.

1. **Sol-gel nanoparticles:** Inside a nitrogen glovebox, diethyzinc in hexane (0.25 mL) purchased from Sigma Aldrich, was diluted in tetrahydrofuran (THF, 0.75 mL). The solution was thoroughly stirred before spin-casting on ITO-substrates for 45 s at 4000 rpm in air. Following spin coating, the substrates were allowed to dry in ambient conditions for 15 minutes and then annealed at 130 °C for 5 minutes. After cooling, the substrates were stored in an inert glovebox environment.

2. **Commercial nanoparticle dispersions (Sigma Aldrich):** ZnO nanoparticle dispersion was bought from Sigma Aldrich and diluted using ethanol or isopropanol (IPA). The dispersions were stored at temperatures below 5 °C and always stirred in an ultrasonic bath for 5-10 minutes prior to usage. This ZnO was spin-coated for 30 s in air at 2000 rpm. The ZnO coated substrates were then annealed at 90 °C to 120 °C for 10-30 minutes.

3. **Commercial nanoparticle dispersions (PV Infinity):** The ZnO nanoparticle dispersion was bought from PV Infinity (5.6%w/v). The nanoparticle ink was stored at temperatures below 5 °C and always stirred in an ultrasonic bath for 5-10 minutes prior to usage. This ZnO was spin-coated for 40 s in air at 3000 rpm. These ZnO coated substrates were then annealed at 50 °C for 10 minutes.

4. **Obtained from collaborators:** ZnO nanoparticles synthesized by our collaborator (S.Bai) at the University of Oxford, dispersed in IPA, were used for tandem solar cell fabrication. These nanoparticles were spun at 4500 rpm for 40 s and did not require any annealing.

Two different types of titanium dioxide (TiO_2) was used for devices prepared in this study. The sol-gel TiO_2 for compact layer and mesoporous TiO_2 paste purchased from Sigma Adrich for the mesoporous layer.

1. **Sol-gel TiO_2 for the compact layer:** 175 µL of titanium (IV) isopropoxide (97 %, 0.6 mmol) and 17.5 µL of 2 M hydochloric acid (HCl) were dissolved in 1.25 mL of anhydrous ethanol in separate vials. The HCl mixture was slowly added to the titanium precursor vial while stirring it. Once a clear solution was obtained, the nanoparticles were filtered using 0.45 µm PVDF filter and then deposited via spin coating at 2000 rpm for 30 s. The substrates were then annealed at 500 °C for 30 minutes followed by cooling them back to room temperature on hot plate.

2. **TiO_2 paste for mesoporous layer:** The paste was diluted in ethanol (2:7 molar ratio) and centrifuged at 5000 rpm for 3-5 minutes. Once thoroughly mixed, the solution was deposited via spin coating at 2000 rpm for 30 s and substrates annealed at 500 °C for 30 minutes.

For CQD solar cells and all hybrid devices incorporating CQDs, the best results were obtained using TiO_2 nanoparticles prepared using the sol-gel method explained above. For perovskite and tandem solar cells, we use both the compact layer and the mesoporous layers as shown in the schematics of device structures.

The CQD devices fabricated for this study have active layers deposited via two main methods: spin-coating and dip-coating. These deposition methods were adapted from the work published by [1] and [2] and optimized as required.

3.3.4.2 Spin-casted active layer

Each CQD active layer consisted of multiple (5 to 12) layers of sequentially deposited CQD layers. Once the oleic-acid (long ligand) capped CQDs were deposited, short-ligands (1,2-benzendithiol (BDT) or 1,2-ethanedithiol (EDT)) were drop-casted on the CQD coated substrate. The concentration of BDT was tuned between $1-2\mu L/mL$ in anhydrous isopropanol and for EDT between $0.01-0.02\mu L/mL$. After allowing the substrate to soak in short-ligand solution for 30-45s, the remaining solution was spun-off. Excess short-ligands that did not attach to the CQDs were subsequently washed off using the short-ligand solvent (IPA, butanol). The washing off was performed by spin-coating the substrates with solvents. A final step of spin-coating the CQD solvent (octane, hexane, chloroform or toluene) was performed to remove any CQDs that were not ligand-exchanged. This solid-state ligand-exchange process was repeated for every CQD layer until a visibly thick 150 nm to 200 nm layer was obtained. Figure 3.4 shows the device architecture used for standard CQD-only devices employing TiO_2 or ZnO as the electron extracting layer and MoOx as the hole extracting layer. 80 nm of Au was deposited via thermal evaporation to complete the device.

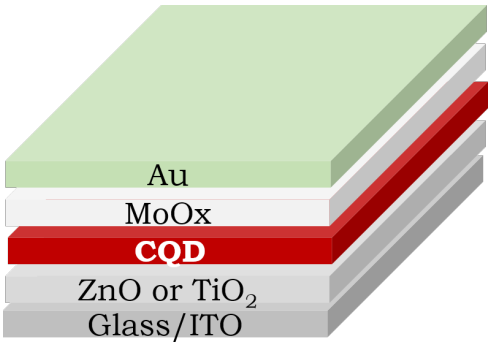

Figure 3.4: Device structure showing each layer deposited for a spin-coated, layer-by-layer deposited CQD solar cell. The CQD layer was deposited by sequentially performing solid-state ligand exchange on 5-6 layers of CQDs.

3.3.5 Perovskite solar cells

A schematic of the perovskite device structure is presented in Figure 3.5. Perovskite solar cells were fabricated using the standard, well-studied perovskite methylammonium iodide ($MAPbI_2$, 1.55 eV bandgap) as the absorbing layer. A combination of compact and mesoporous TiO_2 layers was employed as the electron-transporting layer. We experimented with using either poly(triaryl amine) (PTAA) or Spiro-MeOTAD (2,2',7,7'-Tetrakis[N,N-

di(4-methoxyphenyl)amino]-9,9'-spirobifluorene) as the hole-transporting layer. Methylammonium iodide (MAI) and lead(II)-iodide (PbI_2) were combined in 1:1 molar ratio to prepare the precursor solution. We used 218.6 mg (0.6 M) of MAI and 633.9 mg of PbI_2 in a solvent mixture containing 700 µL dimethylformamide (DMF) and 300 µL dimethyl sulfoxide (DMSO). The PTAA solution was prepared by adding $7-10$ mg of PTAA to 1 mL of toluene. Spiro-MeOTAD solution was prepared by mixing 80 mg with 1 mL of chlorobenzene (CB). One of the two hole-transport dopants, lithium bis(trifluoromethylsul-phonyl)imide (LiTFSI), was prepared by adding 104 mg of LiTFSI salt to 200 µL of acetonytrile (ACN). 1.6 µL of this LiTFSI solution and 2 µL (4-tert-butylpyridine) TBP were subsequently added to the hole-extraction layer as dopants.

The TiO_2 layers (250 nm) were deposited via the processes outlined in Section 3.3.4.1. $MAPbI_2$ layer (280 nm) was deposited by using the anti-solvent method and annealed at 100 °C for 45 minutes. The hole-transporting layers (200 nm) were then spin-coated and if spiro-OMeTAD was used then it was allowed to rest in ambient conditions for durations in the range of 60 minutes to 90 minutes. If PTAA was used, it was spun-cast in the nitrogen glovebox and did not require exposure to air. Finally, a further electron-blocking and hole-transporting MoOx (7 nm) was thermally evaporated followed by 80 nm of Au.

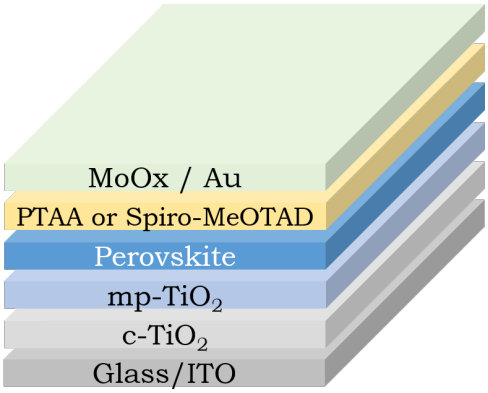

Figure 3.5: Device structure schematic showing layers deposited to fabricate the perovskite solar cells for this study.

3.3.6 Tandem solar cells

One of the most important results of this work was the demonstration of the first prototype of a monolithic, solution-processed, perovskite-CQD tandem solar cell [3, 4]. The difficulty of depositing multiple solution processed layers without destroying the bottom layers has made the realisation of solution-processed tandem solar cells using these two materials so-

far impossible. In this study, we identified the orthogonal solvents that allow deposition of multiple CQDs layers on top of the perovskite cell (discussed in detail in Chapter 4).

The two types of studies used to understand the device physics of our tandem cell are shown in Figure 3.6. While Figure 3.6b shows the layer-by-layer architecture of our monolithic tandem cell, Figure 3.6a illustrates the bottom CQD device being optically filtered by the top perovskite device. The perovskite device used here, for the purpose of filtering, is identical to the individual perovskite device from Section 3.3.5, except with a 1 nm thin MoOx/Au layer in this case. Such a 4-terminal type system allowed us to study the optical properties of the tandem cell without limiting the device performance by current-matching requirements.

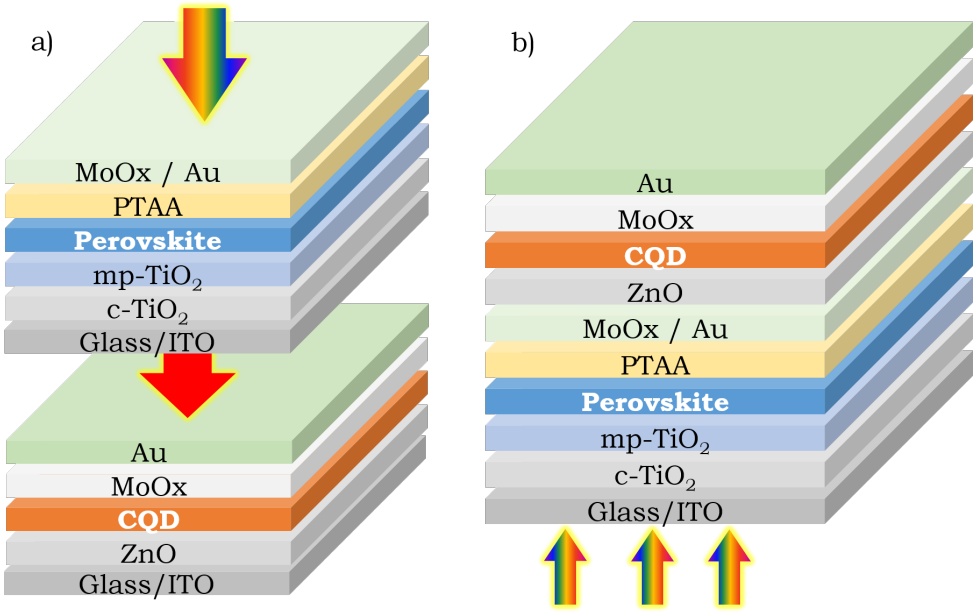

Figure 3.6: Schematic describing two different methods of measurements used for tandem devices a) Optical filtering by placing a perovskite device on top of the bottom CQD device. b) A complete monolithic tandem showing each layer deposited.

3.3.7 Organic light emitting diodes

A complete device structure with layer-by-layer architecture of the host/guest PVK/TIPS-pC LEDs used in our work is illustrated in Figure 3.7. We deposit PEDOT:PSS from an aqueous solution and dried as for the p-Pc/PCBM solar cells. On a PEDOT-substrate we then deposited poly[(9,9-dioctylfluorenyl-2,7-diyl)-co-(4,4'-(N-(4-sec-butylphenyl)diphenylamine)] (TFB) as a hole-transporting layer from 12 mg mL^{-1} solution in toluene and annealed it at 190 °C for 20 minutes. The active layer consisting of TIPS-pentacene dispersed in high-bandgap polymer poly(9-vinylcarbazole) (PVK) was subsequently spun from a

20 mg mL^{-1} PVK solution in tetrahydrofuran (THF). The concentration of TIPS-pentacene in PVK was varied between 1% and 10% by weight to obtain detectable electroluminescence from the LEDs. After deposition, the active layer was annealed at 100 °C for 10 minutes. We employed Bathophenanthroline (BPhen) as the electron-transporting layer which was spun from an 8 mg mL^{-1} methanol solution and annealed at 60 °C for 10 minutes. Lithium fluoride (0.6 nm) and aluminium (100 nm)(LiF/Al) electrodes were then deposited via thermal evaporation. The TFB, BPhen and active layer solutions used for OLED fabrication were stirred overnight at 50 °C and filtered through a 0.2 µm polytetrafluoroethylene (PTFE) membrane filter prior to deposition.

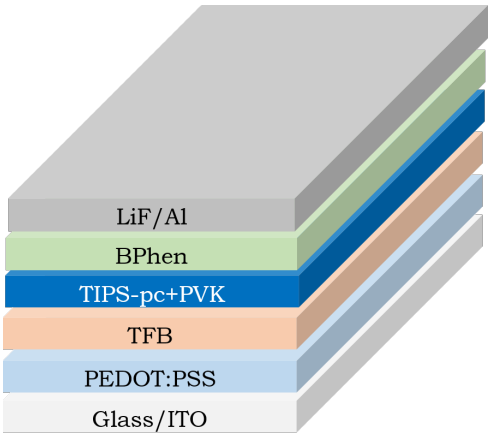

Figure 3.7: Device structure showing each layer deposited via spin-casting for organic TIPS-pc + PVK LEDs.

3.4 Solar cell characterization

All solar cells characterized for this work were loaded into an 8-pixel device holder. Some devices were encapsulated in a glovebox using standard slow drying epoxy. For air sensitive devices that could not be encapsulated, we loaded the 8-pixel device inside a glovebox and covered it with a transparent glass lid using an o-ring.

3.4.1 Current-voltage (I-V) characteristics

The I-V characteristics of solar cells were measured by using a Keithley 2635 source measure unit (SMU) to apply voltage bias to the 8-pixel device holder and record the current generated per unit area. An ABET Sun 2000 AM 1.5 G solar simulator was used as the light source. Light output was always calibrated using a reference Si photocell to

obtain 100 mW/cm^2 output.

3.4.2 External quantum efficiency (EQE)

The EQEs of the solar cells were measured using a 100 W tungsten lamp as the light source dispersed through a monochromator (Oriel Cornerstone 260) onto the device pixel. The incident light was focused to a spot size of <1 mm^2 to illuminate each pixel (4.5 mm^2) individually. A set of photodiodes with known spectral response were used to calibrate the EQE values. ThorLabs SMR05 silicon photodiodes and InGaAs photodiodes (ThorLabs SM1PD2A) were used for UV-Vis and NIR-IR spectral resolution respectively.

3.5 LED characterization

The photons emitted (electroluminescence signal) from an LED pixel were collected using a silicon photodiode with an active area of 100 mm^2. The distance between the LED and the photodiode was manually controlled and recorded. A Keithley 2400 source meter was used to supply voltage to the LEDs and measure the current through the device. Another Keithley 2000 source meter was used to collect the output from the silicon photodiode. A LabView routine collected the data and generated output files containing the external quantum efficiency (EQE, photons generated per electron injected into the device) and current density (mA/cm^2) and luminance (cd/m^2) as a function of applied voltage.

3.5.1 Electroluminescence

Electroluminescence spectra were collected by using an optical fiber connected to an Andor iDus CCD-19295 detector. These measurements were aquired in an identical setup to the one used for magnetic field measurements as explained in Section 3.6.3.

3.6 Steady-state spectroscopy

Thin films deposited via spin-coating on either borofloat glass substrates or spectrosils were used to prepare samples for spectroscopy measurements. For solution measurements, solutions were prepared either in a 10 mm or a 1 mm path length quartz cuvette.

3.6.1 Absorption

Organic films that absorb in the UV-Vis region were measured using a Helwett Packard HP 8453 UV-Vis spectrophotometer. CQDs that absorb in the near-infrared and infrared region were measured using PerkinElmer Lambda 9, a monochromatic, UV-Vis-NIR spectrophotometer. For thin-film samples, a clear substrate identical to the sample substrate was used for background correction or empty scan. In case of solution measurements, clear solvent in an identical or the same cuvette were used to obtain a blank scan for background correction.

3.6.2 Photoluminescence (PL)

Steady-state photoluminescence spectra were obtained by illuminating a 2 mm diameter spot on the sample with a 407 nm pulsed laser. The emission spectra was collected using a 500 mm focal length spectrograph (Princeton Instruments, SpectraPro2500i) and detected with a cooled CCD camera.

3.6.3 Magnetoelectroluminescence (MEL)

Figure 3.8 describes the setup used to measure the magnetoelectroluminescence (MEL). MEL was measured by mounting the device onto a fixed 8-pixel holder. Each of the pixels was electrically excited by applying the required voltage using a Keithley 2400 source meter. The device holder was placed at equidistance from the two poles of an electromagnet. Using LabView, the electromagnet was set to apply random magnetic fields between −300 mT and +300 mT. The magnetic field at the pixel was measured using a portable gauss meter.

The electroluminescence spectra was collected with and without the magnetic field as explained in Section 3.5.1. Magnetic field (B-field) effects on the EL were obtained by measuring the change in emission in the spectral region of interest and normalizing it by the no-field spectra for all B-fields (see equation 3.1).

$$MEL = \frac{EL(B) - EL(B=0)}{EL(B=0)} \tag{3.1}$$

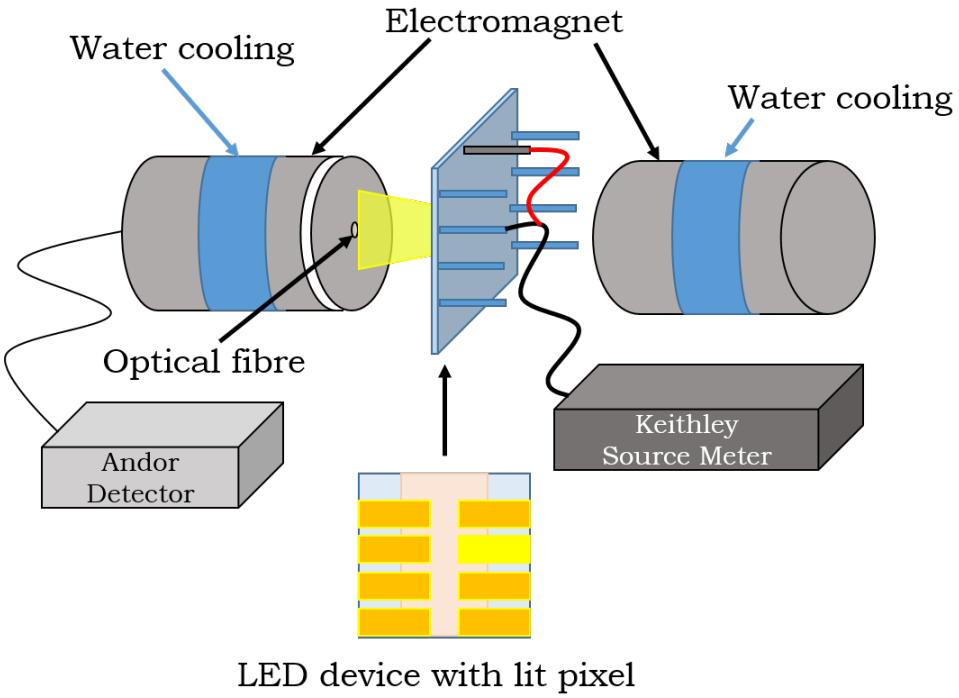

Figure 3.8: Schematic diagram of magnetoelectroluminescence setup showing an LED placed in between the two poles of an electromagnet. The LED is placed with the lit pixel facing the optical fibre. The magnetic field is applied perpendicular to the luminescent device surface. A Keithley source meter is used to electrically excite the LED and an Andor iDus: CCD-19295 detector along with optical fibre used to collect the electroluminescence spectra.

3.7 Transient measurements

Different setups were used to measure time-resolved data from films and devices. Each of these setups are described below.

3.7.1 Time-correlated single photon counting (TCSPC)

TCSPC measurements were carried out using a 407 nm pulsed laser to optically excite the samples. The pulse repition rate was set between 2.5-40 MHz to obtain a time resolution between 25-400 ns. Figure 3.9 describes the operation mechanism of a typical TCSPC setup.

3.7.2 Transient electroluminescence

An electrically-gated intensified CCD (ICCD) camera (Andor iStar DH740 CCI-010) along with a calibrated grating spectrometer (Andor SR303i) were used to measure the time-

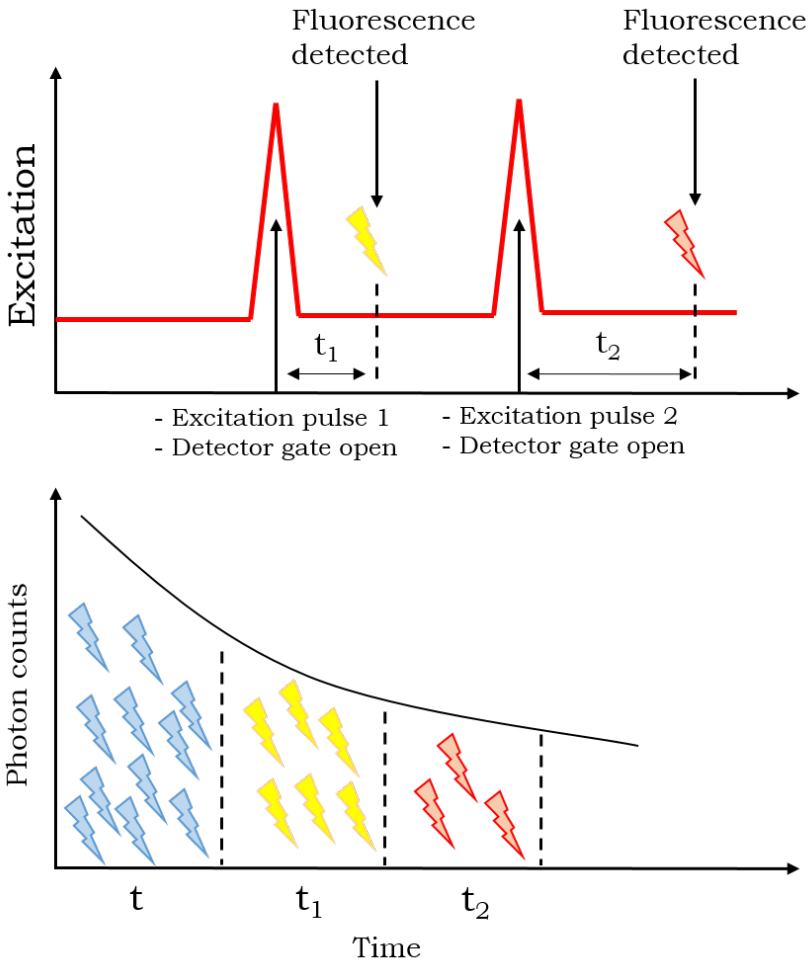

Figure 3.9: Schematic diagram of the time-correlated single photon counting operation. The top graph shows the arrival of the laser (excitation) pulse opening the detector gate and the fluorescence (emitted photon) from the sample, generating a time record. The bottom graph shows a histogram-type binning of the number of photons in each time bin, resulting in the TCSPC signal as required.

resolved EL. ICCD provides a longer time range of time-resolved measurements between 10 ns to 1 ms. The LEDs were mounted on an eight pixel holder similar to the one shown in the schematic Figure 3.8. Both the LED and the camera were connected to a function generator (Helwett Packard 8116A Pulse/function generator). The LEDs were excited using a square pulse with 8 V positive and −4 V negative bias. The duty cycle was set to have 10 % on and 90 % off cycles. The pulse width was varied between 100 ns and 10 µs as required. The transient-EL spectrum from the devices was collected using an optical fibre coupled directly into the slit of the camera.

3.7.3 Transient photocurrent/photovoltage

For transient measurements, the devices were loaded into an air-tight device holder in the inert atmosphere of a glovebox and then connected to nitrogen flow once outside. The device transients were measured using an oscilloscope (Tektronix DPO 3032) connected directly to this device holder.

For transient-photocurrent (TPC) measurements, the device holder was connected to the 50 Ω input of the oscilloscope via a custom transimpedance amplifier to convert the output signal to a voltage signal; whereas the 1 MΩ input of the oscilloscope was used for transient-photovoltage (TPV) measurements.

A 465 nm LED (LED465E, ThorLabs) connected to a wavefunction generator (Agilent 33500B) and a purpose built low-noise PSU was used as the light source for TPC measurements. A white-light bias was provided using a solar simulator (Newport) with AM 1.5 G equivalent output for TPV measurements. A series of ThorLabs neutral density filters were used to attenuate the incident light intensity on the device in order to obtain the required open circuit voltages for comparison, when required.

3.8 Microscopy

Various microscopy techniques have been used in this work to study the film morphology, CQD dispersion and other film properties. In this section we provide details of each of the techniques/setups used.

3.8.1 Atomic force microscopy

An atomic force microscope (AFM) was used to measure the film surface morphology. This characterization was specially helpful for measuring the effect of annealing the pentacene precursor (p-Pc) on crystal formation in the film. AFM measurements also allowed for the measurement of film thicknesses by scratching the film with a sharp object and measuring the step height by using an AFM perpendicular to the direction of the scratch. An aluminium coated 30 nm silicon tip with resonant frequency 325 kHz was used for these measurements.

3.8.1.1 Sample preparation for AFM

The AFM samples were usually prepared on a standard borofloat glass substrate. These films were generally spin-coated from the same solution as used in devices. For e-Pc samples, pentacene was thermally evaporated onto borofloat substrates as in for the device active layer.

3.8.2 Scanning electron microscopy

We used the Hitachi S-5500 In-Lens FE SEM which can provide resolutions as high as 0.4 nm. Acceleration voltage in the range of 5 kV to 15 kV was used for these measurements.

3.8.2.1 Organogel sample preparation for SEM

The organogels were prepared by adding gelator powder to toluene in a vial and placing the vial on a hot plate at 120 °C for 20-25 minutes. Once the solution was clear and the gelator was completely dissolved, the hot plate was switched off and the vial taken off the hot plate. Simultaneously, a needle was maintained at 120 °C in toluene and was used to inject a dilute solution of CQDs into the gelator vial immediately after it was taken off the heat. This ensured that no nucleation was instigated by insertion of a cold needle into the gelator and allowed for dispersion of CQDs in the gel matrix. The organogel samples were prepared on a silica coated silicon wafer substrates. The gel concentration was varied between 2 mg mL^{-1} to 4 mg mL^{-1} to obtain a reasonably dilute film thereby ensuring gel formation. The CQDs (<1 mg mL^{-1} in toluene) were suspended in the vials containing the gelator in toluene as explained above. While still in liquid phase, the mixture was dropped onto the silica coated silicon substrate and was allowed to cool and dry in order to obtain gel formation on the substrate.

3.8.2.2 Cross-section sample preparation for SEM

Devices prepared in the same batch as the working tandem solar cell prototype were used for capturing a cross-section image. The device was cut into ≈ 2mm x 3mm pieces using a diamond glass cutter while making sure to obtain a cross-section through a working pixel. These devices prepared on ITO coated glass substrates, were measured directly and provided good contrast to obtain images presented later in this work.

3.8.3 Scanning transmission electron microscopy

The STEM images were captured using the Hitachi S-5500 In-Lens FE SEM.

3.8.3.1 Organogel sample preparation

TEM grids with copper mesh coated with a layer of holey-carbon were employed for measuring the dispersion of CQDs in the organogels. These grids allowed for the formation of gel-fibres between the holes and, thus, a way to look through them to locate CQDs within the fibres. The concentration of the gelator was set at $4\,\mathrm{mg\,mL^{-1}}$ in order to form thin films while maintaining gel formation as normal. The CQDs were added in a similar manner to the samples prepared for SEM measurements above. The mixture was drop-cast onto the TEM grids while still in liquid phase and the grids were allowed to cool and dry for 1 hr.

3.8.4 Transmission electron microscopy

The FEI Philips Tecnai 20 transmission electrom microscope was used to capture TEM images. An electron acceleration of 200 keV was generally used in bright-field mode for these images.

3.8.4.1 Sample preparation for TEM

TEM Grids (200 mesh Cu, Agar Scientific) were used for all TEM measurements. A very dilute ($1\,\mathrm{mg\,mL^{-1}}$) solution of CQDs in toluene or octane were drop-cast onto the TEM grid inside a glovebox and allowed to dry before measuring. These grids were naturally exposed to air during the measurements.

3.8.5 Grazing Incidence X-ray scattering

Grazing Incidence X-ray scattering experiments were performed by Katharina Broch on the beamline X04SA MS-SurfDiffr (Swiss Light Source, Villigen, Switzerland) with $\lambda = 0.95\,\text{Å}$ and a Pilatus II detector.

Bibliography

1. Yang, L., Tabachnyk, M., Bayliss, S. L., Böhm, M. L., Broch, K., Greenham, N. C., Friend, R. H. & Ehrler, B. Solution-processable singlet fission photovoltaic devices. *Nano Letters* **15,** 354–358 (2014).

2. Zhang, Z., Chen, Z., Yuan, L., Chen, W., Yang, J., Wang, B., Wen, X., Zhang, J., Hu, L., Stride, J. A. *et al.* A New Passivation Route Leading to Over 8% Efficient PbSe Quantum-Dot Solar Cells via Direct Ion Exchange with Perovskite Nanocrystals. *Advanced Materials* **29,** 1703214 (2017).

3. Karani, A., Yang, L., Bai, S., Futscher, M. H., Snaith, H. J., Ehrler, B., Greenham, N. C. & Di, D. Perovskite/colloidal quantum dot tandem solar cells: theoretical modeling and monolithic structure. *ACS Energy Letters* **3,** 869–874 (2018).

4. Karani, A., Yang, L., Greenham, N. C. & Di, D. *Toward high-efficiency solution-processed tandem solar cells* in *Organic, Hybrid, and Perovskite Photovoltaics XIX* **10737** (2018), 107371I.

Chapter 4

Tandem Solar cells

4.1 Introduction

Silicon-based solar cells have been dominating the terrestrial solar-panel market with average power conversion efficiencies (PCEs) of 25 % whereas the highest obtained efficiency of such a cell has recently reached (26.7 ± 0.5) % [1]. Other competitive thin-film technologies such as copper indium gallium selenide (CIGS) and cadmium telluride (CdTe) photovoltaics, have achieved (22.9 ± 0.5) % and (22.1 ± 0.5) % PCEs respectively [1]. These efficiencies are already approaching the threshold for single-junction solar cells of 33 %, based on the Shockley-Queisser (S-Q) limit [2]. However, in order to further reduce the levelised cost of electricity (LCOE) and make solar-powered electricity competitive in the market, it is essential to find ways of improving PCE of solar cells beyond the S-Q limit. One promising way of surpassing the S-Q limit is using multiple semiconductors in a tandem multi-junction structure to efficiently harvest a larger proportion of the solar spectrum whilst minimizing thermalization losses [3]. High-efficiency tandem solar cells with efficiencies of up to ≈ 39 % have been demonstrated [1]. However, these cells are based on III-V semiconductors manufactured by highly expensive processes such as epitaxy [4]. Producing efficient tandem cells using low-cost methods remains a challenge [5].

Rapid development of halide-perovskite solar cells in recent years has pushed their PCEs to (22.7 ± 0.8) % [3] and their performance is competitive with CIGS and CdTe for photovoltaic applications. Bandgap tunability, and low-cost, large-area solution processability are some of the qualities that make perovskites attractive materials for application in tandem solar cells (TSCs) [6]. The constant effort in improving the optical and electrical properties of perovskites has led to perovskites being suitable for use in conjunction with multitude of other semiconductors including silicon, organic materials, kesterites, CIGS and even other perovskites in TSCs [7–14]. Figure 4.1 highlights the rapid progression of innovations in this direction. Perovskites were first employed in a monolithic tandem cell

with kesterites in October 2014 by Todorov et al [8]. In December 2014, Bailie et al. [9] demonstrated four-terminal (4T) tandem cells using perovskite solar cells as the top cell and industrially well-established silicon and CIGS solar cells as the bottom cell. TSCs with two-terminal (2T) monolithic configuration were demonstrated in quick succession thereafter offering structural simplicity and higher theoretical efficiencies compared to other configurations [15]. 2T perovskite/silicon TSCs realised in March 2015 by Mailoa et al. [10] were followed by 2T perovskite/CIGS by Todorov et al. in September 2015 [16] and perovskite/perovskite 2T TSCs by Jiang et al. in December 2015 [11]. With further advances in perovskite bandgap tunability and stability research, Eperon et al. not only demonstrated highly efficient 2T all-perovskite TSCs ($\approx 17\,\%$ PCE) but also demonstrated highly efficient 4T all-perovskite TSCs reaching efficiencies of as high as $20.3\,\%$ with this architecture in August 2016 [7].

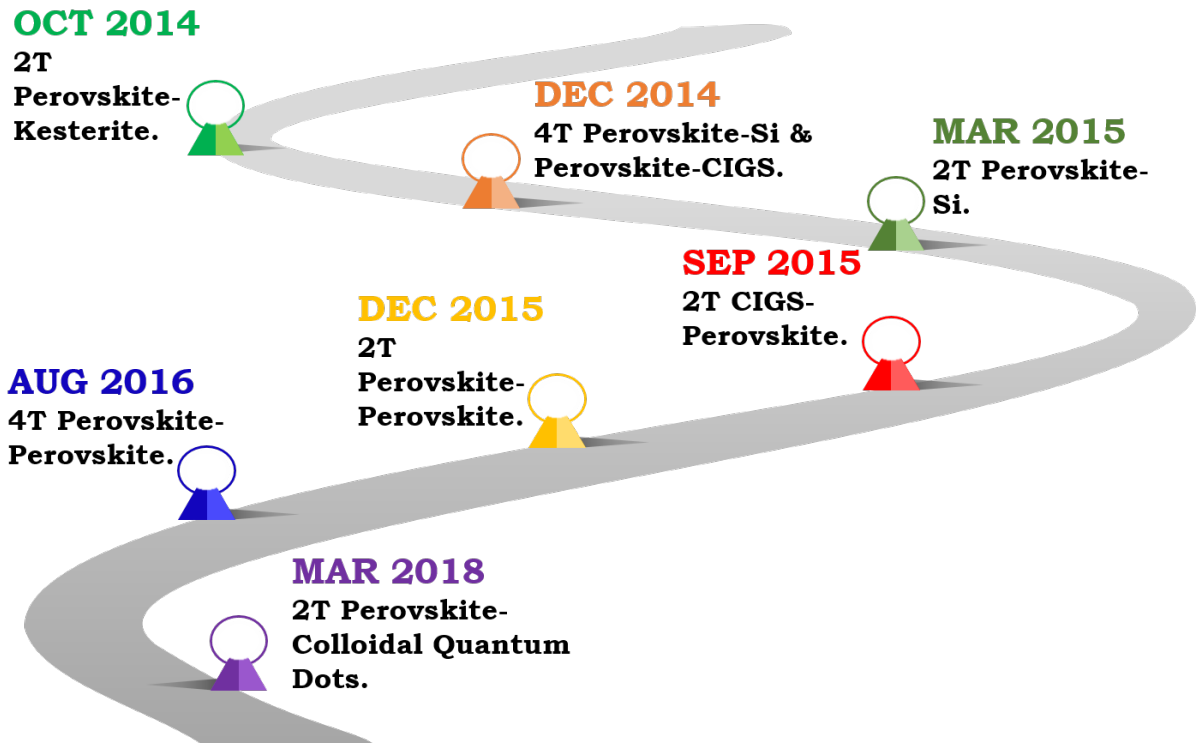

Figure 4.1: Timeline showing the first demonstrations of perovskite based two-terminal (2T) and four-terminal (4T) tandem solar cells.

While highly efficient single-junction perovskite and perovskite/perovskite tandem cells have already been demonstrated [12, 17, 18] it is important to note that the near-infrared photons are not effectively harvested by such devices due to the limited bandgap tunability of the perovskite material family. Therefore, the best perovskite/perovskite and perovskite/organic tandem solar cells utilise photons with wavelengths shorter than

≈1000 nm ($E_{photon} \geq 1.24$ eV) [7, 12, 19]. The stability issue of the low-bandgap tin (Sn)-based perovskite is yet to be overcome [20–22]. Organic/organic tandem devices can also only convert photons with wavelengths up to ≈ 1000 nm ($E_{photon} \geq 1.24$ eV) [23]. The absorption edge of perovskite/Si tandem devices is limited to ≈ 1100 nm ($E_{photon} \geq 1.12$ eV, the bandgap of Si) [24–26]. However, due to the broad bandgap tunability of the chalcogenide colloidal quantum dots (CQDs) including lead sulfide (PbS) and lead selenide (PbSe) [27–29], they can provide an ideal bandgap matching with the perovskite cell in a tandem structure, and can extend the absorption edge further to harvest lower-energy photons (see Figure 4.2). Favourably, both CQD and perovskite material families are known to be highly luminescent [30, 31] providing an opportunity to recycle unused photons which are radiatively emitted (*vide infra*).

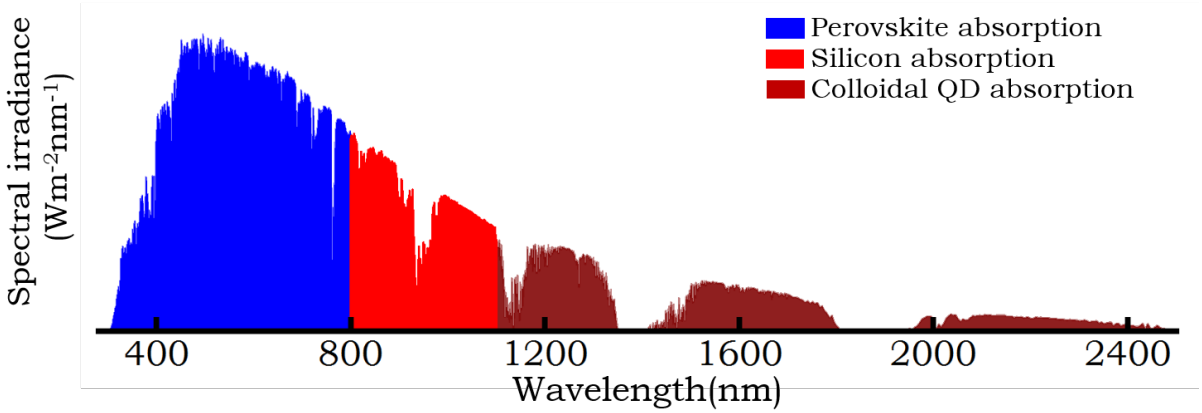

Figure 4.2: Solar spectrum (AM 1.5 global) showing the limit of photocurrent generation by a typical perovskite solar cell with 1.55 eV bandgap, and the lower-energy photons that could be captured by low-bandgap CQDs (Bandgap ≥ 0.65 eV).

In this work we carefully model the detailed balance limit for a TSC prepared using these two highly luminescent materials and find that the radiative coupling between the two sub-cell materials can critically influence the overall device performance. We calculate that the absolute gain from radiative coupling can be as high as 11 % in our devices. Although silicon is the core element of the electronics industry, being an indirect bandgap material, radiative recombination of charges is extremely unlikely in silicon, rendering gain in efficiency through radiative coupling almost impossible [32]. We thus explore the new option of using bandgap-tunable, emissive colloidal quantum dots (CQDs) as the bottom cell active material to absorb the low-energy (red) photons along with perovskite as the emissive top cell active material to absorb the high-energy (blue) photons. We demonstrate the first prototype of a 2T monolithic perovskite-CQD tandem cell (with

1 % PCE) [15] and model that the highest achievable theoretical efficiency from such devices can be as high as ≈ 43 %. Using our model, we estimate that using state-of-art perovskite [33] and CQD [34] devices an overall PCE of ≈ 29 % could be obtained from a perovskite/CQD TSCs.

Parts of this chapter have been adapted from our publications [15] and [35]. Initial experiments on checking the prospects of the project were performed by Le Yang. The fabrication, optimization and characterization was done by myself and guided by Le Yang. The theoretical modelling was conducted by myself with guidance from Dawei Di. The manuscript for our peer-reviewed publication [15] was written together with Le Yang and Dawei Di.

4.2 Theoretical modelling

The Shockley-Queisser detailed balance model (SQ model) which defines the maximum achievable theoretical efficiency for a single p-n junction solar cell is built upon the following assumptions [2, 36]:

1. The cell has a planar geometry and absorbs radiation with photon energies higher than the bandgap from the sun or the surrounding, and at the same time radiates to the surroundings (typically assumed to be a hemisphere).

2. Each photon with energy (E_{photon}) greater than the bandgap (E_g) of the absorbing material creates an electron-hole pair. Thus, the absorption (a) of photons with energy E_{photon} is defined as:

$$a(E_{photon}) = \begin{cases} 1 & \text{if } E_{photon} \geq E_g \\ 0 & \text{if } E_{photon} < E_g \end{cases} . \tag{4.1}$$

3. Apart from photocurrent generation, the only carrier relaxation process is radiative recombination emitting photons with energies above the semiconductor bandgap (E_g).

4. The sun is a blackbody-like radiator, producing isotropic photon fluxes which can be described by Planck distribution (or the standard AM1.5 spectrum for terrestrial solar cells) of the form

$$E(\lambda)\Delta\lambda = \frac{8\pi hc}{\lambda^5}\frac{1}{e^{hc/\lambda kT} - 1}\,, \tag{4.2}$$

where h is the Planck constant. c is the speed of light. k is the Boltzmann constant. T is the blackbody temperature. $E(\lambda)$ is the energy density of radiation in the wavelength interval λ to $\lambda + \Delta\lambda$ where $\Delta\lambda$ a small increment in wavelength.

5. The active layer establishes a uniform chemical potential μ during operation to be in thermal equilibrium with the surroundings. This leads to spontaneous emission β_e and produces an isotropic emitted flux given by

$$\beta_e = \frac{2}{h^3c^2} \cdot \frac{E^2}{e^{(E-\mu)/kT} - 1}\,, \tag{4.3}$$

where $E = hc/\lambda$ is the photon energy and μ can be thought of as a thermodynamic function expressing the ability of an uncharged atom or molecule in a chemical system to perform physical work.

Extending these assumptions for a two-junction perovskite/CQD tandem solar cell, the current density and voltage generated by the tandem cell (J_{tandem}, V_{tandem}) by two sub-cells electrically connected in series (here the perovskite cell and the CQD cell) can be described in terms of their individual current densities (J_{pero}, J_{CQD}) and voltages (V_{pero}, V_{CQD}) using eqs. (4.4) and (4.5) [36–39].

$$J_{tandem} = J_{pero} = J_{CQD} \tag{4.4}$$

$$V_{tandem} = V_{pero} + V_{CQD} \tag{4.5}$$

In order to calculate the current generated by each individual cell (*pero* or *CQD*), not in tandem, we can write the absorption of photons from the incident solar irradiation by each cell as:

$$a_{cell} = \int_{E_{cell}}^{\infty} \Gamma(E)\mathrm{d}E\,, \tag{4.6}$$

where E is the photon energy, $\Gamma(E)$ is the energy-dependent distribution of photon flux based on the AM 1.5 G solar spectrum and E_{cell} is the bandgap of the absorbing semiconductor. When the cell is placed under a top cell in tandem configuration such that the top cell absorbs all the high-energy photons, the limit on integral in eq. (4.6) will go from the bottom cell bandgap $E_{bottomcell}$ to the top cell bandgap $E_{topcell}$. The radiative

blackbody emission from each cell can be defined as:

$$\beta_{cell} = \frac{2\pi q}{h^3 c^2} \cdot \int_{E_{cell}}^{\infty} \frac{E^2}{e^{(E-qV_{cell})/kT} - 1} \mathrm{d}E \,, \tag{4.7}$$

for $cell = pero$ or $cell = CQD$ where V_{cell} is the operating voltage of the respective perovskite ($pero$) or CQD cell, and q is the unit charge. Considering that both the materials used for this study are highly luminescent, from assumptions $3-5$ we can write the photocurrent (J_{cell}) generated by each sub-cell as the total absorption (a_{cell}) minus the total spontaneous emission β_{cell}. We can include a radiative coupling term by considering that the spontaneous emission from each of the sub-cells will be absorbed by the adjacent cell as follows:

$$J_{pero} = a_{pero} + g_1 \cdot \frac{2\pi q}{h^3 c^2} \cdot \int_{E_{pero}}^{\infty} \frac{E^2}{e^{(E-qV_{CQD})/kT} - 1} \mathrm{d}E - g_2 \cdot \beta_{pero} \,, \tag{4.8}$$

$$J_{CQD} = a_{CQD} + g_3 \cdot \frac{2\pi q}{h^3 c^2} \cdot \int_{E_{pero}}^{\infty} \frac{E^2}{e^{(E-qV_{pero})/kT} - 1} \mathrm{d}E - g_4 \cdot \beta_{CQD} \,, \tag{4.9}$$

where g_1-g_4 are geometric factors which are influenced by the spatial power distribution of the radiation. For a simple mono-facial planar radiator (bottom cell) with isotropic radiation, $g = 1$. A planar bi-facial isotropic radiator (top cell) has a $g = 2$.

In equation 4.8, the first term is the photocurrent of the perovskite cell due to the solar irradiation. The second term calculates the additional photocurrent of the perovskite cell by recycling emission from the CQD cell. The third term describes the emission from radiative recombination in the perovskite cell. Similarly, the first term in equation 4.9 considers the CQD photocurrent from the solar irradiation filtered by the perovskite top cell. The second term evaluates the additional CQD photocurrent contribution due to photon recycling from the perovskite cell. The third term describes the emission from radiative recombination in the CQD cell. Note the limit on the radiative coupling term integral are decided by the fact that the top perovskite sub-cell can only absorb and emit photons with energy $E \geq E_{pero}$.

As perovskites and CQDs are luminescent materials [30, 31, 40, 41], it is important to consider the radiative coupling between the two sub-cells while ensuring current matching for a monolithic tandem cell as modeled above. Recycling of emitted photons from solar cells can be an important strategy for enhancing the overall device PCE [42, 43].

4.3 Results and discussion

4.3.1 Tandem device architectures

Tandem solar cell (TSC) architectures are designed based on three important criteria: (a) number of terminals (two or four); (b) optical coupling of the sunlight into the device; (c) radiative coupling of photons between the sub-cells. Each of these criteria becomes significant when optimising the tandem cell performance.

Three of the most commonly used architectures of double-junction TSCs are: (i) mechanically stacked, four-terminal (4T) TSCs (see Figure 4.3a); (ii) optically coupled four-terminal (O-4T) TSCs (see Figure 4.3b); and (iii) monolithic two-terminal (2T) TSCs (see Figure 4.3c) [44]. The top cell, in every configuration, ideally absorbs all high-energy (blue) photons above its bandgap and the unabsorbed low-energy (red) photons are passed on to the bottom cell.

In 4T TSCs, two individual cells are mechanically stacked and connected in parallel with the blue-absorbing cell on top of red-absorbing bottom cell (see Figure 4.3a). Parallel connection of the two cells allows each sub-cell to function electrically independently, relaxing the requirements on current matching in this configuration. Optically, the 4T tandem cells can either have the top cell placed atop the bottom cell or in any other configuration in order to couple maximum sunlight directly into the individual sub-cells.

An O-4T TSC is electrically identical to the normal 4T TSC but with a different strategy applied for optical coupling of sunlight into the device. Unlike the normal 4T TSCs, the blue-absorbing and red-absorbing devices are positioned at an angle as shown in Figure 4.3b. An optical light splitter is used to split the solar spectrum into separate red and blue beams of light. One part (blue beam) of the spectrum is deflected to shine on the blue-absorbing sub-cell and the other is deflected to shine on the red-absorbing sub-cell. This way the two cells have access to the respective regions of the spectrum without any loss of photons reaching the bottom cell due to optical filtering by the top cell as in 4T TSCs.

In a monolithic two-terminal (2T) TSC (figure 4.3c), the top cell and the bottom cell are only separated by a thin, transparent, conductive interlayer which is responsible for extracting charges from both the cells. The (2T) TSCs have sub-cells electrically connected in series. This means that in order to obtain maximum photocurrent from the TSC

the current flowing through the two sub-cells must be equal and will be limited by the sub-cell generating lower photocurrent. Fabricating a 2T TSC can be exacting as the active layers are deposited subsequently layer-by-layer. Finding an appropriate transparent conducting layer to minimise optical losses while maintaining low series resistance of this interlayer makes monolithic architecture a challenging one to realise.

As per the detailed balance model explained in Section 4.2, each of these sub-cells emits some of the absorbed photons through recombination of unextracted charges. Assuming all such recombination events are radiative, the top cell emits blue photons (see Figure 4.3d that can either be absorbed (recycled) by the bottom cell or be lost to the surrounding depending on the tandem configuration. As such, 2T TSCs provide a significant advantage compared to the 4T TSCs when radiative coupling is concerned. Although the photons emitted from the top cell of a 4T tandem device can be optically coupled into the bottom cell, the intermidiate insulation materials and presence of additional electrodes provide various loss pathways. Besides, from an industrial perspective a 2T architecture presents lower parasitic absorption losses and can be cheaper since the cost of extra insulating material is lower compared to a mechanically stacked 4T TSC. Thus in this work, we focus on developing a monolithic 2T TSC with two emissive materials to maximise the benefits from radiative coupling.

4.3.2 Monolithic tandem efficiency estimations

Figure 4.4a shows the detailed balance limit calculated for a two-junction solar cell with and without radiative coupling. These calculations were performed using eqs. (4.8) and (4.9) to find the J-V curve of each device including the J_{SC} and V_{OC}, followed by calculating the current-limiting device and then calculating the tandem device characteristics using eqs. (4.4) and (4.5). We calculated a maximum efficiency of 43 % for a perovskite ($E_g = 1.55\,\text{eV}$)/PbS($E_g = 1.0\,\text{eV}$) tandem cell with radiative coupling between the top and the bottom cell, and 37 % without. It is interesting to note here that peak efficiencies are obtained for different bottom-cell bandgaps under the two separate assumptions. While a 1.0 eV bottom-cell bandgap paired with the 1.55 eV perovskite top cell provides the best performance by assuming radiative coupling, 0.8 eV is the optimum bottom cell bandgap without the coupling. This further emphasizes the importance of bandgap tunability of the bottom-cell material, and CQDs are very suitable for this purpose. Importantly, a significant contribution of radiative coupling to the tandem cell

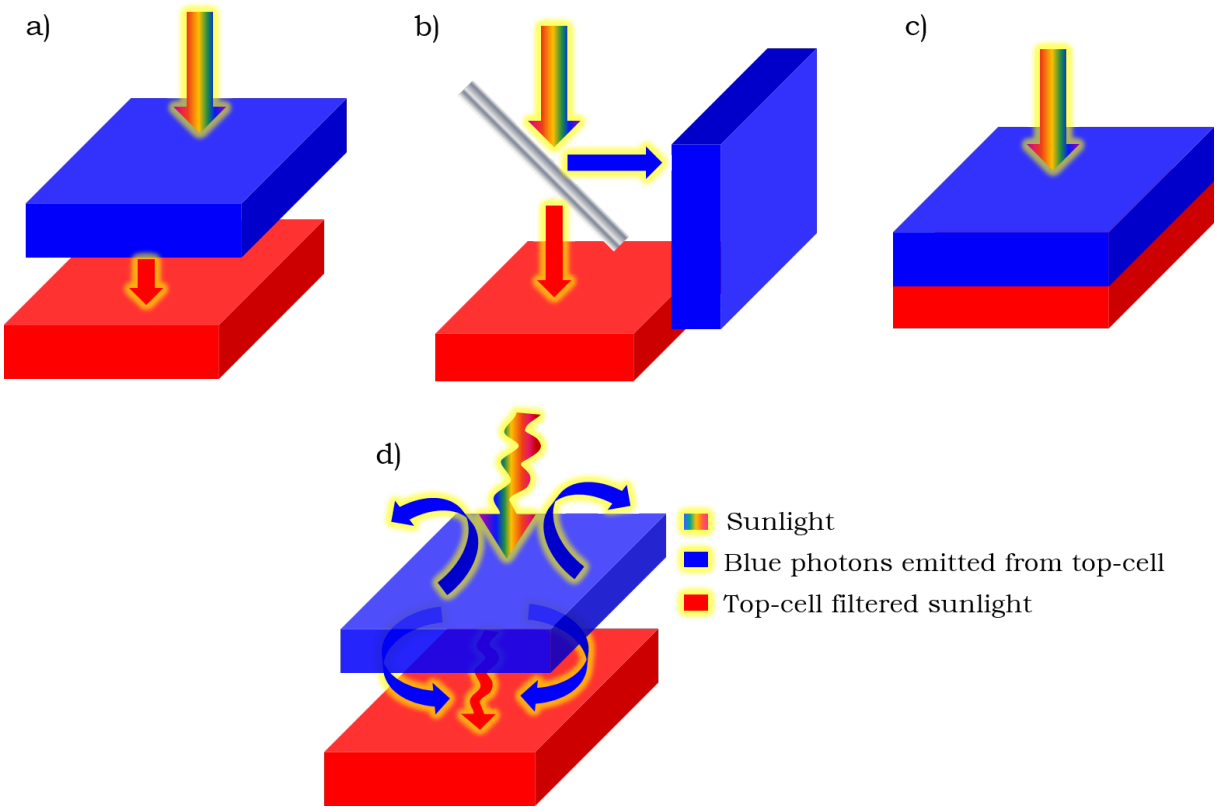

Figure 4.3: Schematic design of the three most commonly used double-junction TSC configurations. a) Four-terminal, mechanically stacked (4T), b) optically coupled four-terminal (O-4T) and c) monolithic two-terminal (2T).d) Schematic diagram illustrating radiative coupling between the top perovskite sub-cell and the bottom CQD sub-cell.

efficiencies is expected for CQD bottom-cell bandgaps of greater than 0.8 eV. The enhancement of power-conversion efficiency due to radiative coupling ranges from $\approx 11\,\%$ for an optimum CQD bandgap of ≈ 1.0 eV, to $\approx 20\,\%$ for CQDs with a bandgap just below the perovskite bandgap. This efficiency gain is primarily due to the recycling of luminescence from the perovskite top cell by the CQD bottom cell. As the bandgap of the bottom cell approaches that of the top cell, the efficiency enhancement due to radiative coupling becomes more apparent as less energy is lost due to thermalisation after photon reabsorption by the bottom cell. In other tandem cell configurations where the top and the bottom cells are not closely connected as in a monolithic structure, the photons emitted from the top cell can be lost to parasitic absorption by the multiple interfaces with different refractive indices. This means that the $> 10\,\%$ efficiency gain due to radiative coupling cannot be utilised completely in other systems, unless the TSC configuration is carefully considered.

As shown in Figure 4.4b, we have calculated the current-voltage (J-V) characteristics for individual cells using the SQ model described in Section 4.2 and obtained a tandem

cell J-V curve with an open-circuit voltage (V_{OC}) of 1.64 V and a short-circuit current (J_{SC}) of 28.4 mA/cm^2, leading to a 1-sun (AM 1.5 G) PCE of 42.8 %.

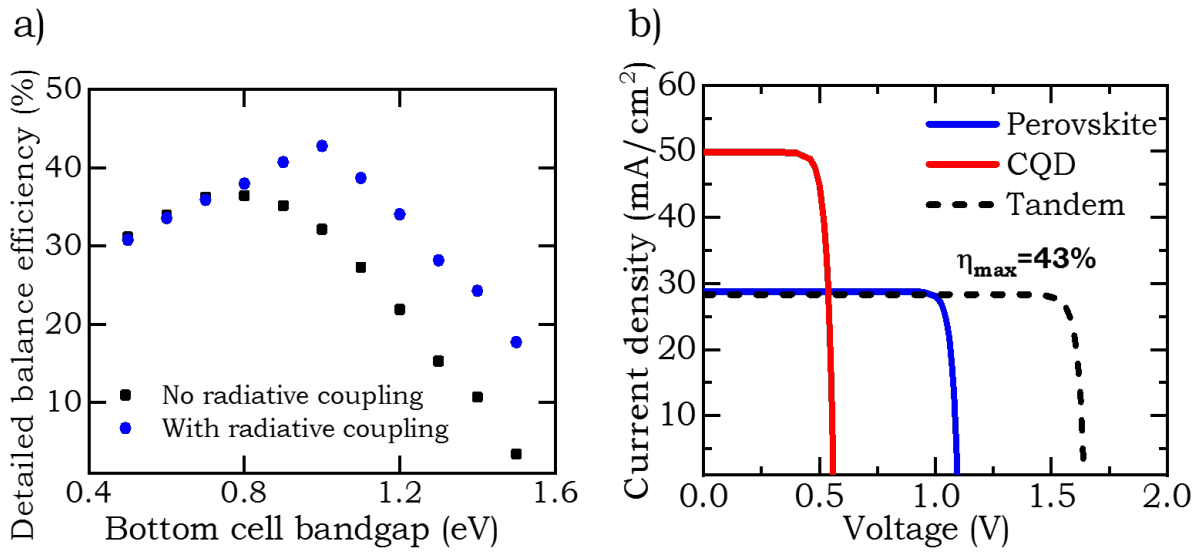

Figure 4.4: a) Theoretical detailed balance efficiency limits as functions of the CQD bottom-cell bandgap in a monolithic tandem cell configuration, with and without considering radiative coupling between sub-cells. The top cell is a typical perovskite cell ($CH_3NH_3PbI_3$ active layer) with a bandgap of 1.55 eV. The maximum achievable efficiency of 43 % is obtained with an ideal CQD bottom-cell bandgap of 1.0 eV. b) Theoretical J-V curves derived from the detailed balance model for ideal individual and tandem cells.

4.3.3 Optically filtered CQD devices

In order to first check the optical compatibility of the perovskite top cell with the CQD bottom cell, we conducted optical filtering experiments. As shown in Figure 4.5, we used a perovskite device stack prepared in an identical fashion to the perovskite unit cell employed in the two-terminal tandem. Detailed experimental methods for the fabrication of perovskite device stacks and the bottom CQD cells have been described in Section 3.6.

Figure 4.6 demonstrates the effect of using various filters, on the J-V characteristics of the CQD individual cell. On covering the individual CQD cell from the glass/ITO side (see Figure 4.5) with longpass filters or the perovskite device stack, we observe significant reduction in the photocurrent from the CQD device. Comparing the effect of using a perovskite device stack as a filter versus using a 630 nm longpass filter, we observe that the J_{SC} reduction is almost the same and the V_{OC} reduction is almost identical in both cases. Assuming that the 780 nm and 830 nm longpass filters provide transmittance profiles of

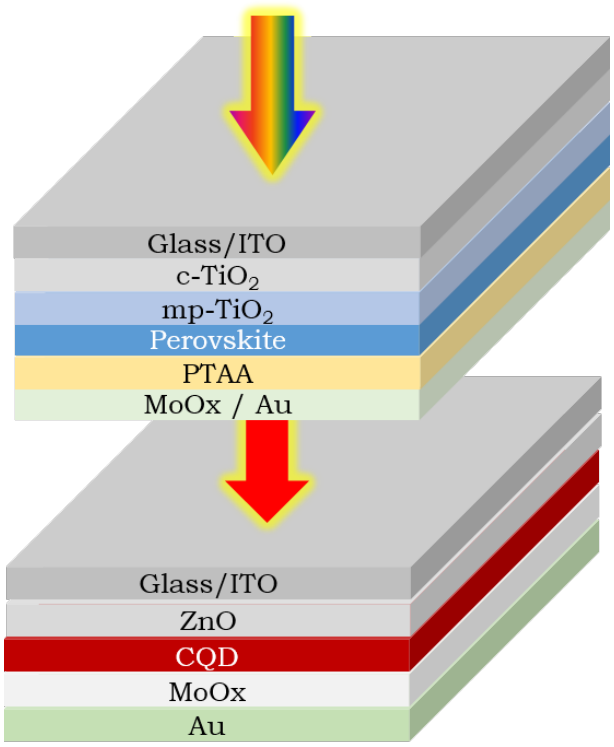

Figure 4.5: Layer-by-layer design of the CQD cells shadowed by perovskite device stacks to demonstrate the effect of optical filtering on the bottom-cell J-V performance.

perovskite films with lower bandgaps, the dark red and the brown lines in Figure 4.6a respectively, show the effect of increasing top-cell (perovskite) bandgap slightly on the bottom-cell J-V parameters. As can be seen from the device characteristics table in Figure 4.6b, the V_{OC} of CQD device D1 reduces by about 28 % of its original value with a 630 nm longpass filter and a similar reduction ($\approx$ 29 %) is observed on D2 (similar CQD device) with a perovskite device stack filter. The J_{SC} of D1 reduces by 56 % of its original value with the 630 nm longpass filter in place whereas for D2 its J_{SC} reduces by 59 % of the original value with a perovskite device stack filter. It is also important to note that the 780 nm and 830 nm longpass filters reduce the V_{OC} and J_{SC} of D1 more than the 630 nm filter (see table in Figure 4.6) as expected, clearly indicating the significance of top-cell bandgap tuning.

4.3.4 Monolithic tandem prototype

Monolithic TSCs are two or more sub-cells connected in series such that the same current flows through the sub-cells and the total voltage is the sum of voltages across each of these sub-cells (see eqs. (4.4) and (4.5)). In order to maximise the power conversion from such devices, it is essential that the current generated by the two sub-cells is well matched.

a)

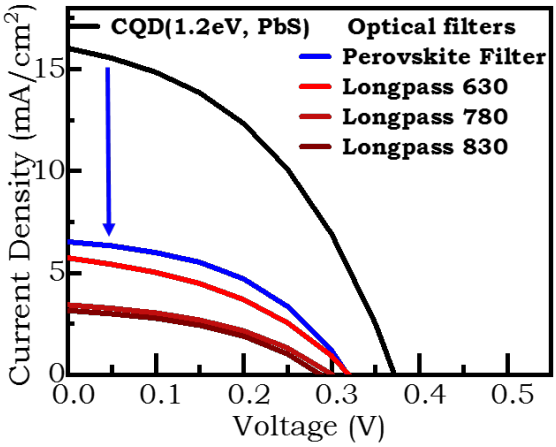

b)

Device/Filter name	Voc (V)	Jsc (mA/cm^2)	FF	PCE (%)
D2 No Filter	0.35	14.2	0.41	2.01
D2 with Perovskite filter	0.29	5.84	0.42	0.71
% loss	*17*	*59*	*-2*	*65*
D1 No Filter	0.34	14.2	0.37	1.76
D1 with Longpass 630	0.28	6.25	0.38	0.69
% loss	*18*	*56*	*-3*	*61*
D1 with Longpass 780	0.26	3.24	0.39	0.35
% loss	*26*	*77*	*5*	*83*
D1 with Longpass 830	0.25	2.88	0.39	0.30
% loss	29	80	5	85

Figure 4.6: Effect on the J-V parameters of a CQD device prepared by layer-by-layer spin-coating method (see Section 3.3.4.2) under a perovskite device stack filter and 630 nm,780 nm and 830 nm longpass filters. The table on the right includes the effect of optical filtering on each of the device parameters including the percentage loss after filtering.

This necessitates careful tuning of the thicknesses of each of the active layers in the device to generate equal current from both the sub-cells. On tuning the thickness of the perovskite layer in glass/ITO/c-TiO_2/mp-TiO_2/perovskite stacks, we found that reducing the thicknesses to 185−200 nm from the initial 280 nm increased the transmittance in the 600 nm to 800 nm range (figure 4.7). We note that changing the thickness of perovskite layer from 280 nm by ≈ 100 nm, in an individual perovskite device its J_{SC} reduced from ≈ 25 mA/cm^2 to ≈ 21 mA/cm^2 and the V_{OC} reduced from 1.02 V to 0.95 V (see first two rows of table in Figure 4.10a). This highlights another challenge of 2T TSCs. To obtain current-matching between the sub-cells in a monolithic TSC, there is usually a trade-off between maintaining the individual top-cell efficiencies and making it transparent enough to allow the low-energy photons to filter through to the bottom cell.

Following the optimisation of the top and bottom cell as described above, we designed and fabricated the first prototype of a solution-processed perovskite/CQD tandem solar cell. The top perovskite sub-cell prepared using methylammonium lead-iodide ($MAPbI_3$) absorbs the high-energy photons and the bottom CQD (PbS) sub-cell absorbs the near-IR photons. The three main issues addressed in the design of such a multi-layer monolithic architecture include: (i) high-temperature annealing steps were avoided apart from the very first layer(s), to prevent thermal degradation of successive layers of materials; (ii) ideal orthogonal solvents have been carefully selected for sequential deposition, to ensure

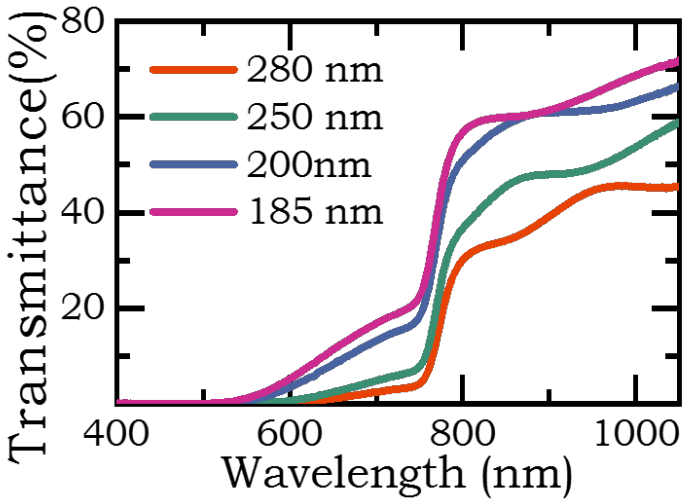

Figure 4.7: Effect of reducing film thickness of perovskite transmittance profile indicating increased transmittance in the region between 600 nm to 800 nm with reduced perovskite film thickness.

intact underlying interfaces and layer thicknesses; and (iii) a transparent recombination layer between the sub-cells has been designed, which also importantly serves as a solvent barrier.

We explored multiple different methods for depositing the TiO_2 and ZnO layers as explained in Section 3.3.4. Perovskites dissolve readily is polar solvents and CQDs in non-polar solvents. Thus, the solvents used for solid state ligand exchange had to be carefully chosen to be polar enough to not dissolve the CQDs while still being non-polar enough to avoid damage to the perovskite layers. Annealing the perovskite device stack above 100 °C would damage the hole-transporting layer if spiro-OMETAD was used for this purpose. Hence, we incorporated PTAA and re-optimised the perovskite device as the subsequent ZnO layer needed annealing for a short-time at 100 °C. Thus bearing these processing restrictions in mind, and followed by careful optimisation of each layer, we finally used a structure shown in Figure 4.9a of glass/ ITO/ c-TiO_2/ mp-TiO_2/ $MAPbI_3$ perovskite/ poly(bis(4-phenyl)(2,4,6-trimethylphenyl)amine (PTAA) / MoOx/ Au or Ag/ ZnO/ CQD (PbS)/ MoOx/ Au.

In figure 4.8 we show the step-by-step fabrication process for perovskite-CQD tandem solar cells. Following the deposition of the compact and mesoporous TiO_2 layers (see section 3.3.4.1), perovskite film (280 nm) was spin-coated and annealed at 100 °C for 45 minutes (see Section 3.3.5 for details). A hole-transporting PTAA layer (180 nm) was then deposited before thermally evaporating 7 nm of MoOx and 0.5 nm of Au interlayer. Zinc-oxide nanoparticles (synthesised by Dr. Sai Bai, University of Oxford) dispersed in

IPA, were then deposited via spin-coating in air at 2500 rpm for 45 s. CQDs active-layer was deposited as per the spin-casting protocol described earlier in section 3.3.4.2. MoOx 7 nm and Au 80 nm were thermally evaporated to complete the device structure. With every batch of TSCs, individual CQDs solar cells and perovskite solar cells were also fabricated in parallel for control measurements. The fabrication process for each of the two sub-cells as individual solar cells is described in Sections 3.3.4 and 3.3.5 respectively.

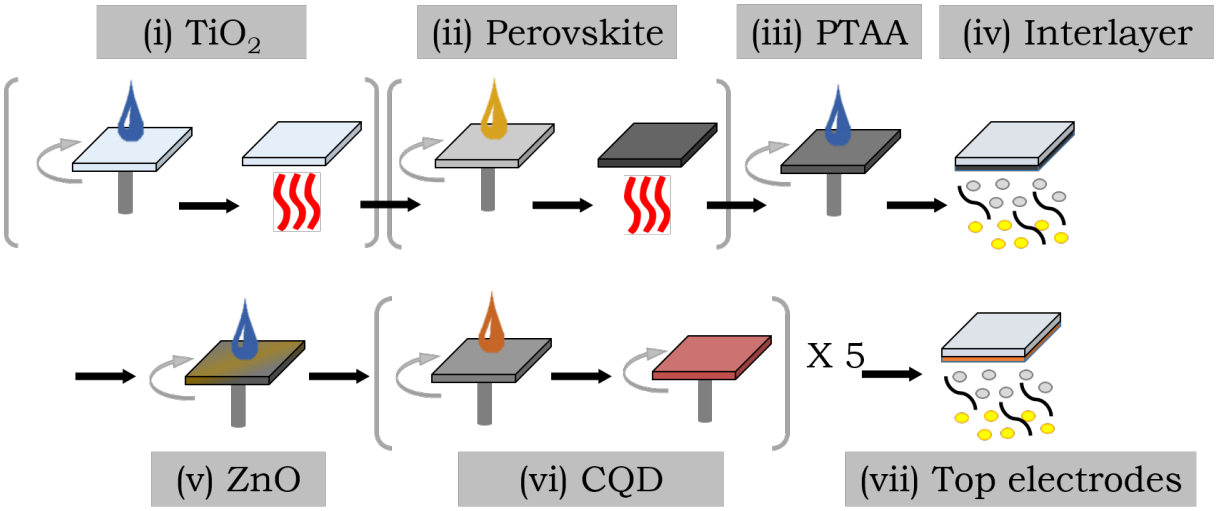

Figure 4.8: Schematic diagram describing the tandem solar cell fabrication process indicating methods of deposition for different layers used.

From the cross-sectional SEM image displayed in Figure 4.9b, it is evident that interfacial and layer integrity have been maintained by our processing sequence. This is an important evidence to prove that the perovskite layers were not physically affected by the deposition of CQDs device stack.

In Figure 4.10a-b we present the preliminary experimental data from monolithic tandem devices based on the empirical performance of the individual cells obtained in our laboratory, a 1.55 eV bandgap perovskite cell with reduced active layer thickness (blue curve, Figure 4.10b) and a 1.03 eV bandgap PbS cell (red curve, Figure 4.10b). From this combination, we anticipate a monolithic tandem cell to exhibit a V_{OC} of 1.2 V, J_{SC} of 11.3 mA/cm^2, fill factor (FF) of 0.57, and an overall PCE of 7.8 % (figure 4.10b black dotted curve, and 'Projected monolithic tandem' in table 4.10a). This projection was calculated using our model but without considering any radiative coupling to give a conservative estimate.

In the initial demonstration of the monolithic tandem devices, we observed voltage addition with a V_{OC} of 1.17 V (figure 4.10b, pink curve) achieved from the integration of a

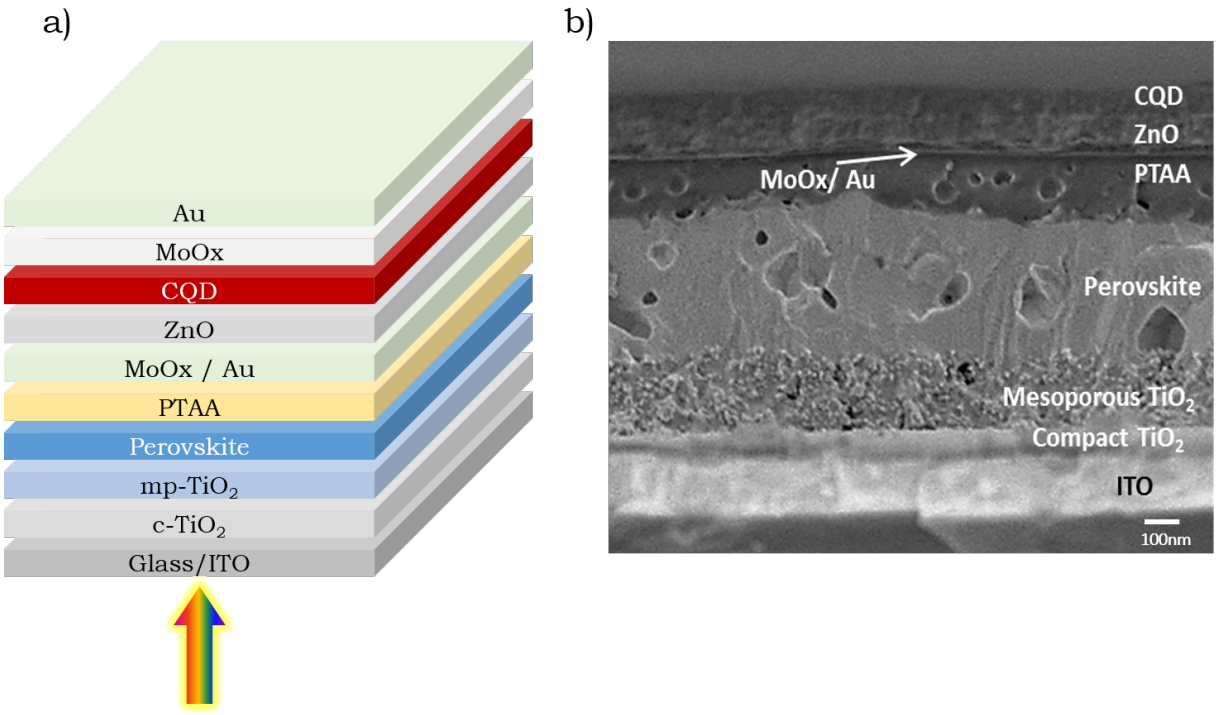

Figure 4.9: a) Layer-by-layer device architecture of the monolithic perovskite/CQD tandem solar cell realised in this work. b) Cross-sectional image obtained using scanning electron microscopy (SEM) technique of the monolithic perovskite/CQD tandem cell indicating intact layers and interfaces of the device architecture.

thin-perovskite cell (185 nm) with V_{OC} of 0.95 V and a CQD cell with V_{OC} of 0.38 V (Figures 4.10a-b). A maximum V_{OC} of 1.31 V was achieved in the perovskite/CQD tandem structure (Figure 4.10a, row 6) with a thick-perovskite layer (280 nm). However we note a significant trade-off between V_{OC} and J_{SC} as we reduced the perovskite film thickness to allow more photons to reach the bottom cell (see Figure 4.10a, rows 6-8). This is expected from tandem cells with poor current matching and charge extraction. We acknowledge that there are some technical difficulties which still need to be addressed in our tandem architecture. In particular, the design and deposition of the tunnel junction need to be optimised further. However, it is important to note that as shown by the optical filtering experiments in Figure 4.6, the bottom cell J_{SC} was limited to $\approx 6\,\mathrm{mA/cm^2}$ from our best CQD devices after filtering out the blue-photons using perovskite device stack. Thus, as per the current matching condition, we expect the bottom CQD cell to limit the J_{SC} of our monolithic TSC to $\approx 6\,\mathrm{mA/cm^2}$ as well. Considering this limitation the PCE from our monolithic TSC was limited to 1.01 % (table 4.10a-b) for the initial demonstration.

Figure 4.10c presents the normalized external quantum efficiency (EQE) of the perovskite and CQD individual cells to illustrate the spectral coverage of the tandem cell.

Considering that the EQE of the tandem cell would generally follow the EQE profiles of the sub-cells, these profiles demonstrate extended IR photon absorption beyond 1100 nm. In a fully optimised perovskite/CQD tandem cell, the extended IR response and EQE coverage are expected to outperform other solution-processed tandem solar cells.

a)

Device name	V_{OC} (V)	J_{SC} (mA/cm^2)	FF	PCE (%)
Thick Perovskite (400 nm)	1.02	25.1	0.56	14.2
Thin Perovskite (280 nm)	0.95	21.2	0.64	13.0
CQD	0.38	19.0	0.50	3.59
Filtered CQD	0.32	6.53	0.45	N/A
Projected monolithic tandem	1.20	11.3	0.57	7.75
Tandem (280 nm perovskite)	1.31	0.11	0.20	0.03
Tandem (230 nm perovskite)	1.17	2.50	0.14	0.41
Tandem (185 nm perovskite)	0.98	5.03	0.20	1.01
Projected monolithic tandem (SoA)	1.51	24.0	0.82	29.7

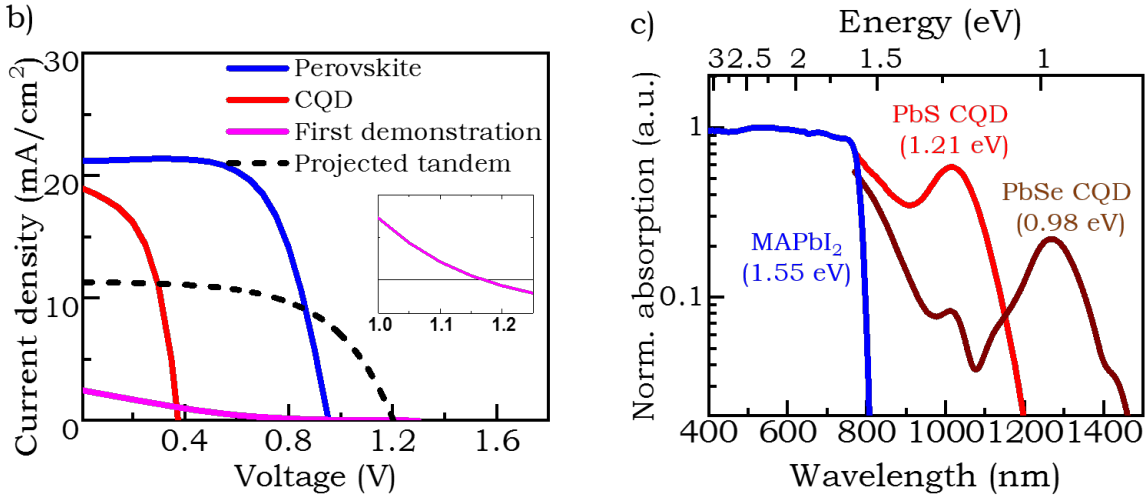

Figure 4.10: a) Table of experimental and projected solar cell characteristics under standard AM 1.5 conditions. Projected monolithic tandem is a semi-empirical tandem device projected from the experimental data of individual 1.2 eV CQD and 1.55 eV perovskite solar cells we fabricated. Projected monolithic tandem (SoA) refers to a tandem device projected from the best state-of-the-art (SoA) CQD and perovskite solar cells from the literature [33, 34]. b) Initial demonstration of voltage addition in the monolithic tandem structure, showing a V_{OC} of 1.17 V and a J_{SC} of 2.5 mA/cm^2 in a 1.55 eV perovskite/1.05 eV CQD tandem cell (pink curve). The black dotted curve shows a projected J-V curve with a V_{OC} of 1.2 V and a J_{SC} of 11 mA/cm^2 with current matching, based on layer thickness optimization for the individual cells we fabricated. The inset shows the V_{OC} of the first demonstration tandem cell (pink curve) indicating the intersection of the curve at zero current density. c) Normalized EQE spectra of individual cells used for the first demonstration of a monolithic tandem showing extended spectral response in the IR-region using low-bandgap lead chalcogenide CQDs as the bottom-cell material.

4.3.5 Further bottom cell optimisation

CQDs for dip-coated CQDs device experiments were synthesized by Zhilong Zhang as per the method described in Section 3.2.

Considering the limited PCEs obtained from our spin-coating method of CQD device fabrication with our set of ligands and solvents, we explored switching to an alternative dip-coating method [29]. With guidance and training from Zhilong Zhang, we significantly improved the CQD device PCE to 6.17 % using 1.2 eV PbS CQDs. Dip-coating was employed to deposit the active layer in the final stages of the project, with the main aim of depositing thick CQD films to optimise the bottom cells in our monolithic tandem TSCs. This processing method allowed us to tune the ligands and solvents used for solid-state ligand exchange temporarily. The complete device structure for dip-coated CQD devices is shown in figure 4.12. The purification process adapted for obtaining the CQDs for these devices was different to our previously described method in Section 3.2. The CQDs were purified in air by adding hexane and acetone in a 1:2 ratio and centrifuging the solution at 7000 rpm for 3 minutes. This purification method yielded clear supernatant and hence CQDs were obtained without any further purification. After disposing off the supernatant, the CQDs were dried as before and the CQDs dispersed in hexane. A concentration of 30 mg mL^{-1} was used for film-deposition purposes.

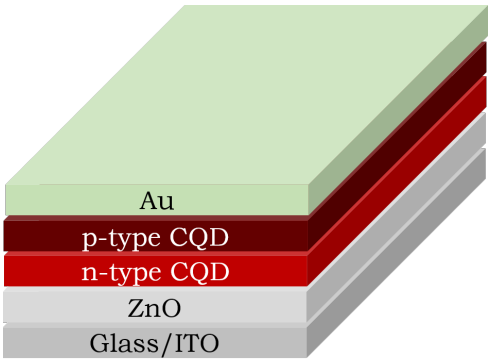

Figure 4.11: Device structure showing each layer deposited for the dip-coated CQD solar cell.

We used 0.02 µL mL^{-1} 3-mercaptopropionic acid (MPA, $\geq$ 99 %, Sigma-Aldrich) in methanol and 0.005 mg mL^{-1} lead(II) iodide (PbI_2) in anhydrous N,N-Dimethylformamide (DMF, 99.8 % as short-ligands for dip-coated CQD devices. Figure 4.12 illustrates the device fabrication process for dip-coated CQD devices. 40 µL of CQD (20 mg mL^{-1} to 30 mg mL^{-1} in hexane) were deposited via spin coating (2500 rpm, 30 s) in air to speed up the drying process for this layer. The CQD coated substrate was then dipped and soaked

in PbI_2 ligand solution beaker for 20 s, dried with nitrogen gun and dipped in acetone containing beaker multiple times to wash off excess ligands. This process was repeated 8 times to obtain the n-type CQD layer. For the next step, we deposit a p-type layer using an identical process but this time using MPA as the p-type ligand. Two further layers were deposited using the dip-coating process with MPA. And finally 80 nm of Au was deposited to complete the device with a hole-extracting electrode.

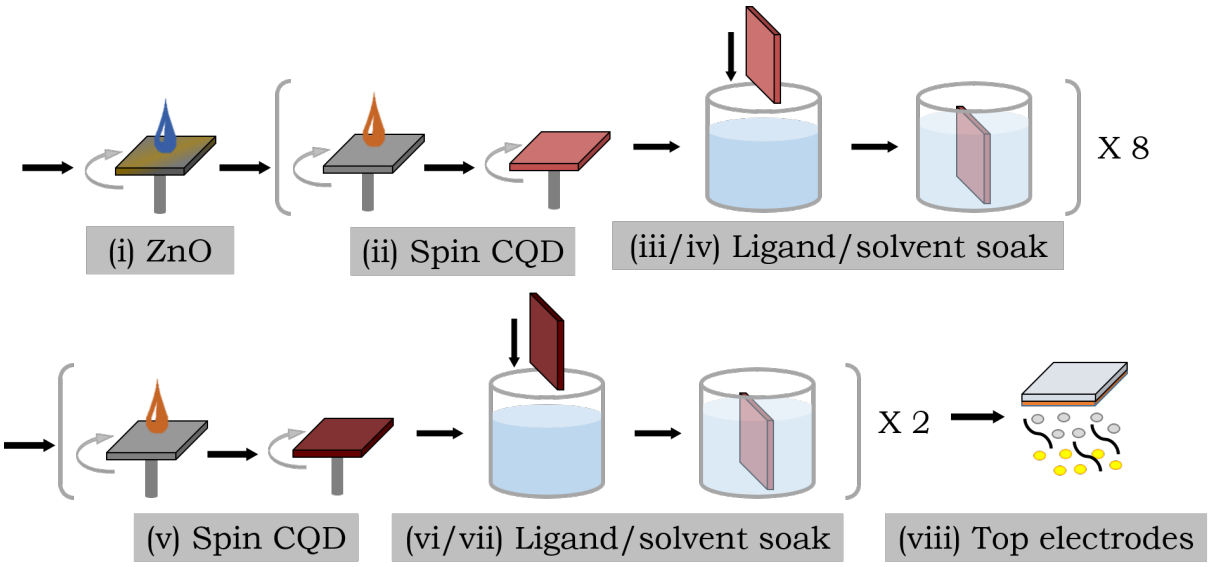

Figure 4.12: Schematic diagram illustrating the device fabrication process for the dip-coated CQD devices.

The important difference and advantage of these devices as compared to the spin-coated devices employed in our monolithic tandem was the freedom of choosing solvents and ligands for primary CQD device optimisation. We used PbI_2 and MPA as the n-tpe and p-type ligands respectively as opposed to 1,2-benzenedithiol (BDT) and 1,2-ethanedithiol (EDT) dissolved in isopropanol used for spin-casted active layers (see Section 3.3.4.2 for further details).

In order to incorporate these CQDs in our monolithic tandem architecture, we performed initial optical filtering tests as for the spin-coated CQD devices explained in Section 4.3.3. On filtering the device with a perovskite device stack, we find that the J_{SC} reduces by $\approx 78\,\%$ of its original value to $5.18\,mA/cm^2$ from $23.3\,mA/cm^2$ and the overall PCE drops by $\approx 83\,\%$ from $6.17\,\%$ to $1.06\,\%$. To confirm that this effect was indeed from the lack of blue-photons reaching the bottom cell, we used longpass filters as done previously in Section 4.3.3. We observed a sequential reduction in the photocurrent generated by the CQD cell on increasing the longpass filter wavelengths from 630 nm to 830 nm as shown in

Figure 4.13. This reduction is consequently due to a substantial photocurrent generation in CQDs from absorption in the UV-vis region of the spectrum. This can be avoided by further increasing the CQD film thickness through sophisticated fabrication methods to ensure that all the photons in the near-IR region are efficiently absorbed [45].

a)

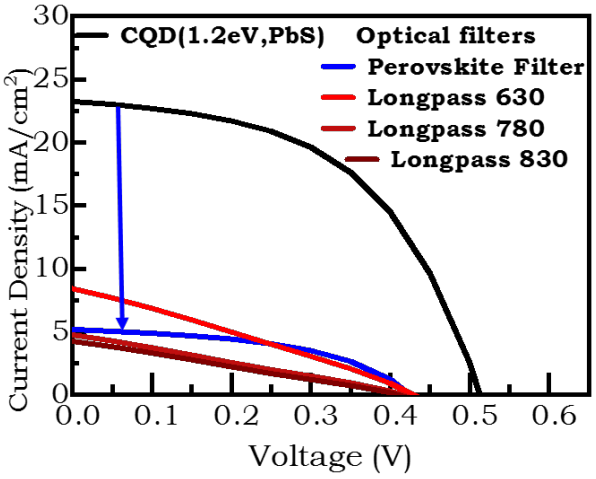

b)

Device/Filter name	V_{OC} (V)	J_{SC} (mA/cm^2)	FF	PCE (%)
CQD (1.2 eV) PbS	0.51	23.3	0.52	6.17
Perovskite filter	0.43	5.18	0.48	1.06
% loss	*17*	*78*	*7*	*83*
Longpass 630 filter	0.43	8.43	0.28	1.01
% loss	*16*	*64*	*46*	*84*
Longpass 780 filter	0.42	4.75	0.26	0.51
% loss	*18*	*80*	*50*	*92*
Longpass 830 filter	0.41	4.25	0.25	0.44
% loss	*19*	*82*	*51*	*93*

Figure 4.13: a) Effect on the J-V parameters of a CQD device prepared by dip-coating method of a perovskite device stack filter and 630 nm,780 nm and 830 nm longpass filters.b) Tabulated device characteristics corresponding to a. including the effect of optical filtering on each of the device parameters also indicating the percentage loss after filtering.

At this stage, incorporating these dip-coated CQD devices would provide no additional advantage to our monolithic tandem as the current flowing through the TSC will still be limited by the CQD cell as seen from optical filtering experiments above. Besides, in order to dip-coat the CQDs layer, we will first have to re-optimise these devices by replacing all the polar solvents used for ligand exchange with more non-polar solvents as for the spin-casted method (see Section 3.3.4.2).

4.4 Conclusions and future work

In conclusion, we have proposed a perovskite/CQD tandem solar cell design which allows both bandgap tunability and solution processability. Detailed balance efficiency of 43 % has been predicted for a perovskite (E_g = 1.55 eV)/CQD (E_g = 1.0 eV) tandem cell under standard AM 1.5 solar illumination. The inter-subcell radiative coupling effect has been demonstrated to recycle photons generated via radiative recombination, resulting in a significant enhancement ($\geq$ 11 % absolute gain) of the overall device efficiency.

For widely-used high-performance perovskite absorbers with a bandgap of ≈ 1.55 eV, the tandem structure has the potential to achieve high efficiency by harvesting near-infrared photons. We have reported initial experimental results of a monolithic perovskite/CQD tandem solar cell, showing evidence of voltage addition of the top and bottom cells. SEM images show that our orthogonal solvent processing method is suitable for establishing the monolithic tandem structure. Due to a large amount of photocurrent generated in the CQD solar cells from blue-photons, when shadowed by the perovskite top-cell, we observe significant reduction in the device performance. This presently limits the TSC performance along with the difficulty of depositing a thick-CQD layer, which would improve the CQD photocurrent generation in the near-IR and IR region of the spectrum.

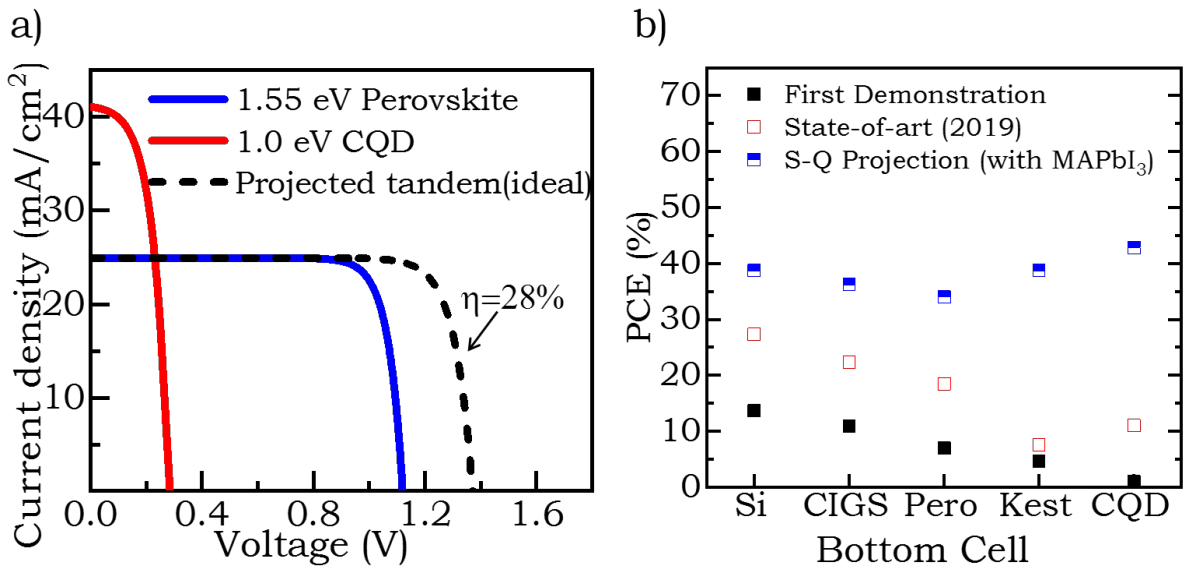

Figure 4.14: a) CQD and perovskite J-V curves and projected tandem cell performance based on state-of-the-art experimental results from [33] for a perovskite cell and from [34] for a CQD cell. b) Power conversion efficiencies (PCEs) of two-terminal tandem solar cells using perovskite as the top cell as a function of bottom cells used. The first demonstration data is from devices referenced in Figure 4.1 and the state-of-art data for bottom cells: Silicon (Si) and CIGS from ref [1], perovskite (Pero) from ref [18], for kesterite (Kest) from ref [46] and for CQD from ref [47].

Combining our model with experimental data from the literature, in Figure 4.14a we illustrate the tandem cell performance that can be expected in practice based on some of the highest performing individual cells. The blue curve in Figure 4.14a shows the J-V characteristics of a 21.6 % PCE perovskite solar cell ($E_g = 1.55$ eV) [33]. The red curve in the same figure shows J-V characteristics of a PbS CQD solar cell,[34] with V_{OC} reduced

to account for a lower bandgap of 1.0 eV, and J_{SC} estimated by considering only photons not absorbed by the perovskite cell (i.e. $E_{photon} < 1.55$ eV). The J-V curve from ref [34] that uses CQDs with a 1.2 eV absorption cut-off was translated to the left by 0.2 eV to account for the reduced bandgap of 1.0 eV, assuming the (bandgap - V_{OC}) difference is not varying across the small range of bandgaps to obtain this red-curve (Figure 4.14a). The black dotted curve, projected based on current-matching of these two cells in series, indicates the postulated PCE for such a monolithic tandem device of 29.7 % assuming that a thick CQDs layer can be deposited atop the perovskite device stack.

In fact, Zhang et al. [47] have recently demonstrated a PbS/perovskite monolithic tandem cell with PCE reaching 11.03 %. In their tandems they have placed the red absorbing cell on top of the blue absorbing cell unlike our monolithic architecture. Their architecture limits the blue-cell PCE as high-energy photons are first absorbed by the red absorbing cell. Such placement of the red-cell atop the blue-cell is mainly due to the difficulty of depositing a thick PbS layer on top of a perovskite device stack, which we overcome in our monolithic architecture. Placing the red-absorbing cell above the blue-absorbing one limits the maximum possible efficiencies obtainable by the tandem cell as the blue-absorbing cell will never be able to perform at its best without all the above-bandgap photons from the sun coupled directly into it. To overcome this limitation and benefit from such tandem architectures, it is essential to place the blue-absorbing cell on top of the red-absorbing cell. It is also important to ensure that the CQD bottom cells have high EQEs in the near infrared and infrared regions where the perovskite top cell is transparent.

As shown in Figure 4.14b the first demonstrations of various 2T TSCs have been followed by continuous research efforts improving the efficiencies rapidly over the course of the next few years, reaching ≈ 28 % PCE with 2T perovskite-silicon TSCs. Modelling using the most-studied $MAPbI_3$ as perovskite top cell, we find that CQDs, with bandgap between 0.95 eV to 1.05 eV could result in monolithic TSC PCEs of as high as 43 % as compared to a perovskite/silicon monolithic tandem PCE of 39 %.

Bibliography

1. Green, M. A., Hishikawa, Y., Dunlop, E. D., Levi, D. H., Hohl-Ebinger, J., Yoshita, M. & Ho-Baillie, A. W. Solar cell efficiency tables (version 53). *Progress in Photovoltaics: Research and Applications* **27,** 3–12 (2019).

2. Shockley, W. & Queisser, H. J. Detailed balance limit of efficiency of p-n junction solar cells. *Journal of Applied Physics* **32,** 510–519 (1961).

3. Todorov, T. K., Bishop, D. M. & Lee, Y. S. Materials perspectives for next-generation low-cost tandem solar cells. *Solar Energy Materials and Solar Cells* **180,** 350–357 (2018).

4. Chiu, P., Law, D., Woo, R., Singer, S., Bhusari, D., Hong, W., Zakaria, A., Boisvert, J., Mesropian, S., King, R. *et al.* 35.8 % *space and* 38.8 % *terrestrial 5J direct bonded cells* in *2014 IEEE 40th Photovoltaic Specialist Conference (PVSC)* (2014), 0011–0013.

5. Polman, A., Knight, M., Garnett, E. C., Ehrler, B. & Sinke, W. C. Photovoltaic materials: Present efficiencies and future challenges. *Science* **352,** aad4424 (2016).

6. Snaith, H. J. Present status and future prospects of perovskite photovoltaics. *Nature Materials* **17,** 372 (2018).

7. Eperon, G. E., Leijtens, T., Bush, K. A., Prasanna, R., Green, T., Wang, J. T.-W., McMeekin, D. P., Volonakis, G., Milot, R. L., May, R. *et al.* Perovskite-perovskite tandem photovoltaics with optimized band gaps. *Science* **354,** 861–865 (2016).

8. Todorov, T., Gershon, T., Gunawan, O., Sturdevant, C. & Guha, S. Perovskite-kesterite monolithic tandem solar cells with high open-circuit voltage. *Applied Physics Letters* **105,** 173902 (2014).

9. Bailie, C. D., Christoforo, M. G., Mailoa, J. P., Bowring, A. R., Unger, E. L., Nguyen, W. H., Burschka, J., Pellet, N., Lee, J. Z., Grätzel, M. *et al.* Semi-transparent perovskite solar cells for tandems with silicon and CIGS. *Energy & Environmental Science* **8,** 956–963 (2015).

10. Mailoa, J. P., Bailie, C. D., Johlin, E. C., Hoke, E. T., Akey, A. J., Nguyen, W. H., McGehee, M. D. & Buonassisi, T. A 2-terminal perovskite/silicon multijunction solar cell enabled by a silicon tunnel junction. *Applied Physics Letters* **106,** 121105 (2015).

11. Jiang, F., Liu, T., Luo, B., Tong, J., Qin, F., Xiong, S., Li, Z. & Zhou, Y. A two-terminal perovskite/perovskite tandem solar cell. *Journal of Materials Chemistry A* **4,** 1208–1213 (2016).

12. Eperon, G. E., Hörantner, M. T. & Snaith, H. J. Metal halide perovskite tandem and multiple-junction photovoltaics. *Nature Reviews Chemistry* **1,** 0095 (2017).

13. Anaya, M., Lozano, G., Calvo, M. E. & Míguez, H. ABX_3 perovskites for tandem solar cells. *Joule* **1,** 769–793 (2017).

14. Wali, Q., Elumalai, N. K., Iqbal, Y., Uddin, A. & Jose, R. Tandem perovskite solar cells. *Renewable and Sustainable Energy Reviews* **84,** 89–110 (2018).

15. Karani, A., Yang, L., Bai, S., Futscher, M. H., Snaith, H. J., Ehrler, B., Greenham, N. C. & Di, D. Perovskite/Colloidal Quantum Dot Tandem Solar Cells: Theoretical Modeling and Monolithic Structure. *ACS Energy Letters* **3,** 869–874 (2018).

16. Todorov, T., Gershon, T., Gunawan, O., Lee, Y. S., Sturdevant, C., Chang, L.-Y. & Guha, S. Monolithic perovskite-CIGS tandem solar cells via in situ band gap engineering. *Advanced Energy Materials* **5,** 1500799 (2015).

17. Forgács, D., Gil-Escrig, L., Pérez-Del-Rey, D., Momblona, C., Werner, J., Niesen, B., Ballif, C., Sessolo, M. & Bolink, H. J. Efficient monolithic perovskite/perovskite tandem solar cells. *Advanced Energy Materials* **7,** 1602121 (2017).

18. Rajagopal, A., Yang, Z., Jo, S. B., Braly, I. L., Liang, P.-W., Hillhouse, H. W. & Jen, A. K.-Y. Highly efficient perovskite–perovskite tandem solar cells reaching 80% of the theoretical limit in photovoltage. *Advanced Materials* **29,** 1702140 (2017).

19. Chen, C.-C., Bae, S.-H., Chang, W.-H., Hong, Z., Li, G., Chen, Q., Zhou, H. & Yang, Y. Perovskite/polymer monolithic hybrid tandem solar cells utilizing a low-temperature, full solution process. *Materials Horizons* **2,** 203–211 (2015).

20. Noel, N. K., Stranks, S. D., Abate, A., Wehrenfennig, C., Guarnera, S., Haghighirad, A.-A., Sadhanala, A., Eperon, G. E., Pathak, S. K., Johnston, M. B. *et al.* Lead-free organic–inorganic tin halide perovskites for photovoltaic applications. *Energy & Environmental Science* **7,** 3061–3068 (2014).

21. Zhao, B., Abdi-Jalebi, M., Tabachnyk, M., Glass, H., Kamboj, V. S., Nie, W., Pearson, A. J., Puttisong, Y., Gödel, K. C., Beere, H. E. *et al.* High Open-Circuit Voltages in Tin-Rich Low-Bandgap Perovskite-Based Planar Heterojunction Photovoltaics. *Advanced Materials* **29,** 1604744 (2017).

22. Leijtens, T., Prasanna, R., Gold-Parker, A., Toney, M. F. & McGehee, M. D. Mechanism of tin oxidation and stabilization by lead substitution in tin halide perovskites. *ACS Energy Letters* **2,** 2159–2165 (2017).

23. Meng, L., Zhang, Y., Wan, X., Li, C., Zhang, X., Wang, Y., Ke, X., Xiao, Z., Ding, L., Xia, R. *et al.* Organic and solution-processed tandem solar cells with 17.3% efficiency. *Science* **361,** 1094–1098 (2018).

24. Bush, K. A., Palmstrom, A. F., Zhengshan, J. Y., Boccard, M., Cheacharoen, R., Mailoa, J. P., McMeekin, D. P., Hoye, R. L., Bailie, C. D., Leijtens, T. *et al.* 23.6%-efficient monolithic perovskite/silicon tandem solar cells with improved stability. *Nature Energy* **2,** 17009 (2017).

25. Futscher, M. H. & Ehrler, B. Modeling the performance limitations and prospects of perovskite/Si tandem solar cells under realistic operating conditions. *ACS Energy Letters* **2,** 2089–2095 (2017).

26. Futscher, M. H. & Ehrler, B. Efficiency limit of perovskite/Si tandem solar cells. *ACS Energy Letters* **1,** 863–868 (2016).

27. Bohm, M. L., Jellicoe, T. C., Rivett, J. P., Sadhanala, A., Davis, N. J., Morgenstern, F. S., Godell, K. C., Govindasamy, J., Benson, C. G., Greenham, N. C. *et al.* Size and energy level tuning of quantum dot solids via a hybrid ligand complex. *The Journal of Physical Chemistry Letters* **6,** 3510–3514 (2015).

28. Chuang, C.-H. M., Brown, P. R., Bulović, V. & Bawendi, M. G. Improved performance and stability in quantum dot solar cells through band alignment engineering. *Nature Materials* **13,** 796 (2014).

29. Zhang, Z., Chen, Z., Yuan, L., Chen, W., Yang, J., Wang, B., Wen, X., Zhang, J., Hu, L., Stride, J. A. *et al.* A New Passivation Route Leading to Over 8% Efficient PbSe Quantum-Dot Solar Cells via Direct Ion Exchange with Perovskite Nanocrystals. *Advanced Materials* **29,** 1703214 (2017).

30. Ning, Z., Gong, X., Comin, R., Walters, G., Fan, F., Voznyy, O., Yassitepe, E., Buin, A., Hoogland, S. & Sargent, E. H. Quantum-dot-in-perovskite solids. *Nature* **523,** 324 (2015).

31. Di, D., Musselman, K. P., Li, G., Sadhanala, A., Ievskaya, Y., Song, Q., Tan, Z.-K., Lai, M. L., MacManus-Driscoll, J. L., Greenham, N. C. *et al.* Size-dependent photon emission from organometal halide perovskite nanocrystals embedded in an organic matrix. *The Journal of Physical Chemistry Letters* **6,** 446–450 (2015).

32. Iyer, S. S. & Xie, Y.-H. Light emission from silicon. *Science* **260,** 40–46 (1993).

33. Yang, W. S., Park, B.-W., Jung, E. H., Jeon, N. J., Kim, Y. C., Lee, D. U., Shin, S. S., Seo, J., Kim, E. K., Noh, J. H. *et al.* Iodide management in formamidinium-lead-halide–based perovskite layers for efficient solar cells. *Science* **356,** 1376–1379 (2017).

34. Lan, X., Voznyy, O., García de Arquer, F. P., Liu, M., Xu, J., Proppe, A. H., Walters, G., Fan, F., Tan, H., Liu, M. *et al.* 10.6% certified colloidal quantum dot solar cells via solvent-polarity-engineered halide passivation. *Nano Letters* **16,** 4630–4634 (2016).

35. Karani, A., Yang, L., Greenham, N. C. & Di, D. *Toward high-efficiency solution-processed tandem solar cells* in *Organic, Hybrid, and Perovskite Photovoltaics XIX* **10737** (2018), 107371I.

36. Nelson, J. *The physics of solar cells* (Imperial College Press, London, 2003).

37. Brown, A. S. & Green, M. A. Limiting efficiency for current-constrained two-terminal tandem cell stacks. *Progress in Photovoltaics: Research and Applications* **10,** 299–307 (2002).

38. Strandberg, R. Detailed balance analysis of area de-coupled double tandem photovoltaic modules. *Applied Physics Letters* **106,** 033902 (2015).

39. Vos, A. D. Detailed balance limit of the efficiency of tandem solar cells. *Journal of Physics D: Applied Physics* **13,** 839–846 (1980).

40. Cho, H., Jeong, S.-H., Park, M.-H., Kim, Y.-H., Wolf, C., Lee, C.-L., Heo, J. H., Sadhanala, A., Myoung, N., Yoo, S., Im, S. H., Friend, R. H. & Lee, T.-W. Overcoming the electroluminescence efficiency limitations of perovskite light-emitting diodes. *Science* **350,** 1222–1225 (2015).

41. Dai, X., Zhang, Z., Jin, Y., Niu, Y., Cao, H., Liang, X., Chen, L., Wang, J. & Peng, X. Solution-processed, high-performance light-emitting diodes based on quantum dots. *Nature* **515,** 96–99 (2014).

42. Marti, A. & Araujo, G. L. Limiting efficiencies for photovoltaic energy conversion in multigap systems. *Solar Energy Materials and Solar Cells* **43,** 203–222 (1996).

43. Pazos-Outón, L. M., Szumilo, M., Lamboll, R., Richter, J. M., Crespo-Quesada, M., Abdi-Jalebi, M., Beeson, H. J., Vrućinić, M., Alsari, M., Snaith, H. J., Ehrler, B., Friend, R. H. & Deschler, F. Photon recycling in lead iodide perovskite solar cells. *Science* **351,** 1430–1433 (2016).

44. Yamaguchi, M., Lee, K.-H., Araki, K. & Kojima, N. A review of recent progress in heterogeneous silicon tandem solar cells. *Journal of Physics D: Applied Physics* **51,** 133002 (2018).

45. Zhou, S., Liu, Z., Wang, Y., Lu, K., Yang, F., Gu, M., Xu, Y., Chen, S., Ling, X., Zhang, Y. *et al.* Towards scalable synthesis of high-quality PbS colloidal quantum dots for photovoltaic applications. *Journal of Materials Chemistry C* **7,** 1575–1583 (2019).

46. Lin, S.-J., Ting, J.-M., Hung, C.-T. & Fu, Y.-S. Effect of the vapor diffusion and improved light harvesting for Perovskite-Cu2ZnSnS4 hybridized solar cells. *Organic Electronics* **59,** 190–195 (2018).

47. Zhang, Y., Gu, M., Li, N., Xu, Y., Ling, X., Wang, Y., Zhou, S., Li, F., Yang, F., Ji, K. *et al.* Realizing solution-processed monolithic PbS QDs/perovskite tandem solar cells with high UV stability. *Journal of Materials Chemistry A* **6,** 24693–24701 (2018).

Chapter 5

Novel pentacene from solution-processed precursor

5.1 Introduction

Singlet exciton fission (SF) provides a way of converting a high-energy photon into two low-energy triplet excitons. It is a spin-allowed process and thus more efficient than intersystem crossing in organic molecules [1]. If harvested efficiently, these triplet excitons can be converted into charge pairs, generating two free electrons from the energy of one photon. As mentioned earlier in Chapter 1, incorporating SF capable molecules into solar cells provides a way of reducing the thermalisation losses which account for almost 33 % of the total losses leading to the Shockley-Queisser limit [2, 3].

Although SF occurs in pentacene with an efficiency of $\approx 200\,\%$ [4, 5] on ultra-fast ($< 100\,\text{fs}$) time scales [6], it has been challenging to extract SF-generated triplets to generate free charges in solar cells [7]. In order to harvest triplets efficiently, we note that the size of SF domains is restricted to $\approx 40\,\text{nm}$ [8]. Poor solubility of unsubstituted acenes in common organic solvents limits the deposition techniques to thermal evaporation only. As such, pentacene and pentacene derivatives have only been shown to contribute to external quantum efficiencies exceeding 100 % in bilayer solar cells [6, 9, 10].

Functionalisation of core acene molecules by adding a variety of side-groups has shown to enhance the solubility of these small molecules significantly [11]. However, bulky side-groups in molecules such as 6,13-bis(triisopropylsilylethynyl) pentacene (TIPS-pc) cause steric hindrance reducing the electron coupling of the chromophores stacked in parallel [12]. This reduction in electron coupling results in reduced charge carrier mobilities in the out-of-plane direction (from the substrate) thus limiting device efficiencies. In this work, we present a novel solution-processable pentacene precursor (p-Pc), 13,6-N-sulfinylacetamido-pentacene, that has thermally cleavable side-groups. On annealing a p-Pc coated substrate we observe complete cleavage of the functional side-group and

200 % efficient SF like in pristine pentacene films [13]. Furthermore, we incorporate p-Pc as the active singlet fission material in bilayer, bulk-heterojunction (BHJ) and hybrid organic-inorganic solar cells.

5.1.1 Singlet Fission for solar cells

In organic molecules, SF is understood to proceed via an intermediate triplet-pair state. When an excited singlet chromophore is in contact with another chromophore in its ground-state, they share the energy and form two triplet excited states, with one triplet on each chromophore [14]. The net spin of these triplets is still zero making singlet fission a spin-conserving process. In order to generate separated triplets the molecular geometries of the surrounding molecules becomes crucial as will be discussed further in Chapter 6. In this study, we incorporate pentacene into a donor-acceptor solar cell (see Figure 5.1) with an intention to extract triplets by splitting the excitons into free charge carriers at the donor-acceptor interface.

In order to incorporate SF molecules into BHJ solar cells we first incorporate p-Pc into a bilayer solar cell and compare its performance with thermally evaporated pentacene. Next, we demonstrate successful integration of p-Pc in p-Pc/$PC_{61}BM$ BHJ devices and observe a significant contribution from SF-generated triplets to device photocurrent.

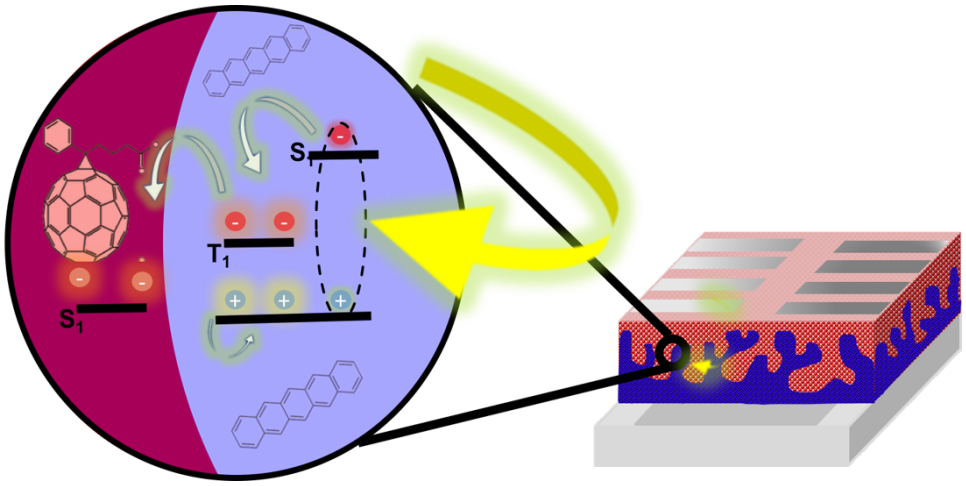

Figure 5.1: Schematic of a singlet fission bulkheterojunction solar cell showing high energy photon capture in the singlet fission material followed by transfer of the triplets (generated in SF process) to a neighboring acceptor molecule (phenyl-C_{61}-butyric acid methyl ester ($PC_{61}BM$) in this case).

5.1.2 Singlet Fission for photon-multiplication applications

Incorporating SF molecules directly as electron donors in organic solar cells can effectively double the photocurrent but it also causes significant loss of photovoltage as the donor LUMO is now at half the original singlet energy. In order to improve the overall efficiency of photovoltaics, alternative methods of utilising SF have been explored including using a SF cell in a tandem configuration with a silicon solar cell [15] and SF-sensitized low bandgap photovoltaics [7]. One such idea that we investigate is SF matrix sensitized with colloidal quantum dots (CQDs) for photon downconversion. The concept of photon-multiplication or down-conversion is illustrated in Figure 5.2. In a photon-multiplier unit, high-energy photons are absorbed in the SF-matrix and two low-energy triplets generated. Subsequently, these triplets are resonantly transferred to the nearest CQDs dispersed in the SF-matrix [16]. The CQDs can thus convert the 'dark' triplet energy states to bright photons and emit low-energy photons for absorption by a low-bandgap photovoltaic device.

In this work, we study CQDs dispersed in a pentacene SF matrix as active layers for photovoltaics. We also study CQD dispersion in these solid-state matrices using electron microscopy and propose a novel hybrid nanostructure using an inert organogel matrix for realization of SF-CQD photon-multiplier units.

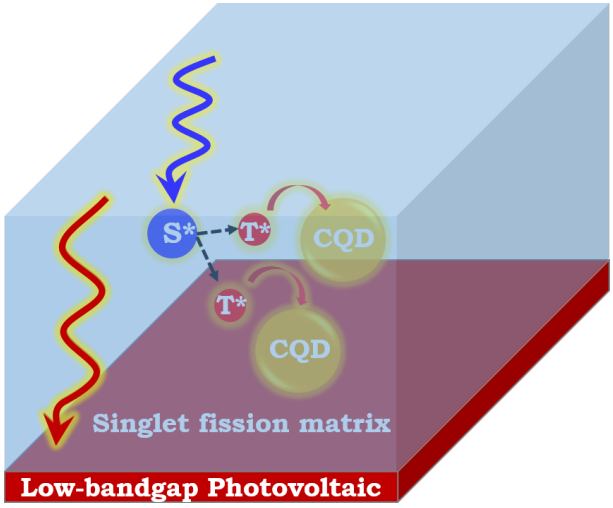

Figure 5.2: Schematic of a photomultiplier unit atop a low-bandgap photovoltaic cell illustrating the photonmultiplication mechanism. The photonmultiplier unit consists of a singlet fission capable organic matrix with CQDs dispersed in it. The singlet fission matrix absorbs a high-energy photon which generates a singlet exciton. This then splits into two low-energy triplet excitons which can be resonantly transferred to dispersed CQDs in the SF matrix. Due to high spin-orbit coupling, these CQDs can then convert the dark triplet excitons into bright photons for use by the low-bandgap photovoltaic underneath.

5.2 Results and discussion

In this section we discuss the results obtained from bilayer, bulkheterojunction and p-Pc/CQD hybrid devices. We explore a novel organogel matrix to suspend CQDs in order to avoid aggregation which is one of the main challenges in realizing p-Pc/CQD solar cells. *Note: Parts of this section are adapted from a collaborative project with Maxim Tabachnyk and Marcus Bohem which has already been published [13]. The AFM data presented in Figures 5.6 and 5.7 along with the FTIR and Grazing incidence X-ray diffraction data presented in Figure 5.5 was collected by Katharina Broch, James Xiao and Maxim Tabachnyk.*

5.2.1 Bilayer organic devices

Figure 5.3 displays the molecular structure of the pentacene precursor molecule 13,6-N-sulfinylacetamido-pentacene (p-Pc) along with thermally cleavable side groups. This molecule is commercially available and was purchased from Sigma Aldrich for this work. On annealing the precursor at 150 °C for at least 10 minutes in solid state, it converts into unsubstituted pentacene in a retro Diels-Alder reaction [17, 18].

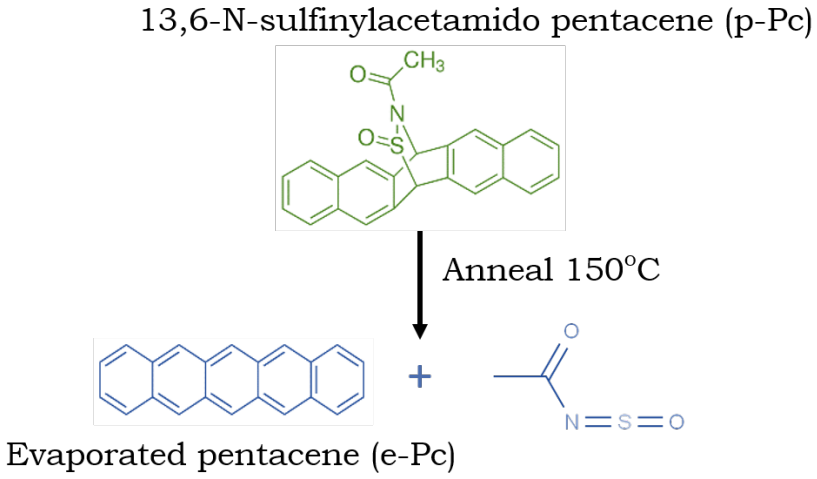

Figure 5.3: Molecular structure of 13,6-N-sulfinylacetamido pentacene (p-Pc) a molecule that allows thermal cleavage of side groups when annealed after deposition, to recover the un-functionalised acene core and N-sulfinylacetamide.

In order to first confirm the complete conversion of the solution-processed pentacene precursor into pristine pentacene we measured and compared the absorption of p-Pc films with evaporated pristine pentacene (e-Pc) films. The p-Pc films were prepared by spin coating a 7 mg mL^{-1} solution of the of precursor in chloroform on a glass substrate followed

by thermal annealing on a hot plate at required temperatures between 150 °C to 300 °C in an inert environment of a nitrogen glovebox. The e-Pc films were prepared by thermal evaporation of molecular pentacene on glass substrates.

The absorbance curves of p-Pc shown in Figure 5.4a display identical peaks in absorbance as the e-Pc films in Figure 5.4b at ≈ 540 nm , 580 nm , 630 nm and 665 nm indicating complete conversion of the precursor into pentacene. For both p-Pc and e-Pc, annealing the films at temperature > 200 °C causes mass loss due to pentacene sublimation which is also indicated in these absorbance Figures as lower magnitude of the absorbance. On

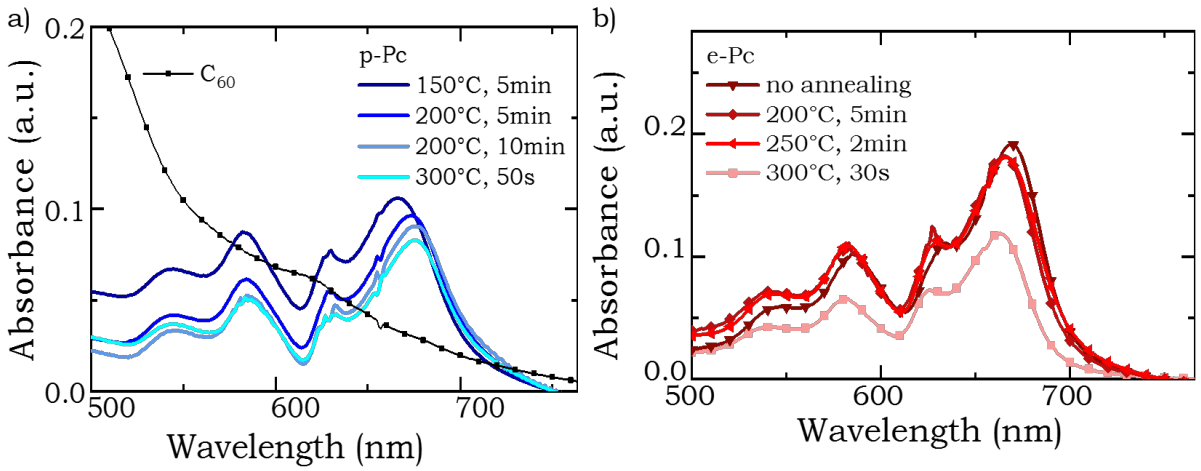

Figure 5.4: a) Absorbance curves obtained by annealing p-Pc films (≈ 100 nm) at different temperatures under identical conditions used for preparing devices. The black line indicates absorbance curve of a 40 nm thick, thermally evaporated C60 layer as reference for EQE data presented later. b) Absorbance curves for e-Pc films (≈ 100 nm) prepared in identical conditions as used in device fabrication.

annealing the p-Pc films at temperatures > 200 °C, the highest absorption peak around 665 nm appears to be slightly red-shifted by c.a. 5 nm. In order to explain this and also find further evidence of complete cleavage of the side-groups from the pentacene precursor, we carried out fourier-transform infrared spectroscopy (FTIR) and x-ray diffraction measurements. From the FTIR data (figure 5.5.a) we can see the complete conversion of the precursor into pentacene. Characteristic vibrational signals [19] of the N-S group at 1372 cm^{-1} and the C-O group at 1745 cm^{-1} which are visible in the pentacene precursor signal (Pc prec) disappear completely when the precursor is annealed (annealed Pc Prec (B)). On comparing the p-Pc signal to pristine pentacene (B-A) we can see that the two signal match well indicating the successful cleavage of side groups.

The x-ray data in Figure 5.5.b shows distinctly different positions of the Bragg peak for

the p-Pc film as compared to the e-Pc film indicating a clear difference in the molecular packing motif for the two films. The annealed e-Pc film obtains a similar bulk-phase crystal structure to p-Pc film with a Bragg peak at $q_z = 0.44\,\text{Å}^{-1}$ which is different from the thin-film phase reported in the literature [19]. We assign the Bragg peak at $q_z = 0.44\,\text{Å}^{-1}$ to the 001 reflection. We measure the lattice spacing perpendicular to the substrate surface (out-of-plane direction) to be 1.43 nm for p-Pc films which is in agreement with the bulk-phase crystal structure reported for pentacene [20]. Similarly the lattice spacing for e-Pc is slightly larger (1.53 nm) indicating that e-Pc grows in the thin-film phase as reported in literature and then transforms to bulk-phase crystal structure on annealing. This is also in agreement with literature where pentacene films adapt a bulk crystal structure either when no preferential direction is provided during crystal growth or when the substrate is heated while depositing the material [21]. The 5 nm peak shift in p-Pc absorbance can be assigned to this phase change from thin-film to bulk crystal phase in the molecular packing motif on annealing the films.

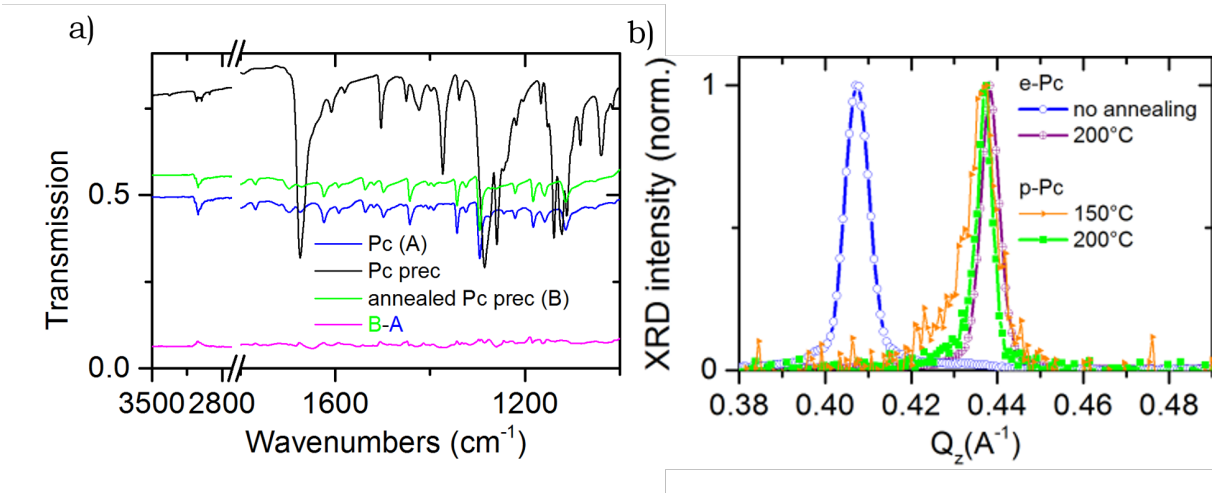

Figure 5.5: Experimental results to understand the crystallinity of two different types of pentacene films (evaporated pentacene: e-Pc and precursor processed pentacene: p-Pc) studied here. a) Infrared transmission of pentacene precursor (Pc prec) changes with annealing and becomes the same as from pentacene (Pc), verifying complete interconversion and no significant residues. b) X-ray diffraction data showing 001 - reflection peak for annealed e-Pc and p-Pc films indicating that p-Pc films crystalizes into bulk phase of pentacene [13]. *Note: Data collected by Katharina Broch and figure prepared by Maxim Tabachnyk.*

To understand the growth of crystal structures in these films, we further study the morphology of films prepared from annealing p-Pc films using atomic force microscopy (AFM). Figure 5.6 shows the growth of larger and flatter crystals with increasing annealing temperatures. We notice that p-Pc forms isolated crystals with diameter as large as 2 µm.

Increasing the temperature and the time for which the substrate is annealed makes these crystals more parallel to the surface of the substrate and larger in size as can be seen clearly in Figures (5.7-5.8).

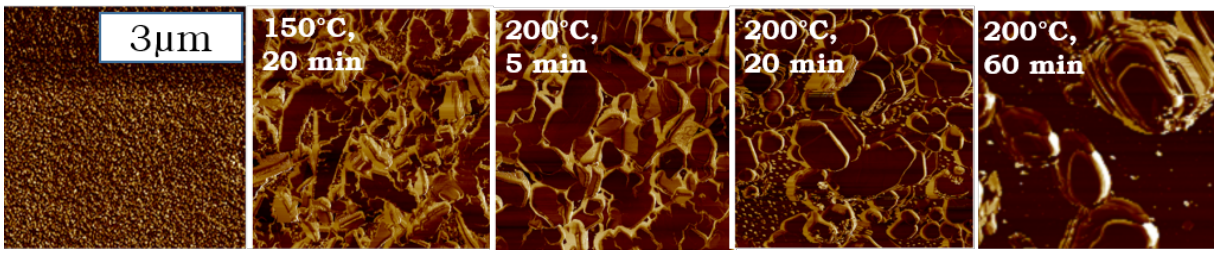

Figure 5.6: Atomic force microscopy images for annealed p-Pc on glass after various annealing conditions show the growth of clusters with higher annealing temperatures and longer annealing times. The crystal planes within the clusters become more parallel to the substrate plane the higher the annealing temperature and time. The average film thickness of all films is 100 nm. The leftmost image is that of p-Pc as-deposited without any annealing.

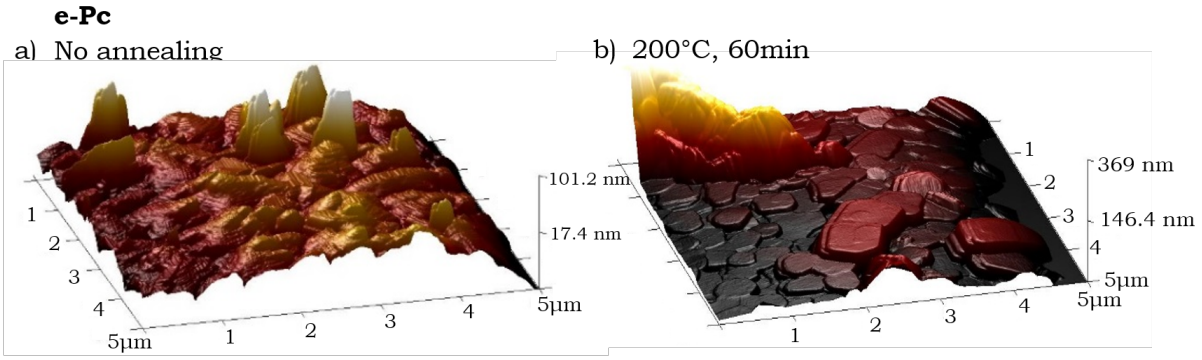

Figure 5.7: 3D AFM images of e-Pc a) pentacene evaporated on a glass substrate b) the same film annealed at 200 °C.

Compared to e-Pc films which are mostly homogeneous with a few sharp peaks about 100 nm high, the p-Pc annealed films appear more inhomogeneous with average peak heights of about 200 nm. Increasing annealing time causes the p-Pc films to form isolated crystals and the randomly oriented surfaces begin to align parallel to the substrate plane. However, we note that the inhomogeneous morphology of the films could potentially help increase the surface interface area with acceptor molecules. After understanding the film morphology in detail we then proceed to incorporate the p-Pc in devices.

Figure 5.9a shows the device structure used in this study where we compare e-Pc and p-Pc as electron donating layers in a bilayer pentacene-C_{60} device. We employ poly(3,4-ethylenedioxythiophene) polystyrene sulfonate (PEDOT:PSS) as the hole transporting

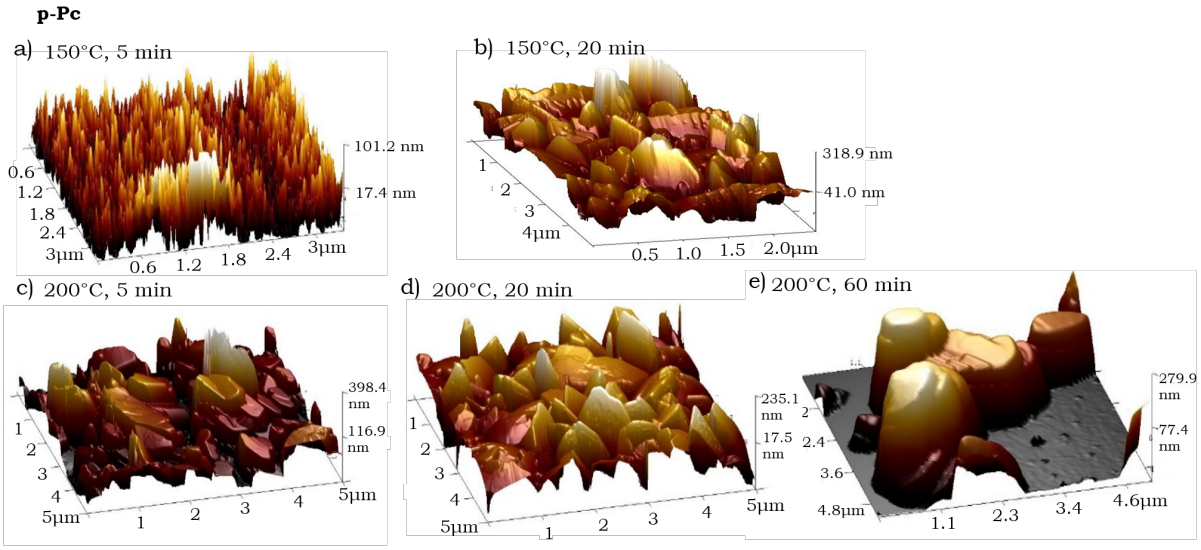

Figure 5.8: 3D AFM images of p-Pc annealed at different temperatures a) 150 °C for 10 minutes, b) 150 °C for 20 minutes, c) 200 °C for 5 minutes, d) 200 °C for 20 minutes, e) 200 °C for 60 minutes.

layer and C_{60} as the electron accepting and transporting layer. On photoexcitation, the pentacene generates triplets efficiently from singlet fission and these are extracted via the C_{60} layer. For these devices, e-Pc and C_{60} were deposited via thermal evaporation whereas PEDOT:PSS and p-Pc were deposited via spin-coating and annealed before depositing the next layer. Finally, aluminium was deposited via thermal annealing using an eight-pixel mask (see Chapter 3 for detailed fabrication process). In Figure 5.10a we compare the

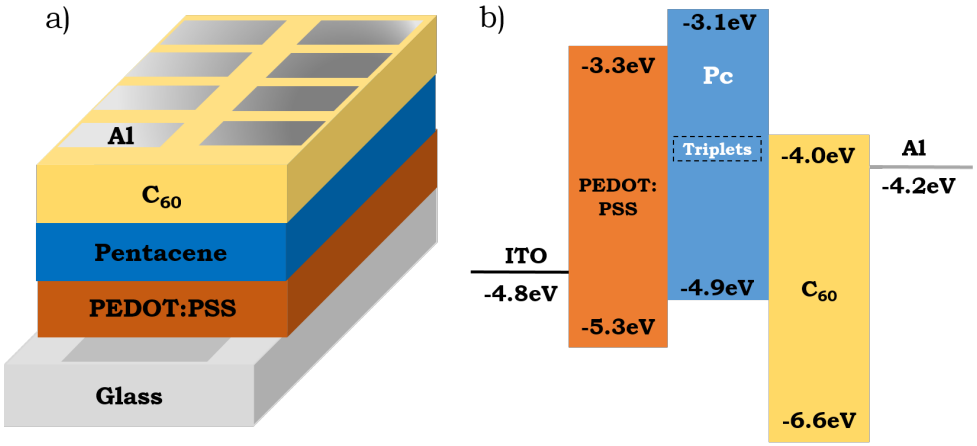

Figure 5.9: a) Device structure employing indium tin oxide (ITO) coated glass slide with poly(3,4-ethylenedioxythiophene) polystyrene sulfonate (PEDOT:PSS) as hole acceptor, pentacene (Pc) and fullerene (C_{60}) as the donor and acceptor respectively in the photo-active layer and aluminium (Al) as the top electrode. b) Energy band structure on the right indicates the HOMO and LUMO levels of organic layers and the workfunction of electrodes.

current-voltage characteristics of e-Pc/C_{60} and p-Pc/C_{60} devices. While the e-Pc device

demonstrates a short-circuit current (J_{SC}) of ≈3 mA/cm^2 there is a significant reduction in the J_{SC} of the p-Pc device. However, the dark current flowing through both the devices is identical. This indicates the existence of additional charge-carrier traps in p-Pc devices as compared to the e-Pc devices as also visible from the lower open-circuit voltage (V_{OC}) of p-Pc devices. Figure 5.10.b shows the comparison of external quantum efficiencies (EQE) obtained from the two types of pentacene/C_{60} devices. The peak EQE from the e-Pc device is 15 % whereas the 665 nm peak is substantially suppressed in p-Pc devices. As observed earlier, the reduction in EQE on annealing e-Pc at 300 °C can be due to loss of mass and due to formation of large isolated crystals in parts of the e-Pc film. In the case of p-Pc devices, we observe a significant enhancement in EQE on annealing the films at 300 °C for 30 seconds when compared to annealing at 200 °C for 5 minutes, while the line-shape of the EQE remains the same.

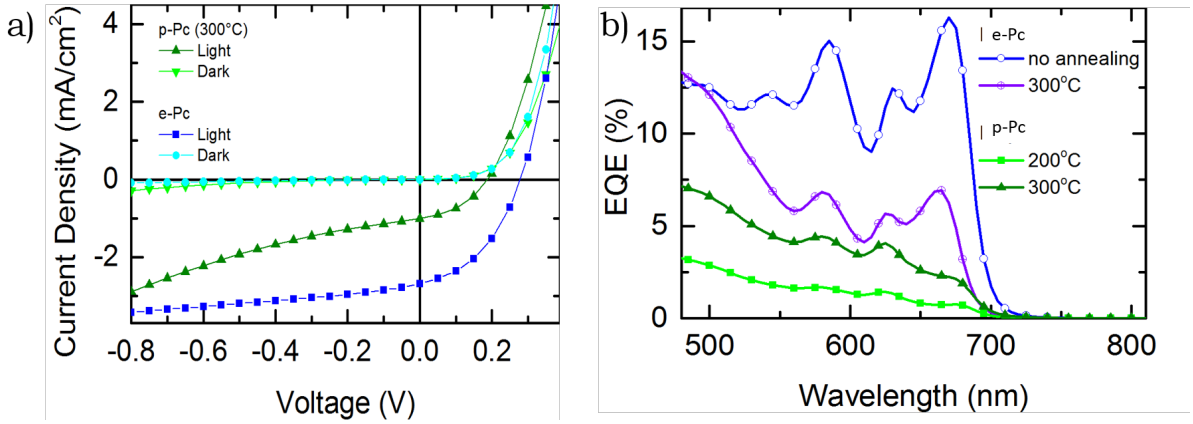

Figure 5.10: Comparison of device performance for champion e-Pc devices versus p-Pc devices. a) Green IV curves of p-Pc device (annealed at 300 °C) shows a reduction of open circuit voltage and short circuit current as compared to blue IV curves of e-Pc devices. It is important to note here that the dark current from both devices is identical. b) EQE comparison of blue e-Pc devices with green p-Pc devices show pentacene contribution reduction from p-Pc films.

The I-V characteristics presented in Figure 5.10 are those of the best performing e-Pc and p-Pc devices. In order to further optimise the p-Pc/C_{60} devices we perform a post-annealing treatment to find optimal temperature for annealing the p-Pc devices. We prepared p-Pc/C_{60} devices as described earlier and annealed the devices post initial measurement at 200 °C for 5 minutes. Data from these experiments is presented in Table 5.1. In the table, rows labelled 'Post-annealing' refer to J-V characteristics measured after annealing the devices at 200 °C for 5 minutes post initial measurements. We observed that the V_{OC} increases on this post-annealing treatment in all cases, perhaps because

annealing the active layer allows for the p-Pc and the C_{60} molecules to obtain an equilibrium morphology whereby the interface area between the donor and acceptor layer is enhanced allowing for a higher charge separation rate. However, the J_{SC} increases when the 200/5 (temperature (°C)/time(minutes)) device is post-annealed but does not increase on post-annealing 200/10, 250/2 or 300/1 devices. It is also interesting to note that higher temperature annealing (250 °C and 300 °C) leads to better device characteristics compared to the 200/5 device. Regardless of careful characterization of the morphology and crystal growth of p-Pc films the device power conversion efficiencies (PCEs) did not match those obtained from e-Pc devices.

Solution processed	V_{OC} (V)	J_{SC} (mA/cm^2)	FF (%)	PCE (%)
200/5	0.13	1.05	0.26	0.04
Post annealing	0.25	1.74	0.33	0.14
200/10	0.10	1.11	0.29	0.03
Post annealing	0.14	0.57	0.25	0.02
250/2	0.12	1.07	0.27	0.04
Post annealing	0.21	0.86	0.35	0.06
300/1	0.18	1.44	0.30	0.08
Post annealing	0.28	1.12	0.32	0.10
Evaporated No annealing	0.36	3.85	0.31	0.42

Table 5.1: Table of J-V characteristics of solution processed p-Pc and C_{60} devices showing change in characteristics on annealing at 200 °C for 5 minutes post fabrication.

Furthermore, Figure 5.11 shows a clear effect of initial annealing temperatures on the EQEs of p-Pc and e-Pc devices. With increasing annealing temperatures, the annealing times were reduced to prevent pentacene sublimation as observed in absorbance spectra at temperatures > 250 °C. As demonstrated earlier with AFM images (figure 5.7 and Figure 5.8), higher temperature and longer annealing times give rise to more uniform surfaces although with large isolated crystals. The smoother film surfaces contribute to higher EQEs in p-Pc devices. However, in e-PC devices, we see the opposite trend (figure 5.11.b)). This could be due to e-Pc subliming as lower EQE (higher annealing temperature) curves also seem to have a larger contribution from C_{60} absorption at wavelengths lower than 550 nm (see Figure 5.4a for C_{60} absorption profile). Hence, in order to study the charge-carrier dynamics in p-Pc devices as compared to the e-Pc devices, we carried out transient photocurrent and transient photovoltage measurements.

To investigate the effect of charge-carrier traps on device performance, we first measured transient photocurrent of p-Pc/C_{60} and e-Pc devices at short-circuit conditions. As shown in the inset of Figure 5.12a the transient photocurrent signal from an e-Pc device

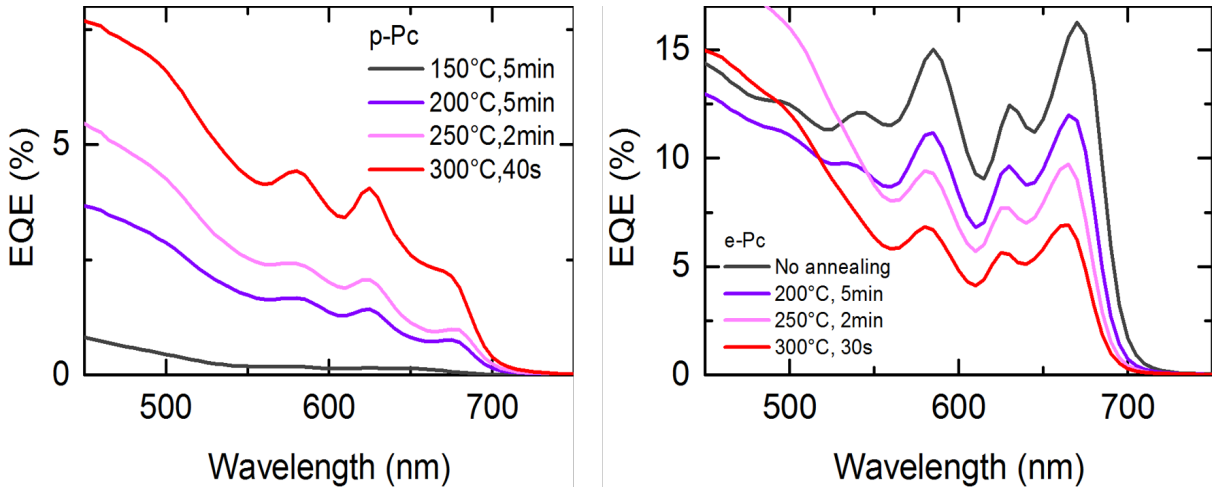

Figure 5.11: Effect of annealing of the pentacene layer on external quantum efficiencies (EQE) of devices. a) Increasing the temperature and reducing annealing times of the p-Pc films show improvement in EQEs whereas b) similar processing of thermally evaporated e-Pc films results in deteriorating EQEs.

demonstrates a fast, instrument-limited photocurrent response to illumination with no delayed decay dynamics. In the case of p-Pc devices however, we can clearly observe delayed dynamics in Figure 5.12.a. There is a delayed response to illumination (>100 µs) in the p-Pc device annealed at 200 °C for 5 minutes which becomes faster in the device annealed at 300 °C for 40 seconds. Such delayed dynamics are typically attributed to charge extraction barriers [22] at the interface or significant charge carrier trapping in a device [23, 24]. The presence of additional negative feature in the photocurrent when illumination is switched off indicates the need for extra charge injection in order to restore equilibrium, providing further evidence for charge carrier trapping in these devices.

We also measured the transient photovoltage in open-circuit conditions to compare the photovoltage decay for e-Pc and p-Pc devices. A continuous wave (cw) background white light bias is applied to obtain comparable V_{OC} of about 0.2 eV in both the p-Pc and e-Pc devices to ensure similar background charge carrier concentrations. We observe faster decay time (shorter lifetime) of charge carriers generated by a perturbation pulse in p-Pc devices (≈ 13 µs) as compared to e-Pc devices (≈ 22 µs). This result is consistent with the TPC results discussed earlier suggesting a larger density of trap states and other defects that accelerate recombination in p-Pc devices. At this point we note that pentacene precursor purchased from Sigma Aldrich has a claimed purity of 97 %. Chemical doping impurities of > 1 % can have a significant impact on electronic properties of the material providing charge trapping and recombination channels. From the FTIR measurements

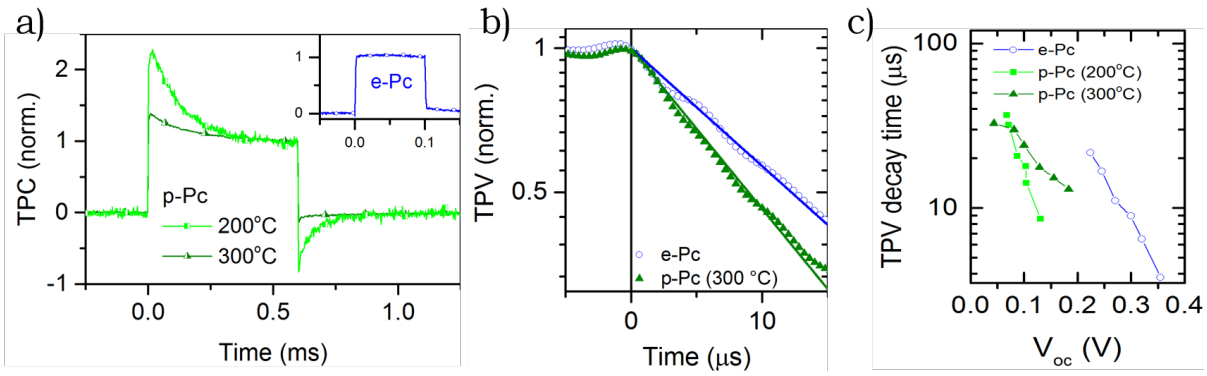

Figure 5.12: a) Transient photocurrent (TPC) kinetics for devices using p-Pc and e-Pc (inset) indicating higher amount of charge traps present in p-Pc annealed at 200 °C as compared to 300 °C and no such features in e-Pc devices. TPC was measures at short circuit and an LED pulse is used to excite the devices at 1 sun intensity at 460 nm for 0.6 ms and 0.1 ms, respectively. b) Transient photovoltage (TPV) decay is measured at open circuit after the LED perturbation is switched off (0 µs). A background cw white light excitation is used to obtain comparable V_{OC} of c.a. 0.2 eV in both device types. Single-exponential fits (solid lines) are used to model the decay indicating longer charge carrier lifetimes in e-Pc devices. c) Photovoltage decay times for evaporated and solution processed Pentacene/C_{60} devices, where ND filters have been used to vary V_{OC}.

discussed earlier 5.5 we ensure that the thermally-cleaved side-groups are removed from the converted p-Pc films and thus it is unlikely that the conversion process leaves any impurities in the films. Thus careful purification of the precursor pentacene to eliminate other chemical impurities affecting the electronic properties of p-Pc films is essential for the device applications of p-Pc.

In Figure 5.12.c we compare the photovoltage decay lifetimes for p-Pc and e-Pc devices where the precursor was annealed at two different temperatures (200 °C and 300 °C). Neutral density (ND) filters were used to vary the white light intensity in order to obtain comparable V_{OC}s for different devices under consideration. We observe that at most voltages, the p-Pc device annealed at 200 °C has much faster decay lifetimes than the p-Pc device annealed at 300 °C. On the other hand, the e-Pc devices display longer lifetimes at low voltages and comparatively faster decay times at higher voltages. This explains that although the e-Pc devices work well at low charge carrier densities (at low V_{OC}s), faster recombination rates at high voltages prevent the devices from achieving high power conversion efficiencies. Considering the limited donor-acceptor interface in bilayer devices, poor charge separation due to very few charge carriers reaching the donor-acceptor interface can explain the faster photovoltage decay in e-Pc devices at high charge-carrier densities.

5.2.2 Bulk heterojunction with PCBM

(Some bulkheterojunction devices presented in this chapter were prepared by Marcus Boehm who was also one of the collaborators in our published work [13].)

Having studied the morphology of p-Pc films in detail and their application in bilayer organic solar cells, we now turn to demonstrate that p-Pc can be used for fabrication of bulk heterojunction solar cells using phenyl-C_{61}-butyric acid methyl ester ($PC_{61}BM$) as the electron acceptor. For this study, we first compared films prepared from two different blends of p-Pc/$PC_{61}BM$ (10:1 molar ratio), one consisting of 40 mg mL^{-1} (thin) and the other 70 mg mL^{-1} (thick) of combined solute in chloroform. These films were prepared by spin-coating the blend on PEDOT-substrates and annealing them at 200 degreeC for 5 minutes. On studying the morphology of films prepared from these two blends we found large crystal formations as can be seen in Figure 5.13. Increasing the combined solute concentration in blend solutions resulted in regions of larger isolated crystals (see Figure 5.13.b). Thus when incorporating the blend in devices, we decided to use an additional $PC_{61}BM$ layer to prevent the large crystals from coming in contact with the electrode and to provide additional interfaces for charge separation while enhancing electron-extraction through $PC_{61}BM$.

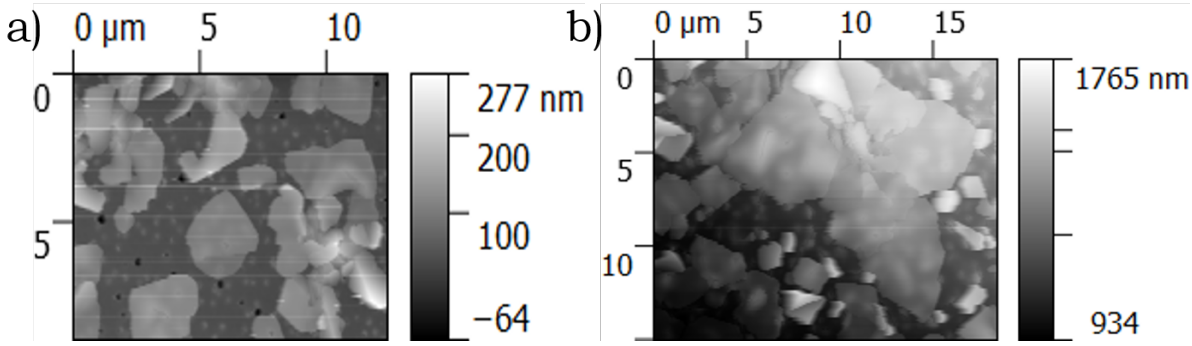

Figure 5.13: Atomic Force Microscopy (AFM) images of p-Pc and PCBM blend films deposited on a glass substrate indicating large crystal formations. a) film prepared from 40 mg mL^{-1} (thin) combined solute concentration b) 70 mg mL^{-1} (thick) combined solute concentration.

To realize bulk heterojunction devices with p-Pc we use $PC_{61}BM$ as the electron acceptor in a blend with p-Pc as the electron donor for the active layer. The devices were fabricated in a similar fashion to the p-Pc/C_{60} bilayer devices. We deposit PEDOT:PSS as the hole-transporting layer by spin coating it on an ITO coated glass substrate from an aqueous solution, followed by a blend of p-Pc and $PC_{61}BM$ (molar ratio 10:1). We

use an additional layer of $PC_{61}BM$ as the electron transporting layer and also to prevent the large p-Pc crystals from coming in contact with the aluminium electrode. Figure 5.14 shows the energy level alignment of each of these layers.

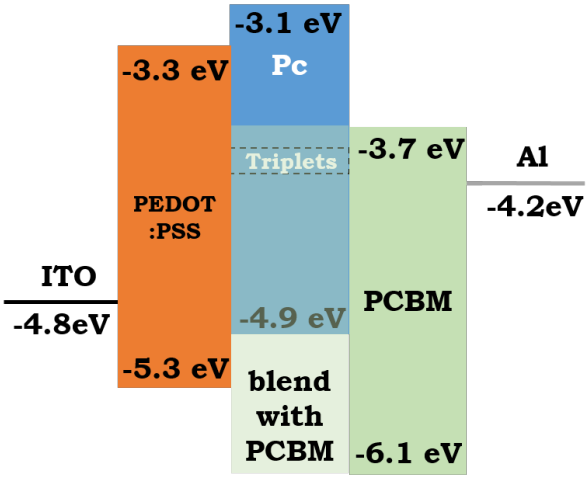

Figure 5.14: Energy band structures for pPc and PCBM devices, indicating the HOMO and LUMO levels of organic layers and the workfunciton of electrodes.

Adding additional $PC_{61}BM$ significantly improved the absorption of active layer in UV-region as can be seen in Figure 5.15.a. On incorporating these blends in devices we observed a substantial contribution from p-Pc to the device EQE. In Figure 5.15.b we plot the absorption profiles of the individual components of the active layer: p-Pc and $PC_{61}BM$, along with the device EQEs. The J_{SC} of the thin-blend device was $\approx 0.44\,mA/cm^2$ and that of the thick-blend device was $\approx 0.54\,mA/cm^2$ and their V_{OC} were 0.46 V and 0.52 V respectively. We observed maximum PCEs of 0.05 % and 0.07 % for the thin-blend and thick-blend devices respectively.

The spectrally resolved photocurrent shows additional contributions to the photocurrent in the spectral region between 520 nm and 700 nm which corresponds to the p-Pc absorption profile. As singlet fission is shown to be extremely efficient in annealed p-Pc films [13], this suggests that triplets generated from singlet fission in p-Pc contribute to the photocurrent generated from these bulk heterojunction devices. It is important here to note that it is unlikely that the additional photocurrent contribution arises from dissociation of singlet excitons, as in pentacene singlet fission is shown to kinetically outcompete charge transfer even in ultrathin bilayer samples of pentacene and fullerene [16]. Furthermore, we observe enhancement in overall EQE of these bulk heterojunction devices as the thickness of the active layer is increased, which was the main aim of using p-Pc as opposed to e-Pc in such devices.

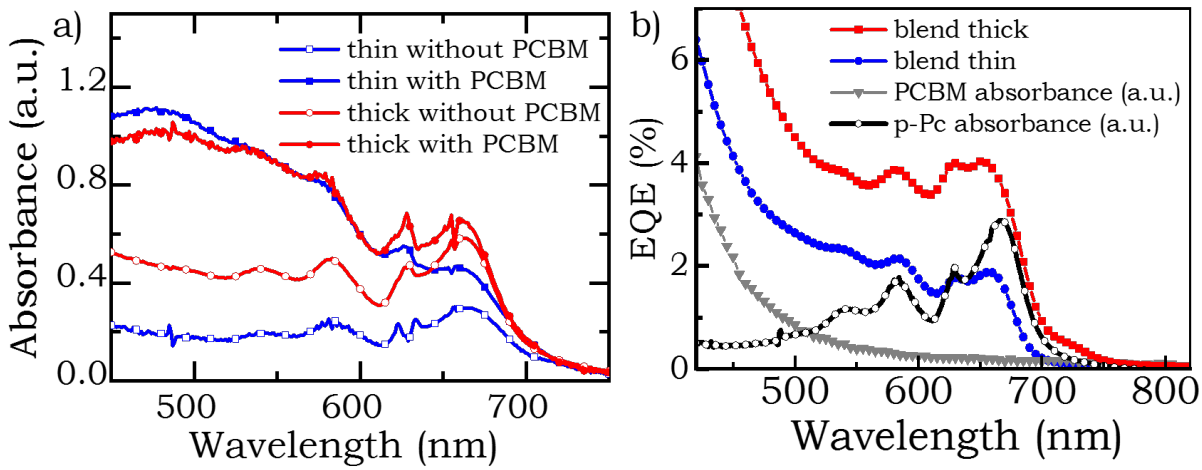

Figure 5.15: Absorption and external quantum efficiency (EQE) plots comparing two different concentrations of p-Pc and PCBM blend films. a) Absorbance curves for 40 mg mL^{-1} and 70 mg mL^{-1} solute concentration p-Pc and PCBM blend films with and without an extra PCBM layer (20 mg mL^{-1} solute concentration). b) Higher concentration films indicating a gain in EQE compared to low concentration films. Also, p-Pc peaks can be seen to contribute to the EQE as compared to the p-Pc absorbance curve.

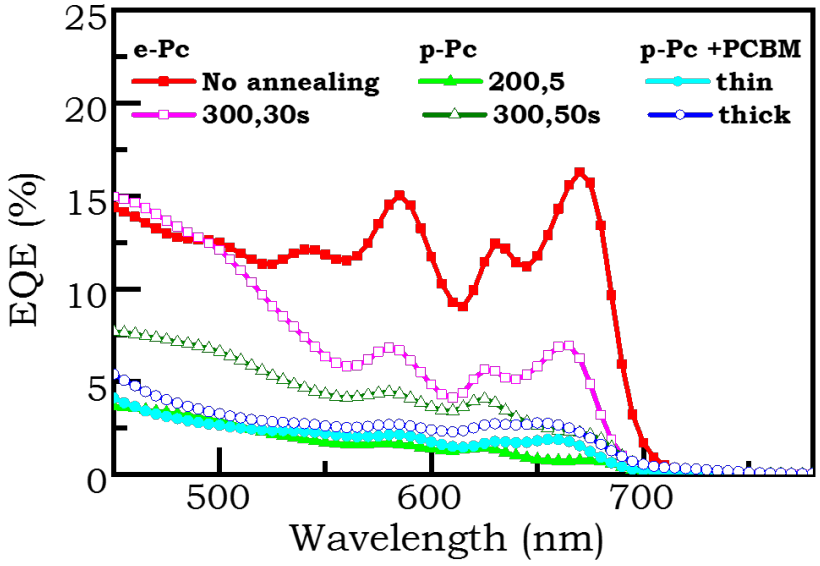

Figure 5.16: Combined plot of EQEs for e-Pc/C_{60} bilayer, p-Pc/C_{60} bilayer and p-Pc/PCBM bulk-heterojunction devices.

Finally in Figure 5.16 we compare external quantum efficiencies (EQEs) of all devices prepared using p-Pc in the active layer. We note that although annealing times and temperatures of p-Pc films allowed us to control the morphology of these films and optimise contact with electron acceptor layers, the overall performance of p-Pc devices could not match e-Pc device performance. As mentioned earlier, we note that the p-Pc purchased from Sigma Aldrich has claimed purity of 97 % and the 3 % material impurity might be significantly contributing to the poor electronic transport in the p-Pc films thus restricting

device performances.

5.2.3 Colloidal quantum dots (CQDs) as triplet-harvester

CQDs used in this section were synthesised by Tom Jellico, James Xiao, Le Yang or Marcus Boehm using processes identical to the one described in Section 3.2 hot-injection method.

Following previous studies [9, 10, 16] where e-Pc and TIPS-pc have been used in conjunction with lead sulphide (PbS) and lead selenide (PbSe) CQDs to generate triplets in pentacene via singlet fission and harvest them using CQDs, we employ p-Pc as electron-donor in our devices. We tried a few different device architectures to successfully incorporate p-Pc as electron donor in solar cells. The detailed fabrication process for all the devices is outlined in Chapter 3 however, we will briefly review the device architectures here. Beginning with a bilayer architecture as shown in Figure 5.17 we sandwich the active layer between two electrodes, ITO and aluminium [9].

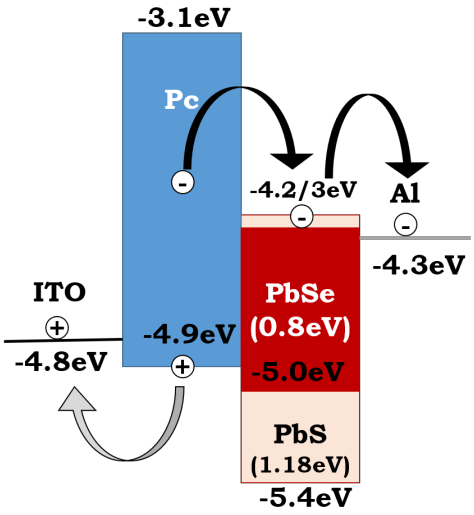

Figure 5.17: Schematic representation of energy levels of different layers of a p-Pc/Colloidal quantum dot (CQD) device indicating triplet transfer to CQD from p-Pc triplets, CQD being the electron transport layer. Starting from the left, the layers include indium tin oxide (ITO) on a glass substrate, p-Pc layer, CQD layers (solid state ligand exchanged), aluminium. The arrows indicate the direction of electron and hole transport.

Next, we introduce additional electron transporting and hole transporting layers in the device architecture. As shown in Figure 5.18 we use titanium dioxide (TiO_2) as the electron transport layer and molybdenum oxide (MoOx) as the hole transport layer. In this particular architecture we first deposit PbS CQDs with bandgaps of 1.1 eV and 0.8 eV on TiO_2 and perform solid state ligand exchange to replace the oleic acid ligands on CQDs

with 1,2 benzenedithiol (BDT) ligands in order to protect the p-Pc layer from excessive solvent exposure. Following the CQD deposition and ligand exchange, we deposit the p-Pc layer and anneal it at 200 °C for 5 minutes. Finally, MoOx (7 nm) and gold (Au, 80 nm) are deposited via thermal evaporation. Further details of fabrication are covered in Section 3.3.2.

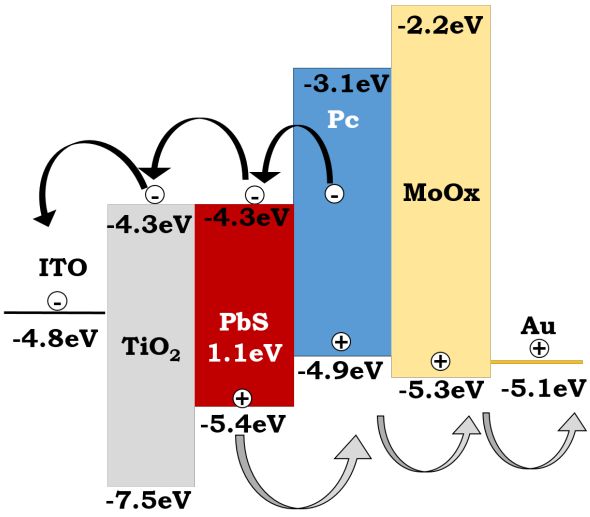

Figure 5.18: Schematic representation of energy levels of different layers of p-Pc/CQD devices where CQDs are used as electron-transport layer. Starting from left, the layers include indium tin oxide (ITO), titanium dioxide (TiO_2), p-Pc (dark blue), lead selenide (dark red) CQDs, molybdenum oxide (MoOx) , gold (Au). An identical structure can be adapted for lead-sulphide (PbS) CQDs. The arrows indicate the direction of electron and hole transport.

The third and final architecture used for this study is displayed in Figure 5.19. Here we use zinc oxide (ZnO) instead of TiO_2 as the electron transport layer. Also, in this architecture we first deposit p-Pc on the ZnO-coated ITO substrate and anneal it at 200 °C for 5 minutes. This architecture was adopted in order to avoid annealing the CQD layer and observe the effect on device performance. We then deposited PbSe CQDs with 0.8 eV bandgaps and performed solid state ligand exchange as mentioned previously. As before MoOX and Au was finally deposited via thermal evaporation to complete the device.

After investigating the above-mentioned device architectures with a bilayer active layer, we also tried to fabricate bulk heterojunction (BHJ) solar cells by suspending CQDs in chloroform along with p-Pc. Table 5.2 lists the performances of champion devices obtained from each of the three architectures presented above along with the BHJ devices. We note that from the various device architectures studied above, the TiO_2/Au structure using PbSe CQDs (1.1 eV bandgap) yielded the best results. This was in agreement with

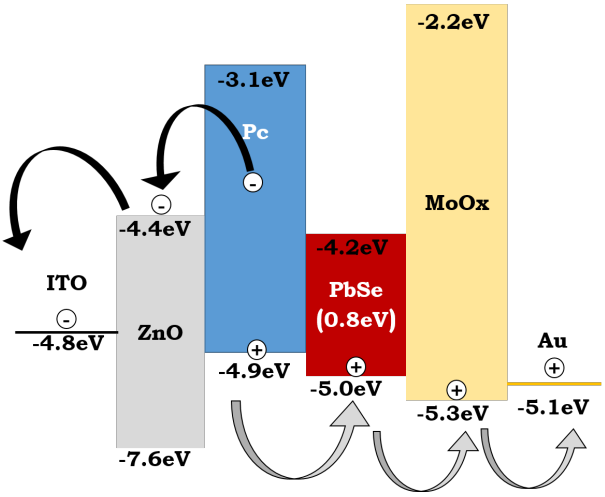

Figure 5.19: Schematic representation of energy levels of different layers of p-Pc/CQD devices where CQDs are used as hole-transporting layer. Starting from left, the layers include indium tin oxide (ITO), zinc-oxide (ZnO), p-Pc (dark blue), lead selenide (dark red) CQDs, molybdenum oxide (MoOx) , gold (Au). An identical structure can be adapted for lead-sulphide (PbS) CQDs.

literature [9, 10, 16] where CQDs with bandgaps between 0.9 eV and 1.25 eV have been shown to successfully seperate triplet excitons from pentacene based molecules. Here we report power conversion efficiencies (PCEs) of control PbSe (0.8 eV) devices reaching 1.27 % and that of PbSe (1.1 eV) devices reaching 1.34 % which are reasonable when compared to the best efficiencies achieved in our lab with e-Pc of 4.7 % [9] and TIPS-pc of 4.8 % [10]. The best p-Pc/CQD blend device was obtained using PbS (1.2 eV) CQDs where we demonstrate PCE reaching 0.77 %.

Looking only at the PEDOT/Al devices in table 5.2 it is interesting to note that although the V_{OC} improves significantly from 0.22 V to 0.71 V in the blend device as compared to the bilayer device, the J_{SC} drops substantially from 4.54 mA/cm^2 to 0.001 mA/cm^2. This can be explained by the fact the bilayer device architecture allows for ligand exchange and thus for replacement of long oleic acid ligands with short BDT ligands whereas in the blends we employ CQDs with long oleic acid ligands attached. Also, the ZnO/Au architecture showed poor PCEs. There could be various reasons for this including p-Pc layer being exposed to various organic solvents in the CQD layer deposition process. Also, looking at the band energy alignments, perhaps this architecture favours transfer of both the electrons and holes to the CQD layer, instead of only hole transfer as predicted in Figure 5.19. This would thus lead to electrons being trapped on CQDs thus resulting in poor device performance.

As the TiO_2 control devices showed measurable performance, we tried varying the

annealing temperatures for the active layer and the p-Pc concentration in p-Pc/CQD blends to investigate their effect on device performance. On altering the temperature we find that annealing the films at 300 °C for 30 seconds is as effective as annealing at lower temperatures for longer times. This is consistent with our previous findings in Section 5.2.1 where we observed lower loss in device efficiencies when annealed at 300 °C due to reduced charge traps present in devices (see Figure 5.12). On increasing p-Pc concentration in blends we noticed general deterioration of the device characteristics which further ascertains the fact that further careful purification of p-Pc is necessary in order to improve device performances with p-Pc.

Electrodes	Active layer	CQD bandgap (eV)	p-Pc conc. (mg/ml)	Annealing temperature/time (°C/min)	V_{OC} (V)	J_{SC} (mA/cm²)	FF (%)	PCE (%)
PEDOT/Al	Bilayer	0.8 (PbSe)	4	200/5	0.22	4.54	24.07	0.24
PEDOT/Al	Blend	0.8 (PbSe)	4	200/5	0.71	0.001	27.37	0.0002
ZnO/Au	CQD Only	0.8 (PbS)	--	--	0.12	0.01	24.59	0.0002
ZnO/Au	CQD Only	1.1 (PbS)	--	--	0.21	0.41	28.56	0.025
ZnO/Au	Bilayer	0.8 (PbS)	4	200/5	0.07	0.11	22.87	0.002
TiO_2/Au	CQD Only	0.8 (PbSe)	--	--	0.31	8.88	46.15	1.27
TiO_2/Au	Bilayer	0.8 (PbSe)	4	200/5	0.24	4.81	38.45	0.44
TiO_2/Au	CQD only	1.1 (PbSe)	--	--	0.49	5.96	45.80	1.34
TiO_2/Au	Bilayer	1.1 (PbSe)	4	200/5	0.43	1.90	17.30	0.14
TiO_2/Au	Blend	1.2 (PbS)	2	150/10	0.52	2.64	21.50	0.30
TiO_2/Au	Blend	1.2 (PbS)	2	200/5	0.52	5.48	27.08	0.77
TiO_2/Au	Blend	1.2 (PbS)	2	300/30s	0.52	4.29	24.57	0.55
TiO_2/Au	Blend	1.2 (PbS)	7	150/10	0.36	0.002	17.64	0.0001
TiO_2/Au	Blend	1.2 (PbS)	7	200/5	0.47	3.45	24.06	0.39
TiO_2/Au	Blend	1.2 (PbS)	7	300/30s	0.52	4.60	23.70	0.54

Table 5.2: Table listing device characteristics of various p-Pc/CQD devices, prepared using active-layer composed of PbS and PbSe CQDs with oleic-acid ligands suspended in chloroform along with p-Pc. The blends were deposited and annealed to convert p-Pc into pentacene at temperatures indicated in the table. p-Pc concentration was varied as recorded for each device in the table whereas the CQD concentration was maintained at 25 mg mL^{-1} for all devices.

Following on from this initial demonstration where p-Pc/CQD blend devices were prepared using CQDs with long oleic acid ligands which limited the J_{SC} in blend devices, we studied the effect of solid-state ligand exchange on p-Pc/CQD blend films. Using transmission electron microscopy (TEM), we investigated the organization of CQDs in p-Pc/CQD films with 4 mg mL^{-1} p-Pc in chloroform and 25 mg mL^{-1} CQDs capped with oleic acid ligands, suspended in chloroform. Based on our previous knowledge of the conversion temperatures for p-Pc films, we studied blend-film morphology and CQD organisation in these films annealed at 150 °C and 200 °C for 10 minutes and 60 minutes

respectively. The top row of images in Figure 5.20 show three images of the same film, with different spatial resolution post annealing the blend film at 150 °C for 10 minutes and the bottom row shows an identical film but with solid-state BDT ligand exchange performed on it before annealing. We note that before ligand exchange, the blend films show good dispersion of CQDs in p-Pc and there are very few regions showing dark-black spots indicating CQD aggregation. On taking a closer look at the dark spots (rightmost image, top row), we observed that these regions had CQDs clustered together and only very few CQDs actually merged to form larger dots. In the TEM images acquired of films where BDT solid-state ligand exchange was performed pre-annealing (bottom row, Figure 5.20) we observed larger regions ($\approx$ 150 nm) with CQD aggregates.

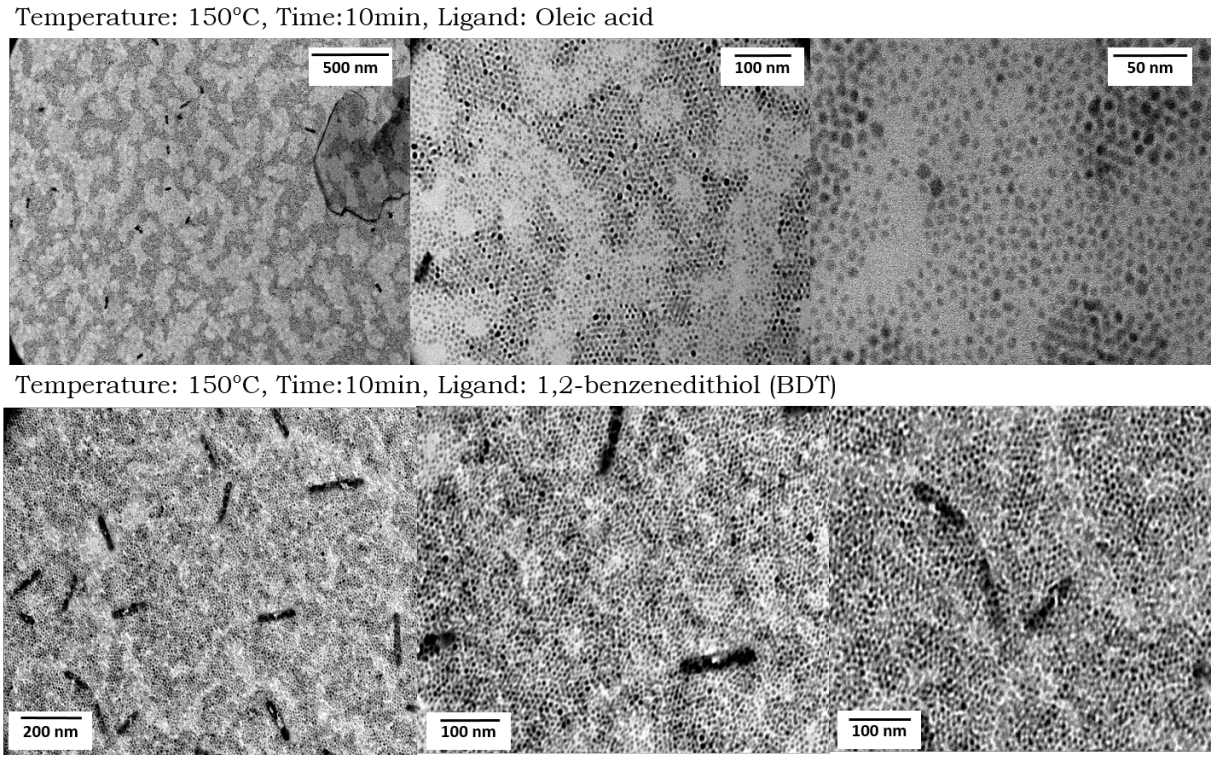

Figure 5.20: Transmission electron microscopy (TEM) images of p-Pc and PbS blends prepared from chloroform solvent. PbS CQDs were suspended in chloroform with oleic acid initially and 1,2-benzene-dithiol (BDT) solid state ligand exchange was performed pre-annealing.The top row contains images with oleic-acid ligand on PbS CQDs and the bottom with BDT ligands post-annealing. Annealed at 150 °C for 10 minutes.

When the p-Pc/CQD films were annealed at 150 °C for 60 minutes (figure 5.21) following a similar procedure as explained above for Figure 5.20 we observe clear regions with phase separated p-Pc regions and CQD regions. The circular features in the TEM image show p-Pc crystals formed from longer annealing of the blend films for 60 minutes. In general the films show CQD dominated regions with high level of CQD aggregation. Al-

though CQD aggregation does not appear to be very prominent in oleic-acid capped CQD blend films (top row, Figure 5.21), in BDT ligand exchanged CQD blend films (bottom row, Figure 5.21) show networks of aggregated CQDs in CQD dominated regions around the p-Pc circular features.

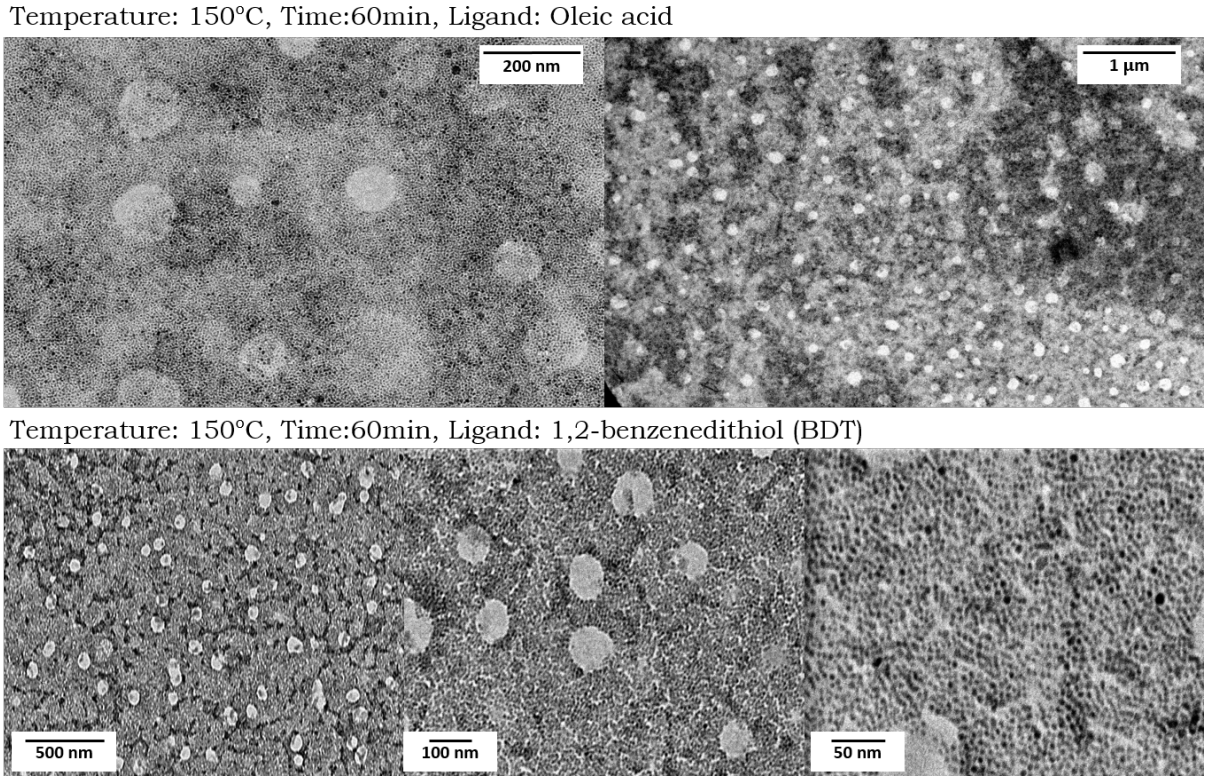

Figure 5.21: Transmission electron microscopy (TEM) images of p-Pc and PbS blends prepared from chloroform solvent. PbS CQDs were suspended in chloroform with oleic acid initially and 1,2-benzene-dithiol (BDT) solid state ligand exchange was performed pre-annealing.The top row contains images with oleic-acid ligand on PbS CQDs and the bottom with BDT ligands post-annealing. Annealed at 150 °C for 60 minutes.

Annealing the blend films at higher temperatures of 200 °C gives rise to many regions of aggregated CQDs and clearly phase separated regions with p-Pc dominance in the circular features and CQD dominated networks around those regions. On performing BDT ligand exchange and annealing the films at 200 °C we observed dark CQD aggregate regions identical to the ones in 150 °C films but in larger quantities. On investigating these regions with higher resolution we can see complete aggregation of the dots (right most images, Figure 5.22). On annealing the films for longer (60 minutes) as shown in Figure 5.23, we observed larger networks of p-Pc crystals and phase separated regions of p-Pc and CQDs with numerous dark spots showing enhanced CQD aggregation in these films.

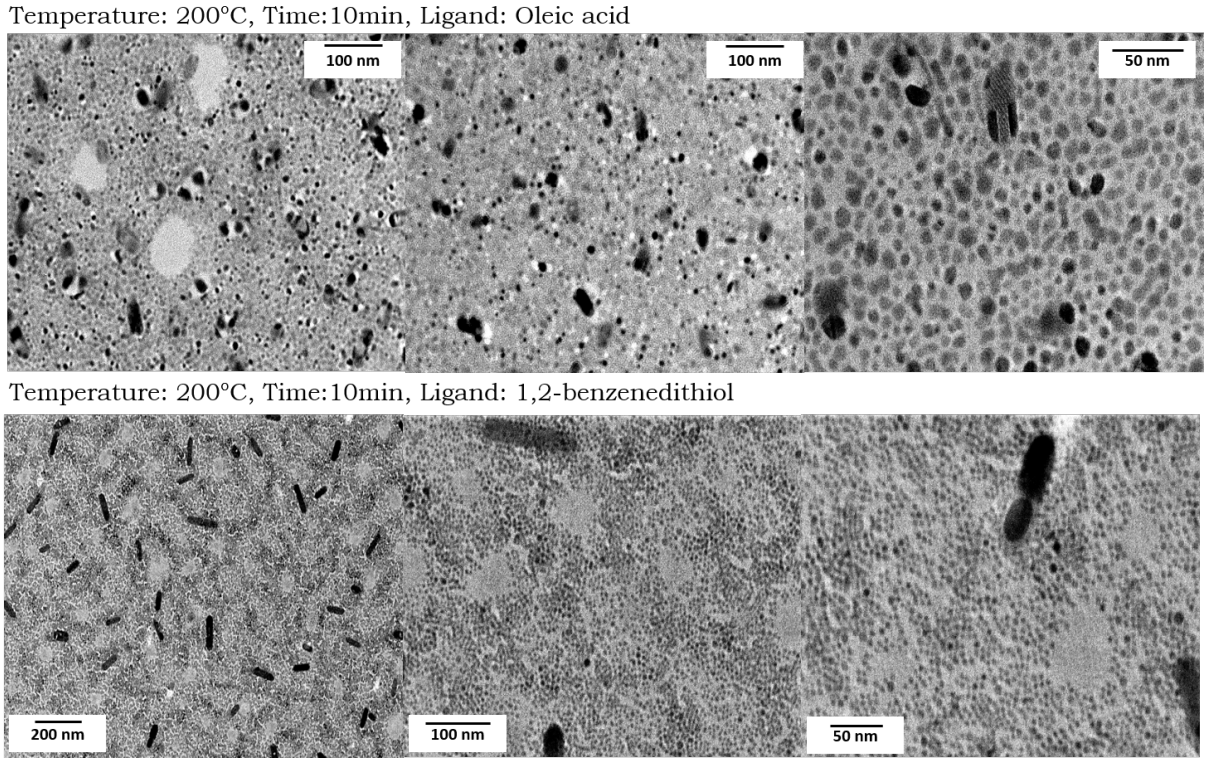

Figure 5.22: Transmission electron microscopy (TEM) images of p-Pc and PbS blends prepared from chloroform solvent. PbS CQDs were suspended in chloroform with oleic acid initially and 1,2-benzene-dithiol (BDT) solid state ligand exchange was performed pre-annealing.The top row contains images with oleic-acid ligand on PbS CQDs and the bottom with BDT ligands post-annealing. Annealed at 200 °C for 10 minutes.

Thus aggregation of CQDs in BDT ligand-exchanged p-PC/CQD films prevents the application of such blends in solar cells. Phase-separated blend films and aggregated CQD regions provide pathways for non-radiative recombinations by trapping excitons in either of the two regions when CQDs are capped with short ligands. When no ligand exchange is performed on oleic acid (long ligand) capped dots, charge transport from one CQD to another becomes a challenge trapping the charges in CQD domain. Hence we need to find an alternative method of forming p-Pc/CQD bulk heterojunction films. We discuss the option of integrating the CQDs in SF-matrices in novel fibrous matrices and discuss the preliminary work on this front in the next section.

5.3 Conclusions and future work

In this work, we demonstrate incorporation of pentacene films prepared from a novel solution-processed precursor (p-Pc) in organic and hybrid solar cells. Following the complete cleavage of attached side-groups on annealing, we demonstrate that the pentacene

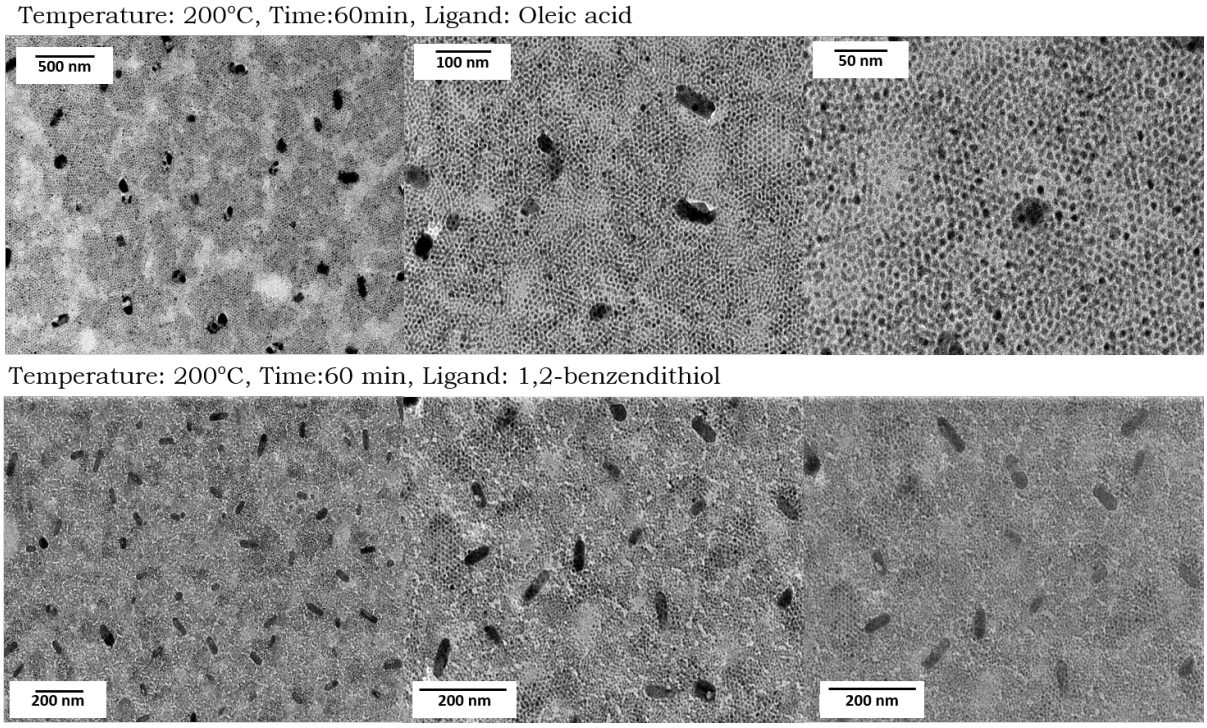

Figure 5.23: Transmission electron microscopy (TEM) images of p-Pc and PbS blends prepared from chloroform solvent. PbS CQDs were suspended in chloroform with oleic acid and 1,2-benzene-dithiol (BDT) ligands respectively. The top row contains images with oleic-acid ligand on PbS CQDs and the bottom with BDT ligands. Annealed at 200 °C for 60 minutes.

formed via the precursor route forms thin-films with bulk-phase molecular packing. Furthermore, we incorporate p-Pc into bilayer devices with C_{60} as the electron acceptor molecule and compare it with pristine pentacene bilayer devices [6]. We find that although singlet fission still remains 200 % efficient [13], the generated triplets get trapped at the interfaces thus limiting device performances.

We also integrate p-Pc in a BHJ with PCBM and observe significant contribution to photocurrent between 500 nm to 700 nm indicating charge generation from SF-generated triplets. Considering the low dielectric constant of organic molecules, we note that separating two triplet excitons into free charge carriers requires twice the amount of energy as compared to separating a singlet exciton. This makes charge-separation challenging and limits power conversion efficiencies of such BHJ devices. We also note that the geometry of SF molecules in the film is critical to allow for successful triplet-diffusion from the triplet-pair state as discussed in detail in Chapter 6. Thus, understanding the molecular alignment of p-Pc molecules in the p-Pc/PC_{61}BM blend films would help optimise these devices further. Besides, the commercially bought pentacene precursor was only 97 %

pure. We suspect that this could be the primary reason limiting the electronic properties of p-Pc films and further purification of the precursor could result in p-Pc device characteristics matching those of pristine pentacene.

We also explore the prospects of resonant energy transfer from small molecules to CQDs, in addition to the charge transfer in organic donor-acceptor framework. To this end, following the work of Ehrler et. al [9] and Yang et. al [10] we prepare bilayer p-Pc/CQD devices and also experiment with p-Pc/CQD BHJ-type blends. Although we obtained significant photovoltage from the BHJ-type p-Pc/CQD devices reaching 0.71 V, extracting photocurrent from these devices remained a challenge. Since triplet diffusion limits the SF domain size to ≈ 40 nm in pentacene and higher optical density improves film absorption, we focussed on optimizing the BHJ-type architecture to efficiently extract SF generated triplets. Using electron microscopy, we investigated the distribution of CQDs in a p-Pc matrix. With oleic-acid (long-ligand) capped CQDs we obtain an isotropic distribution of CQDs in the blend with very few CQD aggregates formed during the p-Pc annealing step. However, the long-ligands prevent efficient charge transport in the CQD domain and therefore limit charge extraction. On replacing the long ligands with short BDT ligands, we find that the concentration of CQD aggregates increases significantly post-annealing. Thus the requirement of thermal-cleavage of side groups limits the application of p-Pc in p-Pc/CQD BHJ devices as it causes the CQDs to form aggregates. Our work so far presents a comprehensive understanding of the advantages and limitations of using the novel pentacene precursor and provides pathways for using singlet fission in photovoltaics.

In order to overcome the challenge of preparing CQDs sensitized SF matrices not only for incorporation in PVs, but also for photon downconversion applications as mentioned in Section 5.1.2, we explore the idea of using an organogel matrix which remains in liquid phase when heated and forms a semi-solid gel-like film when cooled to room temperature. These organogel matrices form a fibrous network and thus provide a novel hybrid nanostructure to incorporate well-dispersed CQDs in an organic framework. Furthermore, once the incorporation of unaggregated CQDs in the gel-matrix is accomplished, these organogels can be prepared with SF capable organic materials. Such that, a photonmultiplication unit can be prepared with the gel-matrix which can perform singlet fission and transfer the singlets to CQDs as mentioned in Section 5.1.2. Alternatively, SF capable molecules can be dispersed in gel matrices along with the CQDs to achieve the same effect.

For preliminary experiments on this front, we worked with an inert, transparent organogel called SucValDoc (see Figure 5.24a for molecular structure), a novel material provided by our chemist collaborators (Francisco Galindo, Universitat Jaume I de Castellon, Spain). These gels are in liquid phase at room temperature, but on being heated at 120 °C for 20 minutes to 25 minutes followed by cooling back down to room temperature, they form fibrous films as shown in the scanning electron microscope (SEM) image in Figure 5.25b. We disperse CQDs in these gels once the gel-solution is taken off the hot-plate post-heating at 120 °C for 20 minutes to 25 minutes such that we do not actively heat the CQDs. This also ensures that the CQDs get enough time to disperse well in the the organogel when it is still in liquid phase before transforming to a semi-solid gel at room temperature.

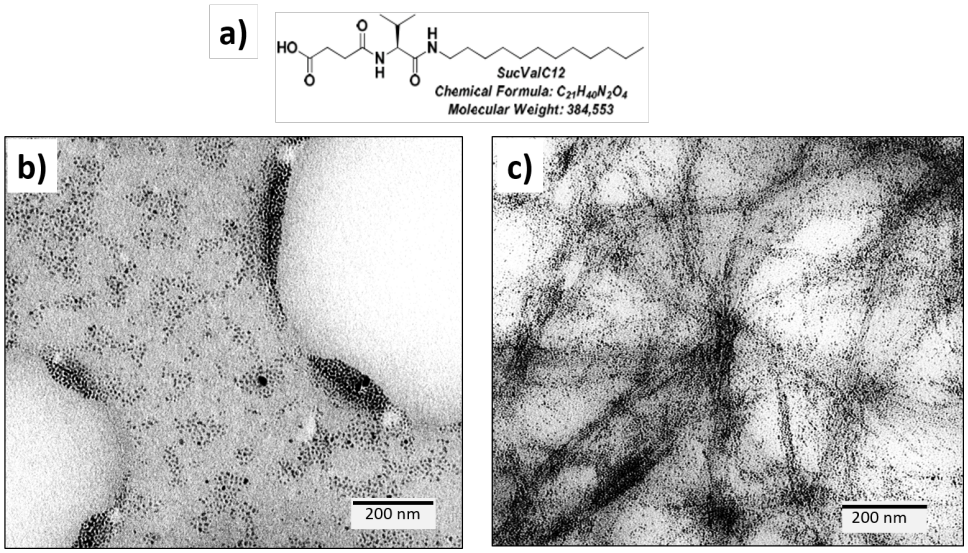

Figure 5.24: a) Molecular structure of SucValDoc an inert organogel. b) Transmission electron microscopy (TEM) image of dilute solution of PbS quantum dots in toluene drop casted onto holey carbon TEM grids and c) TEM image of dilute mixture of SucValDoc organogel and PbS quantum dots showing the embedding of QDs into organogel matrix forming fibrilic structures.

In Figure 5.24a we show an image of PbS CQDs drop casted onto holey-carbon TEM grids. These are special type of TEM films which allow the solvents to escape from the holes in the TEM grid in order to prevent solvent stains and thick films. As can be seen in the CQD covered regions of Figure 5.24a CQDs are well dispersed and isolated. In Figure 5.24b we see the fibrous structure of the organogels also captured on holey-carbon TEM grids. This image clearly shows CQDs embedded in the fibrous structures and empty regions outside the fibrous region indicating complete embedding of CQDs in the gels. However TEM alone was not enough to clearly identify what happens at the

nucleation points or intersections in these fibrous films. It was thus difficult to confirm if the overlapping of various fibrous trails caused CQD aggregation at nucleation points or not. Hence we used scanning transmission electron microscopy (STEM) to get a deeper insight. The scanning electron microscope (SEM) image shown in Figure 5.25a shows

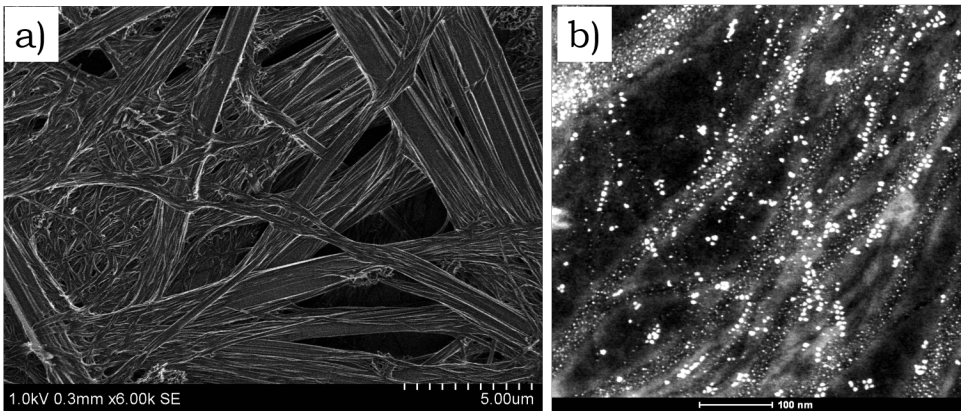

Figure 5.25: a) Scanning electron microscopy (SEM) image with a scale of 5 µm and b) scanning transmission electron microscopy (STEM) image with a scale of 100 nm of solid films prepared with PbS quantum dots suspended in SucValDoc organogel matrix.

the complex fibrous structure of the organogel when deposited on a standard silicon or glass substrate. We dispersed CQDs in organogels as described for the TEM image above and captured an image using scanning tranmission electron microscopy (STEM). Figure 5.25b shows how well the CQDs disperse in organogel fibers also confirming no CQD aggregation at nucleation points. SucValDoc organogel used here is an inert gel however, it is a promising way of suspending CQDs in semi-solid films. Our work thus paves way for using active singlet fission materials in such gel matrices along with CQDs to obtain desired blends of donor SF materials and acceptor CQDs.

Bibliography

1. Merrifield, R., Avakian, P. & Groff, R. Fission of singlet excitons into pairs of triplet excitons in tetracene crystals. *Chemical Physics Letters* **3,** 386–388 (1969).

2. Semonin, O. E. Multiple Exciton Generation in Quantum Dot Solar Cells. *SPIE Newsroom* (2012).

3. Shockley, W. & Queisser, H. J. Detailed balance limit of efficiency of p-n junction solar cells. *Journal of Applied Physics* **32,** 510–519 (1961).

4. Walker, B. J., Musser, A. J., Beljonne, D. & Friend, R. H. Singlet exciton fission in solution. *Nature Chemistry* **5,** 1019 (2013).

5. Zimmerman, P. M., Zhang, Z. & Musgrave, C. B. Singlet fission in pentacene through multi-exciton quantum states. *Nature Chemistry* **2,** 648 (2010).

6. Congreve, D. N., Lee, J., Thompson, N. J., Hontz, E., Yost, S. R., Reusswig, P. D., Bahlke, M. E., Reineke, S., Van Voorhis, T. & Baldo, M. A. External quantum efficiency above 100% in a singlet-exciton-fission–based organic photovoltaic cell. *Science* **340,** 334–337 (2013).

7. Xia, J., Sanders, S. N., Cheng, W., Low, J. Z., Liu, J., Campos, L. M. & Sun, T. Singlet fission: Progress and prospects in solar cells. *Advanced Materials* **29,** 1601652 (2017).

8. Tabachnyk, M., Ehrler, B., Bayliss, S., Friend, R. H. & Greenham, N. C. Triplet diffusion in singlet exciton fission sensitized pentacene solar cells. *Applied Physics Letters* **103,** 190_1 (2013).

9. Ehrler, B., Walker, B. J., Böhm, M. L., Wilson, M. W., Vaynzof, Y., Friend, R. H. & Greenham, N. C. In situ measurement of exciton energy in hybrid singlet-fission solar cells. *Nature Communications* **3,** 1019 (2012).

10. Yang, L., Tabachnyk, M., Bayliss, S. L., Böhm, M. L., Broch, K., Greenham, N. C., Friend, R. H. & Ehrler, B. Solution-processable singlet fission photovoltaic devices. *Nano Letters* **15,** 354–358 (2014).

11. Anthony, J. E., Brooks, J. S., Eaton, D. L. & Parkin, S. R. Functionalized pentacene: improved electronic properties from control of solid-state order. *Journal of the American Chemical Society* **123,** 9482–9483 (2001).

12. Giri, G., Verploegen, E., Mannsfeld, S. C., Atahan-Evrenk, S., Kim, D. H., Lee, S. Y., Becerril, H. A., Aspuru-Guzik, A., Toney, M. F. & Bao, Z. Tuning charge transport in solution-sheared organic semiconductors using lattice strain. *Nature* **480,** 504 (2011).

13. Tabachnyk, M., Karani, A. H., Broch, K., Pazos-Outón, L. M., Xiao, J., Jellicoe, T. C., Novák, J., Harkin, D., Pearson, A. J., Rao, A. *et al.* Efficient singlet exciton fission in pentacene prepared from a soluble precursor. *APL Materials* **4,** 116112 (2016).

14. Smith, M. B. & Michl, J. Singlet fission. *Chemical Reviews* **110,** 6891–6936 (2010).

15. Pazos-Outon, L. M., Lee, J. M., Futscher, M. H., Kirch, A., Tabachnyk, M., Friend, R. H. & Ehrler, B. A Silicon–Singlet Fission Tandem Solar Cell Exceeding 100% External Quantum Efficiency with High Spectral Stability. *ACS Energy Letters* **2,** 476–480 (2017).

16. Tabachnyk, M., Ehrler, B., Gélinas, S., Böhm, M. L., Walker, B. J., Musselman, K. P., Greenham, N. C., Friend, R. H. & Rao, A. Resonant energy transfer of triplet excitons from pentacene to PbSe nanocrystals. *Nature Materials* **13,** 1033–1038 (2014).

17. Afzali, A., Dimitrakopoulos, C. D. & Breen, T. L. High-performance, solution-processed organic thin film transistors from a novel pentacene precursor. *Journal of the American Chemical Society* **124,** 8812–8813 (2002).

18. Shaw, J. E., Stavrinou, P. N. & Anthopoulos, T. D. On-Demand Patterning of Nanostructured Pentacene Transistors by Scanning Thermal Lithography. *Advanced Materials* **25,** 552–558 (2013).

19. Shimanouchi, T. Tables of molecular vibrational frequencies. Consolidated volume II. *Journal of Physical and Chemical Reference Data* **6,** 993–1102 (1977).

20. Kim, S. H., Yoon, W. M., Jang, M., Yang, H., Park, J.-J. & Park, C. E. Damage-free hybrid encapsulation of organic field-effect transistors to reduce environmental instability. *Journal of Materials Chemistry* **22,** 7731–7738 (2012).

21. Faltermeier, D., Gompf, B., Dressel, M., Tripathi, A. K. & Pflaum, J. Optical properties of pentacene thin films and single crystals. *Physical Review B* **74,** 125416 (2006).

22. Pearson, A. J., Eperon, G. E., Hopkinson, P. E., Habisreutinger, S. N., Wang, J. T.-W., Snaith, H. J. & Greenham, N. C. Oxygen Degradation in Mesoporous $Al_2O_3/CH_3NH_3PbI_3$-xCl_x Perovskite Solar Cells: Kinetics and Mechanisms. *Advanced Energy Materials* **6,** 1600014 (2016).

23. Li, Z., Wang, W., Greenham, N. C. & McNeill, C. R. Influence of nanoparticle shape on charge transport and recombination in polymer/nanocrystal solar cells. *Physical Chemistry Chemical Physics* **16,** 25684–25693 (2014).

24. Tremolet de Villers, B. J., MacKenzie, R. C., Jasieniak, J. J., Treat, N. D. & Chabinyc, M. L. Linking Vertical Bulk-Heterojunction Composition and Transient Photocurrent Dynamics in Organic Solar Cells with Solution-Processed MoOx Contact Layers. *Advanced Energy Materials* **4,** 1301290 (2014).

Chapter 6

Role of triplet-pair states in highly efficient singlet-fission molecule tips-pentacene

6.1 Introduction

Having studied tandem solar cells and singlet fission solar cells we now study triplet-triplet annihilation (TTA) or triplet-fusion which is another important strategy to improve the power conversion efficiencies of photovoltaics. As mentioned in Chapter 2, triplet-triplet annihilation or triplet fusion is a well-studied concept that helps harvest the otherwise unabsorbed sub-bandgap photons in solar cells. In Section 4.2 we saw that the Shockley-Queisser model assumes that only photons with energy $E_{photon} \geq E_g$ generate an electron-hole pair for charge generation in a photovoltaic cell, E_g being the semiconductor bandgap. TTA allows for relaxing this assumption by allowing additional charge generation in solar cells by utilising the sub-bandgap photons to surpass the S-Q limit. *Note: In this chapter we will use TTA and TF interchangeably to describe the same process described below.*

Triplet fusion (TF) is the reverse process of singlet fission (SF), whereby two triplet excitons annihilate to form a singlet exciton [1, 2]. Similar to the photon downconversion system mentioned in Section 5.1.2 with CQDs (electron-acceptors) dispersed in a SF-matrix (electron-donor), a photon upconversion (UC) system also has two components, a triplet donor (or sensitizer) and a triplet acceptor. TTA-UC as explained earlier in Section 2.1.4.3 is studied as an important strategy to enhance photovoltaic performance by absorbing sub-bandgap photons [3, 4].

In this work we will study triplet fusion using an organic light emitting diode (OLED) as an alternative system that can exhibit TTA-UC. In OLEDs, both singlet and triplet excitons can be generated via electrical excitation unlike the optical TTA-UC systems. The electrons and holes injected in an OLED can recombine to form either spin-singlet

or spin-triplet excitons with a probability of 25 % or 75 % respectively. Thus, without the need of a triplet sensitizer, OLEDs can be used to generate triplet and singlet excitons simultaneously. In an OLED demonstrating efficient TTA, electrically generated triplet excitons annihilate to form singlet excitons which consequently emit photons to contribute to the device electroluminescence (see Figure 6.1). This process generates delayed emission which can be easily detected by studying the time-dependent electroluminescence to observe the contribution from TTA to emission [5–7]. The TTA process also allows for enhancing the OLED performance by harvesting the dark triplets [5, 8, 9].

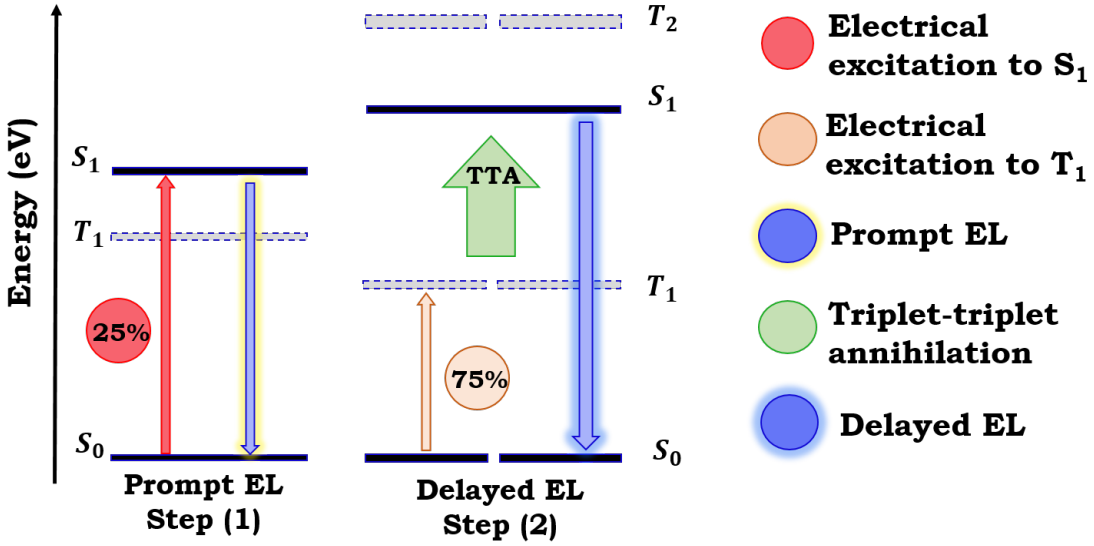

Figure 6.1: Schematic diagram illustrating the triplet-triplet annihilation process contributing to electroluminescence from OLEDs.

As discussed earlier in Chapter 5, the net spin of the two triplets generated from SF is zero. Singlet fission conserves spin and thus can be a faster means to generate triplets than inter-system crossing in organic molecules [10]. Similarly for triplet-triplet annihilation to successfully generate a singlet, their net spin should be zero [1, 2]. As both TTA and SF are spin-dependent processes, studying the effect of an external magnetic field on electroluminescence (EL) from OLEDs provides a useful tool to gain insight into the occurrence of the two processes. Applying an external magnetic field increases the spin mixing between the singlet and quintet triplet-pair states at low fields ($< 100\,\mathrm{mT}$) whereas at high fields ($> 100\,\mathrm{mT}$) the Zeeman splitting between these states reduces the spin mixing. Thus at magnetic fields $< 100\,\mathrm{mT}$ the EL yield is reduced as the bright and dark pair-states are mixed whereas at fields $> 100\,\mathrm{mT}$ the EL yield is enhanced as there are fewer states with singlet character at high fields. In the case where TTA is

dominant and energetically favoured process, we expect an increase in EL at low fields due to increased mixing between the dark and bright pair-states followed by a decrease at high fields (see Section 6.4.2).

Triisopropylsilyethynyl-pentacene (TIPS-pc) demonstrates $\approx 200\,\%$ efficient singlet fission in solutions [11]. In TIPS-pc, singlet fission is understood to proceed via an intermediate triplet-pair state whose energy (E_{TT}) is approximately equal to that of two triplets ($2E_T$) [12]. Singlet fission is exothermic and occurs on sub-picosecond timescales in TIPS-pc. Therefore it is the dominant process in TIPS-pc, outcompeting intersystem crossing and radiative decay. Recently however, Di et al. reported significant contributions from TTA (38 %) to the EL from OLEDs where TIPS-pc was employed as the emitting (guest) molecule dispersed in a PVK (host) matrix [5]. One of the important criteria for observing TTA in such OLEDs is that the singlet and triplet energies of the guest molecule must satisfy the condition $E_S \lesssim 2(E_T)$ such that the two annihilating triplets have enough energy to form a singlet exciton. TIPS-pc has a singlet energy $E_S = 1.83\,\text{eV}$ and deep-lying triplet states whose energy is identified by experiments and calculations to be $\approx 0.85\,\text{eV}$-$1.0\,\text{eV}$ [12–14] (see Figure 6.3.a). Although singlet fission has been shown to be exergonic in solid-state pentacene films [15, 16], observation of delayed EL in PVK/TIPS-pc LEDs indicates that perhaps in certain molecular geometries TTA can indeed occur. The balance between SF and TTA is thus dependent on the constrained morphologies found in composite OLED structures. Furthermore, this makes the role of the triplet-pair intermediate state unclear in terms of its participation in SF and TTA simultaneously, as successful dissociation of the triplet pair into individual triplets will enhance the SF efficiency whereas reforming of singlets from the triplet pair will enhance the TTA efficiency.

The existence of an intermediate triplet-pair state during the conversion of singlet excitons into triplet excitons is well accepted within the community although its role in assisting singlet fission or triplet fusion remains uncertain [17, 18]. In this study we use TIPS-pc/PVK LEDs as a model system to understand the role of an intermediate triplet-pair state in assisting interconversion between singlet and triplet excitons. LEDs provide a unique set-up to directly generate both the singlet and triplet excitons via electrical excitation, which is not achievable by optical excitation alone. We vary the concentration of TIPS-pc in PVK and use magnetoelectroluminescence (MEL) as a tool to identify the dominant mechanism (SF or TTA) in these OLEDs. By modelling the

magnetic field effects using a kinetic scheme incorporating SF and TTA, we find that a higher concentration of TIPS-pentacene molecules increases the rate of forming singlets from the triplet-pair state relative to the rate of dissociation of the triplet-pair via other pathways. However, unfavourable uphill energetics for triplet-pair to singlet conversion prevents TTA from becoming the dominant process in these OLEDs. This inefficiency is expected considering the energy cost for the uphill process of 0.11 eV between the triplet pair E_{TT} and the singlet E_{S_1} states. Thus, our work provides a unique model that can be used to probe the dominant process in OLEDs where SF and TTA are both likely and understand the role of the intermediate pair state in the interconversion between these two states. Understanding the dominant process can provide further information about the molecular geometries of dopant molecules in host/guest OLEDs and help design optimal architectures to maximize the gain from TTA.

6.2 Background

In this section we describe the background theory required to understand the magnetic dependence of electroluminescence in our OLEDs. We describe each of the different terms present in a spin Hamiltonian which is used later in the chapter to model the magneto-electroluminescnce (MEL) from our OLEDs. We also detail the Merrifield theory [19] used to model the underlying singlet-fission and triplet-triplet annihilation processes to understand the MEL.

6.2.1 Spin Hamiltonian

The total energy of a system is defined in quantum mechanics using a Hamiltonian ($\hat{H}$) which gives the sum of the kinetic and potential energy of the system as in Newtonian mechanics [20]. In many-body systems discussed in Section 2 with weak spin-orbit coupling, the state wavefunction can be split into separate spatial and spin parts associated with the orbital-specific and spin-specific Hamiltonians. The action of spin Hamiltonian on the spin part of the wavefunction of a particular state gives information about the how the spin of the system evolves. As the parameters of the spin Hamiltonian are related to the spatial wavefunctions and the local molecular environment, understanding these parameters can give detailed insight into the excited states. In this section we will discuss various interactions (see Figure 6.2) present in a system and the effect on the energy levels

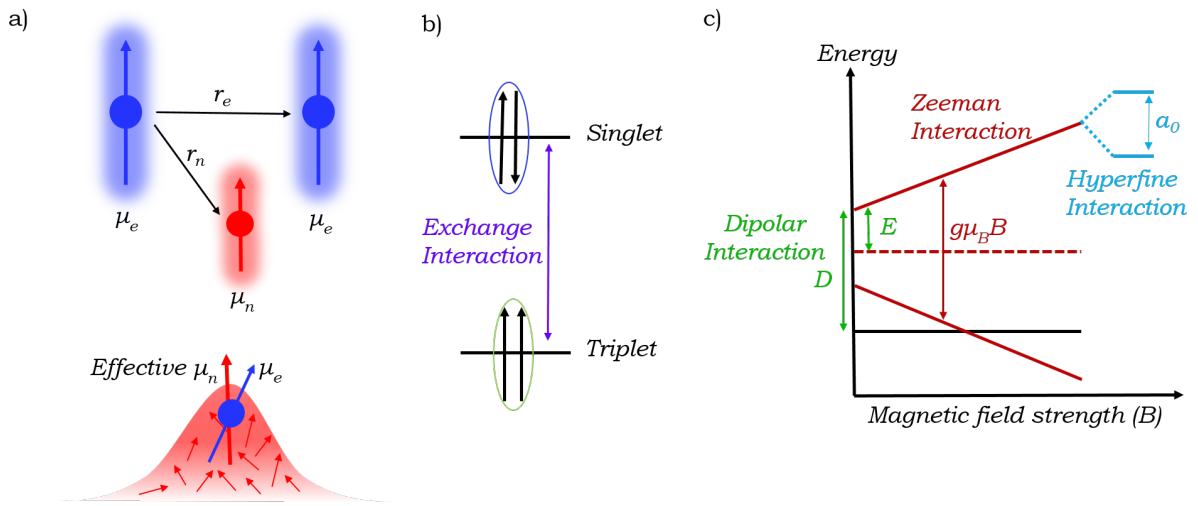

Figure 6.2: a) Spin interactions between a coupled electron-hole pair dipole moment and nuclear spin. b) Splitting of energy levels due to exchange interactions between the electrons forming separate singlet and triplet manifolds. c) Spin interactions within the triplet manifold demonstrating: (i) the splitting of spin sub-levels at zero magnetic field by D and E due to dipolar interactions between two electron spins; (ii) Energy level splitting due to spin interaction with an external magnetic field; (iii) Hyperfine interactions with nuclei in close vicinity.

of the system based on these interactions which are relevant to this study. We discuss each of these interactions thus explaining the components of a full spin Hamiltonian used to describe a many-body system.

6.2.1.1 Hyperfine interactions

As shown in Figure 6.2a, in a molecule, the electronic spins interact with nuclei contributing up to $\approx 1\,\mathrm{mT}$ local fields. This interaction, termed the *hyperfine interaction*, can be split into an isotropic *contact* term $\hat{H}_{hf}^{contact}$ and an anisotropic *dipolar* term $\hat{H}_{hf}^{dipolar}$. The isotropic $\hat{H}_{hf}^{contact}$ is dominated by the nuclei located directly on the molecular subunit containing the electronic spin density; the anisotropic $\hat{H}_{hf}^{dipolar}$ term represents the electron-nuclei dipole-dipole interaction (see Figure 6.2a) between electronic spin interaction with various nuclei present in the molecule. Each of these two components of the hyperfine Hamiltonian are defined as

$$\hat{H}_{hf}^{contact} = a_0 \cdot \hat{S} \cdot \hat{I}\,, \tag{6.1}$$

where a_0 is the contact coupling strength, $\hat{S}$ is the electronic spin operator and $\hat{I}$ is an identity operator; and

$$\hat{H}_{hf}^{dipolar} = a \cdot \left(\frac{\hat{S} \cdot \hat{I}}{r_n^3} - 3 \cdot \frac{(\hat{S} \cdot \hat{r_n})(\hat{I} \cdot \hat{r_n})}{r_n^5} \right), \tag{6.2}$$

where $a = \frac{\mu_0}{4\pi} \cdot g_e \mu_B g_N \mu_N$ with g_e and g_N being the electronic and nuclear g-factors respectively. $\mu_B = e\hbar/2m_e$, $\mu_N = e\hbar/2m_p$ are the electron and nuclear magnetons respectively for e the electron charge, m_e the rest mass of an electron, m_p the rest mass of a proton and $\hbar$ the reduced Planck constant [21]. μ_0 is the permeability of the vacuum and $\hat{r_n}$ is the inter-spin vector with $|\hat{r_n}| = r_n$ [21]. The total hyperfine term is given by

$$\hat{H}_{hf} = \hat{S} \cdot A \cdot \hat{I}\,. \tag{6.3}$$

In general, the hyperfine interactions that are caused by the electronic spin interacting with a bath of nuclear spin as illustrated in Figure 6.2a broaden the electronic spin-energy by $\approx 1\,\mathrm{mT}$ providing a source of spin-mixing in charge-transfer states for organic semiconductors [22, 23].

6.2.1.2 Electron-electron interactions

In addition to interactions with the nuclei, the electron spins also interact with other nearby electrons. Due to the localised nature of excitons in organic molecules, these interactions become very important. Similar to the *hyperfine* interactions, the electron-electron interactions can also be split into an isotropic component, defined as the *exchange* interaction ($\hat{H}_{exchange}$) and an anisotropic component defined as the *dipolar* interaction. The two components take the same form as $\hat{H}_{hf}^{contact}$ and $\hat{H}_{hf}^{dipolar}$ respectively but this time arising from particle statistics explained in Section 2.1.2. As explained earlier in Section 2.1 the difference in symmetry between the spatial wavefunctions of spin-singlet ($\hat{S} = 0$) and spin-triplet states ($\hat{S} = 1$) causes energy splitting between these two levels. This energy level splitting caused by the difference in spin multiplicity of the two states can be included in the Hamiltonian as

$$\hat{H}_{exchange} = -J(\hat{S}_1.\hat{S}_2) \tag{6.4}$$

$$= -J\left(\frac{1}{2}S_{total}(S_{total}+1) - \frac{3}{4}\right) \tag{6.5}$$

$$= \begin{cases} \frac{3}{4}J & \text{if } S_{total} = 0 \\ -\frac{1}{4}J & \text{if } S_{total} = 1 \end{cases}, \tag{6.6}$$

where $\hat{S}_1 = \hat{S}_2 = \frac{1}{2}$, S_{total} is the sum of the individual spins of the two electrons and $J = 2K$ from the exchange integral defined in eq. (2.20) for the exchange interaction between two electrons in the HOMO and LUMO (see Section 2.1.2 for details). In the limit where the exchange interaction is much weaker (*i.e.* J is much smaller) than other interactions, the $\hat{H}_{exchange}$ causes an offset in the energy level splitting of the two electrons which is proportional to J. On the other hand if J is much larger, then the two electron spins couple to form either a singlet or a triplet exciton as the $S = 0$ and $S = 1$ are effectively isolated as shown in Figure 6.2b.

6.2.1.3 Zeeman interaction

The extent to which a spin interacts with a local magnetic field (either from the neighbouring nuclei and electrons or laboratory scale magnets) depends on the magnetic moment. For a system with spin $\hat{S}$ the magnetic moment is defined as

$$\hat{\mu} = -g\mu_B\hat{S}\,, \tag{6.7}$$

where $\mu_B = e\hbar/2m_e$ is the Bohr magneton defined earlier. The interaction of an external magnetic field $\hat{B}$ with this system with spin $\hat{S}$ is defined by $-\hat{B}\cdot\hat{\mu}$. The contribution from this interaction, known as the Zeeman interaction, to the Hamiltonian can then be written as

$$\hat{H_Z} = \hat{B}\cdot g\mu_B\hat{S} = g\mu_B\hat{B}\cdot\hat{S}\,. \tag{6.8}$$

As shown in Figure 6.2c, this corresponds to an energy splitting of the form

$$|\Delta E| = g\mu_B B\,, \tag{6.9}$$

and a change in the spin projection quantum number $|\Delta m_S| = 1$, where B is the magnitude of the applied magnetic field.

6.2.1.4 Zero-field splitting

Considering that the singlet excitons have a net spin of zero, they have no magnetic moment whereas triplet excitons have a net spin of one and thus have an associated magnetic moment. The three triplet states can be written in the total spin and product

basis as

$$|\tau_{\pm}\rangle = \left|\pm\frac{1}{2}, \pm\frac{1}{2}\right\rangle \tag{6.10}$$

$$|\tau_0\rangle = \sqrt{\frac{1}{2}}\left(\left|+\frac{1}{2}, -\frac{1}{2}\right\rangle + \left|-\frac{1}{2}, +\frac{1}{2}\right\rangle\right) \tag{6.11}$$

where $|s, m_s\rangle$ are the eigenstates of the spin operator in z-direction $\hat{S}_z$ with s the individual electron spin quantum number and m_s the corresponding spin projection quantum number for each electron, and $|\tau\rangle$ define the eigenstates of the total spin operator $\hat{S}^2$ of the coupled spin of the two electrons in the triplet state. The total spin operator $\hat{S}$ for $S = 1$ is defined via the spin matrices as

$$\hat{S} = \begin{bmatrix} \hat{S}_x \\ \hat{S}_y \\ \hat{S}_z \end{bmatrix} \tag{6.12}$$

$$\hat{S}_x = \frac{1}{\sqrt{2}}\begin{bmatrix} 0 & 1 & 0 \\ 1 & 0 & 1 \\ 0 & 1 & 0 \end{bmatrix}; \hat{S}_y = \frac{1}{\sqrt{2}i}\begin{bmatrix} 0 & -1 & 0 \\ 1 & 0 & -1 \\ 0 & 1 & 0 \end{bmatrix}; \hat{S}_z = \begin{bmatrix} 1 & 0 & 0 \\ 0 & 0 & 0 \\ 0 & 0 & -1 \end{bmatrix}. \tag{6.13}$$

The dipole-dipole interactions between the two electrons in a triplet state give rise to non-degenerate triplet energy levels in the absence of an external magnetic field, known as the zero-field splitting. The zero-field splitting Hamiltonian due to these dipolar interactions between the three triplet sublevels (eq. (6.10)) is given by

$$\hat{H}_{zfs}(\hat{r}) = \frac{\mu_0}{4\pi}\left[\frac{\mu_1 \cdot \mu_2}{r^3} - \frac{3(\mu_1 \cdot \hat{r})(\mu_2 \cdot \hat{r})}{r^5}\right], \tag{6.14}$$

where μ_1 and μ_2 are the magnetic moments of the two electrons in the triplet state and the $\hat{r}$ is the vector between the two electrons with magnitude r. Using the definition of the magnetic dipole moment we can write the zero-field splitting Hamiltonian as $\hat{H}_{zfs} = \hat{S}.\boldsymbol{D}.\hat{S}$ where the $\boldsymbol{D}$ tensor has eigenvalues D_x, D_y, D_z such that

$$\hat{H}_{zfs} = D_x\hat{S}_x^2 + D_y\hat{S}_y^2 + D_z\hat{S}_z^2\,. \tag{6.15}$$

The $\boldsymbol{D}$ tensor is generally chosen to be traceless and symmetric such that

$$\hat{H}_{zfs} = D\left[\hat{S}_z^2 - \frac{1}{3}S(S+1)\right] + E(\hat{S}_x^2 - \hat{S}_y^2)\,, \tag{6.16}$$

where $D = \frac{3}{2}D_z$ and $E = \frac{1}{2}(D_x - D_y)$.

6.2.2 Triplet pair states

As mentioned earlier, both SF and TTA are expected to proceed via an intermediate triplet-pair state and thus we will now discuss the spin and energy eigenstates of triplet-pairs. Considering the last energy splitting between the singlet and triplet manifold, we can restrict 16 four-electron states to those that represent the ones composed of two triplets. We thus have 9 triplet-pair states consisting of: (i) one singlet state $|S\rangle$, where the total spin of the triplet-pair is 0; (ii) three triplet states $|T_i\rangle$, where the total spin of the triplet pair is 1; (iii) and five quintet states $|Q_i\rangle$, where the total spin of the triplet pair is 2. Therefore we can write the eigenstates of the total spin $\hat{S}^2 = (\hat{S}_A + \hat{S}_B)^2$ for the triplet pair composed of the coupled triplet A and triplet B, with spin projection along the z-axis $\hat{S}_z = (\hat{S}_{a,z} + \hat{S}_{b,z})$ as [19]:

$$|S_0\rangle = \sqrt{\frac{1}{3}}(|00\rangle - |-+\rangle - |+-\rangle) \tag{6.17}$$

$$|T_0\rangle = \sqrt{\frac{1}{2}}(|+-\rangle - |-+\rangle) \tag{6.18}$$

$$|T_{+1}\rangle = \sqrt{\frac{1}{2}}(|+0\rangle - |0+\rangle) \tag{6.19}$$

$$|T_{-1}\rangle = \sqrt{\frac{1}{2}}(|-0\rangle - |0-\rangle) \tag{6.20}$$

$$|Q_0\rangle = \sqrt{\frac{1}{6}}(2\,|00\rangle + |+-\rangle + |-+\rangle) \tag{6.21}$$

$$|Q_{+1}\rangle = \sqrt{\frac{1}{2}}(|+0\rangle + |0+\rangle) \tag{6.22}$$

$$|Q_{-1}\rangle = \sqrt{\frac{1}{2}}(|-0\rangle + |0-\rangle) \tag{6.23}$$

$$|Q_{+2}\rangle = |++\rangle \tag{6.24}$$

$$|Q_{-2}\rangle = |--\rangle \tag{6.25}$$

where the subscript defines the spin projection quantum number for each state. As we can see from the above state equations the quintet states are fully symmetric with respect to any electron exchange. The triplet states however are anti-symmetric with respect to two-electron (exciton) exchange and the singlet state is symmetric with respect to exciton exchange but anti-symmetric with respect to single-electron exchange. This distinct symmetry under particle exchange thus separates these singlet, triplet and quintet pair-states into different manifolds.

6.2.3 Merrifield theory

Merrifield theory has been used extensively in literature to describe triplet-triplet annihilation [1, 19, 24, 25], singlet fission [10, 26, 27] and triplet-polaron quenching [28]. Due to the zero-field splitting of triplet excitons explained in Section 6.2.1.4, the magnetic field causes the singlet character of the triplet-pair states defined as $|\langle S|P_i\rangle|^2$ to evolve with change in the magnetic field. In this section we will briefly review the TTA kinetic scheme using the Merrifield theory. The following is a simplified kinetic scheme to describe the TTA mechanism:

$$\begin{array}{ccccc} & & S_1 + S_0 & & \\ & & \uparrow{\scriptstyle k_S|S_i|^2} & & \\ T + T & \underset{k_{-1}}{\overset{g_i T}{\rightleftharpoons}} & \{P_i\} & \xrightarrow{k_T|T_i|^2} & T + S_0 \\ & & \downarrow{\scriptstyle k_Q|Q_i|^2} & & \\ & & Q + S_0 & & \end{array} \tag{6.26}$$

where $T + T$ defines the triplet-triplet annihilation, P_i are the nine possible intermediate triplet-pair states, $S_1 + S_0$, $T + S_0$, $Q + S_0$ are the singlet, triplet and quintet states that can be generated from TTA with rates k_S, k_T and k_Q respectively. For a triplet-pair wavefunction defined by $|\Psi_i\rangle$, $|S_i|^2 = |\langle\psi_i|S\rangle|^2$, $|T_i|^2 = \sum_{m=1}^{3} |\langle\psi_i|T_m\rangle|^2$ and $|Q_i|^2 = \sum_{m=1}^{5} |\langle\psi_i|Q_m\rangle|^2$ define the probability of forming each of the singlet, triplet and quintet excitons as a result of TTA such that $\sum_n |S_i|^2$=1; $\sum_n |T_i|^2$=3 and $\sum_n |Q_i|^2$=5. Finally, g_i describes the rate of triplet-pair generation from free triplets and k_{-1} describes the rate of its reverse process.

From the above kinetic scheme, we can write a rate equation for the intermediate triplet-pair state in terms of triplet population $[T]$ as

$$\frac{\partial P_i}{\partial t} = g_i[T]^2 - (k_{-1} + k_S|S_i|^2 + k_T|T_i|^2 + k_Q|Q_i|^2)P_i\,. \tag{6.27}$$

Assuming that (i) all of the 9 triplet-pair states are generated with equal probability, *i.e.* $g_i = \frac{1}{9}k_1$ and (ii) quintet states lie too high in energy to be formed by TTA, *i.e.* $k_Q = 0$ we can write the steady state population $\frac{\partial P_i}{\partial t} = 0$ as

$$P_i = \frac{1}{9}k_1[T]^2 \frac{1}{(k_{-1} + k_S|S_i|^2 + k_T|T_i|^2 + k_Q|Q_i|^2)}\,, \tag{6.28}$$

$$P_i = \frac{1}{9} k_1 [T]^2 \frac{1}{(k_{-1} + k_S |S_i|^2 + k_T |T_i|^2)} \,. \tag{6.29}$$

Defining the total TTA rate through the singlet channel as γ_{TTA}, we can write it as

$$\gamma_{TTA}[T]^2 = \sum_i k_S |S_i|^2 P_i \,. \tag{6.30}$$

Substituting eq. (6.29) for P_i in the above, we get

$$\gamma_{TTA}[T]^2 = \sum_i k_S |S_i|^2 \left(\frac{1}{9} k_1 [T]^2 \frac{1}{(k_{-1} + k_S |S_i|^2 + k_T |T_i|^2)} \right) , \tag{6.31}$$

$$\therefore \gamma_{TTA} = \sum_i k_S |S_i|^2 \left(\frac{1}{9} k_1 \frac{1}{(k_{-1} + k_S |S_i|^2 + k_T |T_i|^2)} \right) . \tag{6.32}$$

To simplify this equation further, we note that no triplet-pair eigenstate can simultaneously have a singlet and a triplet character [19] as explained by the symmetry arguments in Section 6.2.2. Therefore either $|S_i|^2 = 0$ and $|T_i|^2 \neq 0$ or $|S_i|^2 \neq 0$ and $|T_i|^2 = 0$. Therefore setting $|S_i|^2 \neq 0$ we arrive at

$$\gamma_{TTA} = \frac{1}{9} k_1 \sum_i \frac{k_S |S_i|^2}{k_{-1} + k_S |S_i|^2} \,. \tag{6.33}$$

In order to find the evolution of γ_{TTA} with magnetic field, we need to use the spin Hamiltonian of the triplet-pair and understand the evolution of the triplet-pair wavefunction under its action. This means that k_T is independent of the magnetic field as the equation for γ_{TTA} is not dependent on $|T_i|^2$.

Redefining $|S_i|^2 = \alpha_i$ and defining a new parameter β for the ratio of rate of decay of the triplet-pair to individual triplets and rate of forming singlets from the triplet-pair state as $\beta = k_{-1}/k_S$, we can further simplify γ_{TTA} to

$$\gamma_{TTA} = \frac{k_1}{9} \sum_i \frac{\alpha_i}{\beta + \alpha_i} \,. \tag{6.34}$$

In order to model the effect of magnetic field on the emission from singlet state, we can further simplify the scheme to

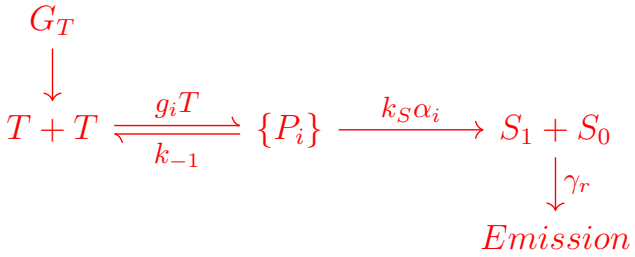

(6.35)

where G_T is a triplet generation rate, and γ_r is the radiative decay rate from the singlet

state. Thus, the steady state population for the singlet state from this scheme can be written as

$$S = \frac{1}{\gamma_r}\left(\sum_i k_S \alpha_i P_i\right) = \frac{1}{\gamma_r}\left(\underbrace{\gamma_{TTA}[T]^2}_{\sum_i k_S |S_i|^2 P_i}\right). \tag{6.36}$$

Defining emission from the singlet state as $\gamma_r S$ we can write an equation in terms of γ_{TTA} as

$$Emission = \gamma_r S = \gamma_r\left(\frac{1}{\gamma_r}(\gamma_{TTA}[T]^2)\right) \tag{6.37}$$

$$\therefore Emission = \gamma_{TTA}[T]^2, \tag{6.38}$$

therefore noting that the emission is directly proportional to γ_{TTA} and thus the magnetic field effects on the emission can be explained using the evolution of spin-dependent γ_{TTA} under the spin Hamiltonian.

6.3 Results and discussion

The light-emitting diode structure used for this study is shown in Figure 6.3. The detailed device fabrication process is explained in Section 3.3.7. Briefly, poly[(9,9-dioctylfluorenyl-2,7-diyl)-co-(4,4'-(N-(4-sec-butylphenyl)diphenylamine)] (TFB) was spin coated as a hole-transporting and electron-blocking layer on PEDOT-substrates (see Section 3.3.7) and annealed at 190 °C for 20 minutes. This step was followed by spin-coating of the active layer consisting of TIPS-pc dispersed in high-bandgap polymer matrix poly(9-vinylcarbazole) (PVK). The concentration of TIPS-pentacene in PVK was varied between 1 % to 10 % by weight to obtain detectable electroluminescence from the LEDs while obtaining a range of different concentrations to study the effect of morphology on the availability of triplet fusion and singlet fission pathways. The active layer was annealed at 100 °C for 10 minutes. Finally, we used bathophenanthroline (BPhen) as the electron-transport and hole-blocking layer which was spun from a methanol solution and annealed at 60 °C for 10 minutes. Lithium fluoride and aluminium (LiF/Al) electrodes were then deposited via thermal evaporation.

Acene molecules demonstrate efficient singlet fission and have been used to understand the intricacies of the SF mechanism in various studies [2, 11, 13, 14, 19]. In order to incorporate these molecules in solutions and films, various silyl groups are attached to acenes, 6,13-bis(triisopropylsilylethynyl) (TIPS) being the most popular side group (see

Figure 6.3a). Addition of such side groups drastically improves the solubility of these molecules in most organic solvents while providing alternative packing motifs of the core acene in solution-processed films.

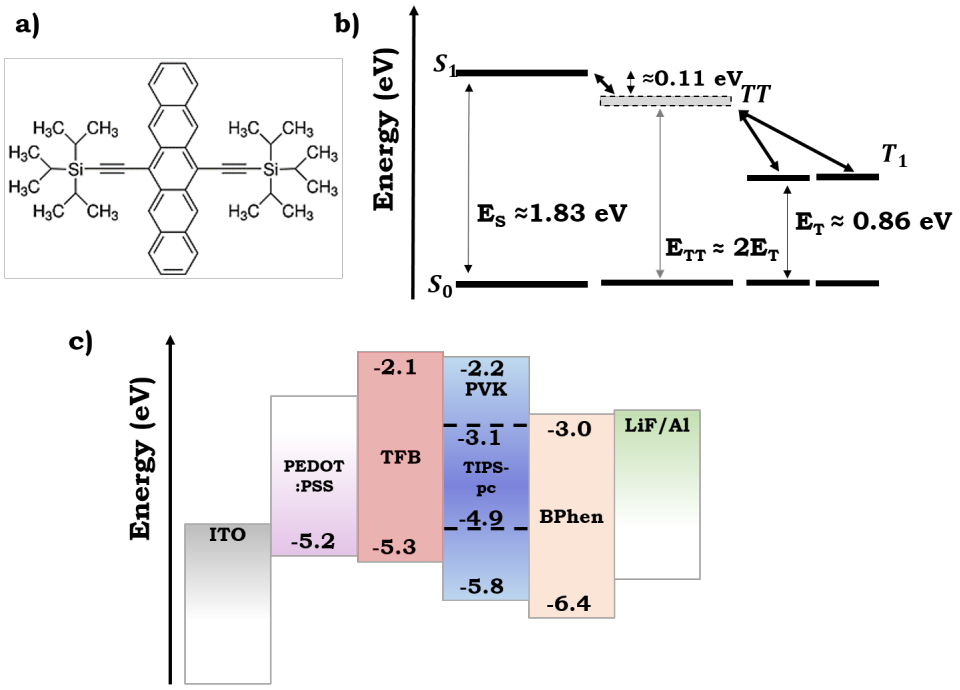

Figure 6.3: a) Molecular structure of 6,13-bis(triisopropylsilylethynyl)pentacene (TIPS-pc), the guest-molecule in OLEDs. b) Illustration of singlet and triplet level energies from literature [12, 13]. c) Energy level diagram indicating the OLED device structure with PEDOT:PSS and TFB as the hole-injecting layers, PVK/TIPS-pc as the host/guest active layer, BPhen as the electron injecting layer and LiF/Al electrodes.

The active-molecule stacking geometry significantly affects the dissociation of the triplet-pair after a singlet fission event by affecting the triplet hopping rates [29]. Therefore, we study TIPS-pentacene dispersed in a polymer matrix to allow a non-restricted and random molecular arrangement. First, to confirm TIPS-pc molecules are well dispersed and not aggregated in TIPS-pc/PVK films, we compare the absorption profiles of neat TIPS-pc (solution and thin-films [11]) with TIPS-pc/PVK thin-films. Spin-coated thin films prepared from TIPS-pc/PVK solutions, with varying TIPS-pc concentration from 0.5 % to 10 % by weight in PVK, were used for this experiment. As shown in Figure 6.4 we see that the absorption spectrum of even the most concentrated (10 % TIPS-pc in PVK) TIPS-pc/PVK film resembles that of the TIPS-pc solution (green dashed line in Figure 6.4). The red-shifted shoulder-peak at $\sim$ 700 nm clearly visible in neat TIPS-pc films (black dashed line in Figure 6.4) is not visible in any of the TIPS-pc/PVK films. Thus we can conclude that there is no significant aggregation of TIPS-pc molecules in these films.

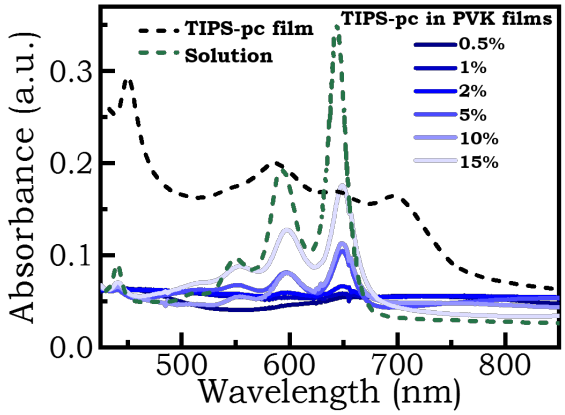

Figure 6.4: Dotted lines show data adapted from [11] showing absorption spectra for TIPS-pc dissolved in chloroform solution and that of a spun-cast film. Line-plots show TIPS-pc doped in PVK polymer matrix films with the legend indicating TIPS-pc concentration by weight in PVK.

In Figure 6.5 we show the normalised photoluminescence (PL) and EL spectra of TIPS-pc/PVK films to compare the height of the two emission peaks in these films. In saturated solutions, Walker et al. reported decreasing ratio of the height of the 680 nm emission peak relative to the 740 nm peak indicating significant reduction of emission as the solute concentration was increased [11]. No significant change in the height ratio of the 680 nm and 740 nm vibronic emission peaks in the TIPS-pc/PVK films was observed in the PL spectra shown in Figure 6.5a. However, quenching of the PL from TIPS-pc due to the presence of singlet fission is evidenced by the very low emission from high-concentration films ($> 5\,\%$ TIPS-pc conc.) as shown by the low signal-to-noise ratio in Figure 6.5a.

In Figure 6.5b we see a better signal-to-noise ratio for the EL spectra from OLEDs prepared with different concentrations of TIPS-pc in PVK. In these EL spectra normalised at the 740 nm peak, we can clearly see decreased contribution from the 680 nm peak with increasing TIPS-pc concentration in PVK. This indicates that there might be some regions present in the films where the TIPS-pc molecules are placed closer together and the singlet can delocalize over multiple molecules, thus slightly red-shifting the 680 nm peak by lowering the singlet energy. However, the concentration of these quasi-aggregated sites is very low in these films as the absorption spectra in Figure 6.4 and the PL spectra in Figure 6.5a do not show any significant aggregation features. The change in peak-height ratio for the EL spectrum (absent for the PL spectrum) also indicates that these quasi-aggregated sites are selectively populated in the OLEDs where both singlet and triplet excitons are electrically excited as opposed to the optically excited TIPS-pc/PVK

films where only singlets are excited.

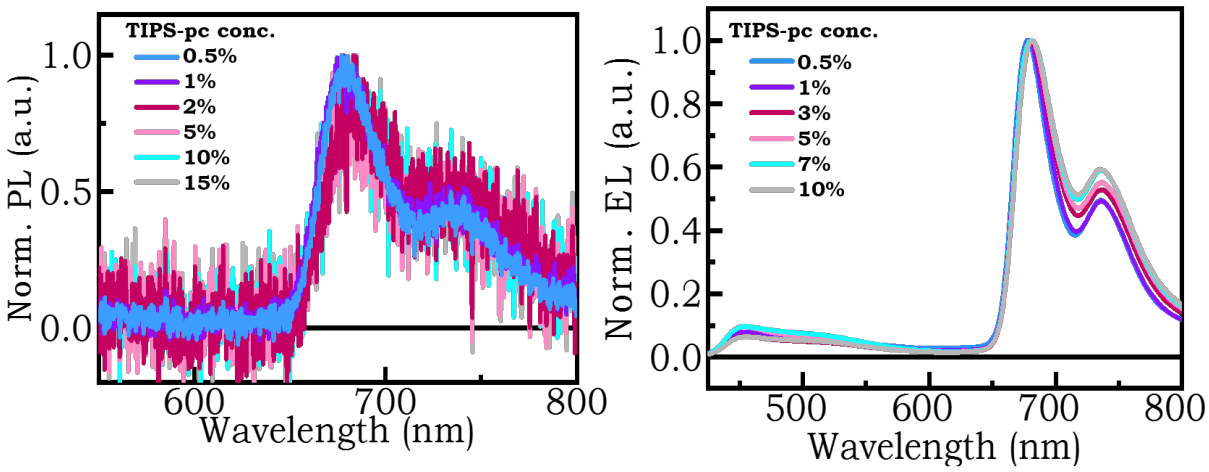

Figure 6.5: a) Photoluminescence (PL) normalised at 660 nm, from TIPS-pc doped PVK thin-films with the legend indicating concentration of TIPS-pc by weight in PVK matrix. b) Electroluminescence (EL) from TIPS-pc doped PVK LEDs with the legend indicating concentration of TIPS-pc by weight in PVK matrix.

On investigating the PL decay lifetimes in TIPS-pc/PVK films, we observed that the emission lifetimes with the lowest TIPS-pc concentration 0.1 % and 0.5 % films were 13.9 ns and 13.7 ns respectively. This is similar to the dilute solution emission lifetime of $\approx$ 13 ns observed by Walker et al. [11]. In Figure 6.6 we show the decay lifetimes of the fast process (first component of emission) for TIPS-pc/PVK films with different concentrations of TIPS-pc in PVK by weight. The scatter plots show raw TCSPC data (see 3.7.1 for experimental details) and the line-plots indicate the exponential fits. We used a single exponential decay function of the form $y = y_0 + Ae^{-t/\tau_1}$ to fit the fast-component decay lifetimes τ_1. As the concentration of TIPS-pc increases in the films τ_1 decreases and we begin to notice an additional slower decay component which indicates the presence of an additional delayed recombination pathway for the singlet excitons.

As shown in Figure 6.7, the device characteristics of TIPS-pc/PVK OLEDs indicate higher current densities and lower luminescence quantum efficiencies (EQEs) as the concentration of TIPS-pc is increased in the PVK matrix. As the concentration of TIPS-pc increases more conducting molecules become available, thus increasing the current densities in these devices at any given applied voltage. This suggests that the bandgap alignment of various layers in these OLEDs successfully make TIPS-pc molecules the recombination hub as the emission shown in Figure 6.5b is predominantly from TIPS-pc. In Figure 6.7b we can see that the number of emitted photons per charge carrier pair injected (EQE) decreases as the TIPS-pc concentration increases. This suggests signi-

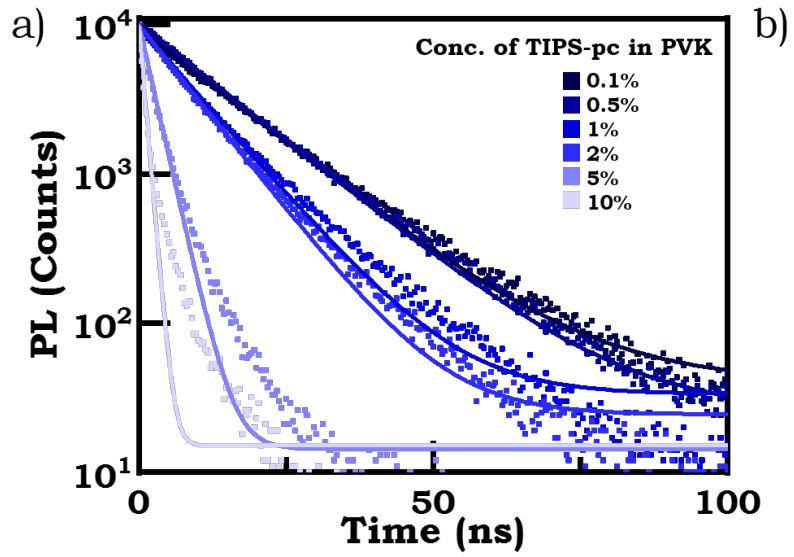

TIPS-pc conc.	t_1 (ns)	Error (±)
0.1%	13.90	0.08
0.5%	13.67	0.04
1%	9.50	0.05
2%	8.63	0.03
5%	2.47	0.02
10%	0.93	0.01

Figure 6.6: Time-correlated single photon counting data used to observe photoluminescence (PL) decay lifetimes. a) Normalised transient PL (scatter) from TIPS-pc doped PVK films fitted with exponential decay function (line-plots) of the form $y = y_0 + Ae^{-t/\tau_1}$ to get lifetimes τ_1. As the concentration of TIPS-pc increases, delayed PL contribution increases. b) Table of lifetimes fitted using single exponential decay function.

ficant exciton quenching by alternative processes present in OLEDs with high TIPS-pc concentration $\geq 5\,\%$.

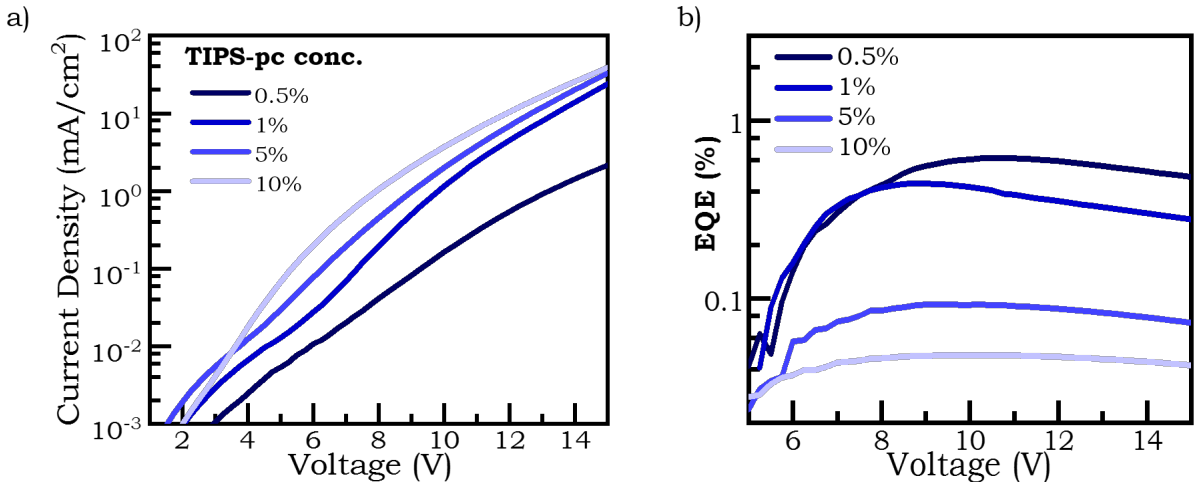

Figure 6.7: a) Current density- Voltage plot for TIPS-pc doped PVK LEDS showing J-V characteristics of LEDs with varying TIPS-pc concentration (by weight) in PVK matrix. b) External luminescence yield (EQE) of TIPS-pc doped PVK LEDs indicating significant reduction in EQE as the dopant concentration increases.

In order to detect the presence of TTA and quantify the magnitude of delayed EL (from TTA) contributing to the total EL in these OLEDs, we performed time-resolved EL measurements. Figure 6.8 shows the transient-EL profile indicating significant con-

tribution from delayed EL to the total EL (detailed measurement methods explained in Section 3.7.2) from TIPS-pc/PVK OLEDs as a function of TIPS-pc concentration. We explore if this contribution is indeed from TTA by fitting a bimolecular decay function as explained below [5].

Because TTA is a bimolecular process, the EL through TTA is directly proportional to the square of the instantaneous triplet concentration (T). Considering the kinetic scheme proposed by Wallikewitz et al. in reference [30] we can use the solution for steady state triplet population

$$T = \frac{T_0}{1 + \gamma_{TTA} T_0 t}\,, \tag{6.39}$$

where T_0 is the instantaneous triplet population at time zero and $b = \gamma_{TTA}$ is the rate of triplet-triplet annihilation. The following equation 6.40 can then be used to fit the delayed EL as also explained by Di and Yang et al. [5]

$$\frac{1}{\sqrt{EL_{delayed}}} = \frac{1}{T_0} + \gamma_{TTA} t\,. \tag{6.40}$$

Dotted lines in Figure 6.8 indicate the fit with eq. (6.40) to line-plots (raw data) for calculating the contribution from delayed EL to the total EL. The intersection of fitted lines with time zero indicates the contribution from the delayed EL to the total EL at time zero. We find that this bimolecular decay accounts for approximately 50 % of the total emission from all TIPS-pc OLEDs, with the delayed component increasing with increasing TIPS-pc concentration (see inset in Figure 6.8).

Investigating the electroluminescence spectra from these OLEDs, we find that although there is some emission from PVK initially, it decays rapidly as compared to the EL from TIPS-pc (see Figure 6.9). On increasing the TIPS-pc concentration from 0.5 % to 10 %, the PVK emission decreases even faster.

To understand the individual contribution from each of the underlying spin-dependent mechanisms, namely singlet fission and triplet fusion, responsible for the delayed EL, we measured the magnetoelectroluminescence (MEL, see Section 3.6.3 for detailed experimental setup). We define $MEL(B)$ for an applied magnetic field (B) as

$$MEL = \frac{EL(B) - EL(B=0)}{EL(B=0)}\,. \tag{6.41}$$

For these experiments we work with TIPS-pc concentrations from 1 % to 7 % in order to maintain similar current densities in the OLEDs at the given applied voltage of 14 V. These set of parameters were chosen in order to obtain measurable EL from the devices

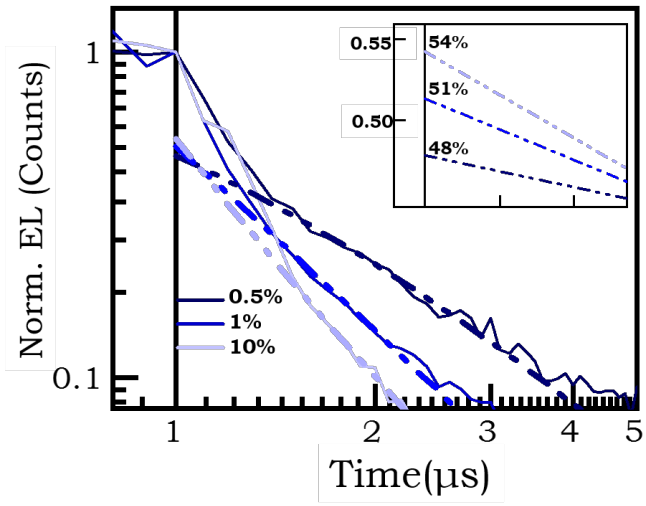

Figure 6.8: Transient electroluminescence (EL) from TIPS-pc/PVK OLEDs fitted with bimolecular decay (dotted lines) to show the contribution from delayed EL to the total EL. Inset shows increased contribution from delayed EL with increasing concentration. Current density through these devices are 0.02 mA/cm^2 for 0.5 % and 1 % LEDs and 0.5 mA/cm^2 for 10 % device at the same applied bias of 8 V positive and −4 V negative bias (see Section 3.7.2 for details).

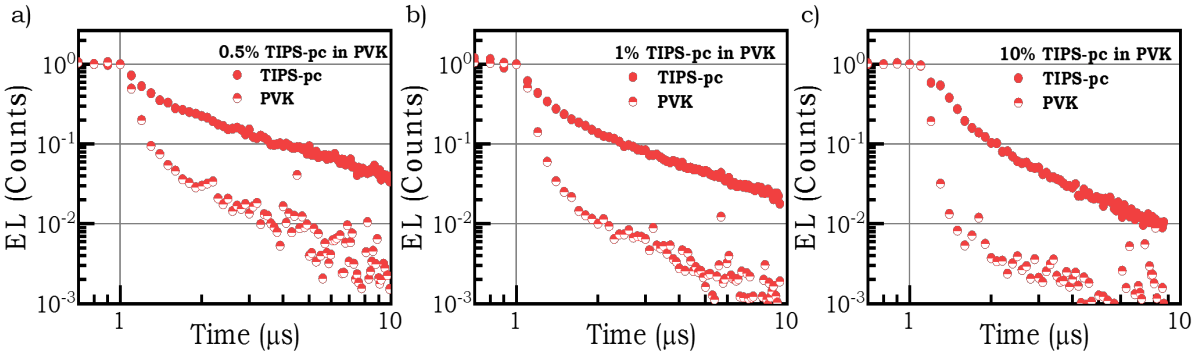

Figure 6.9: Transient electroluminescence (EL) from TIPS-pc/PVK OLEDs indicating the fast decay of PVK emission and long-lasting TIPS-pc emission for TIPS-pc doping concentrations of a) 0.5 %, b) 1 % and c) 10 %. Current densities through these devices are 0.02 mA/cm^2 for 0.5 % and 1 % OLEDs and 0.5 mA/cm^2 for the 10 % device at the same applied bias of 8 V positive and −4 V negative bias for these measurements.

while ensuring that the current densities and thus carrier concentration in each of the measured devices remain comparable. We vary the magnetic field randomly between field strengths of −300 mT to 300 mT and capture the electroluminescence spectrum to generate each of the data points by integrating the region of interest.

The line-shapes obtained from MEL are shown in Figure 6.10. The line-shape of 1 % TIPS-pc device resembles that of singlet-fission dominated effects reported in literature [6, 7, 27, 31] where the MEL is negative at low fields ($B < 60$ mT) and increases as the field strength increases beyond ~ 60 mT eventually becoming positive and saturated. We

observe that the magnitude of MEL increases with increasing concentration of TIPS-pc (see Figure 6.10) for constant applied bias of 14 V shifting the line-shapes lower (more negative) as the concentration of TIPS-pc increases in the OLEDs. We also note that the MEL line-shapes vary significantly with increasing dopant concentration. In particular, the MEL line-shapes do not show zero-crossing for higher TIPS-pc concentration however the MEL effect does not saturate either indicating zero-crossing at higher magnetic field strengths (*i.e.* $B > 300$ mT) for these devices. These results suggest two things: (i) extremely efficient (144 %) and fast (on the scale of 1 ps) singlet fission reported in TIPS-pentacene thin-films [14, 32] dominates the MEL line-shapes, (ii) increasing influence of an alternative process (potentially TTA) on the MEL line-shapes with increasing dopant concentration alters the magnetic field strength required for MEL zero-crossing.

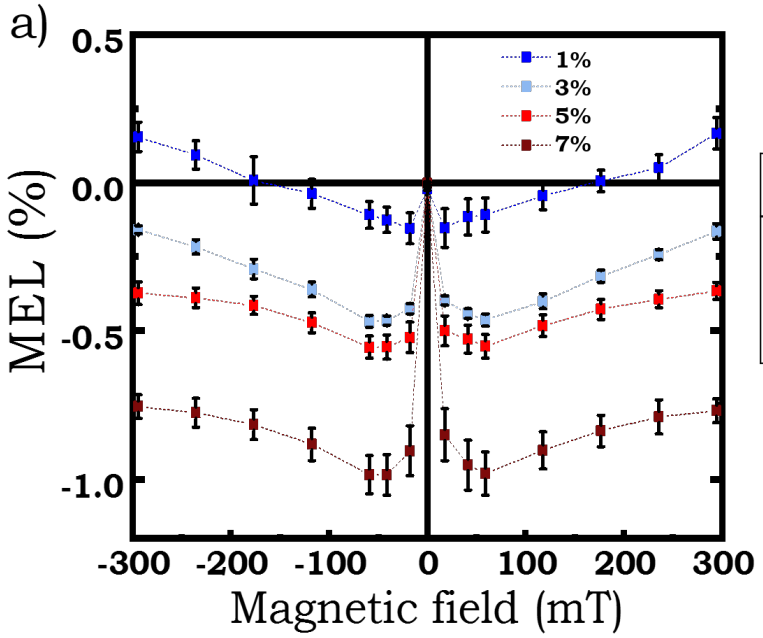

b)

Dopant conc.	Current density (mA/cm²)	EQE (%)
1%	1.2	0.50
3%	1.2	0.23
5%	1.7	0.13
7%	3.1	0.10

Figure 6.10: a) Magnetoelectroluminescence (MEL) from TIPS-pc/PVK OLEDs showing varying magnetic-field effect as the dopant concentration changes. b) Table of current densities recorded for OLEDs operating at a constant bias of 14 V and corresponding EQEs of OLEDs for these measurements.

Recall that previously in Figure 6.5.b we observed increased EL from quasi-aggregated regions with increasing TIPS-pc concentrations in these OLEDs. We separate the MEL signals from the two EL peaks in Figure 6.11. The red crosses indicate the MEL signal from the 740 nm EL peak and the squares indicate the same from 680 nm peak. We observe no significant difference between the MEL signal from the two emission regions except in the 10 % TIPS-pc device. In this device the magnitude of MEL appears to

have increased while the line-shape and sign remain identical to the MEL from 680 nm peak (see Figure 6.12). As expected, this indicates enhanced field-dependent processes (predominantly SF) in the quasi-aggregated regions as compared to the EL from isolated molecules. Note the MEL from 0.5 % TIPS-pc OLEDs indicates positive MEL at low fields we believe that this line-shape is significantly influenced by charge dynamics in PVK, considering the high concentration of PVK in these OLEDs and can not be used to study the TIPS-pc mechanisms alone.

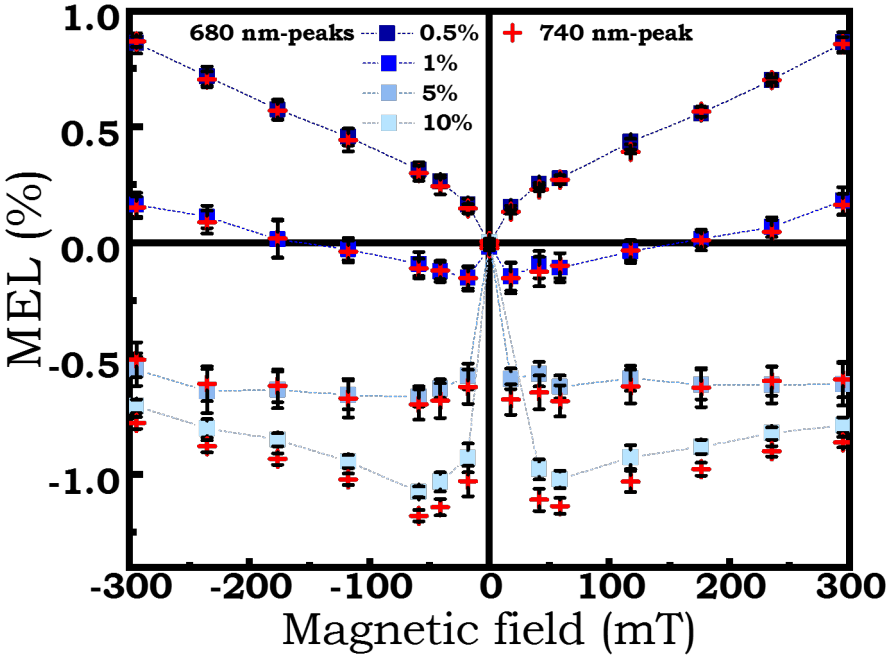

Figure 6.11: Magnetoelectroluminescence (MEL) from TIPS-pc/PVK OLEDs showing (blue-squares) calculated by integrating under the first EL-peak (600 nm to 680 nm) and (red-pluses) calculated by integrating under the second EL-peak (700 nm to 800 nm) measured at an applied voltage of 14 V and current densities of $\approx 1.8\,\mathrm{mA/cm^2}$ for 0.5 % device, $\approx 1.2\,\mathrm{mA/cm^2}$ for 1 % and $\approx 1.7\,\mathrm{mA/cm^2}$ for 5 % devices and applied voltage of 12 V and current densities of $\approx 2\,\mathrm{mA/cm^2}$ for the 10 % device. b) Increased magnitude of MEL from the second EL-peak as compared to the first EL-peak for the 10 % device.

In order to explain SF dominated MEL signals in conjunction with the transient-EL data indicating significant TTA contribution to EL, we develop a kinetic model to understand the underlying mechanisms. We use a kinetic scheme incorporating field-dependent interconversion between singlet and triplet states via the intermediate triplet-pair state to explain the line-shapes in further detail in the following section.

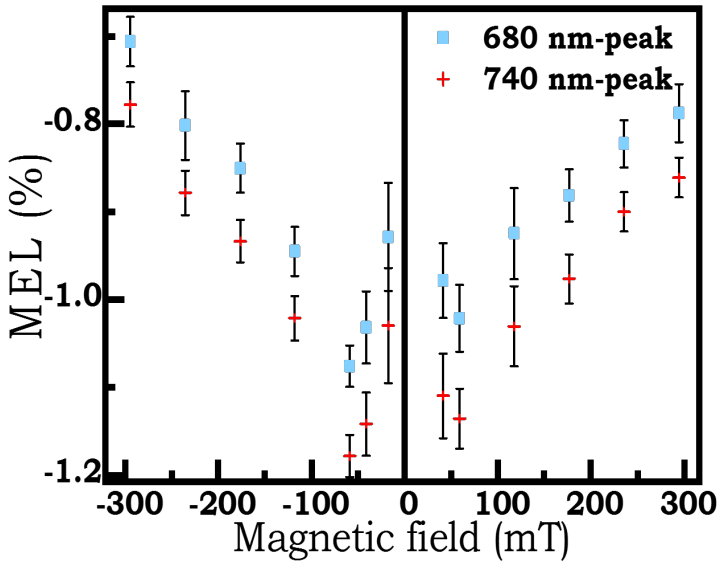

Figure 6.12: Increased magnitude of MEL from the second EL-peak as compared to the first EL-peak for the 10 % device.

6.4 Theoretical MEL Model

In this section we develop a simplified kinetic model based on the well-known Merrifield model [19] which explains magnetic field effects on triplet-triplet annihilation (see appendix 6.2.3 for derivation) and the singlet-fission model developed in previous studies of similar efficient singlet-fission molecules [27] (see appendix B for derivation) that explains magneto-photoluminescence (MPL).

6.4.1 Spin Hamiltonian

For the purpose of this model, we will work with pair Hamiltonian with components described in Section 6.2, similar to the one used in the well-known Merrifield model [19], defined as:

$$\hat{H} = \underbrace{J(\hat{S}_1.\hat{S}_2)}_{\hat{H}_{exchange}} + \sum_{i=1,2} \underbrace{(g\mu_B B.(\hat{S}_i)}_{\hat{H}_{Zeeman}} + \underbrace{D.(\hat{S}_{iz}^2 - (2/3)) + E.(\hat{S}_{ix}^2 - \hat{S}_{iy}^2))}_{\hat{H}_{zfs}}, \tag{6.42}$$

with $\hat{S}_n = (\hat{S}_{nx}, \hat{S}_{ny}, \hat{S}_{nz})$ being the spin-operators for two triplets $n = \{1, 2\}$ and J the coupling parameter for exchange interaction between the two triplets. We will assume $J \ll D$ for this model. B is the magnitude of the external magnetic field and D, E are the zero-field splitting parameters. Finally, g is the Lande g-factor and μ_B the Bohr magneton. For tips-pc we use $D/g\mu_B = 41\,\mathrm{mT}$ and $E/g\mu_B = 6\,\mathrm{mT}$ as experimentally measured in reference [33].

6.4.2 Kinetic Scheme

We focus on two prominent states that define the line-shape of magnetic field effects on EL in these systems as shown in eq. (6.43), the singlet state (S) and the triplet-pair state (P_i). Emission occurs from S with a rate γ_r along with singlet fission which populates the nine P_i states (see Figure 6.13). Singlet fission proceeds from the singlet state to the triplet pair eigenstates with a rate $k_{SF}\alpha_i$ proportional to the singlet character of each state where $\alpha_i = |\langle S|P_i\rangle|^2$. The reverse process, triplet fusion, occurs from the P_i states to the singlet state with a rate $k_{TF}\alpha_i$. Finally, the triplet pairs dissociate with a spin-independent rate γ_d. As changing the external magnetic field changes the singlet-content $|\langle S|P_i\rangle|^2$ of triplet-pair states, this scheme allows us to study the experimentally observed magnetic-field effect on the EL which is defined here as $\gamma_r[S]$.

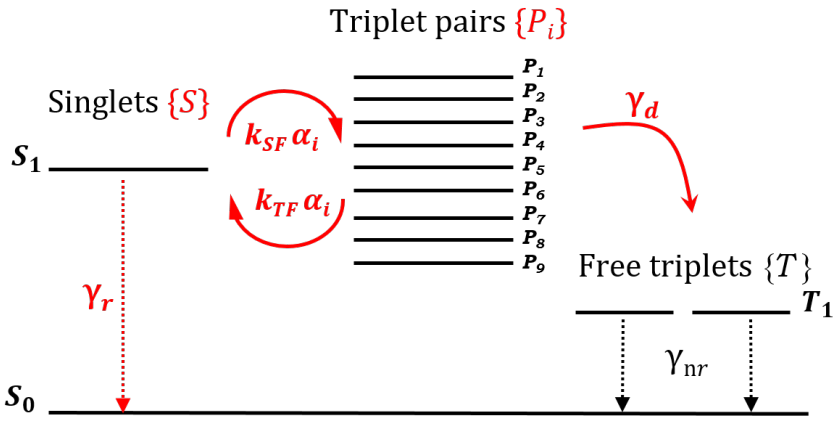

Figure 6.13: Kinetic scheme illustration showing the singlet state, the nine triplet-pair states and the individual triplet states with the rates of conversion between them. The rates are the same as described for the scheme in eq. (6.43) with an additional non-radiative rate γ_{nr} indicating the decay of individual triplets to the ground state.

Considering that OLEDs provide a unique way of populating both the singlet and triplet states via charge recombination we consider a model with generation rates for both of these states as per the scheme below:

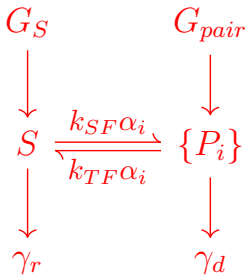

(6.43)

where G_S and G_{pair} are generation rates for the singlet and the triplet-pair states respectively. We assume that each of the nine possible triplet-pair states are generated with

equal probability when any two triplets collide to form a pair-state (P_i) at the same rate G_{pair}. γ_r is the radiative decay rate from singlet states S while γ_d is the spin-independent dissociation rate describing a decay pathway for all triplet-pair states.

We can then write the rate equations for the evolution of the singlet and triplet-pair states as

$$\frac{d[S]}{dt} = -\gamma_r[S] + G_S + \sum_{i=1}^{9} k_{TF}\alpha_i[P_i] - k_{SF}[S]\,, \tag{6.44}$$

$$\frac{d[P_i]}{dt} = G_{pair} + k_{SF}\alpha_i[S] - k_{TF}\alpha_i[P_i] - \gamma_d[P_i]\,. \tag{6.45}$$

Solving for steady-state population we can write

$$[P_i] = \frac{G_{pair} + k_{SF}\alpha_i[S]}{k_{TF}\alpha_i + \gamma_d}\,. \tag{6.46}$$

Substituting this in eq. (6.44) and writing $\varepsilon = \frac{k_{TF}}{\gamma_d}$ we solve for S and define $EL = \gamma_r[S]$ to obtain:

$$EL = \underbrace{\gamma_r G_S\left[\gamma_r + k_{SF}\sum_{i=1}^{9}\left(\frac{\alpha_i}{\varepsilon\alpha_i+1}\right)\right]^{-1}}_{\text{SF-dominated term}} \tag{6.47}$$

$$+ \underbrace{\left(\varepsilon\gamma_r G_{pair}\sum_{i=1}^{9}\left(\frac{\alpha_i}{\varepsilon\alpha_i+1}\right)\right)\left[\gamma_r + k_{SF}\sum_{i=1}^{9}\left(\frac{\alpha_i}{\varepsilon\alpha_i+1}\right)\right]^{-1}}_{\text{TTA-dominated term}}\,. \tag{6.48}$$

This result allows us to clearly identify SF-dominated and TTA-dominated terms separately. Note that in a Merrifield-type model where we are only concerned with triplet generation (i.e. $G_S = 0, k_{SF} = 0$), we arrive at the same result as the Merrifield theory (see Section 6.2.3 for derivation)

$$EL \simeq G_{pair}\sum_{i=1}^{9}\left(\frac{\varepsilon\alpha_i}{\varepsilon\alpha_i+1}\right). \tag{6.49}$$

In Figure 6.14 we show the $MEL = \Delta EL/EL$ line-shapes for varying values of ε. As can be seen clearly, the magnetic field values for zero-crossing of the line-shapes changes with changing ε values and so does the field at which the magnetic field effect saturates.

In the case where $G_{pair} = 0$ and we only excite singlet states (as for PL measurements), we obtain the typical singlet-fission magnetic-field effect line-shape given by (see appendix B for derivation) [27]

$$EL \simeq \frac{\gamma_r G_S}{k_{SF}}\left[\sum_{i=1}^{9}\left(\frac{\alpha_i}{\varepsilon\alpha_i+1}\right)\right]^{-1}. \tag{6.50}$$

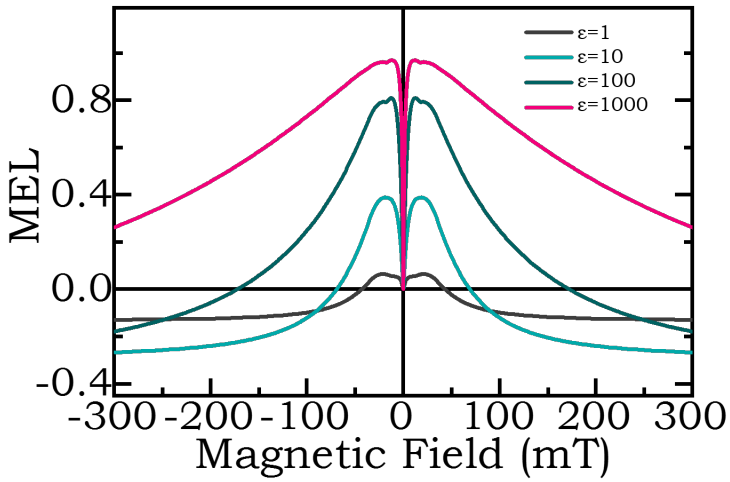

Figure 6.14: Magnetic field effect line-shapes $MEL = \Delta EL/EL$ showing the effect of varying the rate ratio $\varepsilon = k_{TF}/\gamma_d$ on the TTA dominated EL as shown in eq. (6.49).

In an identical fashion to the TTA dominated EL, the SF dominated EL also changes with changing ε. In Figure 6.15 we show this effect by varying the ε value.

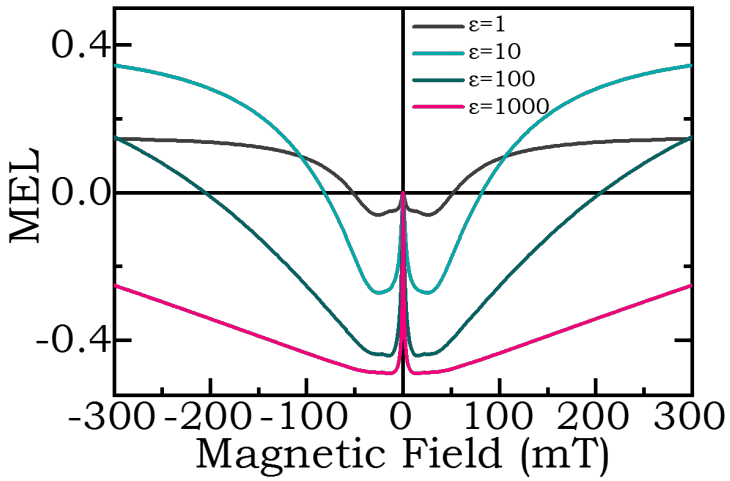

Figure 6.15: Magnetic field effect line-shapes $MEL = \Delta EL/EL$ showing the effect of varying the rate ratio $\varepsilon = k_{TF}/\gamma_d$ on the SF dominated EL shown in eq. (6.50).

In the case of SF dominated EL, the enhanced spin mixing between triplet-pair states at low field $B < 100\,\mathrm{mT}$ as shown in Figure 6.16a causes a reduction in the emission followed by enhancement as the energy splitting between the states increases and the singlet population is retained in the singlet state. In Figure 6.16b we show how the singlet character α_i of each of the nine triplet-pair state varies with varying magnetic field.

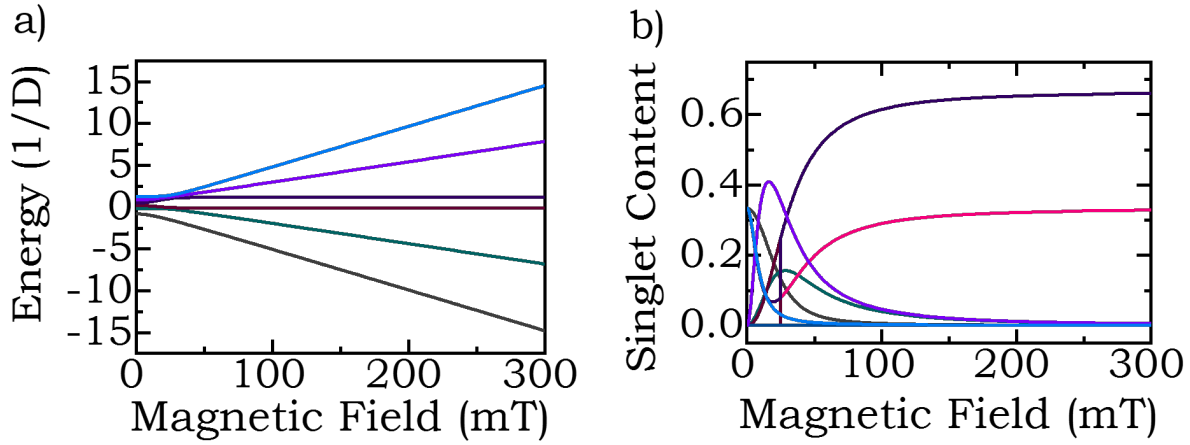

Figure 6.16: Magnetic field dependent signatures of singlet fission dominated system showing: a) The energy level splitting as a function of magnetic field for two-triplet molecules placed parallel to each other with an angle of $\theta = \pi/4$ between the $\boldsymbol{D}$ tensor and the magnetic field, and b) The evolution of singlet character α_i for each of the triplet-pair states as a function of magnetic field for $J \ll D$

6.4.3 Fitting data to model

Considering the highly efficient singlet fission rates reported in TIPS-pentacene [11, 12, 32], we will assume that singlet-fission is the dominant process as compared to radiative decay to ground state from the singlet state. Thus, solving in the limit where rate of radiative emission (γ_r) is much smaller than the singlet-fission rate (k_{SF}) i.e. $\gamma_r \ll k_{SF}\sum_{i=1}^{9}\left[\frac{\alpha_i}{\varepsilon\alpha_i+1}\right]$ we get

$$EL \simeq \frac{\gamma_r G_S}{k_{SF}}\left[\sum_{i=1}^{9}\left(\frac{\alpha_i}{\varepsilon\alpha_i+1}\right)\right]^{-1} + \frac{\gamma_r \varepsilon G_{pair}}{k_{SF}}\sum_{i=1}^{9}\left(\frac{\alpha_i}{\varepsilon\alpha_i+1}\right)\left[\sum_{i=1}^{9}\left(\frac{\alpha_i}{\varepsilon\alpha_i+1}\right)\right]^{-1}, \quad (6.51)$$

$$\implies EL \simeq \frac{\gamma_r}{k_{SF}} G_{pair}\varepsilon\left(\frac{G_S}{G_{pair}}\left(\sum_{i=1}^{9}\left[\frac{\varepsilon\alpha_i}{\varepsilon\alpha_i+1}\right]\right)^{-1}+1\right). \quad (6.52)$$

The MFE defined earlier in eq. (6.41) as $(EL(B)/EL(B=0)-1)$ is therefore independent of rates k_{SF} and γ_r; the line-shape of the field-effect is dictated by the field-dependent term $\left(\sum_{i=1}^{9}\left[\frac{\varepsilon\alpha_i}{\varepsilon\alpha_i+1}\right]\right)^{-1}$. Thus, fitting the MEL data to this model, using ε as a fitting parameter, we can derive information about the ratio of the rate of generation of singlets (k_{TF}) from the P_i states to the rate of dissociation of triplet-pairs into individual triplets (γ_d) as $\varepsilon = k_{TF}/\gamma_d$.

Figure 6.17 displays the fit of our model to MEL data from the OLEDs. We operate LEDs at a constant voltage, and measure the electroluminescence under the influence of an

external magnetic field. We capture the entire electroluminescence spectrum to generate the data points with measured uncertainty as displayed in Figure 6.17 by integrating emission from TIPS-pentacene. We compare the line-shapes of the MEL with our kinetic model and find that ε increases with increasing TIPS-pentacene concentration.

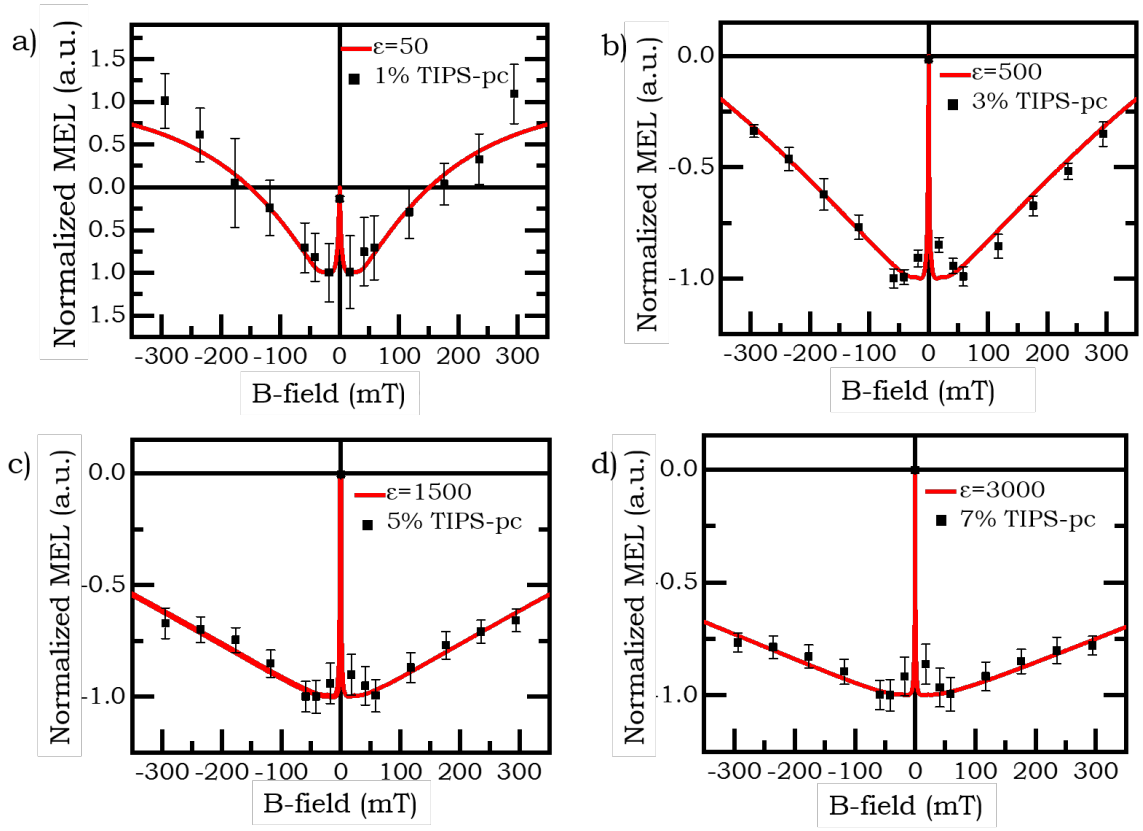

Figure 6.17: Magnetoelectroluminescence data (black squares) with kinetic model fitted (red line). Each of the four graphs indicate different concentrations of TIPS-pentacene in PVK (polymer matrix) and different $\varepsilon = k_{TF}/\gamma_d$ i.e. the ratio of rate of forming singlets to the rate of dissociating through other pathways from the triplet-triplet pair state. The ratio G_S/G_{pair} is assumed to be 2/3 as the ratio of singlet:triplet generation in OLEDs is 1:3 and for triplet-pair it can be expected to be $\sim$ 1:3/2.

Recall that $\varepsilon = k_{TF}/\gamma_d$ where k_{TF} is the rate of triplet fusion and γ_d is the rate of dissociation of the triplet-pairs. This result thus implies that as we increase the concentration of TIPS-pentacene in our LEDs, triplet-fusion increases. This however doesn't contribute to an increase in the external EL quantum yield (see Figure 6.7). Thus, we conjecture that although higher concentration of TIPS-pentacene molecules increases generation of singlet excitons through enhanced triplet fusion, an efficient singlet fission channel still dominates thus quenching the EL yield of such devices. This rapid interconversion between the singlet and triplet-pair states also explains the delayed EL component contributing over 50 % to the total EL.

6.5 Conclusions and future work

In conclusion, we have used TIPS-pc/PVK OLEDs as a model system demonstrating simultaneous singlet fission and triplet fusion, to study the correlation between singlet fission and triplet fusion via the intermediate triplet-pair state. On measuring the absorption and photoluminescence (PL) from the TIPS-pc/PVK films, we observed solution-like features in these films indicating well dispersed TIPS-pc molecules in the PVK matrix with no significant aggregation. Furthermore, we studied the time-resolved PL and noticed that the PL decay lifetimes for films with 0.1 % and 0.5 % TIPS-pc concentration in PVK were identical to those found in dilute TIPS-pc solution of ≈ 13 ns. We observed that this monoexponential decay for low concentration films changes to a biexponential decay for higher concentration (5 % to 10 %) films indicating alternative PL decay channels present in the films. On studying the corresponding time-resolved EL from OLEDs prepared using these blends, we observed that a bimolecular delayed-EL component contributed ≈ 50 % to the total EL, which has previously been assigned to triplet-triplet annihilation by Di and Yang et al. [5] in similar OLEDs.

Having established the presence of significant TTA in our devices we also observed that increasing the dopant (TIPS-pc) concentration in the PVK matrix from 1 % to 10 % resulted in ≈ 10 times lower EQE while the current flowing through the devices increased. We believe that this EL quenching could be due to the fast and efficient singlet fission which enhances as a function of TIPS-pc concentration in our devices. Although we observed no significant aggregation-induced changes in the transition energies in the absorption spectra, we do observe decreasing height of the 680 nm emission peak with respect to the 780 nm peak in the EL spectrum (see Figure 6.5b) with increasing TIPS-pc concentration, indicating presence of quasi-aggregated regions in high-concentration films. However, we note that Walker et al. observe similar reduction in the height ratios of the two peaks in their photoluminescence spectra for different concentration of TIPS-pc solutions, where, in their highest concentration solution, they assign this feature to emission from the triplet-pair excimer [11]. Thus perhaps this slightly red-shifted reduction in the 680 nm EL peak is indicative of the increased triplet-pair concentration in the higher TIPS-pc concentration OLEDs.

As singlet fission is known to proceed via an intermediate triplet-pair (TT) state and conversion of this intermediate triplet-pair into individual triplets defines the efficiency of

fission [11, 12, 29], the same dependence on intermolecular geometry is expected for TTA. In order to understand which of these two processes dominate in our devices (SF or TTA) and to investigate the role of an intermediate TT state in singlet-triplet interconversion, we study the magnetic-field dependence of EL. We observe two trends in MEL line-shapes with increasing TIPS-pc concentration: (i) the magnitude of MEL signal increases making the line-shapes more negative, and (ii) the magnetic field strength required for MFE zero-crossing (from negative MEL to positive MEL) increases, changing the line-shapes.

To extract more information about the underlying processes from the MEL data we develop a kinetic model encompassing both SF and TTA based on the Merrifield theory to fit the data [19, 27]. We fit the data using a fitting parameter $\varepsilon = k_{TF}/\gamma_d$ which decides the direction in which the reaction proceeds once a triplet-pair is formed (either via TTA or SF); it either goes back to forming a singlet with a high triplet-fusion rate k_{TF} or dissociates and decays with a rate γ_d. On fitting the data we observe that ε increases with increasing TIPS-pc concentration in the OLEDs thus indicating that formation of a singlet from the TT-pair becomes a more likely outcome as TIPS-pc concentration increases in TIPS-pc/PVK OLEDs. This effect in broadening of the MEL line-shapes due to increasing ε is called the *kinetic broadening* which indicates the presence of long-lived triplet-pairs. This is understandable as the higher the TIPS-pc concentration, more and more triplet pairs are formed in the OLEDs. The presence of two competing processes SF and TTA results in long-lived triplet pairs some of which eventually form a singlet exciton and result in radiative emission.

As mentioned earlier, dissociation of the triplet-pair into individual triplets strongly depends on the geometry of the surrounding molecules [29], which in turn dictates the efficiency of singlet-fission. In our OLEDs, the triplet pairs generated seem to preferentially form singlets from the triplet-pairs as the concentration of TIPS-pc increases indicating the preferential geometry of TIPS-pc molecules for converting the triplet-pair into a singlet exciton instead of forming free triplet excitons. The MEL model developed in this work therefore provides a way to probe the direction of reaction from the TT-pair state and thus can be a useful tool to optimize the active layer molecular packing motif in OLEDs where the emitting molecule is capable of both SF and TTA, as in our devices. This could then provide a way to strategically enhance the electroluminescence of such OLEDs by utilizing TTA-formed singlets.

Bibliography

1. Merrifield, R. Diffusion and mutual annihilation of triplet excitons in organic crystals. *Accounts of Chemical Research* **1,** 129–135 (1968).

2. Smith, M. B. & Michl, J. Singlet fission. *Chemical Reviews* **110,** 6891–6936 (2010).

3. Gray, V., Dzebo, D., Abrahamsson, M., Albinsson, B. & Moth-Poulsen, K. Triplet–triplet annihilation photon-upconversion: towards solar energy applications. *Physical Chemistry Chemical Physics* **16,** 10345–10352 (2014).

4. Cheng, Y. Y., Fückel, B., MacQueen, R. W., Khoury, T., Clady, R. G., Schulze, T. F., Ekins-Daukes, N., Crossley, M. J., Stannowski, B., Lips, K. *et al.* Improving the light-harvesting of amorphous silicon solar cells with photochemical upconversion. *Energy & Environmental Science* **5,** 6953–6959 (2012).

5. Di, D., Yang, L., Richter, J. M., Meraldi, L., Altamimi, R. M., Alyamani, A. Y., Credgington, D., Musselman, K. P., MacManus-Driscoll, J. L. & Friend, R. H. Efficient Triplet Exciton Fusion in Molecularly Doped Polymer Light-Emitting Diodes. *Advanced Materials* **29,** 1605987 (2017).

6. Jia, W., Chen, Q., Chen, L., Yuan, D., Xiang, J., Chen, Y. & Xiong, Z. Molecular spacing modulated conversion of singlet fission to triplet fusion in rubrene-based organic light-emitting diodes at ambient temperature. *The Journal of Physical Chemistry C* **120,** 8380–8386 (2016).

7. Tang, X., Hu, Y., Jia, W., Pan, R., Deng, J., Deng, J., He, Z. & Xiong, Z. Intersystem Crossing and Triplet Fusion in Singlet-Fission-Dominated Rubrene-Based OLEDs Under High Bias Current. *ACS Applied Materials & Interfaces* **10,** 1948–1956 (2018).

8. Gärditz, C., Mückl, A. G. & Cölle, M. Influence of an external magnetic field on the singlet and triplet emissions of tris-(8-hydroxyquinoline) aluminum (III)(Al q 3). *Journal of Applied Physics* **98,** 104507 (2005).

9. Kondakov, D. Characterization of triplet-triplet annihilation in organic light-emitting diodes based on anthracene derivatives. *Journal of Applied Physics* **102,** 114504 (2007).

10. Merrifield, R., Avakian, P. & Groff, R. Fission of singlet excitons into pairs of triplet excitons in tetracene crystals. *Chemical Physics Letters* **3,** 386–388 (1969).

11. Walker, B. J., Musser, A. J., Beljonne, D. & Friend, R. H. Singlet exciton fission in solution. *Nature Chemistry* **5,** 1019 (2013).

12. Zimmerman, P. M., Zhang, Z. & Musgrave, C. B. Singlet fission in pentacene through multi-exciton quantum states. *Nature Chemistry* **2,** 648 (2010).

13. Ehrler, B., Walker, B. J., Böhm, M. L., Wilson, M. W., Vaynzof, Y., Friend, R. H. & Greenham, N. C. In situ measurement of exciton energy in hybrid singlet-fission solar cells. *Nature Communications* **3,** 1019 (2012).

14. Yang, L., Tabachnyk, M., Bayliss, S. L., Böhm, M. L., Broch, K., Greenham, N. C., Friend, R. H. & Ehrler, B. Solution-processable singlet fission photovoltaic devices. *Nano Letters* **15,** 354–358 (2014).

15. Jundt, C., Klein, G., Sipp, B., Le Moigne, J., Joucla, M. & Villaeys, A. Exciton dynamics in pentacene thin films studied by pump-probe spectroscopy. *Chemical Physics Letters* **241,** 84–88 (1995).

16. Vilar, M. R., Heyman, M. & Schott, M. Spectroscopy of low-energy electrons backscattered from an organic solid surface: pentacene. *Chemical Physics Letters* **94,** 522–526 (1983).

17. Stern, H. L., Musser, A. J., Gelinas, S., Parkinson, P., Herz, L. M., Bruzek, M. J., Anthony, J., Friend, R. H. & Walker, B. J. Identification of a triplet pair intermediate in singlet exciton fission in solution. *Proceedings of the National Academy of Sciences* **112,** 7656–7661 (2015).

18. Dover, C. B., Gallaher, J. K., Frazer, L., Tapping, P. C., Petty II, A. J., Crossley, M. J., Anthony, J. E., Kee, T. W. & Schmidt, T. W. Endothermic singlet fission is hindered by excimer formation. *Nature Chemistry* **10,** 305 (2018).

19. Merrifield, R. Magnetic effects on triplet exciton interactions. *Pure and Applied Chemistry* **27,** 481–498 (1971).

20. Tang, C. L. *Fundamentals of quantum mechanics: for solid state electronics and optics* (Cambridge University Press, 2005).

21. Weil, J. A. & Bolton, J. R. *Electron paramagnetic resonance: elementary theory and practical applications* (John Wiley & Sons, 2007).

22. Lee, S.-Y., Paik, S.-Y., McCamey, D. R., Yu, J., Burn, P. L., Lupton, J. M. & Boehme, C. Tuning hyperfine fields in conjugated polymers for coherent organic spintronics. *Journal of the American Chemical Society* **133,** 2019–2021 (2011).

23. Zarea, M., Carmieli, R., Ratner, M. A. & Wasielewski, M. R. Spin dynamics of radical pairs with restricted geometries and strong exchange coupling: The role of hyperfine coupling. *The Journal of Physical Chemistry A* **118,** 4249–4255 (2014).

24. Johnson, R., Merrifield, R., Avakian, P. & Flippen, R. Effects of magnetic fields on the mutual annihilation of triplet excitons in molecular crystals. *Physical Review Letters* **19,** 285 (1967).

25. Johnson, R. & Merrifield, R. Effects of magnetic fields on the mutual annihilation of triplet excitons in anthracene crystals. *Physical Review B* **1,** 896 (1970).

26. Geacintov, N., Pope, M. & Vogel, F. Effect of magnetic field on the fluorescence of tetracene crystals: exciton fission. *Physical Review Letters* **22,** 593 (1969).

27. Bayliss, S. L., Weiss, L. R., Rao, A., Friend, R. H., Chepelianskii, A. D. & Greenham, N. C. Spin signatures of exchange-coupled triplet pairs formed by singlet fission. *Physical Review B* **94,** 045204 (2016).

28. Ern, V. & Merrifield, R. Magnetic field effect on triplet exciton quenching in organic crystals. *Physical Review Letters* **21,** 609 (1968).

29. Wakasa, M., Yago, T., Sonoda, Y. & Katoh, R. Structure and dynamics of triplet-exciton pairs generated from singlet fission studied via magnetic field effects. *Communications Chemistry* **1,** 9 (2018).

30. Wallikewitz, B. H., Kabra, D., Gélinas, S. & Friend, R. H. Triplet dynamics in fluorescent polymer light-emitting diodes. *Physical Review B* **85,** 045209 (2012).

31. Liu, H., Jia, W., Zhang, Y., Zhang, Q., Lei, Y., Lu, C., Ling, Y. & Xiong, Z. Tuning magneto-electroluminescence in organic light emitting diodes by controlling the competition between singlet fission and triplet fusion. *Synthetic Metals* **198,** 6–9 (2014).

32. Ramanan, C., Smeigh, A. L., Anthony, J. E., Marks, T. J. & Wasielewski, M. R. Competition between singlet fission and charge separation in solution-processed blend films of 6, 13-bis (triisopropylsilylethynyl) pentacene with sterically-encumbered perylene-3, 4: 9, 10-bis (dicarboximide) s. *Journal of the American Chemical Society* **134,** 386–397 (2011).

33. Bayliss, S. L., Thorley, K. J., Anthony, J. E., Bouchiat, H., Greenham, N. C. & Chepelianskii, A. D. Localization length scales of triplet excitons in singlet fission materials. *Physical Review B* **92,** 115432 (2015).

Chapter 7

Conclusions

In the previous chapters we have discussed three important strategies for surpassing the Shockley Queisser limit: (i) tandem solar cells, (ii) singlet fission sensitization and (iii) triplet-triplet annihilation.

In Chapter 4, we demonstrate a monolithic, solution-processed perovskite/CQD tandem solar cell. We highlight the importance of inter-subcell radiative coupling effect in improving the tandem solar cell efficiencies. Recycling the photons generated via radiative recombination in the top cell by utilising them for photocurrent generation in the bottom cell results in a significant enhancement ($\geq$ 11 % absolute gain) of the overall device efficiency. We discuss the individual device optimisation and describe the orthogonal solvent processing method adapted for the fabrication of our devices. Using SEM images we show that this deposition method maintains the integrity of each of the ten deposited layers. We report a two-terminal, monolithic perovskite/CQDs tandem solar cell with PCE of 1 % showing clear evidence of voltage addition of the two sub-cells. The CQD sub-cell limits the short-circuit current densities in our tandem devices thus limiting their efficiency.

The two main reasons restraining photocurrent generation in the CQD devices were identified to be: (i) significant amount of photocurrent being generated from high-energy (blue) photons due to relatively thin (100 nm to 150 nm) CQD layer; (ii) the difficulty of depositing a thick CQD layer using the spin-coating method. Thus we explored an alternative dip-coating method for depositing the CQDs which allowed us to increase the thickness of the CQD layers up to 200 nm. This method resulted in CQD device PCE reaching 6 % for 1.2 eV CQDs which was previously limited by spin-coating method to 3.6 %. This was a significant improvement considering the maximum efficiency of such devices reported in literature at the time was 10.6 % [1]. However, the photocurrent generated from the dip-coated CQD device after filtering out the blue photons with the perovskite-cell stack was still limited to 6 mA/cm^2 which would still make the CQD device the current-limiting sub-cell in perovskite/CQD tandem solar cells. Combining our model with experimental data from the literature we project that the tandem cell performance

of 29 % can be expected using the monolithic tandem architecture proposed by our work. Furthermore, using the same model we show that a detailed balance efficiency of 43 % can be achieved using 1.55 eV perovskite as the top-cell semiconductor along with 1.0 eV CQDs as the bottom-cell semiconductor.

In Chapter 5 we demonstrate incorporation of pentacene films prepared from a novel solution-processed precursor (p-Pc) in singlet fission (SF) sensitized organic and hybrid solar cells. Following the complete cleavage of attached side-groups on annealing, we demonstrate that the pentacene formed via the precursor route forms thin-films with bulk-phase molecular packing. Furthermore, we incorporate p-Pc into bilayer devices with C_{60} as the electron acceptor molecule and compare it with pristine pentacene bilayer devices [2]. We find that although singlet fission still remains 200 % efficient [3], the generated triplets are trapped at the interfaces thus limiting device performances.

We also integrate p-Pc in bulk heterojunction (BHJ) solar cells with $PC_{61}BM$ and observe significant contribution to photocurrent between 500 nm and 700 nm indicating charge generation from SF-generated triplets. Following the work of Ehrler et al. [4] and Yang et al. [5] we prepare bilayer p-Pc/CQD devices and also experiment with p-Pc/CQD BHJ-type blends. Although we obtained significant photovoltage from the BHJ p-Pc/CQD devices reaching $\sim$ 0.7 V, extracting photocurrent from these devices remained a challenge. Since triplet diffusion length of $\approx$ 40 nm in pentacene [6] limits the SF domain size to 40 nm and higher film thickness improves light absorption, we focused on optimizing the BHJ-type architecture to efficiently extract SF-generated triplets. By using electron microscopy, we investigated the distribution of CQDs in a p-Pc matrix. The requirement of thermal-cleavage of side groups from the pentacene precursor was seen to limit the application of p-Pc in p-Pc/CQD BHJ devices as the thermal annealing causes aggregation and merger of the CQDs. We speculate that the chemical impurity of 3 % present in the commercially bought pentacene precursor could be the primary reason limiting the electronic properties of p-Pc films and further purification of the precursor could result in p-Pc device characteristics matching those of pristine pentacene. Our work presents a comprehensive understanding of the advantages and shortcomings of using the novel pentacene precursor and provides pathways for using singlet fission in photovoltaics.

In Chapter 6 we study triplet-triplet annihilation in TIPS-pc/PVK OLEDs which is an interesting system demonstrating simultaneous singlet fission and triplet fusion. Using a range of different concentrations of TIPS-pc by weight in a polymer matrix and

confirming that our TIPS-pc/polymer films are aggregate free, we fabricate OLEDs using this host/guest active layer. From the device characteristics, we observe that at a constant applied voltage, the current flowing through our devices increases with increasing TIPS-pc concentration while the external quantum efficiencies decrease indicating the presence of efficient SF in these devices. However, on studying the time-resolved EL from these devices we notice about 50 % contribution from a bimolecular delayed process to the total EL which we assign to TTA based on previous work [7]. Since SF and TTA are both spin-dependent mechanisms, we use magnetic-field effects on the EL as a probe to understand the underlying mechanisms in these OLEDs and develop a model based on the Merrifield theory to explain these effects [8, 9].

The overall magnetoelectroluminescence (MEL) line-shapes from our OLEDs resemble those of singlet fission dominated MEL reported in literature [10–12]. However, we observe two additional trends in MEL line-shapes with increasing TIPS-pc concentration: (i) the magnitude of MEL signal increases, and (ii) the B-field required for zero-crossing (from negative MEL to positive MEL) increases, changing the line shapes. We fit our data using the kinetic model developed in this work and use $\varepsilon = k_{TF}/\gamma_d$ as the fitting parameter which decides the direction in which the reaction proceeds once a triplet-pair is formed (either via TTA or SF); it either goes back to forming a singlet with a high triplet-fusion rate k_{TF} or diffuses via other pathways with a rate γ_d. On fitting the data we observe kinetic broadening as ε increases with increasing TIPS-pc concentration in the OLEDs. Thus indicating that formation of a singlet from the triplet-pair becomes a more likely outcome as TIPS-pc concentration increases in TIPS-pc/PVK OLEDs.

We note that the dissociation of a triplet-pair into individual triplets strongly depends on the geometry of surrounding molecules [13], and this dissociation rate in turn dictates the efficiency of a singlet-fission event. Thus the fate of the triplet-pair can be indicative of which of the two processes (SF or TTA), will dominate in a device. The MEL model developed in this work, provides a way to probe the direction of reaction from the TT-pair state and thus can be a useful tool to optimize the active layer molecular packing motif in OLEDs where the emitting molecule is capable of both SF and TTA, as in our devices. Thus the model developed in our work provides a way to understand the dominant spin-dependent mechanism in OLEDs and can be adapted to strategically utilise TTA for enhancing TTA based OLEDs.

Bibliography

1. Lan, X., Voznyy, O., García de Arquer, F. P., Liu, M., Xu, J., Proppe, A. H., Walters, G., Fan, F., Tan, H., Liu, M. *et al.* 10.6% certified colloidal quantum dot solar cells via solvent-polarity-engineered halide passivation. *Nano Letters* **16,** 4630–4634 (2016).

2. Congreve, D. N., Lee, J., Thompson, N. J., Hontz, E., Yost, S. R., Reusswig, P. D., Bahlke, M. E., Reineke, S., Van Voorhis, T. & Baldo, M. A. External quantum efficiency above 100% in a singlet-exciton-fission–based organic photovoltaic cell. *Science* **340,** 334–337 (2013).

3. Tabachnyk, M., Karani, A. H., Broch, K., Pazos-Outón, L. M., Xiao, J., Jellicoe, T. C., Novák, J., Harkin, D., Pearson, A. J., Rao, A. *et al.* Efficient singlet exciton fission in pentacene prepared from a soluble precursor. *APL Materials* **4,** 116112 (2016).

4. Ehrler, B., Walker, B. J., Böhm, M. L., Wilson, M. W., Vaynzof, Y., Friend, R. H. & Greenham, N. C. In situ measurement of exciton energy in hybrid singlet-fission solar cells. *Nature Communications* **3,** 1019 (2012).

5. Yang, L., Tabachnyk, M., Bayliss, S. L., Böhm, M. L., Broch, K., Greenham, N. C., Friend, R. H. & Ehrler, B. Solution-processable singlet fission photovoltaic devices. *Nano Letters* **15,** 354–358 (2014).

6. Tabachnyk, M., Ehrler, B., Bayliss, S., Friend, R. H. & Greenham, N. C. Triplet diffusion in singlet exciton fission sensitized pentacene solar cells. *Applied Physics Letters* **103,** 190_1 (2013).

7. Di, D., Yang, L., Richter, J. M., Meraldi, L., Altamimi, R. M., Alyamani, A. Y., Credgington, D., Musselman, K. P., MacManus-Driscoll, J. L. & Friend, R. H. Efficient Triplet Exciton Fusion in Molecularly Doped Polymer Light-Emitting Diodes. *Advanced Materials* **29,** 1605987 (2017).

8. Merrifield, R. Magnetic effects on triplet exciton interactions. *Pure and Applied Chemistry* **27,** 481–498 (1971).

9. Bayliss, S. L., Weiss, L. R., Rao, A., Friend, R. H., Chepelianskii, A. D. & Greenham, N. C. Spin signatures of exchange-coupled triplet pairs formed by singlet fission. *Physical Review B* **94,** 045204 (2016).

10. Tang, X., Hu, Y., Jia, W., Pan, R., Deng, J., Deng, J., He, Z. & Xiong, Z. Intersystem Crossing and Triplet Fusion in Singlet-Fission-Dominated Rubrene-Based OLEDs Under High Bias Current. *ACS Applied Materials & Interfaces* **10,** 1948–1956 (2018).

11. Jia, W., Chen, Q., Chen, L., Yuan, D., Xiang, J., Chen, Y. & Xiong, Z. Molecular spacing modulated conversion of singlet fission to triplet fusion in rubrene-based organic light-emitting diodes at ambient temperature. *The Journal of Physical Chemistry C* **120,** 8380–8386 (2016).

12. Liu, H., Jia, W., Zhang, Y., Zhang, Q., Lei, Y., Lu, C., Ling, Y. & Xiong, Z. Tuning magneto-electroluminescence in organic light emitting diodes by controlling the competition between singlet fission and triplet fusion. *Synthetic Metals* **198,** 6–9 (2014).

13. Wakasa, M., Yago, T., Sonoda, Y. & Katoh, R. Structure and dynamics of triplet-exciton pairs generated from singlet fission studied via magnetic field effects. *Communications Chemistry* **1,** 9 (2018).

Appendix A

List of Publications

1. Karani, A., Yang, L., Greenham, N.C. and Di, D., 2018, September. Toward high-efficiency solution-processed tandem solar cells. In Organic, Hybrid, and Perovskite Photovoltaics XIX (Vol. 10737, p. 107371I). International Society for Optics and Photonics.

2. Karani, A., Yang, L., Bai, S., Futscher, M.H., Snaith, H.J., Ehrler, B., Greenham, N.C. and Di, D., 2018. Perovskite/colloidal quantum dot tandem solar cells: theoretical modeling and monolithic structure. ACS Energy Letters, 3(4), pp.869-874.

3. Tabachnyk, M., Karani, A.H., Broch, K., Pazos-Outn, L.M., Xiao, J., Jellicoe, T.C., Novk, J., Harkin, D., Pearson, A.J., Rao, A. and Greenham, N.C., 2016. Efficient singlet exciton fission in pentacene prepared from a soluble precursor. APL Materials, 4(11), p.116112.

4. Davis, N.J., Allardice, J.R., Xiao, J., Karani, A., Jellicoe, T.C., Rao, A. and Greenham, N.C., 2019. Improving the photoluminescence quantum yields of quantum dot films through a donor/acceptor system for near-IR LEDs. Materials Horizons, 6(1), pp.137-143.

5. Zhao, B., Lee, L.C., Yang, L., Pearson, A.J., Lu, H., She, X.J., Cui, L., Zhang, K.H., Hoye, R.L., Karani, A. and Xu, P., 2018. In Situ Atmospheric Deposition of Ultrasmooth Nickel Oxide for Efficient Perovskite Solar Cells. ACS Applied Materials & Interfaces, 10(49), pp.41849-41854.

6. Karani, A., Weiss, L. R., Macpherson, S., Greenham, N. C., 2019. Triplet-triplet annihilation process in highly efficient singlet-fission molecule tips-pentacene OLEDs. *In preparation*

Appendix B

Appendices for Chapter 6

Derivation for EL kinetic scheme

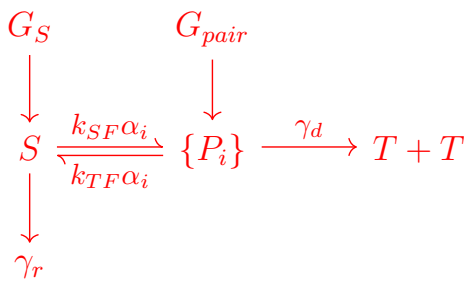

(B.1)

$$\frac{d[S]}{dt} = -\gamma_r[S] + G_S + \sum_{i=1}^{9} k_{TF}\alpha_i[P_i] - \sum_{i=1}^{9} k_{SF}\alpha_i[S] \tag{B.2}$$

$$\frac{d[P_i]}{dt} = G_{pair} + k_{SF}\alpha_i[S] - k_{TF}\alpha_i[P_i] - \gamma_d[P_i] \tag{B.3}$$

Solving for steady-state population:

$$[P_i] = \frac{G_{pair} + k_{SF}\alpha_i[S]}{k_{TF}\alpha_i + \gamma_d} \tag{B.4}$$

Substituting this in B.2 and writing $\varepsilon = \frac{k_{TF}}{\gamma_d}$

$$-\gamma_r[S] + G_S + \sum_{i=1}^{9} k_{TF}\alpha_i \left[\frac{G_{pair} + k_{SF}\alpha_i[S]}{k_{TF}\alpha_i + \gamma_d}\right] - \sum_{i=1}^{9} k_{SF}\alpha_i[S] = 0 \tag{B.5}$$

$$G_S = \gamma_r[S] - \sum_{i=1}^{9} k_{TF}\alpha_i \left[\frac{G_{pair} + k_{SF}\alpha_i[S]}{k_{TF}\alpha_i + \gamma_d}\right] + \sum_{i=1}^{9} k_{SF}\alpha_i[S] \tag{B.6}$$

Substitute $k_{TF}/\gamma_d = \varepsilon$ to simplify the above to

$$G_S = \gamma_r[S] - \sum_{i=1}^{9} \left[\frac{\varepsilon\alpha_i G_{pair} + k_{SF}\varepsilon\alpha_i^2[S]}{\varepsilon\alpha_i + 1}\right] + \sum_{i=1}^{9} k_{SF}\alpha_i[S] \tag{B.7}$$

$$G_S = \gamma_r[S] - \left(\sum_{i=1}^{9} \left[\frac{\varepsilon\alpha_i G_{pair} + k_{SF}\varepsilon\alpha_i^2[S]}{\varepsilon\alpha_i + 1} - k_{SF}\alpha_i[S]\right]\right) \tag{B.8}$$

$$G_S = \gamma_r[S] - \left(\sum_{i=1}^{9} \left[\frac{\varepsilon\alpha_i G_{pair} + k_{SF}\varepsilon\alpha_i^2[S] - k_{SF}\varepsilon\alpha_i^2[S] - k_{SF}\alpha_i[S]}{\varepsilon\alpha_i + 1} \right] \right) \tag{B.9}$$

$$G_S = \gamma_r[S] - \sum_{i=1}^{9} \left[\frac{\varepsilon\alpha_i G_{pair}}{\varepsilon\alpha_i + 1} \right] + k_{SF} \sum_{i=1}^{9} \left[\frac{\alpha_i}{\varepsilon\alpha_i + 1} \right][S] \tag{B.10}$$

$$G_S + \sum_{i=1}^{9} \left[\frac{\varepsilon\alpha_i G_{pair}}{\varepsilon\alpha_i + 1} \right] = \gamma_r[S] + k_{SF} \sum_{i=1}^{9} \left[\frac{\alpha_i}{\varepsilon\alpha_i + 1} \right][S] \tag{B.11}$$

$$[S] = G_S \left(\gamma_r + k_{SF} \sum_{i=1}^{9} \left[\frac{\alpha_i}{\varepsilon\alpha_i + 1} \right] \right)^{-1} + G_{pair}\varepsilon \sum_{i=1}^{9} \left[\frac{\alpha_i}{\varepsilon\alpha_i + 1} \right] \left(\gamma_r + k_{SF} \sum_{i=1}^{9} \left[\frac{\alpha_i}{\varepsilon\alpha_i + 1} \right] \right)^{-1} \tag{B.12}$$

Defining electroluminescence as $EL = \gamma_r[S]$

$$EL = \gamma_r G_S \left(\gamma_r + k_{SF} \sum_{i=1}^{9} \left[\frac{\alpha_i}{\varepsilon\alpha_i + 1} \right] \right)^{-1} + \gamma_r G_{pair}\varepsilon \sum_{i=1}^{9} \left[\frac{\alpha_i}{\varepsilon\alpha_i + 1} \right] \left(\gamma_r + k_{SF} \sum_{i=1}^{9} \left[\frac{\alpha_i}{\varepsilon\alpha_i + 1} \right] \right)^{-1} \tag{B.13}$$

It is important to notice here that if the G_S is set to 0, the second term will giverise to a line-shape similar to an all-TTA scheme. With a limit that $\gamma_r \gg k_{SF}$ or considering no SF channel. Solving for the case where the rate of radiative emission from the singlet state (γ_r) is much smaller than the singlet fission rate (k_{SF}) i.e. $\gamma_r \ll k_{SF} \sum_{i=1}^{9} \left[\frac{\alpha_i}{\upsilon\alpha_i + 1} \right]$

$$EL \simeq \frac{\gamma_r G_S}{k_{SF}} \left[\sum_{i=1}^{9} \left(\frac{\alpha_i}{\varepsilon\alpha_i + 1} \right) \right]^{-1} + \frac{\gamma_r \varepsilon G_{pair}}{k_{SF}} \sum_{i=1}^{9} \left(\frac{\alpha_i}{\varepsilon\alpha_i + 1} \right) \left[\sum_{i=1}^{9} \left(\frac{\alpha_i}{\varepsilon\alpha_i + 1} \right) \right]^{-1} \tag{B.14}$$

$$EL \simeq \frac{\gamma_r}{k_{SF}} \left(G_S \left(\sum_{i=1}^{9} \left[\frac{\alpha_i}{\varepsilon\alpha_i + 1} \right] \right)^{-1} + G_{pair}\varepsilon \right) \tag{B.15}$$

In the case where $\gamma_r \gg k_{SF} \sum_{i=1}^{9} \left[\frac{\alpha_i}{\upsilon\alpha_i + 1} \right]$

$$EL \simeq G_S \left(1 - \frac{k_{SF}}{\gamma_r} \sum_{i=1}^{9} \left[\frac{\alpha_i}{\varepsilon\alpha_i + 1} \right] \right) + \varepsilon G_{pair} \sum_{i=1}^{9} \left[\frac{\alpha_i}{\varepsilon\alpha_i + 1} \right] \left(1 - \frac{k_{SF}}{\gamma_r} \sum_{i=1}^{9} \left[\frac{\alpha_i}{\varepsilon\alpha_i + 1} \right] \right) \tag{B.16}$$

Singlet-fission only scheme

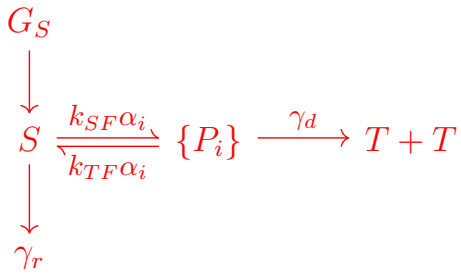

(B.17)

The rate equations :

$$\frac{d[S]}{dt} = -\gamma_r[S] + G_S + \sum_{i=1}^{9} k_{TF}\alpha_i[P_i] - \sum_{i=1}^{9} k_{SF}\alpha_i[S] = 0 \tag{B.18}$$

$$\frac{d[P_i]}{dt} = k_{SF}\alpha_i[S] - k_{TF}\alpha_i[P_i] - \gamma_d[P_i] = 0 \tag{B.19}$$

From (39):

$$[P_i] = \frac{k_{SF}\alpha_i}{k_{TF}\alpha_i + \gamma_d}[S] \tag{B.20}$$

Substituting this in (45), we finally have

$$-\gamma_r[S] + G_S + \sum_{i=1}^{9} k_{TF}\alpha_i\left[\frac{k_{SF}\alpha_i}{k_{TF}\alpha_i + \gamma_d}[S]\right] - \sum_{i=1}^{9} k_{SF}\alpha_i[S] = 0 \tag{B.21}$$

$$G_S = \gamma_r[S] - \sum_{i=1}^{9} k_{TF}\alpha_i\left[\frac{k_{SF}\alpha_i}{k_{TF}\alpha_i + \gamma_d}[S]\right] + \sum_{i=1}^{9} k_{SF}\alpha_i[S] \tag{B.22}$$

Write $k_{TF}/\gamma_d = \upsilon$ and use the identity $\sum_{i=1}^{9} \alpha_i = 1$ to simplify the above to

$$G_S = \gamma_r - k_{SF}\sum_{i=1}^{9}\left[\frac{\upsilon\alpha_i^2}{\upsilon\alpha_i + 1} - \alpha_i\right][S] \tag{B.23}$$

$$G_S = \gamma_r + k_{SF}\sum_{i=1}^{9}\left[\frac{\alpha_i}{\upsilon\alpha_i + 1}\right][S] \tag{B.24}$$

$$[S] = G_S\left[\gamma_r + k_{SF}\sum_{i=1}^{9}\left[\frac{\alpha_i}{\upsilon\alpha_i + 1}\right]\right]^{-1} \tag{B.25}$$

Thus, as $PL = \gamma_r[S]$

$$PL = \gamma_r G_S \left[\gamma_r + k_{SF} \sum_{i=1}^{9} \left[\frac{\alpha_i}{v\alpha_i + 1}\right]\right]^{-1} \tag{B.26}$$

In the case where $\gamma_r \ll k_{SF} \sum_{i=1}^{9} \left[\frac{\alpha_i}{v\alpha_i+1}\right]$

$$PL \simeq \frac{\gamma_r G_S}{k_{SF}} \left[\sum_{i=1}^{9} \left[\frac{\alpha_i}{v\alpha_i + 1}\right]\right]^{-1} \tag{B.27}$$

In the case where $\gamma_r \gg k_{SF} \sum_{i=1}^{9} \left[\frac{\alpha_i}{v\alpha_i+1}\right]$

$$PL \simeq G_S \left[1 - \frac{k_{SF}}{\gamma_r} \sum_{i=1}^{9} \left[\frac{\alpha_i}{v\alpha_i + 1}\right]\right] \tag{B.28}$$

Triplet-triplet annihilation and MFEs

In this section we will explore the effect of magnetic field on triplet-triplet annihilation (TTA) process and use it to explain the magnetic field data observed in experiments.The Merrifield theory [87] provides a detailed description of the effect of a magnetic field on TTA and SF. And the same theory can then be used to explain triplet-polaron interaction. The following is a simplified kinetic scheme to describe the TTA mechanism:

$$\begin{array}{ccccc} & & S_1 + S_0 & & \\ & & \uparrow{\scriptstyle k_S|S_n|^2} & & \\ T + T & \underset{k_{-1}}{\overset{g_n T}{\rightleftharpoons}} & \{P_n\} & \xrightarrow{k_T|T_n|^2} & T + S_0 \\ & & \downarrow{\scriptstyle k_Q|Q_n|^2} & & \\ & & Q + S_0 & & \end{array} \tag{B.29}$$

where T+T defines triplet annihilation, P_n defines the intermediate T-T pair state, S_1+S_0, $T + S_0$, $Q + S_0$ define the singlet, triplet and quintet states post annihilation. Other definitions: $|S_n|^2 = |\langle\psi_n|S\rangle|^2$; $|T_n|^2 = \sum_{m=1}^{3} |\langle\psi_n|T_m\rangle|^2$; $|Q_n|^2 = \sum_{m=1}^{5} |\langle\psi_n|Q_m\rangle|^2$ such that $\sum_n |S_n|^2$=1;$\sum_n |T_n|^2$=3 and $\sum_n |Q_n|^2$=5;finally g_n describe the rate of triplet pair generation from free triplets and k_{-1} describes the reverse process. Now we can write a rate equation for the intermediate triplet-pair state as follows:

$$\frac{\partial P_n}{\partial t} = g_n[T]^2 - (k_{-1} + k_S|S_n|^2 + k_T|T_n|^2 + k_Q|Q_n|^2)P_n \tag{B.30}$$

And assuming that:

- All of the 9 triplet-pair states are generated with equal probability, i.e. $g_n = \frac{1}{9}k_1$
- Quintet states lie too high in energy to be formed by TTA, i.e. $k_Q = 0$.

Thus for steady state population, we can write:

$$\frac{\partial P_n}{\partial t} = 0 \tag{B.31}$$

$$P_n = \frac{1}{9}k_1[T]^2 \frac{1}{(k_{-1} + k_S|S_n|^2 + k_T|T_n|^2 + k_Q|Q_n|^2)} \tag{B.32}$$

$$P_n = \frac{1}{9}k_1[T]^2 \frac{1}{(k_{-1} + k_S|S_n|^2 + k_T|T_n|^2)} \tag{B.33}$$

From the kinetic scheme above, the total TTA rate $\gamma[T]^2$ to singlet channel is given by:

$$\gamma_{TTA}[T]^2 = \sum_n k_S|S_n|^2 P_n \tag{B.34}$$

Substituting for P_n

$$\gamma_{TTA}[T]^2 = \sum_n k_S|S_n|^2 \left(\frac{1}{9}k_1[T]^2 \frac{1}{(k_{-1} + k_S|S_n|^2 + k_T|T_n|^2)}\right) \tag{B.35}$$

$$\therefore \gamma_{TTA} = \sum_n k_S|S_n|^2 \left(\frac{1}{9}k_1 \frac{1}{(k_{-1} + k_S|S_n|^2 + k_T|T_n|^2)}\right) \tag{B.36}$$

To find the rate of TTA and its evolution under different B-field, we need to use the spin Hamiltonian of triplet-triplet pair and find the evolution of triplet-triplet wavefunction with B-field. To simplify further, we note that no triplet-pair state can simultaneously have a singlet and a triplet character [87], and $|T_n|^2 = 1$ for a pure triplet state, regardless of triplet-basis states which means that k_T is independent of B-field. Thus, we can simplify the eq. B.36 as:

$$\therefore \gamma_{TTA} = \frac{1}{9}k_1 \sum_n \frac{k_S|S_n|^2}{k_{-1} + k_S|S_n|^2} \tag{B.37}$$

Redefining $|S_n|^2 = \alpha_i$ and defining a new parameter β for the ratio of rate of decay of the triplet-pair to individual triplets and rate of forming singlets from the triplet-pair state $\beta = \frac{k_{-1}}{k_S}$.

$$\gamma_{TTA} = \frac{k_1}{9} \sum_i \frac{\alpha_i}{\beta + \alpha_i} \tag{B.38}$$

We can simplify the scheme to determine the effect of B-field on γ_{TTA}:

$$\begin{array}{ccccc} G_T & & & & \\ \downarrow & & & & \\ T + T & \underset{k_{-1}}{\overset{g_n T}{\rightleftharpoons}} & \{P_i\} & \xrightarrow{k_S \alpha_i} & S_1 + S_0 \\ & & & & \downarrow \gamma_r \\ & & & & \textit{Emission} \end{array} \tag{B.39}$$

$$\frac{\partial S}{\partial t} = \sum_i k_S \alpha_i P_i - \gamma_r S \tag{B.40}$$

$$\frac{\partial S}{\partial t} = 0 \implies \sum_i k_S \alpha_i P_i = \gamma_r S \tag{B.41}$$

$$\therefore S = \frac{1}{\gamma_r} \left(\sum_i k_S \alpha_i P_i \right) \tag{B.42}$$

Substituting for P_i in terms of γ_{TTA} we can write an equation for S in terms of $[T]^2$:

$$\therefore S = \frac{1}{\gamma_r} \Bigg(\underbrace{\gamma_{TTA}[T]^2}_{\sum_n k_S |S_n|^2 P_n} \Bigg) \tag{B.43}$$

Defining PL as:

$$PL = \gamma_r S = \gamma_r \left(\frac{1}{\gamma_r} \left(\gamma_{TTA}[T]^2 \right) \right) \tag{B.44}$$

$$\therefore PL = \gamma_{TTA}[T]^2 \tag{B.45}$$

where

$$\gamma_{TTA} = \frac{k_1}{9} \sum_i \frac{\alpha_i}{\beta + \alpha_i} = \frac{k_1}{9} \sum_i \frac{\varepsilon \alpha_i}{1 + \varepsilon \alpha_i} \tag{B.46}$$